HIGH-FREQUENCY MODULATED-BACKSCATTER COMMUNICATION USING MULTIPLE ANTENNAS

A Dissertation
Presented to
The Academic Faculty

by

Joshua David Griffin

In Partial Fulfillment
of the Requirements for the Degree
Doctor of Philosophy in the
School of Electrical and Computer Engineering

Georgia Institute of Technology
May 2009

HIGH-FREQUENCY MODULATED-BACKSCATTER COMMUNICATION USING MULTIPLE ANTENNAS

Approved by:

Professor Gregory D. Durgin, Advisor
School of Electrical and Computer Engineering
Georgia Institute of Technology

Professor Mary Ann Ingram
School of Electrical and Computer Engineering
Georgia Institute of Technology

Professor Andrew Peterson
School of Electrical and Computer Engineering
Georgia Institute of Technology

Dr. Pavel Nikitin
Lead Engineer
Intermec Technologies Corporation

Professor Paul Steffes
School of Electrical and Computer Engineering
Georgia Institute of Technology

Date Approved: January 23, 2009

To my parents,

David and Ellen Griffin,

for their ever-present love and support.

ACKNOWLEDGEMENTS

A project of this magnitude is not possible without the help and support of many and I owe a great deal of thanks to those who assisted. I would like to begin by thanking my advisor, Professor Gregory Durgin, for not only his technical expertise and guidance, but his constant encouragement and merciful attitude. I have learned a tremendous amount from him both as an advisor and as a friend. I also thank the members of The Propagation Group: Yenpao "Albert" Lu for his antenna expertise and designs; Alex Trzecieski for his programming help; Rikai Huang for her antenna designs and measurements; Joel Prothro for wandering through Japan with me; Lorne Liechty for keeping me moving; and Joey Duvall for her help with antenna and fading measurements.

I owe a special thanks to Ryan Pirkl; in fact, he deserves his own paragraph. I am thankful for many fruitful discussions with him and his expert help with my hardware design and data processing.

In addition, I thank Dr. William Barott for his hardware advice and Professor Bernard Kippelen and Dr. Andreas Haldi for use of their laboratory space. I also thank my committee – Professor Paul Steffes, Professor Andrew Peterson, Professor Mary Ann Ingram, Dr. Pavel Nikitin, and Professor Gregory Durgin – for their time and valuable feedback. In particular, I thank Dr. Pavel Nikitin for taking time away from his work and family travel to my defense; I am grateful.

Though what follows is often considered cliqué, I assure you that it is not in this case. I sincerely thank Jesus Christ for giving me the the opportunity, skills, and support necessary to complete this degree. I hope to use wisely the gifts He has given me in order to bring Him honor and praise.

TABLE OF CONTENTS

LIST OF TABLES

LIST OF FIGURES

LIST OF SYMBOLS OR ABBREVIATIONS

$(\cdot)^*$	Denotes the complex conjugate of $(\cdot)$.
λ	Carrier frequency wavelength (m).
λ_o	Wavelength of the 5.79 GHz carrier used in the fading measurements.
$\mathbf{E}\{\cdot\}$	Denotes ensemble average of $\{\cdot\}$.
$\mathcal{N}(\mu, \sigma^2)$	A normal distribution with mean μ and variance σ^2.
τ	Power transmission coefficient.
Θ	RF-tag antenna on-object gain penalty.
$\tilde{\Gamma}(t)$	The complex, time-varying, RF-tag-antenna-load reflection coefficient.
$\tilde{\mathbf{H}}^b(t, \vec{r})$	The $N \times L$ complex, baseband-channel impulse response matrix of the backscatter link that is a function of time t and RF-tag position $\vec{r}$.
$\tilde{\mathbf{H}}^f(t, \vec{r})$	The $L \times M$ complex, baseband-channel impulse response matrix of the forward link that is a function of time t and RF-tag position $\vec{r}$.
$\tilde{\mathbf{S}}(t)$	The narrowband, $L \times L$ signaling matrix that describes the time-varying modulation applied to the signals scattered from the RF-tag antennas.
$\tilde{\vec{n}}(t)$	The $N \times 1$ matrix of noise components.
$\tilde{\vec{x}}(t)$	The $M \times 1$ vector of signals input to the reader transmitter antennas.
$\tilde{\vec{y}}(t, \vec{r})$	The $N \times 1$ vector of baseband signals received through the $M \times L \times N$, dyadic backscatter channel that is a function of time t and RF-tag position $\vec{r}$.
B	Path blockage loss.
B_b	Tag-to-reader link blockage loss.
B_f	Reader-to-tag blockage loss.
F	Backscatter link budget fade margin.
F_α	Fade margin for bistatic, collocated reader antennas.
F_β	Fade margin for bistatic, dislocated reader antennas.
F_p	Power-up link fade margin.
G_T	Load-matched, free-space gain of the reader transmitter antenna.
G_t	Load-matched, free-space gain of the RF-tag antenna.
K	The Rician K factor defined as the ratio of specular to nonspecular multipath power in a channel whose fading follows a Rician distribution.

M	Backscatter modulation factor.
P_T	Power transmitted by the reader (W).
P_t	Power coupled into the RFIC (W).
r	Reader-to-tag separation distance (m).
r_b	Tag-to-reader separation distance (m).
r_f	Reader-to-tag separation distance (m).
X	Polarization mismatch loss.
X_b	Tag-to-reader polarization mismatch.
X_f	Reader-to-tag polarization mismatch.
$Z_{\text{RFIC}}^{A,B}$	The input impedance of an RF-tag's RFIC in modulation state A or B.
ADC	Analog-to-digital converter.
ASK	Ampltidue-shift keying.
BAP	Battery-assisted, passive RF tag.
BER	Bit error rate.
CDF	Cumulative density function.
CF	Characteristic function.
CFA	Current-feedback amplifier.
CPW	Coplanar waveguide.
CW	Continuous wave.
DAC	Digital-to-analog converter.
DAT	Dual-antenna RF tag.
FET	Field-effect transistor.
GaAs	Gallium arsenide.
IF	Intermediate frequency.
i.i.d.	Independent, identically distributed.
ISM	Industrial, scientific, and medical.
LNA	Low-noise amplifier.
LO	Local oscillator.
LOS	Line-of-sight.

MMSE Minimum mean-square-error.

MRC A diversity combining technique known as maximal ratio combining.

MSE Mean-square-error.

NLOS Non-line-of-sight.

PDF Probability density function.

PHEMT Pseudomorphic, high electron mobility transistor.

PN Pseudo-random.

PSK Phase-shift keying.

RCS Radar cross-section.

RFIC Radio frequency integrated circuit.

RFID Radio frequency identification.

RX Receiver.

SAT Single-antenna RF tag.

SINR Signal-to-interference-plus-noise-ratio.

SVN Subversion.

TX Transmitter.

VFA Voltage-feedback amplifier.

SUMMARY

Backscatter radio – the broad class of systems that communicate using scattered electromagnetic waves – is the driving technology behind many compelling applications such as radio frequency identification (RFID) tags and passive sensors. These systems can be used in many ways including article tracking, position location, passive temperature sensors, passive data storage, and in many other systems which require information exchange between an interrogator and a small, low-cost transponder with little-to-no transponder power consumption. Although backscatter radio is maturing, such systems have limited communication range and reliability caused, in part, by multipath fading. The research presented in this dissertation investigates how multipath fading can be reduced using multiple antennas at the interrogator transmitter, interrogator receiver, and on the transponder, or RF tag. First, two link budgets for backscatter radio are presented and fading effects demonstrated through a realistic, 915 MHz, RFID-portal example. Each term in the link budget is explained and used to illuminate the propagation and high-frequency effects that influence RF tag operation. Second, analytic envelope distributions for the $M \times L \times N$, dyadic backscatter channel – the general channel in which a backscatter system with M transmitter, L RF tag, and N receiver antennas operates – are derived. The distributions show that multipath fading can be reduced using multiple-antenna RF tags and by using separate transmitter and receiver antenna arrays at the interrogator. These results are verified by fading measurements of the $M \times L \times N$, dyadic backscatter channel at 5.8 GHz – the center of the 5725-5850 MHz unlicensed industrial, scientific, and medical (ISM) frequency band that offers reduced antenna size, increased antenna gain, and, in some cases, reduced object attachment losses compared to the commonly used 902-928 MHz ISM band. Measurements were taken with a custom backscatter testbed and details of its design are provided. In the end, this dissertation presents both theory and measurements that demonstrate multipath fading reductions for backscatter-radio systems that use multiple antennas.

CHAPTER I

INTRODUCTION

Chapter Overview: This chapter provides the following:

- An introduction to backscatter radio and an overview of its technical challenges.
- An introduction to multipath fading and diversity techniques.
- A review of related research literature.
- A brief overview of the research presented in this dissertation.

Since the concept of modulating backscatter for communication was proposed by Stockman in 1948 [1], considerable research and development has been invested in the area of backscatter radio by both industry and academia. What began as steady developmental work in the 1970's has crescendoed to a virtual backscatter-radio research and development explosion in the 21st century [2]. This excitement has been driven by many compelling backscatter-radio applications such as radio frequency identification (RFID), passive sensors, and passive data storage. Current or possible applications of backscatter radio include parcel tracking, temperature sensors, inventory tracking, position location, passive memory sticks, and so on. The growth of backscatter-radio technology is expected only to increase as many yet undiscovered applications that require communication with little-to-no power consumption are identified.

Given the ever increasing use of backscatter radio, one might be tempted to think that it has completely matured as a technology; however, the reality is that much basic research is still needed to improve backscatter-radio system performance, reduce transponder cost, and reduce the size of the transponder footprint. The research presented in this dissertation focuses on backscatter-radio performance; specifically, how backscatter-radio range and communication reliability are affected by multipath fading. However, before discussing

multipath fading, it is worthwhile to define a few basic terms and concepts related to backscatter radio.

1.1 Backscatter-Radio Basics

Backscatter radio is a broad term that refers to any system in which a transponder, or *RF tag*[1], communicates with an interrogator, or *reader*, by modulating the electromagnetic fields scattered from the RF-tag's antenna(s). The RF tag modulates the scattered fields using *load modulation* – i.e., modulating the electromagnetic field by changing the load presented to the RF-tag antenna [3], shown in Figure 1. Typically, backscatter-radio systems operate in the far-field of the reader antennas, though it is possible for far-field tags to be used in the near field [4]. In far-field systems, traveling waves propagate between the reader and the RF tag and the power carried by the waves scattered from the RF tag is proportional to $|\tilde{\Gamma}(t)|^2$, where $\tilde{\Gamma}(t)$ is the time-varying, complex load reflection coefficient.

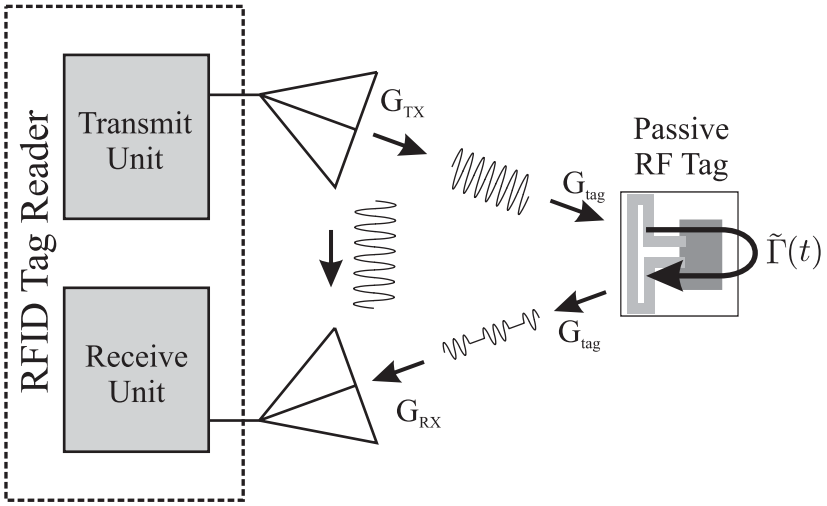

Figure 1: In a backscatter-radio system, the reader transmits a signal to the RF tag which is modulated using load modulation and scattered back to the reader receiver (Reprinted from [5], © 2008 IEEE).

The use of traveling waves and the need for relatively small readers and tags require

[1]In many instances, the terms *RFID tag* and *RF tag* are used interchangeably. Such use is incorrect, however, since RFID is an acronym for radio frequency identification and is simply one application of an RF tag.

that backscatter-radio systems use high frequencies. In the United States, backscatter-radio systems typically operate in the unlicensed, industrial, scientific, and medical (ISM) frequency bands available at 902-928 MHz and 2400-2483.5 MHz with the 902-928 MHz band experiencing the heaviest commercial use. Though it receives less attention, the 5725-5850 MHz ISM band is also available for backscatter radio. As discussed in Chapter 4, there are several potential benefits offered by this frequency band.

Another characteristic of backscatter RF tags is that they can be either passive or semi-passive, depending on their source of power. A *passive* RF tag operates its circuitry using power rectified from the incident wave transmitted by the reader. A *semi-passive* tag – sometimes called a battery-assisted passive (BAP) tag – uses a small battery or other onboard power source to provide DC power for tag operation. In both passive and semi-passive tags, no power is used to amplify and transmit signals; instead, the mechanism of communication is scattered waves. Passive and semi-passive backscatter tags are different from what is commonly called an *active* RFID tag. Such a tag is actually a transceiver that transmits and receives signals instead of scattering waves, as is done by transponder (i.e., passive and semi-passive backscatter RF tags are transponders). In this dissertation, the term "RF tag" will refer to both passive and semi-passive backscatter tags that operate in the far-field of the reader, unless specified otherwise.

Backscatter-radio systems are related to lower frequency, inductively coupled tag systems; however, the mechanism of communication is different. While both types of systems use load modulation, traveling waves do not propagate in inductively coupled systems. Instead, a change in the RF-tag antenna load produces a corresponding change in the reader antenna impedance through inductive coupling. Such systems typically operate in the frequency bands at 125/134 kHz (low frequency tags) or 13.56 MHz (high-frequency tags) and have up to a 1 m range [3, 6].

Of course, real-world use of RF tags cannot always be neatly arranged in the far-field-backscatter and near-field-inductive categories. For example, when a far-field, backscatter tag is used in the near-field of the reader antenna, it is difficult to classify the mechanism of communication as either near-field inductive (or near-field capacitive) or as backscattered

traveling waves. Instead, communication is accomplished as a combination of the two.

1.2 Backscatter-Radio Challenges

The potential of backscatter radio is great and so are the challenges faced in designing reliable, low-cost backscatter systems with adequate range. Accordingly, current research topics cover a wide range of issues including research on antenna designs for RF tags and readers [7]; techniques to improve isolation between the reader transmitter and receiver [8]; low-power, full-featured, integrated-circuit designs for RF tags [9–11]; data anti-collision algorithms [12,13]; methods for RF-tag position location [14]; data security measures; near-field backscatter radio [4]; RF-tag design using organic semiconductors [15]; and efforts to understand the basic physics of backscatter propagation [16]. At the physical level, polarization mismatch loss; object attachment loss resulting from impedance mismatch and reduction in RF-tag antenna gain caused by object proximity; small-scale, multipath-fading loss; and blockage loss all make backscatter-radio design challenging[2].

Small-scale multipath fading alone can significantly reduce an RF-tag's read range and reliability. Small-scale fading is caused by waves scattered from objects located in the vicinity of the backscatter-radio system. If scatterers were *not* present, a transmitted wave would exhibit perfectly defined wavefronts (i.e., contours of constant phase) that travel away from the transmitter in time. In other words, a single homogenous wave, or *specular wave*, would propagate through the environment with a constant amplitude at any given point, discounting path loss [17]. With scatterers present, however, the total field at any point in space is the linear combination of the specular wave and many *nonspecular and diffuse waves* [17] – i.e., *multipath waves* that are reflected or diffracted from scatterers. These multipath waves arrive at the receiver with different amplitudes, phases, and angles of arrival and combine constructively and destructively at different points in space. The result is that the power received by the RF tag and at the reader receiver varies as a function of position – *small-scale multipath fading*. It is the destructive combination of the multipath waves – a *fade* – that can render a backscatter system inoperable. For example, Figure 2

[2]See Chapter 2 for an example and discussion of these losses.

shows a plot of the power received by a passive RF tag in a multipath environment. As the RF tag is moved, the peaks and fades of the received power are both above and below the RF-tag's sensitivity level – i.e., the minimum power required to turn on the passive RF tag. The result is that the RF tag will not be able to operate at every position.

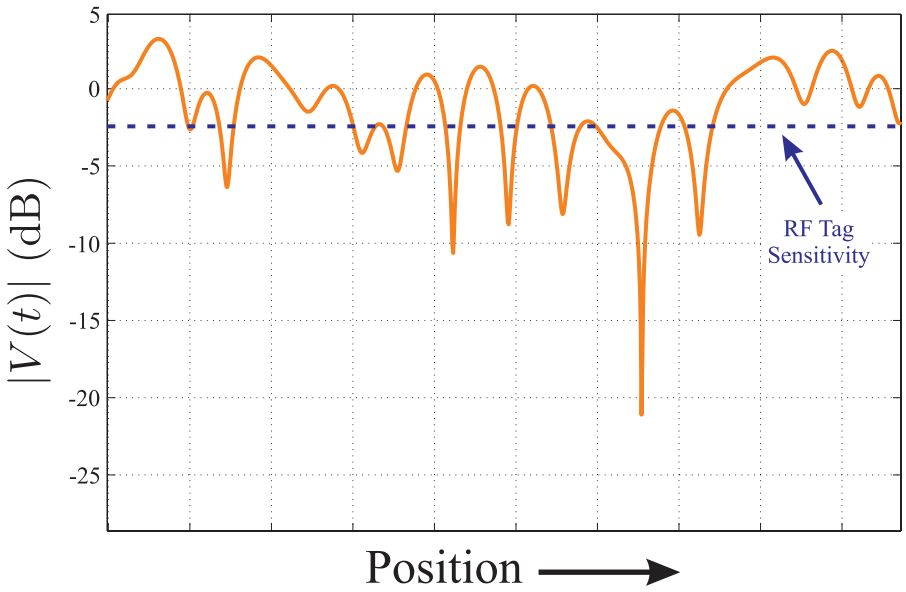

Figure 2: A plot of the power received by an RF tag. Multipath waves cause peaks and fades to occur as the RF tag is moved and limits the number of positions at which the tag can operate. Note that the sensitivity of this RF tag is hypothetical and does not necessarily represent that of a real RF tag.

Although small-scale fading is a significant problem, relatively few measurements have been reported. Fading on the signal received by the RF tag have been reported by Mitsugi *et al.* [18, 19] and Polivka *et al.* [20]. Others have also studied fading on the signal received by the reader – Kim *et al.* [21] made measurements of the backscatter channel reporting envelope cumulative distribution functions (CDFs) for the modulated-backscatter signal received at the reader and Banerjee *et al.* [22, 23] have presented fading measurements as well as spatial and frequency diversity gain measurements at 915 MHz. The fading on the signal received by the reader has radically different fading statistics than that received by the RF tag resulting in more severe fading [21].

Another type of fading that can affect backscatter radio is *large-scale fading*, the counterpart of small-scale fading. Large-scale fades are caused, not by multipath waves, but

by objects that completely or partially block waves from reaching the RF tag or receiver. Large-scale fades usually occur over a distance of several wavelengths while small-scale fading occurs on the order of a single wavelength. Both large- and small-scale fades are solely a function of receiver or RF-tag position, though other types of fading that vary with time or frequency, are possible. For example, time-varying fades result in temporal power fluctuations and can be caused by time-varying scatterers or transmitter movement. If the bandwidth of the signal is large enough, the different path lengths of multipath signals can cause power fluctuations as a function of frequency – *frequency-selective fading* [17]. While temporal, frequency, or spatial fading can all occur in backscatter-radio systems, small-scale fading is the most severe given the narrow bandwidths and relatively low data rates commonly used; though new backscatter-radio applications may change this assertion. Therefore, small-scale multipath fading is the focus of the research presented in this dissertation.

A common method to analyze small-scale multipath fading is to model the variation of the signal using stochastic-process theory. It is worth noting that, although small-scale fading can be modeled using stochastics, the fields *are* deterministic and governed by Maxwell's equations. It is the complexity and sheer number of field/obstacle interactions that occur in a typical channel that make stochastic-process theory a useful tool. In this approach, the behavior of the signal is modeled as a random variable whose value is determined by a prescribed probability distribution. The random variable can represent most any aspect of the received signal including its power, amplitude, and phase; however, it is most useful to let the random variable represent the *envelope*, or amplitude, of the received signal. Its usefulness comes from the fact that the envelope is proportional to power and can be measured by both a sophisticated coherent receiver as well as a simple envelope detector. For example, in Figure 2, the envelope probability distribution function (PDF) of the multipath fading could be found by constructing a histogram of the envelope (which can be found from the power) of the received signal at each position. This PDF could then be used to judge the transmit power necessary to overcome multipath fading, as discussed in Chapter 3.

As a brief example of how multipath fading can affect a backscatter-radio system, consider such a system operating in an environment that causes the power in the specular and nonspecular waves to be equal. In other words, the Rician K factor is equal to 0 dB, as discussed in Chapter 2. Table 2 in Chapter 2 shows that the reader must transmit 12 dB more power than is necessary in a non-fading channel to ensure that the RF tag fails to receive adequate power only 5% of the time[3]. If the reader cannot supply the extra 12 dB of power, all other factors being equal, the RF-tag range will be reduced by 75%. Though this is severe, small-scale fading is even more pronounced in the modulated-backscatter signal received at the reader, as explained in Chapter 3. Therefore, any method to reduce or overcome small-scale fading in the backscatter channel can significantly improve backscatter-radio reliability and range.

1.3 Solutions for Small-Scale Multipath Fading

One way to overcome the effects of small-scale fading is through the use of *diversity*. Diversity is general technique in which multiple, uncorrelated copies of a signal – *diversity branches* – are combined so that signal fades are reduced [17, 24]. The reasoning behind this approach is that if the fading in the different diversity branches is uncorrelated, then the probability is small that the signal on all of the branches will fade simultaneously. Therefore, diversity works best when diversity branch correlation is low and when the number of diversity branches is large. Diversity branches can be decorrelated in many ways that fall into two general categories: temporal diversity and antenna diversity [17].

Temporal Diversity: Temporal diversity is used to mitigate both time- and frequency-varying fading. While these techniques have been studied extensively for use in conventional transmitter-to-receiver channels, some have begun to apply them to backscatter radio. In one such case, a backscatter-radio system capable of using *frequency diversity* was designed by Liu *et al.* [25], but no tests of a frequency diversity scheme have been reported. In a frequency diversity scheme, multiple copies of the signal are transmitted on different

[3]The outage probability is defined in Section 2.2.4

frequencies that are spaced such that their fading statistics are uncorrelated. These diversity branches are combined at the receiver to create a single signal with reduced fading.

As an aside, the Federal Communications Commission (FCC) requires that systems operating the unlicensed ISM frequency bands, occupied by many backscatter-radio systems, use frequency hopping – i.e., the system must jump from one frequency to the next in the band at a specified rate [6]. The goal of this requirement is to reduce interference from nearby systems; however, it also reduces fading for backscatter-radio systems. If the RF tag is located in a deep fade at one frequency, adequate power may be available when the system switches to another. Though such a scheme is beneficial, greater gains are available using antenna diversity, discussed in the next paragraph.

Antenna Diversity: *Antenna diversity* uses spatial separation, the properties of antennas (the polarization or pattern), or a combination of both to provide uncorrelated diversity branches. Antenna diversity is commonly used to mitigate small-scale fading in transmitter-to-receiver channels and, like temporal diversity, has been used by some in backscatter radio. For instance, Ingram *et al.* [26] were the first to discuss using transmit diversity (a particular approach for implementing antenna diversity) in backscatter-radio systems to mitigate small-scale fading. Since then, Kim *et al.* [21] have made the first measurements of the backscatter channel reporting signal envelope CDFs and path loss measurements at 2.4 GHz. Literature shows that other researchers have employed multiple antennas in backscatter-radio systems. However, when multiple antennas were included on the reader, they were not used to combat small-scale multipath fading but for reducing data collisions when multiple RF tags are present [27, 28]; for locating RF tags [29]; or to detect the direction of movement of an RF tag through a reader portal [30]. Two exceptions are Kim *et al.* [31], who tested an antenna array that could be used for spatial and polarization diversity in low frequency (433 MHz) RFID systems (technically not a backscatter system) and Rahmati *et al.* [32] who reported reliability improvements using a commercially available tag reader with two antennas (presumably using a switched antenna diversity). Others have also proposed using multiple antennas on the RF tag. Again, these antennas were not

motivated by small-scale multipath fading, but were used to increase the power available to the tag by increasing the number of antennas in a given tag footprint [33, 34], to form a retrodirective patch array to direct the modulated backscatter towards the reader [35], and to increase the gain of the RF-tag antenna in the direction of the reader with a frequency steerable patch array [36].

Therefore, though progress has been made, there is still much basic research needed to reduce the effects of small-scale fading in backscatter-radio systems. The next section will overview how this research contributes to this goal.

1.4 Research Overview

The research presented in this dissertation seeks to answer the following question:

> *Can multipath fading be reduced for backscatter-radio systems using multiple antennas at the reader transmitter, receiver, and RF tag?*

This investigation begins in Chapter 2 by describing the major issues related to the RF chain of a backscatter-radio system. Two link budgets are provided that describe both the power received by the RF tag and that backscattered to the reader receiver. In Chapter 3, a general framework for describing the $M \times L \times N$, dyadic backscatter channel – i.e., the channel in which a backscatter-radio system with M transmitter, L RF-tag, and N receiver antennas operates – is presented. Using this information, analytic envelope PDFs are derived for the $M \times L \times N$, dyadic backscatter channel that experiences heavy multipath fading (Rayleigh fading). The analytic PDFs are then used to show that small-scale multipath fading can be reduced using multiple RF-tag antennas – a *pinhole diversity* gain – and by adequately spacing the reader transmitter and receiver antennas, which reduces *link correlation*[4]. The first half this research concludes in Chapter 4 by condensing all of the presented theory into four practical guidelines for backscatter-radio design. This chapter also includes an example showing the potential benefits of operating backscatter-radio systems in the 5725-5850 MHz ISM frequency band.

[4]Link correlation is defined in Chapter 3

The second half of this research is experimental in nature and presents multipath-fading measurements for the $M \times L \times N$ backscatter channel under line-of-sight (LOS) and non-line-of-sight (NLOS) conditions in the 5725-5850 MHz ISM frequency band. Chapter 5 gives details of the backscatter testbed designed for this measurement campaign including details of the custom microwave devices that were designed and prototyped – a custom direct-conversion receiver, reader patch antennas, and two RF tags. The measurement results are presented in Chapter 6 in terms of fading CDFs and fade margins which are compared to the analytic distributions discussed in Chapter 3. Conclusions drawn from the research and potential future projects are presented in Chapter 7 and derivations and testbed documentation are included in the appendices.

CHAPTER II

LINK BUDGETS FOR BACKSCATTER-RADIO SYSTEMS

Chapter Overview: This chapter provides the following:

- A power-up link budget to calculate the power coupled into the tag RFIC.
- A backscatter link budget to calculate the modulated-backscatter power received at the reader.
- A detailed description of each link budget term.
- A realistic, RFID-portal example at 915 MHz that demonstrates use of the link budgets.

Passive backscatter-radio design is complicated by the fact that power must be supplied to the RF tag as well as scattered back to the reader receiver. Understanding the propagation mechanisms that govern these signals is important for both designing reliable backscatter tags and readers and for developing new, backscatter-radio systems. This chapter provides two link budgets that describe the power received by the RF-tag radio frequency integrated circuit (RFIC) and the modulated-backscatter power received at the reader [37]. Each term of the link budgets accounts for a particular propagation mechanism or transmission line effect and a detailed discussion of each is given. This chapter concludes by demonstrating use of the link budgets through an example of a passive, backscatter RFID portal operating at 915 MHz. The material in this chapter has been adapted from [37].

2.1 Backscatter-Radio Link Budgets

The first radio link budget is the linear-scale, *power-up link budget* that describes the amount of power received by the tag RFIC, discounting any loss factors internal to the chip.

$$P_t = \frac{P_T G_T G_t \lambda^2 X \tau}{(4\pi r)^2 \Theta B F_p} \tag{1}$$

P_t - power coupled into the tag RFIC (W)

P_T - power transmitted by the reader (W)

G_T - load-matched, free-space gain of the TX antenna

G_t - load-matched, free-space gain of the tag antenna

λ - carrier frequency wavelength (m)

X - polarization mismatch

τ - power transmission coefficient

r - reader-to-tag separation distance (m)

Θ - RF-tag antenna on-object gain penalty

B - path blockage loss

F_p - power-up link fade margin

Equation (1) is similar to the Friis free-space link budget equation [38], but accounts for losses X, τ, Θ, B, and F_p commonly encountered in the backscatter channel. The second radio link budget is the *backscatter link budget* that governs the amount of modulated-backscatter power received by the reader.

$$P_R = \frac{P_T G_R G_T G_t^2 \lambda^4 X_f X_b M}{(4\pi)^4 r_f^2 r_b^2 \Theta^2 B_f B_b F} \tag{2}$$

M - backscatter modulation factor

r_f - reader-to-tag separation distance (m)

r_b - tag-to-reader separation distance (m)

X_f - reader-to-tag link polarization mismatch

X_b - tag-to-reader link polarization mismatch

B_f - reader-to-tag link blockage loss

B_b - tag-to-reader link blockage loss

F - backscatter link budget fade margin

All other terms are as defined for (1). Equation (2) resembles the radar equation [39] which reflects the fact that, in many ways, a backscatter radio is a small radar system. Backscatter radio differs from conventional radar in that the signal transmitted from the reader is used

to power the RF tag (for passive RF tags) and that the RF tag intentionally communicates information back to the reader.

The backscatter link budget will take different forms depending on the antenna configuration of the RF-tag reader. In the *monostatic* configuration, the reader uses a single antenna to transmit and receive. In this case $r_f = r_b$, $X_f = X_b$, $B_f = B_b$, and F is equal to the monostatic fade margin, F_{m}. In the *bistatic* configuration, where separate antennas are used at the reader to transmit and receive, two forms of (2) are possible. If the reader antennas are closely spaced, then the *bistatic collocated* fade margin, F_α is used; however, if the antennas are widely separated, the *bistatic dislocated* fade margin, F_β, is used. The link budget terms determined by the reader antenna configuration are summarized in Table 1. It should be noted that the G_t^2 and Θ^2 terms in (2), while exact for the monostatic case, are only approximate for a bistatic reader. This is because the angles of arrival and departure of waves at the RF-tag antenna are not the same when separate reader transmitter and receiver antennas are used.

Table 1: Backscatter link budget parameters that are determined by the reader antenna configuration – monostatic, bistatic collocated, or bistatic dislocated.

Monostatic	**Bistatic Collocated**	**Bistatic Dislocated**
$r_f = r_b$ $X_f = X_b$ $B_f = B_b$ $F = F_{\mathrm{m}}$	$F = F_\alpha$	$F = F_\beta$

To clarify the notation in Equation (1) and (2), it should be understood that the RF channel in which a backscatter-radio system operates is composed of two parts – the *forward link* and the *backscatter link*. The forward link, also called the reader-to-tag link, describes signal propagation from the reader transmitter to the RF tag and link budget parameters that pertain to this link are denoted by a subscript f. Similarly, the backscatter link, or the tag-to-reader link, describes signal propagation from the RF tag to the reader receiver and link budget parameters that pertain to this link are denoted by a subscript b. These terms will be used interchangeably throughout this dissertation.

2.2 Backscatter-Radio Channel Losses

This section presents details of the physical propagation mechanisms and losses that affect backscatter-radio communication.

2.2.1 Polarization Mismatch

The polarization of an antenna is defined by the polarization of its transmitted waves [38]. The power that an antenna receives is maximized when the polarization of the incident wave is matched to that of the antenna. When this is not the case, the power lost relative to the maximum power received with a polarization match is given by two power polarization mismatch factors, X_f and X_b, for the forward and backscatter links, respectively. Each of these factors varies from 0, with a complete polarization mismatch, to 1 for a perfect polarization match.

In a backscatter system, polarization mismatch is of great importance because the orientation of the RF tag is arbitrary. As the orientation of the tag changes, X_f and X_b can easily render the backscatter-radio system inoperable. One way to ensure that the RF tag receives power, no matter its orientation, is to transmit a circularly polarized wave from the reader transmitter. Doing so will result in $X = X_f = X_b = 3$ dB, but will prevent a complete polarization match. Another method is to use two linearly-polarized antennas on the RF tag that are oriented at 45° with respect to each other in conjunction with cross-polarized reader antennas [37]. This method can prevent a complete polarization mismatch while providing self-interference mitigation[1] [37].

2.2.2 Power Transmission Coefficient

Impedance is the ratio of voltage to current that a given device can accept. When a voltage (or current) wave traveling in a device with impedance Z_A is fed into a device with impedance Z_L, the voltage (or current) wave must increase or decrease to conform to the voltage to current ratio specified by Z_L. In order to change, a reflected wave is launched

[1]Self-interference is the strong, unmodulated signal that propagates directly from the reader transmitter to the reader receiver, shown in Figure 1. Care must be taken to make sure that this signal does not saturate the reader receiver.

that travels in the opposite direction of the original wave. The result is that not all of the power carried by the original wave is transferred to the second device. This result is general and pertains to any situation in which transmission-line theory can be applied including an antenna with an attached load. Given an antenna impedance Z_A and a load impedance Z_L, the normalized amount of power delivered to the load, the power transmission coefficient τ [7, 38], is

$$\tau = \frac{4\,\mathcal{R}e\{Z_A\}\mathcal{R}e\{Z_L\}}{\mathcal{R}e\{Z_A + Z_L\}^2 + \mathcal{I}m\{Z_A + Z_L\}^2} \qquad 0 \leq \tau \leq 1 \tag{3}$$

When $Z_A = Z_L^*$, where $(\cdot)^*$ denotes the complex conjugate, maximum power transfer occurs and $\tau = 1$.

RF tags are particularly susceptible to impedance mismatch losses. RF-tag antenna impedance detuning caused by object attachment [7, 40, 41], close object proximity [42], and antenna deformation [43, 44] will all reduce τ. Mismatches can also be caused by variations in the input of impedance of the RFIC as the received power changes [40, 45]. As an example of antenna detuning, Figure 8 shows that the simulated impedance of a half-wave folded dipole drops from its design value of $300 + j100\,\Omega$ to a virtual short circuit as it is brought close to an infinite, perfectly conducting plane. The result is that $\tau \approx 0$. It should be noted that object proximity and attachment will cause a change in both the antenna's impedance and its gain, discussed in Section 2.2.6.

2.2.3 Modulation Factor

As discussed in Chapter 1, an RF tag modulates the signal backscattered from its antenna by switching the load impedance between two or more states. Typically, a binary modulation scheme (two reflection coefficient states) is used and the amount of modulated-backscatter power is described by the modulation factor M, which Prothro *et al.* [46] defined to be

$$M = \frac{1}{4}\left|\Gamma_A - \Gamma_B\right|^2 \tag{4}$$

where the reflection coefficient is defined as [18]

$$\Gamma_{A,B} = \frac{Z_{\text{RFIC}}^{A,B} - Z_{\text{ant}}^*}{Z_{\text{RFIC}}^{A,B} + Z_{\text{ant}}} \tag{5}$$

and $Z_{\text{RFIC}}^{A,B}$ is the input impedance of the RF port of the RFIC, Z_{ant} is the input impedance of the RF-tag antenna, and $(\cdot)^*$ is complex-conjugate operator. These impedances are shown in Figure 3. This equation assumes the DC component of the received backscattered signal is removed, the backscatter signal has a 50% duty cycle, and an equal number of tag impedance states (data bits) are received.

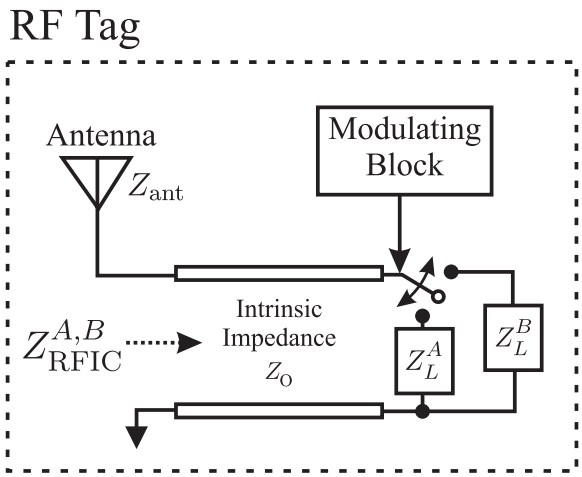

Figure 3: A simplified block diagram of an RF tag. The input impedance of the tag's RFIC $Z_{\text{RFIC}}^{A,B}$ is changed between states A and B by switching the load between Z_L^A and Z_L^B (Reprinted from [37], © 2009 IEEE).

The choice of the modulation factor presents a tradeoff in design parameters [6]. While an open and short circuit, shown on the Smith chart in Figure 4, maximize the power scattered back to the reader, they also minimize the power coupled into the RF tag (see Section 2.2.2). Instead, designers of some commercially available RF tags use amplitude-shift-keying (ASK) modulation and switch the reflection coefficient between a matched load and a short, $M = 0.25$, to balance the power backscattered and absorbed by the RFIC [10]. The short can be easily achieved with a field-effect transistor (FET) and, if designed properly, enough power can be received during the matched load state to operate while in the short circuit state. Other designers use phase-shift-keying (PSK) and simply modulate the reactive component of the chip impedance [11]. This allows constant power to be supplied to the RFIC regardless of the modulation state.

The power backscattered from an RF tag can also be characterized using the tag's effective *radar cross-section* (RCS). Over the years, much research on the RCS of loaded

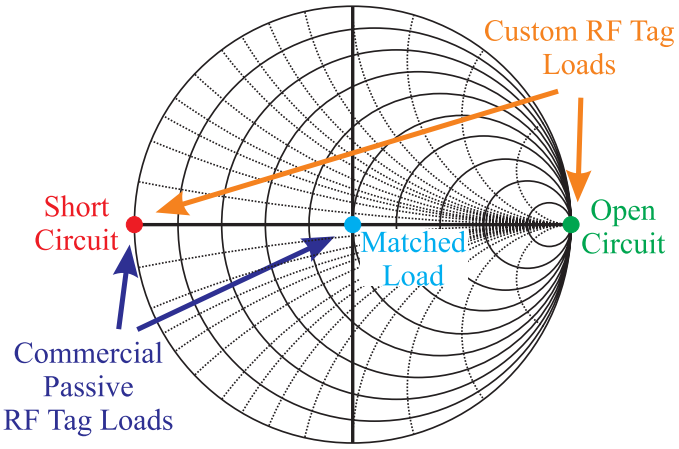

Figure 4: A smith chart showing the open circuit and matched loads used in commercially available passive RF tags. For the custom RF tags discussed in Section 5.3.2, the load was switched between an open and short circuit to maximize the power backscattered to the reader.

antennas has been done with the goal of making "stealthy" antennas – antennas with zero RCS (non-scattering) – for military applications. For modulated-backscatter applications, the goal is to maximize an antenna's RCS while still absorbing enough power to turn on the tag's RFIC. The theory of loaded antenna RCS for modulated-backscatter applications has been presented by Nikitin and Rao [47], Penttilä *et al.* [48], and Fuschini *et al.* [49], among others. In general, the RCS σ_{RCS} can be written in terms of a load-dependent *antenna component* and a load-independent *structural component*,

$$\sigma_{\text{RCS}} = \frac{\lambda^2}{4\pi} G_t^2 |A_s - \Gamma_{A,B}|^2, \tag{6}$$

where A_s is a complex-valued term that represents the structural component and $\Gamma_{A,B}$, defined in (5), represents the antenna component [50]. Since the backscattered signal is proportional to the difference between modulation states, the differential RCS [51] is

$$\Delta\sigma_{\text{RCS}} = \frac{\lambda^2 G_t^2}{4\pi} |\Gamma_A - \Gamma_B|^2 \tag{7}$$

Note that differential RCS is only dependent on the antenna load, not the structural component of the RCS.

2.2.3.1 *Understanding the Backscattered Signal*

Equation (4) shows that the modulated-backscatter power is dependent on the difference between the complex reflection coefficients of each impedance state. While it may not seem intuitive for the backscattered information to be contained in the difference between two reflection states, recall that an RF-tag antenna scatters waves just like any other object in the backscatter channel. What differentiates the RF-tag backscattered signal from other scattered signals is that the RF-tag signal changes with time. If a direct-conversion receiver[2] is used in a static channel, the signals scattered from objects in the channel will be converted to a DC signal $\tilde{V}_{\mathrm{DC}}$ while the time-varying signal from the RF tag $\tilde{V}_{\mathrm{data}}$ will oscillate at the modulation rate, as shown in Figure 5. The baseband signal at any given time epoch is

$$\text{Baseband Received Signal} = \tilde{V}_{\mathrm{DC}} + \tilde{V}_{\mathrm{data}} \tag{8}$$

Therefore, the desired, modulated-backscatter signal can be extracted from the total received signal by blocking $\tilde{V}_{\mathrm{DC}}$ with a series capacitor.

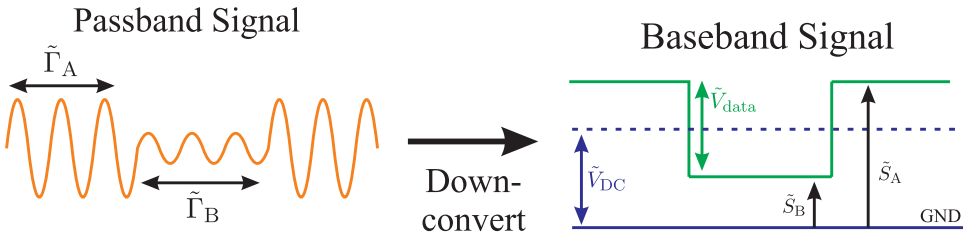

Figure 5: The passband and baseband signal received from a backscatter RF tag. The baseband signal is composed of an unmodulated DC signal $\tilde{V}_{\mathrm{DC}}$ and an oscillating data signal $\tilde{V}_{\mathrm{data}}$.

To see how $\tilde{V}_{\mathrm{DC}}$ and $\tilde{V}_{\mathrm{data}}$ relate to the reflection coefficient at the RF tag, consider the IQ diagram shown in Figure 6. In this figure, the signal received by the reader in RF-tag impedance state A $\tilde{S}_{\mathrm{A}}$ is the vector sum of the transmitted carrier (plus other smaller, unmodulated, scattered signals) $\tilde{C}$ and the modulated-backscatter signal, which is proportional to the RF-tag antenna load reflection coefficient $\tilde{\Gamma}_{\mathrm{A}}$. Likewise, the received signal in RF-tag impedance state B $\tilde{S}_{\mathrm{B}}$ is the sum of $\tilde{C}$ and a signal proportional to $\tilde{\Gamma}_{\mathrm{B}}$.

[2] A direct-conversion receiver converts the spectrum of the received, high-frequency, passband signal directly to a signal whose spectrum is centered around DC. A discussion of the direct-conversion receiver designed for this dissertation is provided in Section 5.3.3.

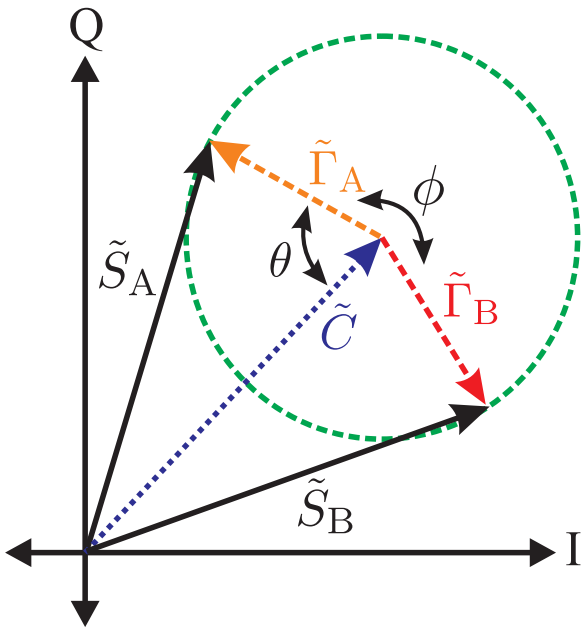

Figure 6: An IQ diagram showing the components of the backscatter signal received at the reader. The received signal $\tilde{S}_{A,B}$ is the vector sum of the transmitted carrier (plus other smaller, unmodulated, scattered signals) $\tilde{C}$ and the modulated-backscatter signal, which is proportional to the RF-tag antenna load reflection coefficient $\tilde{\Gamma}_{A,B}$.

The baseband equation for $\tilde{S}_A$ and $\tilde{S}_B$ received with a coherent, direct-conversion receiver can be written as follows:

$$\tilde{S}_A = \frac{1}{2}\tilde{h}^b\tilde{\Gamma}_A\tilde{h}^f\tilde{x} \tag{9}$$

$$\tilde{S}_B = \frac{1}{2}\tilde{h}^b\tilde{\Gamma}_B\tilde{h}^f\tilde{x} \tag{10}$$

where $\tilde{h}^f$ and $\tilde{h}^b$ are the baseband, complex coefficients of the forward and backscatter links, respectively, and $\tilde{x}$ is the magnitude of the tone transmitted from the reader[3]. By examining Figure 5, $\tilde{S}_A$ and $\tilde{S}_B$ can be written in terms of $\tilde{V}_{DC}$ and $\tilde{V}_{data}$, as shown by Prothro *et al.* [46]:

$$\tilde{S}_A = \tilde{V}_{DC} + \frac{1}{2}\tilde{V}_{data} \tag{11}$$

$$\tilde{S}_B = \tilde{V}_{DC} - \frac{1}{2}\tilde{V}_{data} \tag{12}$$

[3]Equations (9) and (10) are simplified versions of (20) given in Chapter 3 under the assumption of a static, narrowband channel with a backscatter-radio system using 1 transmitter, 1 RF-tag, and 1 receiver antenna. Furthermore, it has been assumed that additive noise is negligible. A discussion of the backscatter channel is provided in Chapter 3 and these assumptions are revisited in Section 5.4.

Likewise, $\tilde{V}_{\mathrm{DC}}$ and $\tilde{V}_{\mathrm{data}}$ can be written in terms of $\tilde{S}_{\mathrm{A}}$ and $\tilde{S}_{\mathrm{B}}$ as follows:

$$\tilde{V}_{\mathrm{DC}} = \frac{\tilde{S}_{\mathrm{A}} + \tilde{S}_{\mathrm{B}}}{2} = \frac{1}{4}\tilde{\mathrm{h}}^{b}\tilde{\mathrm{h}}^{f}(\tilde{\Gamma}_{\mathrm{A}} + \tilde{\Gamma}_{\mathrm{B}})\tilde{x} \tag{13}$$

$$\tilde{V}_{\mathrm{data}} = \frac{\tilde{S}_{\mathrm{A}} - \tilde{S}_{\mathrm{B}}}{2} = \frac{1}{4}\tilde{\mathrm{h}}^{b}\tilde{\mathrm{h}}^{f}(\tilde{\Gamma}_{\mathrm{A}} - \tilde{\Gamma}_{\mathrm{B}})\tilde{x} \tag{14}$$

Therefore, if $\tilde{V}_{\mathrm{DC}}$ is removed from the total received signal (given by (8)), then (14) shows that the modulated-backscatter signal is proportional to the difference between the complex reflection coefficients. Of course, the formulation of $\tilde{V}_{\mathrm{data}}$ would be different if a reference other than the DC level had been chosen.

It should be noted that the modulation factor in (4) cannot be directly calculated from the square of $\tilde{V}_{\mathrm{data}}$ in (14). In (14), $\tilde{V}_{\mathrm{data}}$ is proportional to $\frac{1}{2}\tilde{\mathrm{h}}^{b}\tilde{\mathrm{h}}^{f}$ because $\tilde{S}_{\mathrm{A}}$ and $\tilde{S}_{\mathrm{B}}$ are written using the baseband channel notation given by Durgin [17]. In (4), the baseband channel coefficients – $\frac{1}{2}\tilde{\mathrm{h}}^{b}\tilde{\mathrm{h}}^{f}$ – are removed so that $0 \leq M \leq 1$. The other link budget parameters account for channel effects.

2.2.4 Multipath Fade Margins

Multipath fading was discussed in Section 1.2 where it was stated that fading can be analyzed using stochastic-process theory. Envelope distributions are especially useful and the particular envelope distribution to be used is determined by the link budget in question and the propagation characteristics of the channel. Once an appropriate probability distribution has been chosen, a safety factor, or *fade margin*, is included in the link budget to ensure that the backscatter-radio system can operate with a certain outage probability. For any channel, the fade margin in the linear scale can be calculated as

$$\text{Fade Margin} = 10\log_{10}\left[\frac{\left[F_{\mathbf{A}}^{-1}(\text{Outage Probability})\right]^{2}}{P_{\mathrm{av}}}\right] \tag{15}$$

where $F_{\mathbf{A}}$ is the CDF of the received signal envelope, $\mathbf{A}$ is a random variable representing the signal envelope, and P_{av} is the average power of the channel. In words, the fade margin is the additional power that must be transmitted from the reader to maintain the specified outage probability in a channel *with* fading compared to that *without*. The following paragraphs describe the appropriate distributions for the different configurations of the backscatter channel described by (1) and (2).

2.2.4.1 The Power-up Fade Margin, F_p

The two probability distributions most commonly chosen to model fading in the power-up link budget (1) are the Rayleigh and Rician distributions. A Rician distribution is used when a strong line-of-sight (LOS) path exists between the reader and the RF tag; otherwise, the Rayleigh distribution is used. The level of fading is described by the Rician K factor – the ratio of the power in the specular LOS signal to the power in the nonspecular, scattered signal. Reported Rician K factors for backscatter channels are $-\infty$ dB and 2.8 dB [21], though higher values are certainly possible. These numbers represent the K factors of the individual forward and backscatter portions of the link where it has been assumed that each half of the link has the same K factor.

2.2.4.2 The Monostatic, Backscatter-Link Fade Margin, F_{m}

Fading in the monostatic, backscatter link, though caused by the same physical mechanisms, is described by radically different distributions than those of the power-up radio link. The reason for this difference is that the fading in the reader-to-tag link is multiplied by the fading in the tag-to-reader link. The fading of the backscattered signal can be modeled using a product-Rayleigh (for the non-line-of-sight (NLOS) case) or a product-Rician (for the LOS case) distribution. Since a single antenna is used to transmit and receive in a monostatic reader, the forward and backscatter channels are identical. Intuitively, this means that the forward and backscatter channels may fade simultaneously resulting in the deepest fading of all the backscatter links [52].

2.2.4.3 The Bistatic, Collocated Backscatter-Link Fade Margin, F_α

The bistatic, collocated link differs from the monostatic link in that two separate, but closely spaced, reader antennas are used to transmit and receive. In terms of fading, this means that the reader-to-tag and tag-to-reader links will be less correlated. Hence, when compared to the monostatic backscatter link, fading in the bistatic collocated link will always be less severe because the likelihood that both halves of the link fade simultaneously is less.

2.2.4.4 The Bistatic, Dislocated Backscatter-Link Fade Margin, F_β

In the bistatic, dislocated backscatter link, the reader transmitter and receiver antennas are separated by a very large electrical distance. This large separation causes the fading in the reader-to-tag and tag-to-reader links to be statistically uncorrelated and, since the fading is modeled by complex-Gaussian random variables, independent. Therefore, the fading in this link will be the least severe of the all the backscatter links, but still worse than the power-up link.

2.2.5 Calculated Fade Margins

Table 2 shows fade margins for several different channels and levels of fading. The outage probability is shown in the left column and is defined as the likelihood that the power received at the reader receiver has faded below P_{av} by an amount equal to the fade margin [37],

$$\text{Outage Probability} = Pr[P_{\text{R}} \leq P_{\text{av}}/(\text{Fade Margin})]. \tag{16}$$

For example, for the power-up link with $K = 0$ dB, the required fade margin F_{p} to guarantee that signal fades render the system inoperable with a only a 10% probability is 9 dB. In other words, an additional 9 dB of power must be transmitted to limit system failures to 10%.

Table 2: Small-scale multipath fade margins for the power-up (F_{p}), monostatic (F_{m}), and bistatic-dislocated (F_β) backscatter links. Fade margins are reported in dB (Modified from [37], © 2009 IEEE).

	$K = -\infty$ dB			$K = 0$ dB			$K = 3$ dB			$K = 10$ dB		
Outage Probability	F_{p}	F_{m}	F_β	F_{p}	F_{m}	F_β	F_{p}	F_{m}	F_β	F_{p}	F_{m}	F_β
0.5	2	6	4	1	5	3	1	3	2	0	1	1
0.1	10	22	15	9	20	14	7	16	11	3	7	5
0.05	13	29	19	12	26	17	10	21	15	4	9	6
0.01	20	43	28	19	40	26	16	34	22	6	13	9
0.005	23	49	32	22	46	29	19	40	26	7	15	10
0.001	30	63	40	29	60	37	26	54	33	9	20	13

2.2.6 On-object Antenna Gain Penalties

Though an RF-tag antenna may perform well when separated by several wavelengths from conductive and dielectric materials, its operation may cease completely when brought close or attached to an object. Aside from altering the input impedance (discussed in Section 2.2.2), object attachment reduces the antenna's radiation efficiency and distorts the antenna pattern limiting both the backscattered power for communication and, for a passive RF tag, the power available for RFIC operation. In (1) and (2), the on-object gain penalty Θ accounts for these losses and is defined in the linear scale as the ratio of the load-matched, free-space gain G_t of the RF-tag antenna to the gain of the RF-tag antenna attached to an object $G_{\mathrm{on-object}}$.

$$\Theta = \frac{G_t}{G_{\mathrm{on-object}}} \tag{17}$$

In (17), the power used to calculate G_t and $G_{\mathrm{on-object}}$ should be averaged over the half-space facing away from the object. This makes Θ a useful "rule-of-thumb" for design engineers regardless of the angle-of-arrival of waves at the RF tag. Unfortunately, calculating $G_{\mathrm{on-object}}$ is difficult analytically and is complicated by Θ's dependence on material properties, object geometry, frequency, and antenna type. Therefore, the best method to determine $G_{\mathrm{on-object}}$ is through careful simulation or measurement.

Measurements, shown in Table 3, have demonstrated that Θ can range from 0.9 dB on cardboard to 10.4 dB on an aluminum slab [53].

Table 3: On-object gain penalties for various materials measured at 915 MHz in the dB scale [53] (Reprinted from [37], © 2009 IEEE).

Cardboard Sheet	Acrylic Slab	Pine Plywood	De-ionized Water	Ethylene Glycol	Ground Beef	Aluminum Slab
0.9	1.1	4.7	5.8	7.6	10.2	10.4

Initially, some of the gain penalties in Table 3 may not seem significant; however, recall that the backscatter link budget (2) decreases as $1/\Theta^2$, so an aluminum slab may result in over a 20 dB loss in backscattered power. Furthermore, the power-up link, (1), decreases as $1/\Theta$. Even though the losses caused by Θ are not as severe as those seen in the backscatter

link budgets, passive RF tags are generally more sensitive to changes in the power-up link.

2.2.7 Path Blockages

When an object intrudes on or completely blocks the LOS path between the reader and the RF tag, the power received by the RF tag or backscattered to the reader will decrease. In the wireless literature, the large-scale power fades caused by blockages are often modeled with a log-normal distribution,

$$f_B(b) = \frac{1}{\sigma_B\sqrt{2\pi}} \exp\left(-\frac{(b-\mu_B)^2}{2\sigma_B^2}\right) \tag{18}$$

where b is the index of the PDF, μ_B is the average value of B, and σ_B is the standard deviation of B – all in the dB scale. No study of path blockages has been reported for backscatter radio because many commercial, passive backscatter systems depend on a LOS channel for operation. However, as more backscatter systems operate in NLOS channels – which is currently possible for semi-passive tags and will become more common for passive tags as their power consumption is reduced – path blockage statistics will become more significant in link budget calculations.

2.2.8 Path Loss

Though not represented by a particular term in Equations (1) - (2), path loss accounts for the decrease in received power as the distance from the transmitter increases. In theory, an electromagnetic wave propagating away from an antenna will have a spherically shaped phase-front. Since antennas only radiate a finite amount of power and the surface area of a sphere increases with the square of its radius, the power density observed at a distance r from the source will decrease as $1/r^2$ – free-space path loss. When the radiator is not in free space, reflections and diffractions will change the rate at which power decreases and is accounted for by a path loss exponent n. In the decibel scale, the simplest path loss model is given by

$$L_p = P_0 + 10n\log(r) \tag{19}$$

where P_0 is a constant, n is the path loss exponent, and r is the reader-to-tag separation distance in meters [21]. Many path loss models and path loss exponents have been studied

for conventional transmitter-to-receiver links [54]. In general, path loss exponents for indoor channels vary widely from building to building and even from room to room. Though few measurements have been conducted for backscatter links, it has been found that path loss exponents are very close to free-space values [21]. Therefore, in (1) and (2), $n = 2$ for the forward and backscatter links; however, when semi-passive tags are considered, these values may vary because of their large operating range.

2.3 RFID-Portal Example

In this section, the radio link budgets described in Section 2.1 are demonstrated through an example of an RFID portal operating at 915 MHz. This section defines the RF-tag system parameters, describes the propagation environment, and then plots the link budgets as a function of the reader-to-tag separation distance for two different object attachments.

2.3.1 RF-Tag Reader

In this system, tagged objects pass through a passageway, or portal, to which the reader's antennas are fixed. The reader has the ability to operate with a single transmitter and receiver antenna (monostatic mode) or with two widely-spaced transmitter and receiver antennas (the dislocated bistatic mode). In either mode, the transmitter and receiver antennas are right-hand circularly polarized patch antennas that resonate at 915 MHz with a gain of 7 dBi. The sensitivity of the reader is -80 dBm [40, 55].

2.3.2 RF Tag

Figure 7 shows the equivalent circuit of the RF-tag antenna, impedance transformation network, and antenna port of the tag RFIC. The RF tag uses a single folded dipole antenna that is linearly-polarized with a free-space, load-matched gain of 2.1 dBi and an approximate free-space terminal impedance of $300 + j100\,\Omega$, determined from Figure 8 [46]. The input impedance at the antenna port of most tag RFICs can be modeled as a series resistor of a few ohms (often less than $30\,\Omega$) in series with a capacitor that is a fraction of a picofarad [6]. For this example, it is assumed that the tag RFIC uses ASK modulation and switches its impedance between two states, $Z^A_{\text{RFIC}} = 20 - j350\,\Omega$ and $Z^B_{\text{RFIC}} = 2 - j0.1\,\Omega$ (an approximate

short circuit). The non-zero input impedance of Z^B_{RFIC} reflects the fact that field-effect transistors cannot provide a true short circuit, but are modeled as a small shunt resistance in parallel with a small capacitance whose values depend upon the transistor implementation and biasing. For efficient power transfer from the antenna to the tag RFIC, a matching network is used to transform the antenna impedance to $Z_{IN} = 20 + j350\,\Omega$ creating a conjugate impedance match with the tag RFIC in impedance state A. In most RF tags, lumped-element impedance transformation networks are not used; instead, the necessary inductance or capacitance is incorporated directly in the structure of the planar antenna [6]. In this example, the matching network is treated separately from the antenna structure for illustrative purposes. As mentioned previously, the power required for the tag to power-up varies widely by design; in this example, we assume that -13 dBm is required at 915 MHz [40, 56].

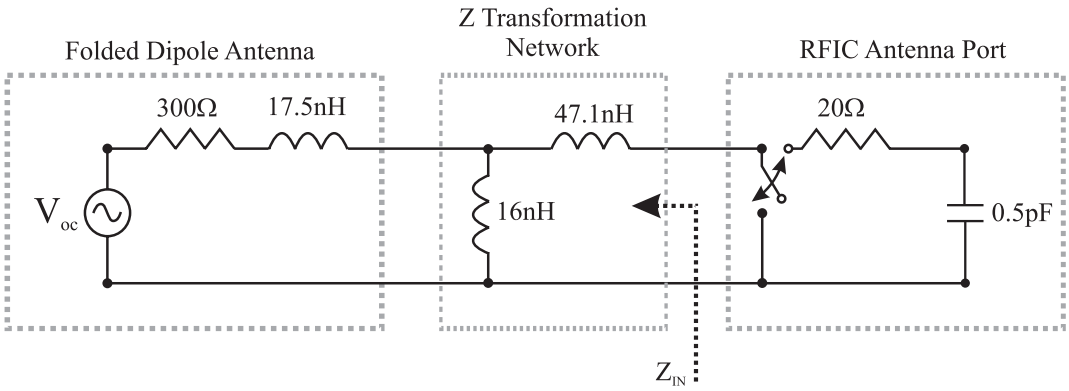

Figure 7: The equivalent circuit of the folded dipole RF-tag antenna, impedance transformation network, and RFIC antenna port used in the 915 MHz portal example (Reprinted from [37], © 2009 IEEE).

2.3.3 The Propagation Environment

The RF-tag system operates in a cluttered environment that experiences small-scale multipath fading due to multipath propagation. As the RF tag passes in front of the reader's antennas, a LOS path exists resulting in a Rician K factor of 3 dB. Furthermore, it is assumed that no blockages impair the LOS path and a 5% outage probability is desired. Some of the tagged objects passing through the portal are made of cardboard and, for illustration of one of the worst-case propagation scenarios, it is assumed that others are made

of aluminium.

2.3.4 Link Budget Calculations

The information in the previous paragraphs combined with Table 2 and Table 3 provide all of the parameters necessary to calculate the terms in the link budgets. A brief description of each is provided below and summarized in Table 4.

Transmit Power, P_T: In the United States, the Federal Communications Commission (FCC) limits the power that an RF-tag system can transmit to 4 W of equivalent isotropic radiated power (EIRP). EIRP power is simply the product of the transmitted power and transmitter antenna gain ($P_{EIRP} = G_T P_T$) in the linear scale. Since the reader's antennas have a gain of 7 dBi (5 in the linear scale), the maximum continuous wave (CW) power transmitted is limited to 29 dBm (or 800 mW).

Modulation Factor, M, and Power Transmission Coefficient, τ: The RF tag modulates backscatter by switching its input impedance between two states. When the RF tag is attached to a cardboard object, the antenna's impedance changes little from its free-space value, $Z_{IN} = 20 + j350$ as seen at the output of the impedance transformation network. Using Z_{IN}, Z^A_{RFIC}, and Z^B_{RFIC} in (4), the modulation factor on cardboard is found to be $M = 0.25$ in the linear scale. Using (3), the power transmission coefficient on cardboard is $\tau = 1$ in the linear scale.

As the RF tag is brought close to an aluminum object, the impedance of the folded dipole antenna drops rapidly, as shown in Figure 8. For a very small object-to-tag separation distance of 0.005λ, which approximates object attachment, the terminal impedance of the antenna drops to approximately $0.5 + j25\Omega$. The corresponding impedance seen at the output terminals of the impedance transformation network is $Z_{IN} = 0.31 + j290\,\Omega$. This assumes that the values of the impedance transformation network are not altered by close metal proximity – an assumption that may not be valid for a matching network incorporated into the antenna structure. Using Z_{IN}, Z^A_{RFIC}, and Z^B_{RFIC} in (4) and (3), the modulation factor and power transmission coefficient are found to be $M = 3.5\times10^{-5}$ and $\tau = 6.2\times10^{-3}$,

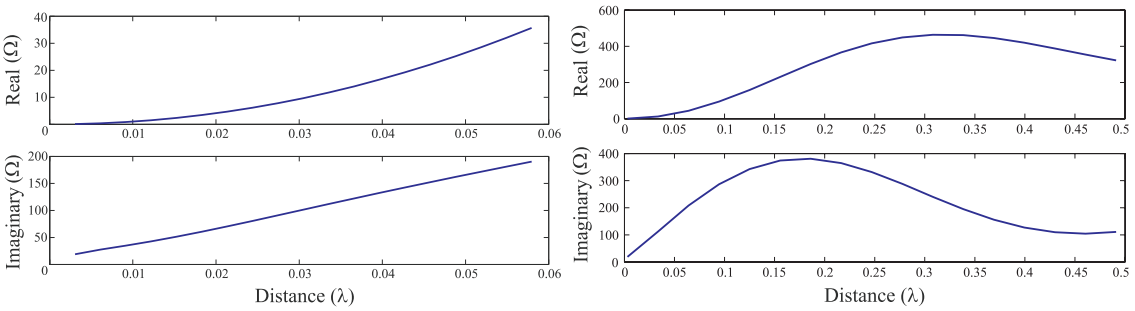

Figure 8: Folded dipole antenna impedance (simulated using NEC) as a function of the electrical distance from a perfectly conducting half-plane at 915 MHz [46] for electrical spacings of (a) 0.005λ to 0.06λ and (b) 0.005λ to 0.5λ (Reprinted from [37], © 2009 IEEE).

respectively (both in the linear scale).

Gain Penalty, Θ: From Table 3, the gain penalty for cardboard and metal are $\Theta = 0.9$ dB (1.2 in the linear scale) and $\Theta = 10.4$ dB (11 in the linear scale), respectively.

Fade Margins: To maintain a 5% outage probability in a multipath environment with $K = 3$ dB, the required fade margins from Table 2, are $F_{\mathrm{p}} = 10$ dB (10 in the linear scale) for the power-up link, $F_{\mathrm{m}} = 21$ dB (126 in the linear scale) for the reader in the monostatic mode, and $F_{\beta} = 15$ dB (32 in the linear scale) for the reader in the bistatic, dislocated mode.

Polarization Mismatch, X: Since the reader's antennas are circularly polarized and the RF-tag antenna is linearly polarized, a 3 dB polarization mismatch will result on both the reader-to-tag and tag-to-reader links; therefore, $X_f = X_b = 0.5$ in the linear scale.

Table 4: 915 MHz RF-tag portal example parameters in the linear scale (Reprinted from [37], © 2009 IEEE).

Material	P_T (mW)	$G_{T,R}$	G_t	$X_{f,b}$	F_{p}	F_{m}	F_β
Cardboard	800	5	1.6	0.5	10	126	32
Aluminum	800	5	1.6	0.5	10	126	32

Material	λ (m)	M	τ	Θ	B
Cardboard	0.33	0.25	1	1.2	1
Aluminum	0.33	3.5×10^{-5}	6.2×10^{-3}	11	1

2.3.5 Discussion

Figure 9(a) shows plots of the power-up link, described by (1), for three different cases along with the minimum power threshold for tag RFIC operation. In the first power-up link budget, X, τ, Θ, B, and F are all equal to 1 (in the linear scale). This is the Friis free-space link budget – a link budget that assumes free-space path loss, no impedance or polarization mismatches, no path blockages, and no multipath fading. The second case is the power-up link for an RF tag attached to cardboard and the third is the power-up link for an RF tag attached to an aluminum object. Note the extreme optimism of the Friis free-space link budget. Compared to the realistic second and third cases, an RF-tag system designed using the Friis link budget may overestimate its range by several meters. In the second case, though cardboard attachment itself does little to affect the tag's operation, fading and polarization mismatches reduce the range of the RF tag to less than 2 m. In the third case, the reduced antenna impedance results in an extremely small power transmission coefficient τ that, along with a large gain penalty, prevents the RF tag from turning on.

Similarly, Figure 9(b) shows plots of the backscatter links described by (2) for an RF tag attached to cardboard and aluminum and the minimum power threshold for signal detection – i.e., the receiver's sensitivity. A brief comparison of Figure 9(a) and Figure 9(b) shows that the range of the RF tag is limited by the power-up link (1), not the backscattered power. The effect of the reader antenna configuration is also seen; the monostatic link is several dB worse than the bistatic, dislocated case regardless of material attachment. Like

the power-up link, the low antenna impedance caused by aluminum attachment results in an extremely small modulation factor M. The small amount of modulated power scattered from the RF tag is below the reader's sensitivity threshold and is, therefore, undetected.

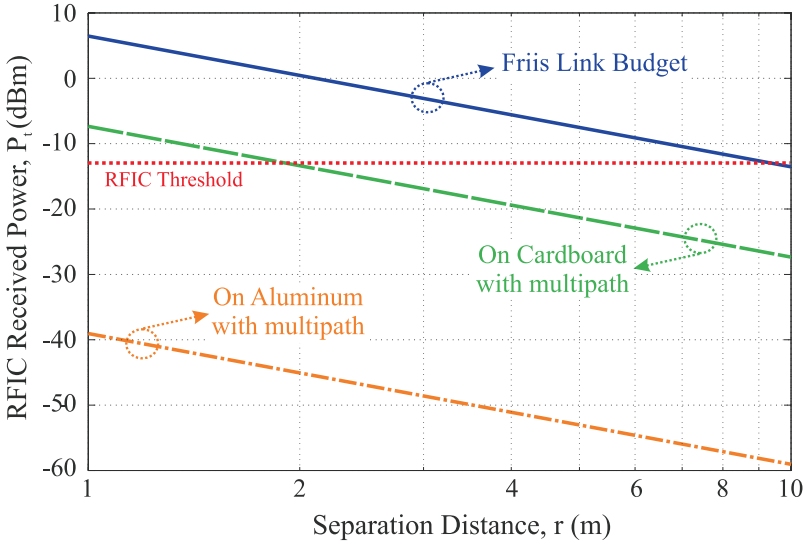

(a) Power-up Links

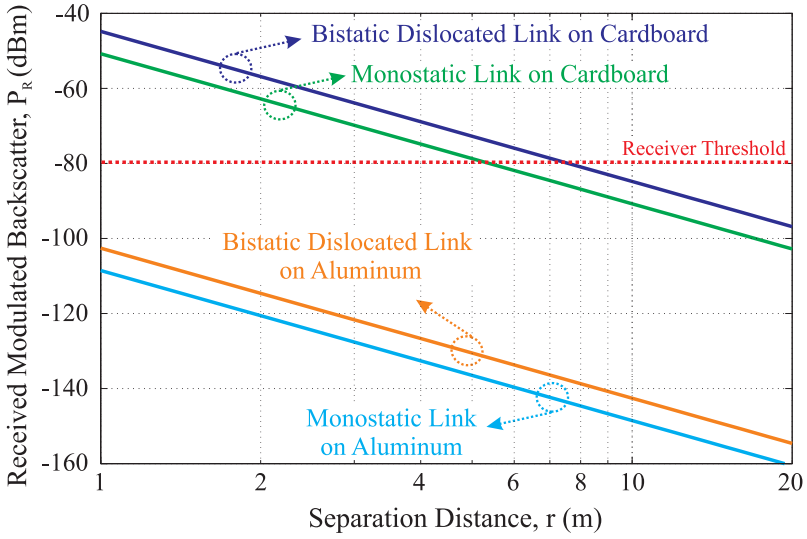

(b) Backscatter Links

Figure 9: Power-up and backscatter links plotted as a function of reader-to-tag separation distance, r. In (b), it is assumed that $r = r_f = r_b$ (Reprinted from [37], © 2009 IEEE).

2.4 Conclusion

This chapter has presented two link budgets that completely describe the major propagation mechanisms affecting UHF and microwave backscatter communication. These tools are

useful for predicting backscatter-radio system performance and will help reduce expensive prototyping iterations. Furthermore, these link budgets may be used with the theory and design guidelines presented in Chapter 3 and Chapter 4 to show how multiple antennas can reduce small-scale fading and improve backscatter system range and reliability.

CHAPTER III

FADING DISTRIBUTIONS FOR THE M × L × N DYADIC BACKSCATTER CHANNEL

Chapter Overview: This chapter provides the following:

- A detailed description of the $M \times L \times N$, dyadic backscatter channel.
- New, analytic envelope PDFs for the $M \times L \times N$, dyadic backscatter channel with Rayleigh-fading links.
- Demonstration of pinhole diversity gains that reduce multipath fading for backscatter-radio systems.
- A discussion of the effects of link correlation and how it can be reduced to minimize small-scale multipath fading.
- A description of multipath fading distributions for the LOS, $M \times L \times N$, dyadic backscatter channel.

This chapter defines and discusses the $M \times L \times N$, dyadic backscatter channel and shows that small-scale fading can be reduced using RF tags with more than one antenna. This chapter lays the theoretical framework for the measurements presented in Chapter 6 and is adapted from [52] and [5].

3.1 The M × L × N Dyadic Backscatter Channel

The most general backscatter channel is the $M \times L \times N$, *dyadic*[1] *backscatter channel* – a pinhole channel [57] that describes the propagation of signals in a backscatter-radio system consisting of M transmitter, L RF-tag, and N receiver antennas. In a pinhole channel, propagation paths are forced to converge at a point in space which causes the propagation paths to be correlated. In conventional transmitter-to-receiver channels, this has been

[1]The term "dyadic" has a double meaning. It reflects both the two-fold nature of the channel created by the forward and backscatter links and the fact that the modulated signals are represented in matrix form.

shown to reduce the rank of the channel matrix and limit channel capacity [57] and available diversity gains. In RF channels, the point of convergence may be a diffracting edge [58, 59], a hallway or tunnel [58], a metal screen [57], rings of scatterers separated by a long distance [60], or the antenna(s) of a mobile station that is (are) found in amplify-and-forward channels [61]. In the dyadic backscatter channel, the point of convergence is (are) the RF-tag antenna(s). All of these pinhole channels, except the amplify-and-forward and dyadic backscatter channels, cease their pinhole behavior under LOS conditions. The dyadic backscatter and amplify-and-forward channels remain pinholes in both LOS and NLOS conditions making them some of the only true pinhole channels.

The hallmark of any pinhole channel is that it can be modeled as the cascade of two channels. In the $M \times L \times N$, dyadic backscatter channel, shown in Figure 10(a), these channels are called the forward and backscatter links. The forward link, $\tilde{\mathbf{H}}^f(t, \vec{r}\,)$, describes signal propagation from the M transmitter antennas to the L RF-tag antennas and the backscatter link, $\tilde{\mathbf{H}}^b(t, \vec{r}\,)$, describes the propagation of signals scattered from the L RF-tag antennas to the N receiver antennas.

In mathematical terms, the received, baseband signal from the $M \times L \times N$, dyadic backscatter channel is

$$\tilde{\vec{\mathrm{y}}}(t, \vec{r}\,) = \frac{1}{2} \int_{-\infty}^{+\infty} \int_{-\infty}^{+\infty} \tilde{\mathbf{H}}^b(\tau_b; t, \vec{r}\,) \tilde{\mathbf{S}}(t - \tau_b) \tilde{\mathbf{H}}^f(\tau_f; t - \tau_b, \vec{r}\,) \tilde{\vec{\mathrm{x}}}(t - \tau_b - \tau_f) d\tau_b d\tau_f + \tilde{\vec{\mathrm{n}}}(t). \quad (20)$$

In (20), $\tilde{\vec{y}}(t, \vec{r}\,)$ is an $N \times 1$ vector of received, baseband signals; $\tilde{\mathbf{H}}^b(\tau_b; t, \vec{r}\,)$ is the $N \times L$, complex, baseband-channel impulse-response matrix of the backscatter link; and $\tilde{\mathbf{H}}^f(\tau_f; t, \vec{r}\,)$ is the $L \times M$, complex, baseband-channel impulse-response matrix of the forward link [17]. $\tilde{\mathbf{S}}(t)$ is the narrowband, $L \times L$ signaling matrix, $\tilde{\vec{x}}(t)$ is an $M \times 1$ vector of signals transmitted from the reader transmitter antennas, and $\tilde{\vec{n}}(t)$ is an $N \times 1$ vector of noise components.

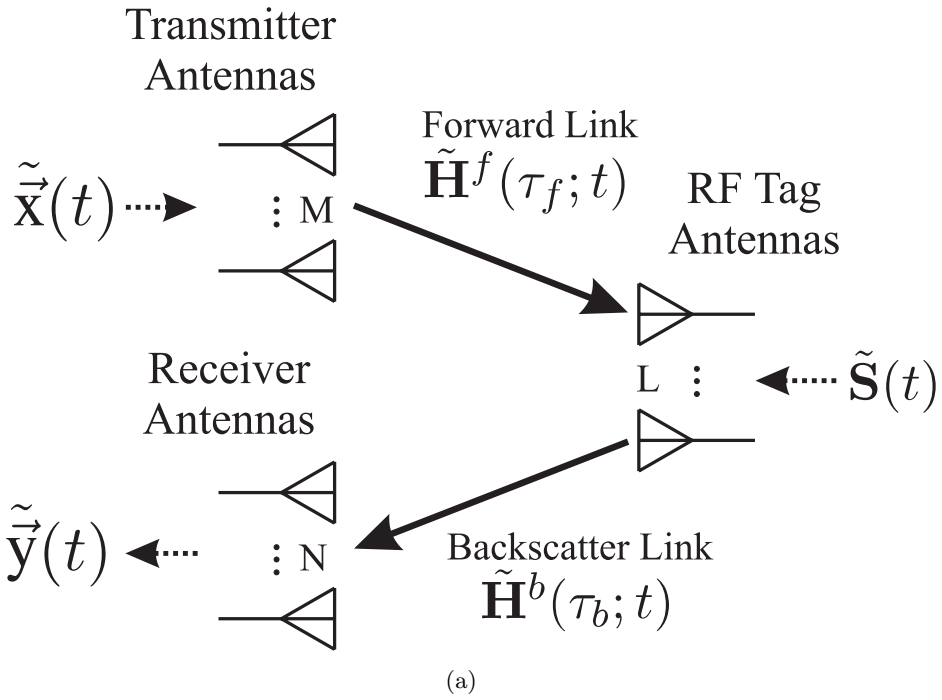

(a)

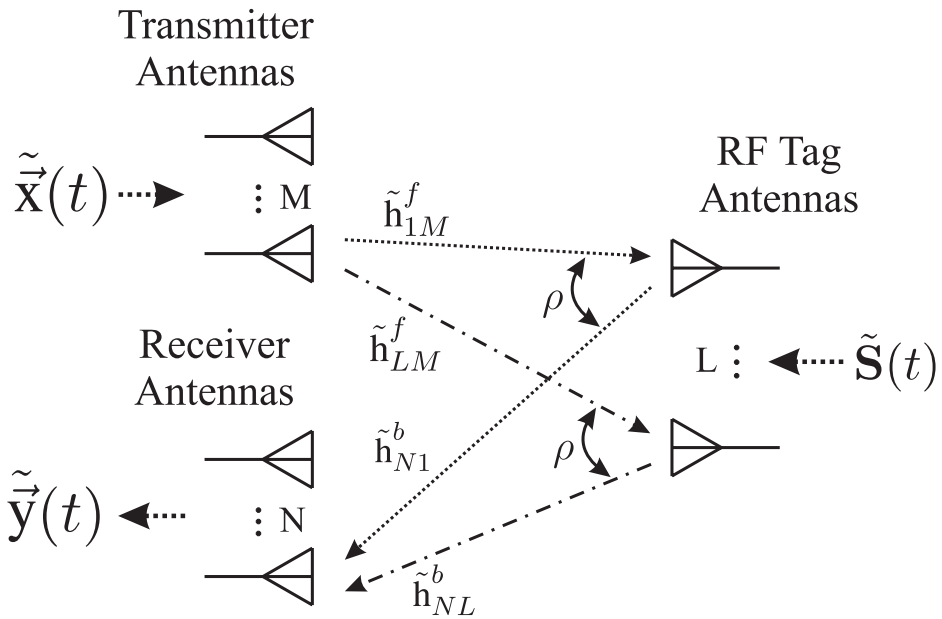

(b)

Figure 10: (a) The general, $M \times L \times N$, dyadic backscatter channel with M transmitter antennas, L RF-tag antennas, and N receiver antennas described mathematically by (20) (Reprinted from [5], © 2008 IEEE). (b) The path from the m^{th} transmitter antenna to the n^{th} receiver antenna is shown where $\tilde{h}^f_{lm}$ and $\tilde{h}^b_{nl}$ are elements of the forward and backscatter-link matrices, $\tilde{\mathbf{H}}^f$ and $\tilde{\mathbf{H}}^b$, respectively. Elements of the forward and backscatter-link matrices that terminate or originate on a common RF-tag antenna have link correlation ρ (Reprinted from [52], © 2007 IEEE).

3.1.1 The Signaling Matrix

The narrowband signaling matrix, $\tilde{\mathbf{S}}(t)$, is an $L \times L$ matrix that describes the time-varying modulation that an RF tag places on radio signals absorbed and scattered by the L tag antennas. Therefore, it is natural to define the signaling matrix as the L port scattering matrix commonly used in RF hardware design. A comprehensive discussion of the general L port scattering matrix is given by Pozar [62]; however, two notes are worth mentioning. First, the signaling matrix of a passive or semi-passive RF tag has elements $\tilde{\mathrm{s}}_{ij}(t)$ with magnitude less than unity, $|\tilde{\mathrm{s}}_{ij}(t)| \leq 1$, since there is no amplification of the backscattered signal. Second, though it is not required that the signaling matrix be symmetric, most RF tags will satisfy this property.

The signaling matrix may take several different forms depending upon the physical implementation of the modulation circuitry and RF-tag antennas.

3.1.1.1 Identity Signaling Matrix

If each RF-tag antenna modulates backscatter with the same signal and no signals are transferred between the antennas, the signaling matrix is equal to a normalized identity matrix,

$$\tilde{\mathbf{S}}(t) = \tilde{\mathrm{s}}(t)\mathbf{I}_{\mathrm{L}} = \tilde{\Gamma}(t)\mathbf{I}_{\mathrm{L}} \tag{21}$$

where $\mathbf{I}_{\mathrm{L}}$ is the $L \times L$ identity matrix and $\tilde{\Gamma}(t)$ is the complex, RF-tag antenna load reflection coefficient.

3.1.1.2 Diagonal Signaling Matrix

If the RF-tag antennas modulate backscatter with different signals and no signals are transferred between the antennas, the signaling matrix is a diagonal matrix,

$$\begin{aligned} \tilde{\mathbf{S}}(t) &= \mathrm{diag}\left[\tilde{\mathrm{s}}_{11}(t) \ldots \tilde{\mathrm{s}}_{LL}(t)\right] \\ &= \mathrm{diag}\left[\tilde{\Gamma}_1(t) \ldots \tilde{\Gamma}_{\mathrm{L}}(t)\right]. \end{aligned} \tag{22}$$

3.1.1.3 Full Signaling Matrix

If the RF-tag antennas modulate backscatter independently, i.e., with different signals, and signals are transferred between the antennas, the full signaling matrix,

$$\tilde{\mathbf{S}}(t) = \begin{bmatrix} \tilde{\mathrm{s}}_{11}(t) & \dots & \tilde{\mathrm{s}}_{1L}(t) \\ \vdots & \ddots & \vdots \\ \tilde{\mathrm{s}}_{L1}(t) & \dots & \tilde{\mathrm{s}}_{LL}(t) \end{bmatrix}, \tag{23}$$

is used. Signal transfer between antennas is represented by the off-diagonal elements (i.e., $\tilde{\mathrm{s}}_{ij}$ where $i \neq j$). The fact that power can be transferred between the RF-tag antennas gives the designer a potential additional degree of freedom in signal scheme design; however, at this point, no application of the full signaling matrix has been identified.

For the remainder of this chapter, it is assumed that the signaling matrix has the form of (21), the identity signaling matrix, with binary reflection of signals, $\tilde{\Gamma} = \pm 1$, to provide maximum signal power.

3.2 M × L × N Dyadic Backscatter Channel Envelope PDF

Using the $M \times L \times N$, dyadic backscatter channel synthesized in the previous section, envelope distributions of the signal received at the n^{th} receiver can be derived. In this channel, each element of the forward link $\tilde{\mathbf{H}}^f$ and the backscatter link $\tilde{\mathbf{H}}^b$ is an independent, identically distributed (i.i.d.), complex-Gaussian random variable. The elements of the backscatter and forward links can be written, respectively, as $\tilde{\mathrm{h}}^b = (w_b + jv_b)$ and $\tilde{\mathrm{h}}^f = (w_f + jv_f)$ where $w_{f,b}$ and $v_{f,b}$ are $\sim \mathcal{N}(\mu_{f,b}, \sigma^2_{f,b}/2)$. Here, $\mu_{f,b}$ and $\sigma^2_{f,b}$ are the mean and variance of $\tilde{\mathrm{h}}^f$ and $\tilde{\mathrm{h}}^b$, respectively.

Link Correlation: In the $M \times L \times N$, dyadic backscatter channel, propagation paths that originate or terminate on a common RF-tag antenna can have *link correlation* ρ, shown in Figure 10(b). Link correlation simply describes the correlation, or relationship, between fading in the forward and backscatter links. Link correlation can be controlled by varying the spacing between the reader transmitter and receiver antennas. Details may be found in

Appendix B.4 and work by Griffin and Durgin [52]. Mathematically, this means that

$$\rho = \frac{2\,\mathrm{Cov}(w_f, w_b)}{\sigma_b \sigma_f} = \frac{2\,\mathrm{Cov}(v_f, v_b)}{\sigma_b \sigma_f} \tag{24}$$

where $\mathrm{Cov}(\cdot,\cdot)$ is the covariance operator. While ρ is convenient for analysis, a more practical metric is the correlation between the envelopes of $\tilde{\mathrm{h}}^f_{lm}$ and $\tilde{\mathrm{h}}^b_{nl}$ – *link envelope correlation* – since this correlation can be easily calculated from measured data. It can be shown that envelope correlation ρ_e is related to link correlation by $\rho_e \approx \rho^2$ [63,64]. In remainder of this dissertation, both ρ and ρ_e will be used when appropriate.

The signal received at the n^{th} receiver antenna is proportional to the sum of ML complex-Gaussian products, described by (25) and Figure 11,

$$\tilde{\mathrm{y}}_n(t,\vec{r}) \propto \sum_{j=1}^{L} \underbrace{(\tilde{\mathrm{h}}^f_{j1} + \ldots + \tilde{\mathrm{h}}^f_{jM})}_{\tilde{\mathrm{g}}^f_j} \tilde{\mathrm{h}}^b_{nj}. \tag{25}$$

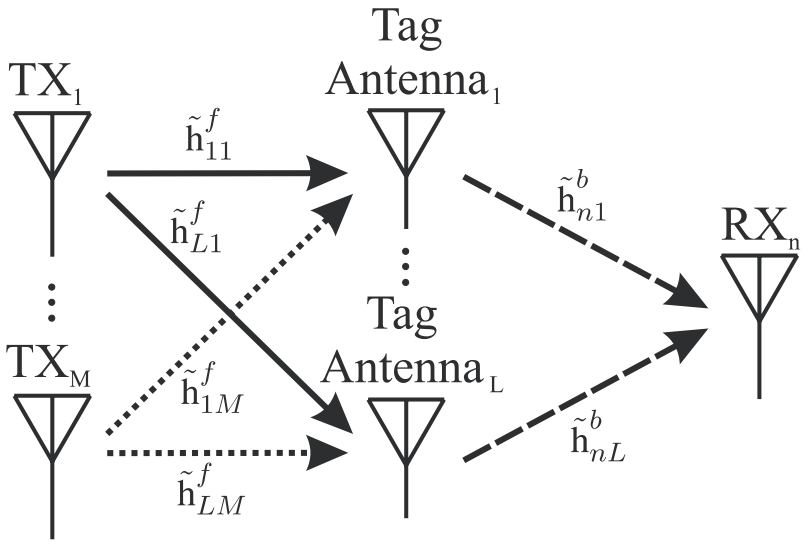

Figure 11: In a backscatter-radio system, the signal received at the n^{th} receiving antenna is the sum of ML complex-Gaussian products. However, only L of these products are statistically independent (Reprinted from [5], © 2008 IEEE).

In (25), each element of the backscatter-link matrix, $\tilde{\mathrm{h}}^b$, is multiplied by M, i.i.d., forward-link elements, $(\tilde{\mathrm{h}}^f_{j1} + \ldots + \tilde{\mathrm{h}}^f_{jM})$, which can be expressed as a single complex-Gaussian random variable, $\tilde{\mathrm{g}}^f_j$, with mean $M(\mu_f + j\mu_f)$ and variance $M\sigma_f^2$. Therefore, the signal received at the n^{th} receiver antenna is proportional to the sum of L, i.i.d., complex-Gaussian products.

3.2.1 Rayleigh-Fading Links

In a typical $M \times L \times N$, dyadic backscatter channel, LOS propagation dominates and the elements of the forward and backscatter matrices follow a Rician distribution ($\mu_{f,b} \neq 0$). The $M \times L \times N$ Rician envelope PDF will be discussed in Section 3.2.2, but first, the lower bound of this case, the $M \times L \times N$, dyadic backscatter channel with Rayleigh-fading forward and backscatter links, will be studied. In this case, the elements of the forward and backscatter links can be written, respectively, as $\tilde{\mathrm{h}}^{b} = (w_b + jv_b)$ and $\tilde{\mathrm{h}}^{f} = (w_f + jv_f)$ where $w_{f,b}$ and $v_{f,b}$ are $\sim \mathcal{N}(0, \sigma_{f,b}^2/2)$. The envelope PDF of the $M \times L \times N$, dyadic backscatter channel $f_{\mathbf{A}}(\alpha, \rho)$ can be derived from that of the product of two Rayleigh random variables, as shown in Appendix B.

This PDF, $f_{\mathbf{A}}(\alpha, \rho)$, is best understood by examining three special cases: the case with uncorrelated forward and backscatter links ($\rho = 0$), that with fully-correlated forward and backscatter links ($\rho = 1$), and that with link correlation in the range $0 < \rho < 1$. As shown in Appendix B, analytical expressions can be found for the PDF with $\rho = 0$ and $\rho = 1$; however, the case of $0 < \rho < 1$ requires numerical techniques. Plots of the PDF for $0 < \rho < 1$ are given in Section 3.3.4.

3.2.1.1 Uncorrelated Links, $\rho = 0$

The envelope PDF for the case of $\rho = 0$ is

$$f_{\mathbf{A}}(\alpha, 0) = \alpha^{L} \left(\frac{2}{\sqrt{M}\sigma_b\sigma_f} \right)^{1+L} \frac{2^{1-L}}{\Gamma(L)} \mathrm{K}_{\nu}\left(\frac{2\alpha}{\sqrt{M}\sigma_b\sigma_f} \right) \tag{26a}$$

where $\mathbf{A}$ is the random channel envelope, α is the index of the PDF, $\Gamma(\cdot)$ is the gamma function, and $\mathrm{K}_{\nu}(\cdot)$ is a modified bessel function of the second kind with order $\nu = 1 - L$. The mean and variance of (26a), respectively, are

$$\mu_{\mathbf{A}} = \frac{\sqrt{M}\sigma_b\sigma_f}{2} \frac{\pi(2L)!}{4^{L} L!(L-1)!} \tag{26b}$$

and

$$\sigma_{\mathbf{A}}^2 = ML\sigma_b^2\sigma_f^2 \left(1 - \frac{L}{4} \left[\frac{\pi(2L)!}{4^{L}(L!)^2} \right]^2 \right). \tag{26c}$$

Simplified expressions for the PDF, mean, and variance are given in Table 5 for several $M \times L \times N$ channel configurations.

Table 5: Simplified envelope statistics for $M \times L \times N$, dyadic backscatter channels with uncorrelated ($\rho = 0$), Rayleigh-fading links (Reprinted from [5], © 2008 IEEE).

	$f_{\mathbf{A}}(\alpha, 0)$	$\mu_{\mathbf{A}}$	$\sigma^2_{\mathbf{A}}$
$L = 1$	$\frac{4\alpha}{\zeta^2}\mathrm{K}_0\left(\frac{2\alpha}{\zeta}\right)$	$\frac{\pi}{4}\zeta$	$\left(1 - \frac{\pi^2}{16}\right)\zeta^2$
$L = 2$	$\frac{4\alpha^2}{\zeta^3}\mathrm{K}_{-1}\left(\frac{2\alpha}{\zeta}\right)$	$\frac{3\pi}{8}\zeta$	$\left(2 - \frac{9\pi^2}{64}\right)\zeta^2$
$L = 3$	$\frac{2\alpha^3}{\zeta^4}\mathrm{K}_{-2}\left(\frac{2\alpha}{\zeta}\right)$	$\frac{15\pi}{32}\zeta$	$\left(3 - \frac{225\pi^2}{1024}\right)\zeta^2$
$L = 4$	$\frac{2\alpha^4}{3\zeta^5}\mathrm{K}_{-3}\left(\frac{2\alpha}{\zeta}\right)$	$\frac{35\pi}{64}\zeta$	$\left(4 - \frac{1225\pi^2}{4096}\right)\zeta^2$

where $\zeta = \sqrt{M}\sigma_b\sigma_f$

3.2.1.2 Fully-Correlated Links, $\rho = 1$

The envelope PDF for the case of $\rho = 1$, which may occur only in a $1 \times L \times 1$, dyadic backscatter channel in which a single reader antenna is used to transmit and receive, is

$$f_{\mathbf{A}}(\alpha, 1) = \alpha^{L/2}\left(\frac{1}{\sigma_b\sigma_f}\right)^{1+L/2}\frac{2^{1-L/2}}{\Gamma(L/2)}\mathrm{K}_\nu\left(\frac{\alpha}{\sigma_b\sigma_f}\right) \tag{27a}$$

where $\mathrm{K}_\nu(\cdot)$ is a modified bessel function of the second kind with order $\nu = 1 - L/2$ and all other terms are as defined for (26a). The mean and variance of (27a), respectively, are

$$\mu_{\mathbf{A}} = \sigma_b\sigma_f\Psi \tag{27b}$$

where

$$\Psi = \begin{cases} \dfrac{\pi L!}{2^L(L/2-1)!(L/2)!} & \text{for even } L, \\ \dfrac{2^L\left[(L/2-1/2)!\right]^2}{2(L-1)!} & \text{for odd } L, \end{cases}$$

and

$$\sigma^2_{\mathbf{A}} = 2L\sigma_b^2\sigma_f^2\left(1 - \frac{\Lambda}{2L}\right) \tag{27c}$$

where

$$\Lambda = \begin{cases} \left[\dfrac{\pi L!}{2^L (L/2)!(L/2-1)!}\right]^2 & \text{for even } L, \\ \left[\dfrac{2^{L-1}\left[(L/2-1/2)!\right]^2}{(L-1)!}\right]^2 & \text{for odd } L. \end{cases}$$

Simplified expressions for the PDF, mean, and variance are given in Table 6 for several $M \times L \times N$ channel configurations.

Table 6: Simplified envelope statistics for $M \times L \times N$, dyadic backscatter channels with fully-correlated ($\rho = 1$), Rayleigh-fading links (Reprinted from [5], © 2008 IEEE).

	$f_{\mathbf{A}}(\alpha, 1)$	$\mu_{\mathbf{A}}$	$\sigma^2_{\mathbf{A}}$
$L = 1$	$\frac{1}{\zeta}\exp\left(\frac{-\alpha}{\zeta}\right)$	ζ	ζ^2
$L = 2$	$\frac{\alpha}{\zeta^2}\mathrm{K}_0\left(\frac{\alpha}{\zeta}\right)$	$\frac{\pi}{2}\zeta$	$4\zeta^2\left(1 - \frac{\pi^2}{16}\right)$
$L = 3$	$\sqrt{\frac{2\alpha^3}{\pi\zeta^5}}\mathrm{K}_{-1/2}\left(\frac{\alpha}{\zeta}\right)$	2ζ	$2\zeta^2$
$L = 4$	$\frac{\alpha^2}{2\zeta^3}\mathrm{K}_{-1}\left(\frac{\alpha}{\zeta}\right)$	$\frac{3\pi}{4}\zeta$	$8\zeta^2\left(1 - \frac{18\pi^2}{256}\right)$

where $\zeta = \sigma_b \sigma_f$

3.2.2 Rician-Fading Links

Similar to the Rayleigh-fading case in Section 3.2.1, the envelope PDF of the signal received at the n^{th} receiver antenna through the $M \times L \times N$, dyadic backscatter channel with Rician-fading links can be derived from the PDF of the product of two Rician random variables. Although analytic solutions are not possible, this PDF can be solved numerically by applying the techniques used in Appendix B to the product-Rician PDF given in Appendix A.4. This can be done only for the case of independent forward and backscatter links because no expression for the product of two dependent Rician random variables is available. Plots of these PDFs are presented in Section 3.3.4.

3.3 Diversity Gains in the Dyadic Backscatter Channel

This section explores the effects of multiple RF-tag antennas and link correlation on the level of small-scale multipath fading in the $M \times L \times N$, dyadic backscatter channel. It is shown that using multiple RF-tag antennas results in a pinhole diversity gain that reduces small-scale fading. Likewise, it is shown that reducing link correlation can have a similar effect.

3.3.1 The Benefits of Multiple RF-Tag Antennas

Figure 12 shows plots of (26a) and (27a) along with the PDF of a conventional, transmitter-to-receiver, Rayleigh-fading channel. Each PDF has been normalized to unit power, that is, $\mathbf{E}\{\mathbf{A}^2\} = 1$ where $\mathbf{E}\{\cdot\}$ denotes the ensemble average.

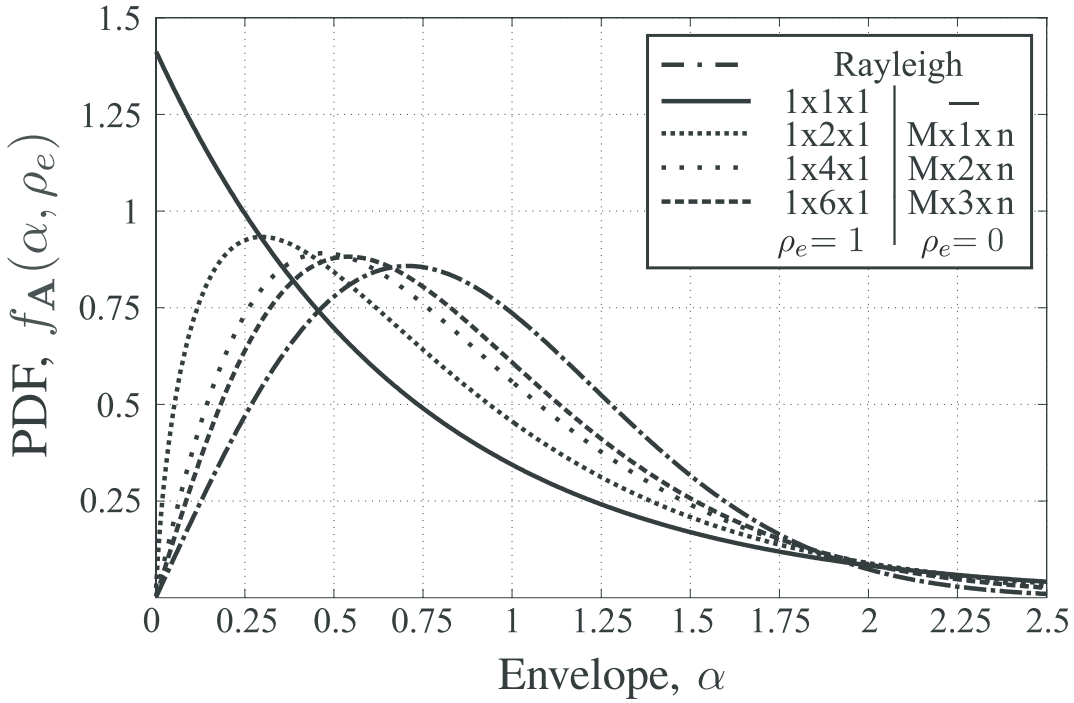

Figure 12: Plots of the envelope PDF at the n^{th} receiver antenna, with $\rho_e = 0$ and $\rho_e = 1$, for several dyadic backscatter channels along with the PDF of a conventional, transmitter-to-receiver, Rayleigh-fading channel. Each PDF has been normalized to unit power, that is, $\mathbf{E}\{\mathbf{A}^2\} = 1$ where $\mathbf{E}\{\cdot\}$ denotes the ensemble average (Reprinted from [5], © 2008 IEEE).

In Figure 12, it can be seen that the PDF of the dyadic backscatter channel has deeper fades than that of the conventional Rayleigh channel, but improves as RF-tag antennas are added. This is evident from the fact that the area bounded by the PDF curve for α less

than a given value – which gives the probability that the envelope will be between zero and the given value – decreases as RF-tag antennas are added. The most significant change is seen for the fully-correlated channel, $\rho_e = 1$, where the PDF changes from an exponential distribution for the $1 \times 1 \times 1$ channel to a product-Rayleigh distribution for the $1 \times L \times 1$ channel ($L > 1$). Not only does the PDF change as RF-tag antennas are added, but also with ρ_e, as shown in Figure 13(a) and Figure 13(b). These figures have same normalization as Figure 12. As ρ_e is reduced, the PDFs improve for both the $1 \times 1 \times 1$ and $1 \times 2 \times 1$ channels. Improvements as RF-tag antennas are added can also be seen in Figure 14(a).

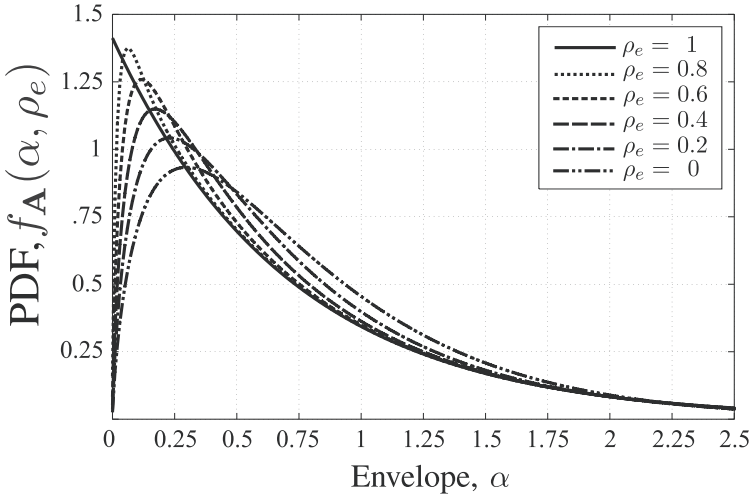

(a) Normalized $1 \times 1 \times 1$, dyadic-backscatter-channel PDF

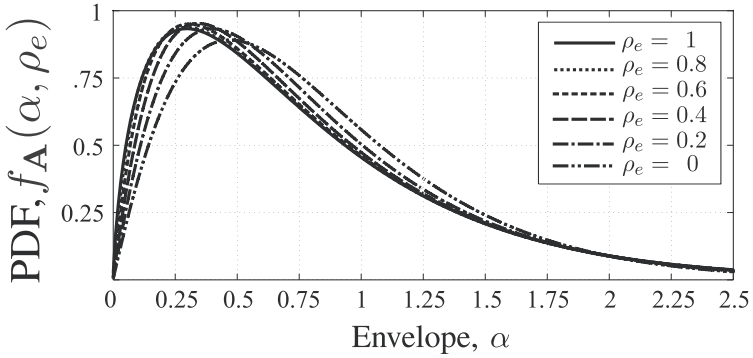

(b) Normalized $1 \times 2 \times 1$, dyadic-backscatter-channel PDF

Figure 13: The PDF of the signal received at the n^{th} reader-receiver antenna for (a) the $1 \times 1 \times 1$ and (b) $1 \times 2 \times 1$ channels with different ρ_e values. Each distribution has been normalized to unit power (i.e., $\mathbf{E}\{\mathbf{A}^2\} = 1$ where $\mathbf{E}\{\cdot\}$ denotes the ensemble average). These figures are reprinted from [52], © 2007 IEEE.

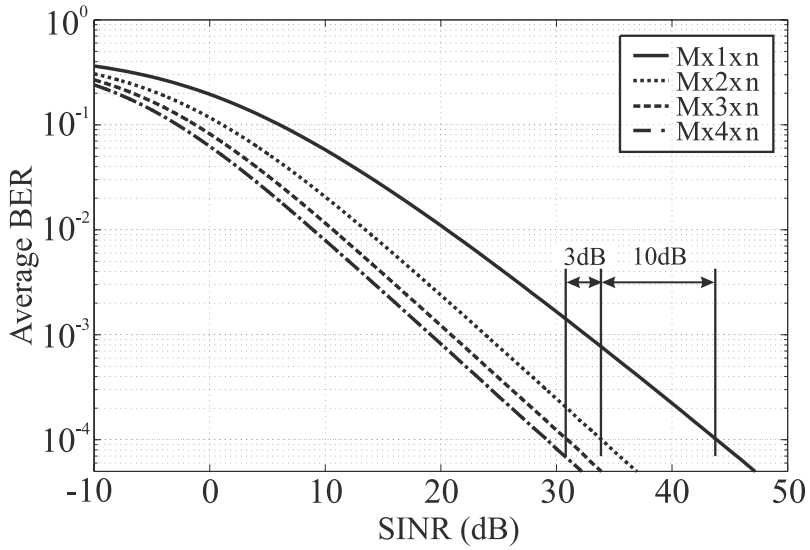

(a) Gains due to pinhole diversity and increased RF-tag scattering aperture.

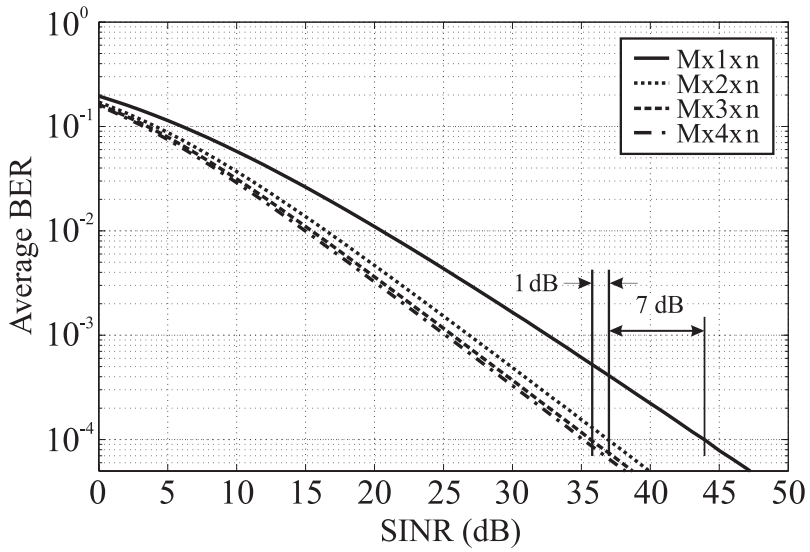

(b) Gains due solely to pinhole diversity.

Figure 14: Average BER plots for backscatter-radio systems operating in various dyadic backscatter channels with independent, Rayleigh-fading, forward and backscatter links; uncoded BPSK modulation; and noise and interference that is additive, white, and Gaussian. Each curve represents the average BER of the signal received at the n^{th} reader-receiver antenna with no diversity combining. Each BER curve is plotted against the SINR at the n^{th} reader-receiver antenna in the $1 \times 1 \times 1$ channel. In (a), the simulated, random channel matrix is normalized by M for constant transmit power and the BER improvements are caused by both pinhole diversity gains and a larger tag scattering aperture as RF-tag antennas are added. In (b), the simulated, random channel matrix is normalized by ML to show the BER improvements caused solely by pinhole diversity gains. These figures are reprinted from [5], © 2008 IEEE.

Figure 14(a) plots simulated, average BER curves versus the signal-to-noise-plus-interference-ratio (SINR) for various dyadic backscatter channels with independent, Rayleigh-fading forward and backscatter links. The simulations use uncoded, coherent, binary-phase-shift keying (BPSK) modulation with noise and interference that is additive, white, and Gaussian. In these Monte Carlo simulations, 69×10^6 channel realizations were used to approximate the ensemble average of the BER and the simulated, random channel matrix was normalized by the number of transmit antennas M for constant transmit power.

As RF-tag antennas are added, the slopes of the BER curves increase, and the curves are shifted in a manner similar to that caused by conventional diversity and coding techniques. For a BER of 10^{-4}, there is a 10 dB gain from the $1 \times 1 \times 1$ channel to the $1 \times 2 \times 1$ channel, with slightly larger gains for the $L = 3$ and $L = 4$ cases. Like the PDFs, the average BER curves are also a function of ρ_e, shown in Figure 15.

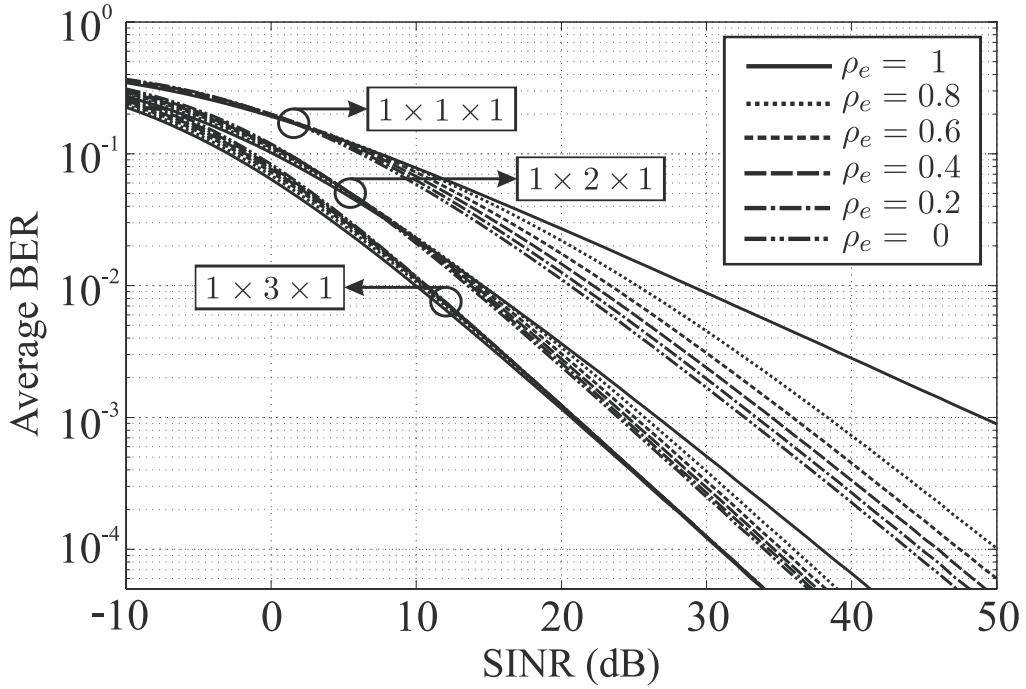

Figure 15: Average BER plots for the $1 \times 1 \times 1$, $1 \times 2 \times 1$, and $1 \times 3 \times 1$ dyadic backscatter channels for several values of link envelope correlation, ρ_e. In these Monte Carlo simulations, Rayleigh-fading forward and backscatter links; uncoded BPSK modulation; and noise and interference that is additive, white, and Gaussian were assumed. Each curve represents the average BER of the signal received at the n^{th} reader-receiver antenna with no diversity combining. Each BER curve is plotted against the SINR at the n^{th} reader-receiver antenna in the $1 \times 1 \times 1$ channel (Reprinted from [52], © 2007 IEEE).

For each dyadic backscatter channel (i.e., the $1 \times 1 \times 1$, $1 \times 2 \times 1$, and $1 \times 3 \times 1$ channels), the average BER improves as ρ_e is lowered; however, the number of RF-tag antennas has stronger effect.

In summary, this section has shown that the PDF and the average BER of the dyadic backscatter channel are affected by both the number of RF-tag antennas and the level of link envelope correlation. An explanation of these effects is given in the following sections.

3.3.2 Pinhole Diversity Gains

One source of the PDF improvements in Figure 12 and the communication gains in Figure 14(a) and Figure 15 is a *pinhole diversity* gain caused by the use of multiple RF-tag antennas. The term pinhole diversity is derived from the fact that each RF-tag antenna corresponds to a pinhole in the channel that provides a set of spatially-separated propagation paths, or pinhole diversity branches. Equation (25) shows that, for an RF tag with L antennas, L diversity branches are formed by the independent, complex-Gaussian-product terms of the dyadic backscatter channel. As L increases, the probability that the envelope will fade is reduced and, as L becomes very large, the derived envelope distributions become Rayleigh, as expected. This is shown mathematically in Appendix B.3.

Since pinhole diversity does not require diversity branch combining at the reader, it is often assumed that it is equivalent to diversity combining without channel knowledge in a transmitter-to-receiver channel – i.e., the non-coherent addition of diversity branches received through a transmitter-to-receiver channel. However, pinhole diversity differs from both non-coherent diversity combining and conventional, coherent diversity combining in two important aspects.

3.3.2.1 PDF Shape Change

Non-coherent diversity-branch combining in a transmitter-to-receiver, Rayleigh-fading channel only increases the power (or variance) of the received signal. Pinhole diversity gains, on the other hand, are caused by the summation of terms that have a product-Rayleigh distribution and result in a favorable change in the shape of the PDF. This is can be seen in Figure 12 in which each PDF has been normalized to unit power. In fact, the number of

pinholes available in the channel determines the shape of the PDF. Analysis of (25) shows that this is a general result; when normalized to equal power, the $1 \times L \times 1$ channel with uncorrelated, Rayleigh-fading links has the same PDF shape as the $1 \times 2L \times 1$ channel with fully-correlated, Rayleigh links.

3.3.2.2 Reader Design Simplification

In a transmitter-to-receiver channel, gain combining, switch combining, or gain combining in conjunction with space-time block codes must be used to affect a favorable change in the PDF shape. Pinhole diversity gains, on the other hand, can be realized in the dyadic backscatter channel using *only* multiple RF-tag antennas to modulate backscatter – no change in the reader receiver hardware, reader transmitter hardware, or signaling scheme is required.

It should be noted that as Rayleigh products are summed, the power of the channel distribution does increase and can be attributed to an increase in the RF-tag effective scattering aperture as antennas are added. This increase in scattered power can itself result in improved BER performance [26]. The BER plot shown in Figure 14(a) reflects both this increase in effective scattering aperture and improved PDF shape caused by pinhole diversity. To see the BER improvement caused solely by pinhole diversity, the simulated, random channel matrix has been normalized by ML, in Figure 14(b), so that the channel power is held constant with respect to both M and L. Figure 14(b) shows that pinhole diversity causes a 7 dB and 8 dB gain for the $1 \times 2 \times 1$ and $1 \times 3 \times 1$ channels, respectively, compared to the $1 \times 1 \times 1$ channel. Actual communication gains in a backscatter-radio system are due to both pinhole diversity gains and increased effective scattering aperture; therefore, all performance comparisons should be based on Figure 14(a).

3.3.3 Link Envelope Correlation

A second source of improvement evident in Figure 12, Figure 14(a), and Figure 15 is the reduction of link envelope correlation ρ_e. In a conventional transmitter-to-receiver channel, spatial fading correlation will hinder communication and limit available diversity gains. In a pinhole channel, such as the dyadic backscatter channel, ρ_e can have the same effect.

Previous work on realistic pinhole channels has focused on situations in which the two links of the pinhole channel – i.e., the forward and backscatter links – are likely dissimilar (e.g. outdoor propagation [60] or amplify-and-forward channels [61]) justifying the assumption of independent links. In many backscatter-radio systems, however, reader transmitter and receiver antennas may be closely spaced or even collocated giving rise to a potentially large ρ_e. A high degree of link envelope correlation will occur when the dominant mechanism of wave propagation (i.e., LOS or NLOS) and the angles of arrival/departure at the reader are similar. Since a high level of link envelope correlation implies that the propagation environment of the forward and backscatter links are similar, fully-correlated links can *only* occur when the reader transmitter and receiver antennas are collocated and have the same antenna patterns. If the antennas are spatially separated and/or the antenna patterns are different, ρ_e will be reduced. This allows the designer some control over the level of link envelope correlation. The separation distance and pattern required to reduce ρ_e to an acceptable level will vary depending upon the channel.

In the analysis presented in Section 3.2, it is assumed that ρ_e is equal for each set of paths (see Figure 10). In an actual dyadic backscatter channel, antenna coupling, close spacing of RF-tag antennas, and the scattering environment will likely cause ρ_e to be different for each RF-tag antenna. In addition, these effects may also cause fading correlation between the modulated-backscatter signals received from each RF-tag antenna.

3.3.4 Limits on Pinhole Diversity Gains

In Section 3.3.2, it was shown that a pinhole diversity gain is available in dyadic backscatter channels with Rayleigh-fading links; however, pinhole diversity in a Rician backscatter channel – Rician fading is the most common type of fading found in the forward and backscatter links – has not yet been investigated. In a Rician channel, a strong, LOS specular wave dominates other multipath waves and results in less severe fading. To investigate this case, envelope PDFs of the signal received at the n^{th} reader-receiver antenna in an $M \times L \times N$, dyadic backscatter channel with independent, Rician-fading links are plotted in Figure 16 and Figure 17.

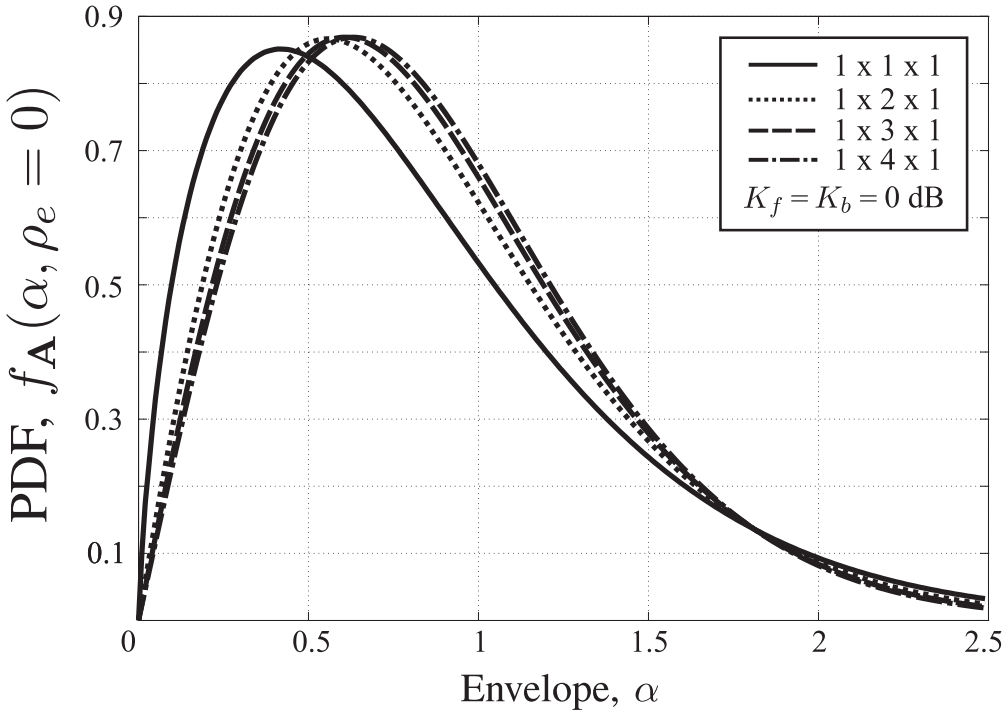

(a) The dyadic backscatter channel with Rician-fading links for $K_f = K_b = 0$ dB

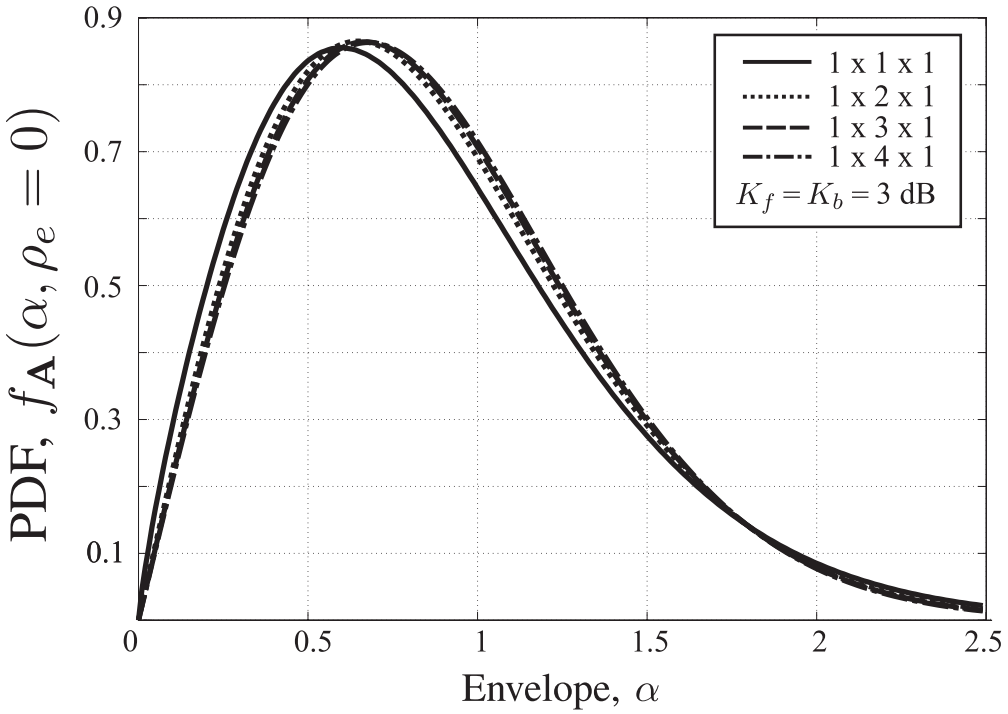

(b) The dyadic backscatter channel with Rician-fading links for $K_f = K_b = 3$ dB

Figure 16: Plots of the envelope PDF at the n^{th} receiver antenna in a dyadic backscatter channel with Rician-fading links for (a) $K_f = K_b = 0$ dB and (b) $K_f = K_b = 3$ dB. In each plot, $\rho_e = 0$ and each PDF has been normalized to unit power, that is, $\mathbf{E}\{\mathbf{A}^2\} = 1$ where $\mathbf{E}\{\cdot\}$ denotes the ensemble average.

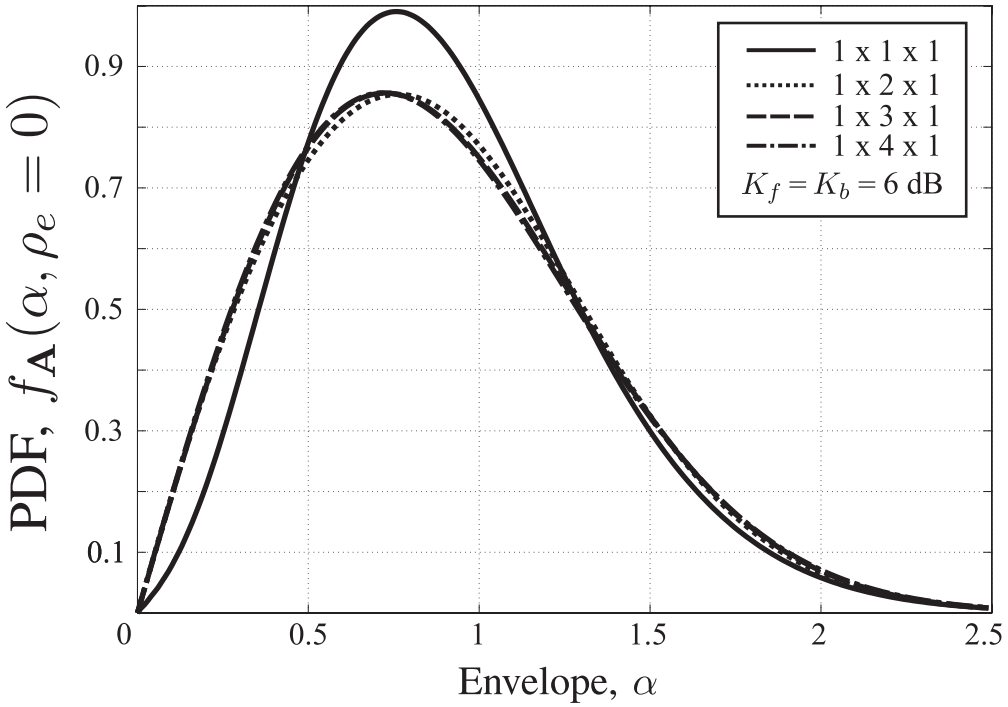

(a) The dyadic backscatter channel with Rician-fading links for $K_f = K_b = 6$ dB

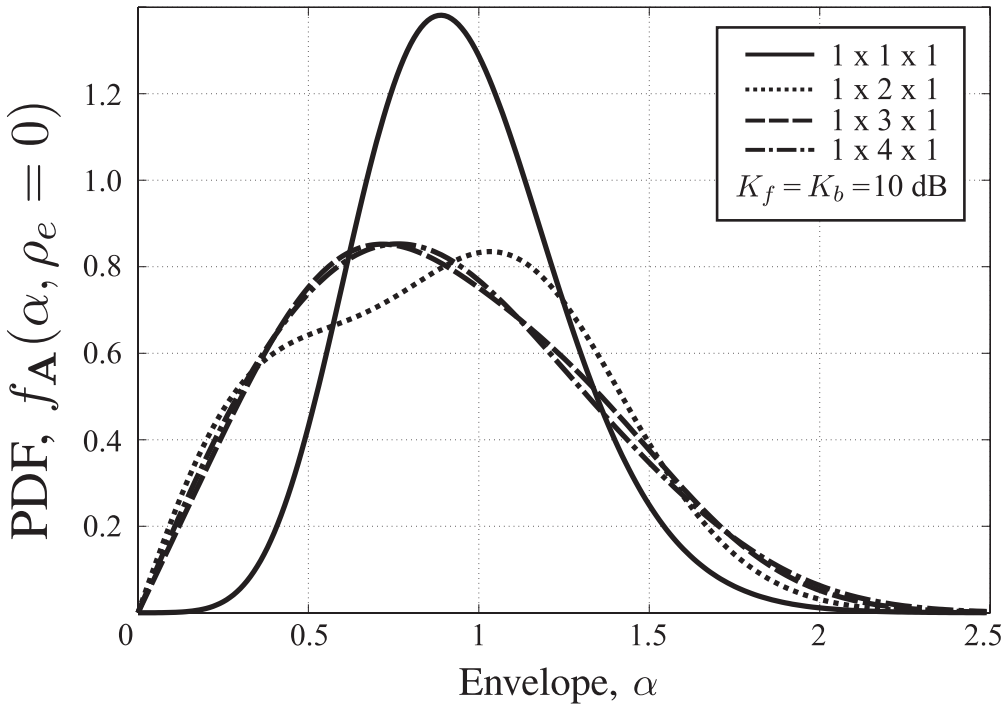

(b) The dyadic backscatter channel with Rician-fading links for $K_f = K_b = 10$ dB

Figure 17: Plots of the envelope PDF at the n^{th} receiver antenna in a dyadic backscatter channel with Rician-fading links for (a) $K_f = K_b = 6$ dB and (b) $K_f = K_b = 10$ dB. In each plot, $\rho_e = 0$ and each PDF has been normalized to unit power, that is, $\mathbf{E}\{\mathbf{A}^2\} = 1$ where $\mathbf{E}\{\cdot\}$ denotes the ensemble average.

The PDFs plotted in Figure 16 and Figure 17 were calculated numerically using the procedure discussed in Section 3.2.2. In Figure 16, it can be seen that, for K less than approximately 3 dB, the probability of receiving a small envelope is greater in the $M \times 1 \times n$ channel than in the $M \times 2 \times n$, $M \times 3 \times n$, or $M \times 4 \times n$ channels. However, for K greater than approximately 3 dB, Figure 17 shows that pinhole diversity gains disappear and fading in the $M \times 1 \times n$ channel is less severe than the $M \times L \times n$ channel (for $L > 1$).

The severe fading observed in the backscatter channel with $K = 10$ dB is caused by the interference of multiple specular waves propagating in the channel. Since the channel has a very high K factor, a specular wave will be scattered off each RF-tag antenna. According the formulation of the PDF plotted in Figure 17, the modulated-backscatter signal received from each RF-tag antenna is statistically independent. Therefore, for an RF-tag with two antennas, the two specular waves received by the reader will interfere and cause severe fading. Measurements in Chapter 6 show, however, that correlation between the modulated-backscatter signals received from real RF-tag antennas can reduce the Rician-fading severity. The numerical approximations for the PDFs shown in Figure 16 and Figure 17 are very similar to that of a channel experiencing two-wave with diffuse power (TWDP) propagation [65].

3.3.5 Conventional Diversity Gains

As discussed previously, pinhole diversity causes the shape of the channel envelope PDF to change favorably and contributes to BER improvements; however, if conventional diversity combining techniques are used at the reader, even greater gains are available. Figure 18 shows average BER curves for backscatter-radio systems using maximal ratio combining (MRC), the optimal diversity-combining technique for a fading channel, at the reader receiver. No diversity combining is performed at the RF tag. In these Monte Carlo simulations, 69×10^6 channel realizations were used to approximate the ensemble average of the BER and the receiver had perfect knowledge of the independent, Rayleigh-fading forward and backscatter links. Comparison of the BER plots for the $M \times L \times 1$ channel in Figure 14(a) and Figure 18 shows that MRC offers no further improvement over that caused by

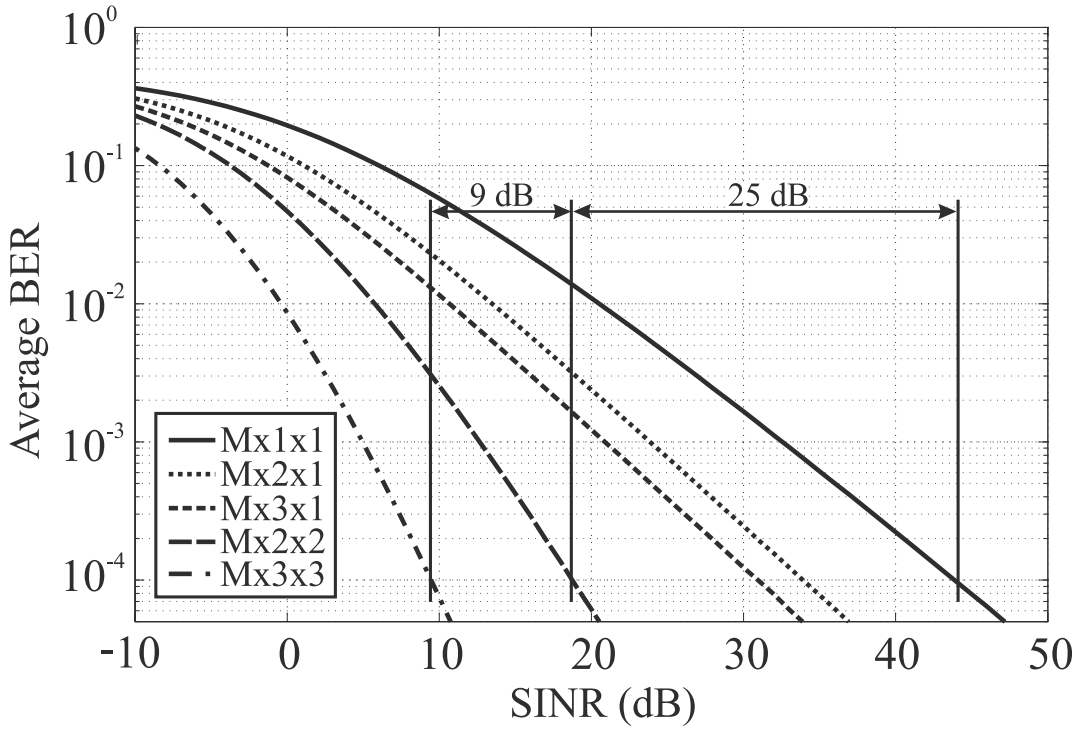

Figure 18: Average BER plots for backscatter-radio systems operating in various dyadic backscatter channels with independent, Rayleigh-fading forward and backscatter links; uncoded BPSK modulation; and noise and interference that is additive, white, and Gaussian. Each curve represents the average BER of the received signal using MRC with perfect channel knowledge at the reader receiver. The random channel matrix used in this simulation has been normalized by M for constant total transmit power. Each BER curve is plotted against the SINR at the n^{th} reader-receiver antenna in the $1 \times 1 \times 1$ channel (Reprinted from [5], © 2008 IEEE).

pinhole diversity gains (and increased scattering aperture), since the $M \times L \times 1$ channel offers only a single diversity branch to the MRC combiner at the reader receiver. However when $N > 1$, MRC gains and pinhole diversity gains combine for a significant communication performance improvement. At a BER of 10^{-4}, the $M \times 2 \times 2$ and $M \times 3 \times 3$ channels show up to a 25 dB and 34 dB gain with respect to the $1 \times 1 \times 1$ channel, respectively. These gains reflect both a power gain due to the increased RF-tag scattering aperture and an improved PDF due to pinhole diversity and maximal ratio combining. Like pinhole diversity gains, MRC gains will decrease as the K factor of the channel increases.

3.4 Range and Reliability Examples

This chapter has has provided analytic expressions and numerical approximations for the PDF of the $M \times L \times N$, dyadic backscatter channel with Rayleigh and Rician links, respectively. The chapter has also shown how fading in these channels can be decreased through pinhole diversity gains, minimizing link correlation, and using conventional diversity combining. This section will use the previous BER plots and link budgets to show how these gains translate into range and reliability improvements.

Reliability Improvement: One way to show a reliability improvement is to use the BER versus SINR plots shown in Figure 14(a) and Figure 18. Suppose that an RF tag is a fixed distance from the reader such that there is adequate power to operate a passive RF tag (no such limitation is required for a semi-passive tag). If the channel worsens, by the introduction of interfering signals or increased fading from additional scatterers, the SINR at the reader may drop below the threshold required for successful detection of the signal. This may happen even though the passive RF tag is still powered. As Figure 14(a) shows, an RF tag using multiple antennas will have a lower SINR threshold for a given BER. For a BER of 10^{-4}, the threshold is up to 10 dB lower for an RF tag using two antennas to modulate backscatter than for an RF tag using one antenna – a significant reliability increase. Figure 18 shows that an even greater SINR improvement – up to 25 dB for an $M \times 2 \times 2$ system – will be realized using MRC at the reader receiver. In each of these cases, it is assumed that the RF tag is a fixed distance from the reader and that the RF tag is powered.

For completeness, it should be mentioned that the SINR gain mentioned above may be reduced in an actual $1 \times 2 \times 1$ channel since the target BER may be greater than 10^{-4}, indoor path loss may be larger or smaller than free-space path loss (assumed in the link budgets from Section 2.1), and the statistics of interfering signals may not be white and Gaussian (assumed in Figure 14(a)). Even so, since the source of this gain (i.e., the pinhole diversity gain and an increased RF-tag scattering aperture) only requires uncorrelated signal envelopes at the backscatter-radio system antennas, multiple RF-tag antennas will provide

gains regardless of assumptions about path loss and noise-plus-interference statistics.

Range Improvement: Suppose that a backscatter-radio system operates in channel with Rayleigh-fading links and all parameters of the channel, except the reader-to-tag separation distance, are held constant. As the separation distance increases, path loss will decrease the power received at the reader causing the SINR to decrease. At some distance from the reader, which is determined by the reader sensitivity, the SINR will fall below the threshold required to maintain a target BER. Using multiple RF-tag antennas lowers this threshold allowing the reader-to-tag-to-reader separation distance $r = r_f + r_b$ to increase further without exceeding the desired BER. For a backscatter-radio system using two RF-tag antennas and a target BER of 10^{-4}, Figure 14 shows that a up to a 10 dB SINR gain is available. Therefore, according to (2) in Section 2.1, if all link budget terms are held constant and the fade margin is decreased by 10 dB, the range of the RF tag can increase by up to 78%.

Of course, the range improvement realized depends on the error metric used and the characteristics of the channel. For example, if the outage probability defined by (16) is considered, the range increase for a backscatter-radio system using two RF-tag antennas compared to that using a single antenna can be derived from the fade margins in Table 7 and Table 2, respectively. If the RFID-portal example in Section 2.3 is considered, the fade margin given in Table 7 drops to 13 dB for a two antenna RF tag compared to 15 dB (from Table 2) for a single antenna RF tag. According to (2), this results in a 12% range increase. However, if the same system were to operate in a backscatter channel with Rayleigh-fading links, up to a 26% range increase would be realized. It should be noted that these range gains assume sufficient power is available for an RF tag to operate.

3.4.1 Discussion

The analysis of this chapter has assumed that the modulated-backscatter signals received from each RF-tag antenna at the reader are independent; however, correlation will exist as a function of the RF tag and reader antenna element spacing, electromagnetic coupling between array elements, and the angle spectrum of the multipath waves [17]. In a rich

Table 7: Fade margins for the signal received at the n^{th} reader antenna using a bistatic, dislocated reader (F_β) in the $M \times 2 \times N$, dyadic backscatter channel. Fade margins are reported in dB.

Outage Probability	$K = -\infty$ dB	$K = 0$ dB	$K = 3$ dB	$K = 10$ dB
0.5	2.7	2.3	1.9	0.8
0.1	12	11	10	9.9
0.05	15	14	13	13
0.01	23	22	20	20
0.005	26	25	24	23
0.001	33	32	31	30

scattering environment, such correlation can be reduced at the reader by separating array elements by at least $\lambda/2$ [24]; however, footprint constraints may require smaller spacing of RF-tag antennas resulting in higher correlations and reduced pinhole diversity gain. At very worse, RF-tag antenna envelope correlation will reduce the $M \times L \times N$, dyadic backscatter channel to an effective $M \times 1 \times N$ channel with added power caused by the increased RF-tag scattering aperture. Fortunately, research shows that diversity antennas with less than $\lambda/2$ spacing can also have low correlation [66, 67]. Even in the case where pinhole diversity fails, MRC combining at the reader can be used to increase the RF-tag range and reliability.

3.5 Conclusion

The $M \times L \times N$, dyadic backscatter channel is a pinhole channel with deeper small-scale fades than a conventional transmitter-to-receiver channel. Pinhole diversity can mitigate this fading by changing the shape of the fading distribution resulting in reduced fading for Rician backscatter links with K less than approximately 3 dB. Examples have demonstrated that pinhole diversity gains lead to increased backscatter-radio communication reliability and up to a 78% range increase. These gains require no channel knowledge or diversity combining at the reader, only the modulation of backscatter using multiple RF-tag antennas and separate, adequately-spaced reader transmitter and receiver antennas. Even greater range and reliability gains are available if MRC is used at the reader receiver.

CHAPTER IV

BACKSCATTER-RADIO DESIGN GUIDELINES

Chapter Overview: This chapter provides the following:

- Four design guidelines for backscatter-radio system design.
- Arguments for the use of the 5725-5850 MHz ISM frequency band for backscatter radio.
- An example demonstrating the potential performance of a backscatter-radio system operating in the 5725-5850 MHz ISM frequency band.

In Chapter 3, a detailed discussion of small-scale multipath fading in the $M \times L \times N$, dyadic backscatter channel was presented. It was shown that a pinhole diversity gain is available for RF tags that use multiple antennas to modulate backscatter in Rician channels with K less than approximately 3 dB. Link envelope correlation and conventional diversity combining techniques were also discussed. Although the previous chapter was largely theoretical, the presented theory leads to several very practical design guidelines for backscatter radio which have been adapted from [5] for this chapter. These are presented in Sections 4.1 through 4.3 and followed by a 5.8 GHz RFID system example demonstrating the potential benefits of using the 5725-5850 MHz ISM frequency band for backscatter radio. This example has been adapted from [37] for this chapter.

4.1 Design Guideline 1: Use Multiple RF-Tag Antennas

The pinhole diversity gains presented in Chapter 3 are only available to RF tags with more than one antenna. Figure 12 and Figure 14(a) show a large improvement for an RF tag with two antennas, with only slightly more for each additional antenna. Based on this, using two RF-tag antennas is the best balance of the RF-tag footprint and pinhole diversity gains. Furthermore, each RF-tag antenna must be used to modulate backscatter; pinhole

diversity gains and increased scattering aperture are not available to RF tags that use one antenna for communication and another to receive power. Also, using cross-polarized RF-tag antennas will reduce correlation between signals scattered from each antenna. However, the favorable correlation effects of cross-polarization must be balanced with the detrimental effects of unequal diversity branch power [17] caused by cross-polarization.

4.2 Design Guideline 2: Use Separate Reader Antennas

In Figure 12, a comparison of PDFs with independent and fully-correlated links shows that the correlated case is worse than that of independent links. This difference can also be seen by comparing monostatic fade margin F_{m} and the bistatic-dislocated fade margin F_{β} in Table 2. A fully-correlated link represents an extreme case that can only occur if a single reader antenna is used for both transmitting and receiving. Using separate, adequately-spaced transmitter and receiver antennas avoids this problem.

4.3 Design Guideline 3: Use Reader Antenna Arrays

As shown in Section 3.3.5, great gains for backscatter-radio systems are available through the use of conventional antenna diversity at the reader. Hence, whenever cost effective, it is beneficial to use an antenna array at the reader receiver (or at the transmitter) to provide multiple diversity branches to a conventional diversity combiner. The elements of the reader array should be adequately spaced to reduce fading correlation.

4.4 Design Guideline 4: Use a High Frequency

One way to effectively implement these design guidelines is to operate backscatter-radio systems at a higher frequency than is normally used. In the United States, the two most commonly used frequency bands are the 902-928 MHz and 2400-2483.5 MHz ISM bands; however, another ISM frequency band is available at 5725-5850 MHz. In this band, the wavelength is much smaller than that found in the 902-928 MHz band and leads to the following benefits:

4.4.1 Small Antennas

Since antenna dimensions scale with wavelength, as illustrated in Figure 19, antennas in the 5725-5850 MHz ISM band can be made small enough to allow multiple antennas to be used on each RF tag without increasing, and possibly decreasing, their footprint size compared to the footprint of a 902-928 MHz RF tag. This will allow many small objects to be tagged, an extremely important step toward realizing widespread use of RF tags. In addition, the small wavelength of the 5725-5850 MHz ISM band will allow very compact antenna arrays to be constructed at the reader; in fact, these arrays may be small enough for use on mobile and hand-held readers.

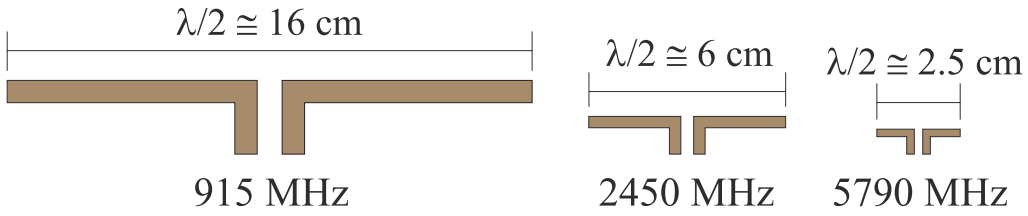

Figure 19: Half-wave dipoles for 915 MHz, 2450 MHz, and 5790 MHz drawn proportionally (not actual size) to show the relative decrease in size with increasing frequency (Reprinted from [37], © 2009 IEEE).

4.4.2 Increased Antenna Gain

For a fixed antenna aperture, (28) shows that additional antenna gain is available at higher frequencies (smaller wavelengths) [38].

$$\mathrm{G} = \frac{4\pi}{\lambda^2}\mathrm{A_{eff}} \tag{28}$$

For example, according to (28), there is an additional 7.8 dB of antenna gain available at 5790 MHz compared to 2450 MHz and an additional 16.4 dB compared to 915 MHz.

4.4.3 Increased Object Immunity

As was shown in Section 2.3, when an antenna is attached-to or brought close-to a metallic object, its impedance will change and potentially reduce the power transmission coefficient τ and modulation factor M. From Figure 8 in Section 2.3, it can be seen that the impedance

of the antenna will increase significantly even if its electrical distance from the metal is increased by only a fraction of a wavelength. Though this electrical distance may be increased by physically moving the antenna away from an object, it may also be increased by decreasing the wavelength (i.e., increasing the frequency). For example, Figure 8 shows that the real part of the impedance at an electrical distance of 0.01λ is $\approx 2\,\Omega$ at 915 MHz. If the physical distance is unchanged and the frequency is increased to 5790 MHz, the electrical distance becomes 0.06λ with a corresponding real impedance of $\approx 40\,\Omega$. This increase will result in a larger power transmission coefficient τ and modulation factor M.

The assertion that increased frequency will result in increased object immunity is based upon the fact that the physical size of an antenna's near-field becomes smaller as the frequency is increased. As the near-field region becomes smaller, nearby objects will intrude less into the near-field and, as a result, have a smaller effect on its fields. The NEC simulations shown in Figure 8 indicate that this is the case for the impedance of a folded-dipole antenna as its distance from a perfectly conducting half-plane is increased; however, the antenna's behavior on dielectric objects has not been simulated. Furthermore, even though increased frequency may improve an antenna's performance on metal, the improvement may not be enough for the tag to operate. In addition, pattern distortion and on-object gain penalties may still render the RF tag inoperable. Therefore, it should be concluded that, although simulations indicate object immunity improvements as the frequency is increased, more investigation is needed for different object materials and geometries.

4.4.4 Additional Bandwidth

An additional benefit of using the 5725-5850 MHz ISM is the increased bandwidth that is available compared to the 902-928 MHz ISM band. This bandwidth will make high data rate and spread spectrum backscatter communication possible [12].

4.5 High-Frequency Example

Consider the same RF-tag system described in Section 2.3. If this system were redesigned to operate at 5.79 GHz, then the high-frequency benefits described above would apply. The resulting changes in the link budget parameters are described in the following sections and

summarized in Table 8.

4.5.1 Increased Antenna Gain

If the antenna's effective area remains constant, (28) dictates that an additional 16.4 dB of gain is available as λ decreases from 33 cm at 915 MHz to 5 cm at 5.79 GHz. Therefore, at 5.79 GHz, the reader antenna gains are now 23.4 dBi (219 in the linear scale) and the RF-tag antenna gain is now 18.5 dBi (71 in the linear scale).

4.5.2 Multiple Tag Antennas and MRC

At 5.79 GHz, it is practical to use two antennas on each RF tag and a two element antenna array at the reader receiver. If maximal ratio combining (MRC) is performed on the diversity branches received from the two-element receiver array, then F_β is reduced to 8 dB (6.3 in the linear-scale) for a 5% outage probability. This result was obtained through Monte Carlo simulation of the backscatter channel with $\rho_e = 0$. For this example, the power-up fade margin F_p remains unchanged from the 915 MHz example.

4.5.3 Increased Object Immunity

From the example in Section 2.3, the RF-tag antenna attached to a metal object is 0.005λ from the metal surface at 915 MHz. If the RF tag now operates at 5.79 GHz and its physical distance from the metal surface is unchanged, the electrical separation distance becomes 0.033λ. At this distance, Figure 8 shows that the antenna's input impedance is now approximately $10 + j100\,\Omega$ which corresponds to $Z_{IN} = 2.3 + j319\,\Omega$ at the output terminals of the impedance transformation network, shown in Figure 7. From (3) and (4), the power transmission coefficient and modulation factor for metal attachment are now $\tau = 0.13$ and $M = 4.4 \times 10^{-3}$ (both in the linear scale), respectively. Because of cardboard's weak effect on the antenna impedance, τ and M for cardboard attachment do not change from the 915 MHz example.

To complete this example, the transmitted power must be decreased to 12.6 dBm (or 18.3 mW) to meet FCC power limitations with the increased reader antenna gains. Since no measurements of gain penalties at 5790 MHz are available, 915 MHz gain-penalty values

from Table 3 are used.

Table 8: 5.79 GHz RF-tag portal example parameters in the linear scale (Reprinted from [37], © 2009 IEEE).

Material	P_T (mW)	$G_{T,R}$	G_t	$X_{f,b}$	F	F_β	λ (m)	M	τ	Θ	B
Cardboard	18.3	219	71	0.5	10	6.3	0.05	0.25	1	1.2	1
Aluminum	18.3	219	71	0.5	10	6.3	0.05	4.4×10^{-3}	0.13	11	1

4.5.4 Discussion

Figure 20(a) compares the power-up link budgets evaluated at 915 MHz and 5790 MHz and shows surprising results. For cardboard attachment, the links are almost identical; the power sacrificed to higher path loss at 5790 MHz is balanced by increased antenna gain at the RF tag. For metal attachment, increased object immunity combines with the increased antenna gain at 5790 MHz to make the link approximately 13 dB better than that at 915 MHz. Similar improvement is seen for the bistatic, dislocated links shown in Figure 20(b). Here, the reduced fading, increased RF-tag antenna gain, and the greatly increased reader-receiver antenna gain cause the links at 5790 MHz to perform approximately 24 dB and 45 dB better than those at 915 MHz for cardboard and aluminum attachment, respectively.

While these gains still do not now allow the RF tag to operate while attached to the aluminum slab, they may do so for other, less-extreme material attachments and result in significant range and reliability improvements. Semi-passive tags will immediately benefit from the gains evident in Figure 20(b) since their performance is not constrained by the more stringent power-up link. Passive tags will also experience significant benefits; however, the benefits shown in Figure 20(a) will be limited in some commonly used tag RFIC technologies by parasitic capacitance that increases power consumption at high frequencies. However, with careful circuit layout and use of technologies other than conventional silicon, it should be possible to adequately reduce the power consumption of high-frequency tag RFICs at reasonable manufacturing costs. Such high-frequency, low-power RFICs will have operating ranges comparable to their low-frequency counterparts, but with the added advantage of reduced fading and increased object immunity.

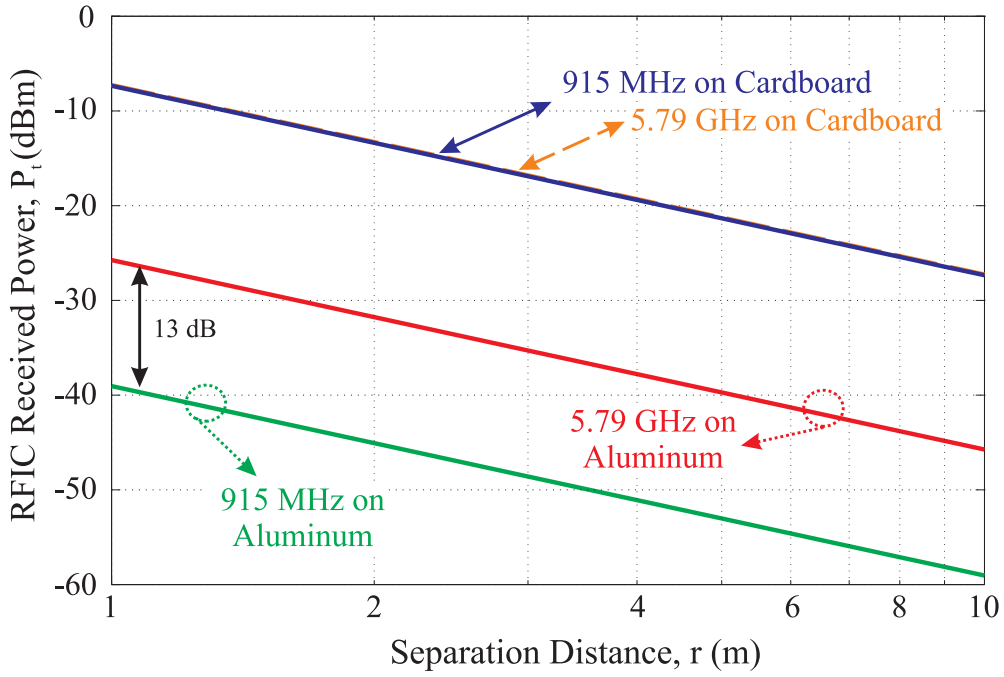

(a)

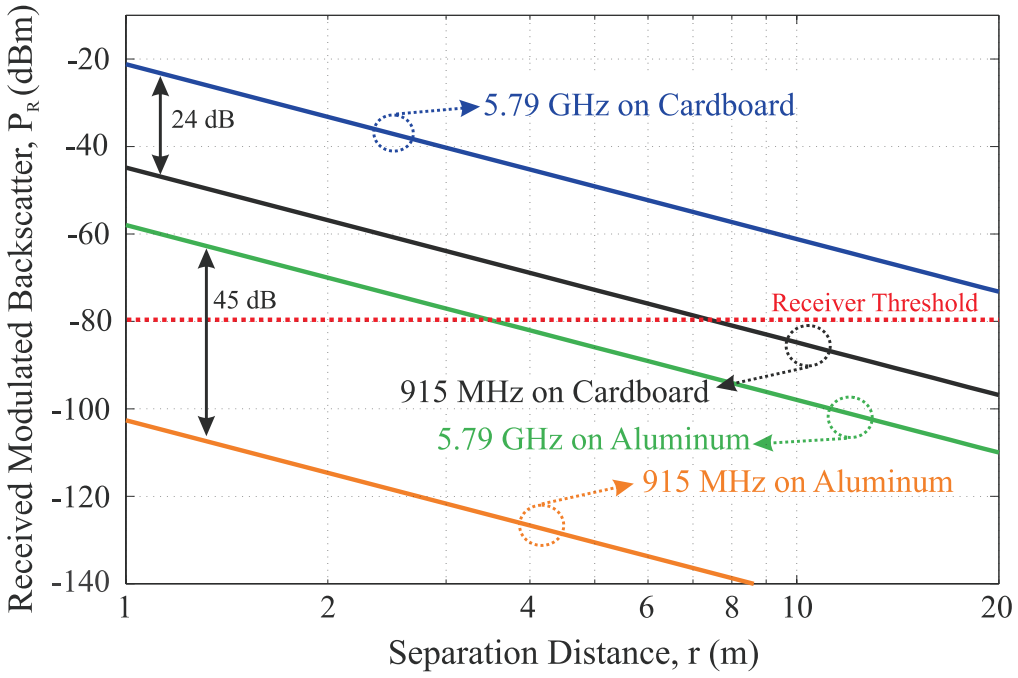

(b)

Figure 20: Power-up and backscatter links plotted as a function of reader-to-tag separation distance, r. In (b), it is assumed that $r = r_f = r_b$ (These figures are reprinted from [37], © 2009 IEEE).

For example, Curty *et al.* [10] have reported a tag RFIC made using technology other than conventional silicon that operates at a high frequency with low power consumption. Their tag RFIC consumes $2.7\mu W$ (-25 dBm) at 2.45 GHz and was fabricated using 0.5 μm silicon-on-sapphire technology.

It should be noted that while use of 5.79 GHz will allow for increased RF-tag antenna gain, it will also increase the antenna's directivity. The result will be an RF tag that is more orientation sensitive than that at 915 MHz. If the RF-tag's orientation is fixed or its range very small, the increased directivity will not be an issue; however, for other applications, it may pose a serious, but not insurmountable problem. In such cases, multiple reader antennas can be used to power the RF tag from different spatial positions. Furthermore, as tag RFIC technology advances and the required turn-on power is decreased, the RF-tag antenna gain and, as a result, directivity can be reduced without sacrificing tag range.

4.6 Conclusion

This chapter has presented four practical design guidelines that, if implemented, will enable backscatter-radio systems to realize the gains discussed in Chapter 3. The benefits of implementing these design guidelines in the 5725-5850 MHz ISM frequency band were illustrated with an example showing that, in theory, high-frequency backscatter-radio systems can have comparable range to their lower-frequency counterparts. Such high-frequency systems benefit from increased antenna gain, reduced small-scale fading, and increased object immunity compared to systems operating in the 902-928 MHz or 2400-2483.5 MHz frequency bands. Of course, the words of caution mentioned in Section 4.4.3 must be heeded.

CHAPTER V

EXPERIMENTAL DESIGN

Chapter Overview: This chapter provides the following:

- A brief overview of the differences between conventional and backscatter channel sounding.
- An overview of the backscatter measurement campaign.
- A description of the backscatter testbed.
- A detailed description of the signal processing used in the backscatter testbed.
- A description of the calibration procedure used for each measurement.
- A discussion of noise effects on the measured signals.

This chapter marks the beginning of the experimental portion of this dissertation. The goal of the measurements performed in this research was to measure multipath fading in the backscatter channel, calculate an estimate of the fading distribution, and compare the distribution estimate with the fading distributions discussed in Chapter 3. This chapter provides an overview of the testbed used to make the fading measurements.

5.1 The Challenges of Backscatter Channel Sounding

While the backscatter channel has many similarities with a conventional transmitter-to-receiver channel, the analysis presented in Chapter 3 has revealed several significant differences. The same is true for the methods required to obtain empirical, backscatter-channel data – *channel sounding*. The most significant difference between conventional and backscatter channels is that, in a backscatter channel, the modulated, backscattered signal must be separated from the unmodulated carrier transmitted from the reader. Therefore, the backscatter channel cannot be measured by transmitting a CW tone and extracting the magnitude and phase of the received signal – even for narrowband measurements. However,

since RF tags have the ability to modulate the amplitude and phase of the backscattered signal, any channel sounding method that uses either PSK or ASK modulation is appropriate, though it is often most practical to for the tag to use a binary symbol alphabet. For wideband channels, sounding methods used in conventional transmitter-to-receiver channels such as pulsed response, pulse compression, or spread spectrum techniques [54] could potentially be adapted for backscatter channel sounding, though no such attempts have been reported in the literature.

For narrowband, backscatter channel sounding with a coherent receiver, the simplest sounding waveform is generated by modulating backscatter with a square wave and passing the received signal through a matched filter at the reader. The output of the matched filter, sampled at time $t = 0$, will contain periodic peaks that are scaled versions of the complex channel coefficients. Though simple, this waveform does not provide significant discrimination between the peaks and the noise floor (limiting dynamic range) nor the ability to distinguish from which RF-tag antenna the backscatter signal originated. Both of these drawbacks can be overcome by modulating backscatter with a pseudo-random noise (PN) code [68]. Typically used for wideband channel measurements, the PN code allows channel samples to be determined from the autocorrelation of the received signal. This spread spectrum scheme works well in the presence of interferers and, if each RF-tag antenna modulates backscatter with a different PN code, allows the signals from multiple RF-tag antennas to be separated. It can also be used to simultaneously separate signals from multiple RF tags [12]. In particular, maximal length sequences, or *m-sequences*, have excellent autocorrelation properties and can be generated by simple shift register circuitry – a benefit for RF tags.

Another difference between conventional and backscatter channel sounding is the required spatial sampling rate. The spatial Nyquist rate for a backscatter channel is twice that of a conventional channel. This is shown in Figure 21 where the total path length from the reader transmitter to the RF tag and back to the reader receiver $|\vec{r}_{\mathrm{f}} + \vec{r}_{\mathrm{b}}|$ is proportional to $2\,\vec{r}_{\mathrm{tag}}$,

$$|\vec{r}_{\mathrm{f}} + \vec{r}_{\mathrm{b}}| = |2\,\vec{r}_{\mathrm{tag}} - \vec{r}_{\mathrm{tx}} - \vec{r}_{\mathrm{rx}}|. \tag{29}$$

It is worth noting that (29) is only an approximate relationship. This is because a signal may scatter off of the RF tag more than once before propagating back to the reader receiver; however, these components usually contain negligible power, in which case (29) is exact.

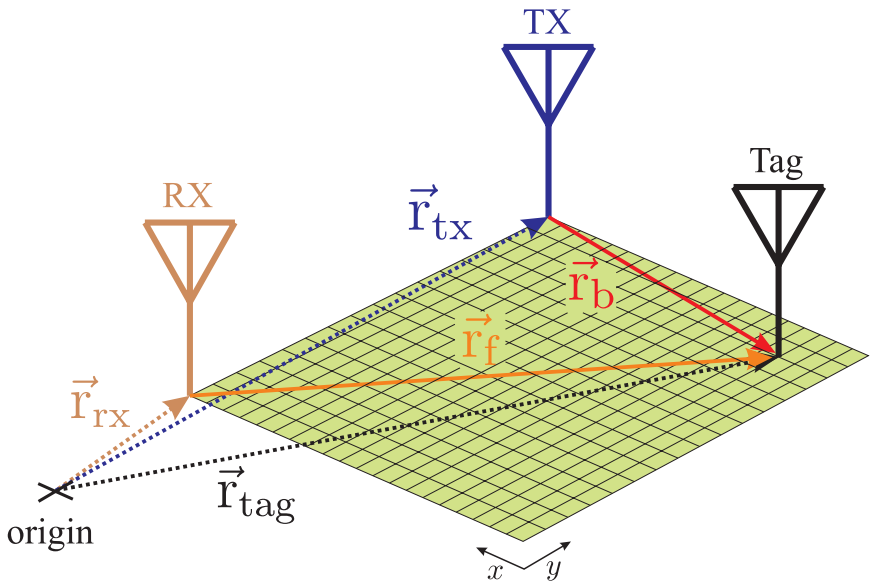

Figure 21: The relationships between the total distance between the transmitter-to-tag-to-receiver link $\vec{r}_f + \vec{r}_b$ and the position of the receiver, transmitter, and RF tag. Equation (29) shows that $\vec{r}_f + \vec{r}_b$ is proportional to $2\,\vec{r}_{tag}$.

5.2 Measurement Campaign Plan

The goal of this measurement campaign was to determine the envelope distribution of the $M \times L \times N$ backscatter channel at 5.79 GHz ($\lambda_o = 5.2$ cm) as a function of RF-tag position and compare it with the theory presented in Chapter 3. The theory suggests that certain channels will exhibit small-scale multipath fade reductions more than others; therefore, the following channels were chosen for measurement:

- **Monostatic, 1 × 1 × 1 Channel:** A single patch antenna was used at the reader to transmit and receive and a single-antenna RF tag (SAT) modulated the backscatter.
- **Monostatic, 1 × 2 × 1 Channel:** Again, a single patch antenna was used at the reader to transmit and receive, but a dual-antenna RF tag (DAT) modulated the backscatter.

- **Bistatic, 1 $\times$ 1 $\times$ 2 Channel:** In this channel, the reader transmitter antenna was separated from the two receiver antennas by several wavelengths and the SAT was used to modulate backscatter.

- **Bistatic, 1 $\times$ 2 $\times$ 2 Channel:** Like the previous channel, a single transmitter and two receiver antennas were used at the reader and the DAT was used to modulate the backscattered signal. Again, the transmitter and receiver antennas were widely spaced.

Each of these channel configurations were measured under NLOS and LOS conditions in rooms E558 and E560 of the Van Leer Building on the Georgia Institute of Technology Atlanta campus, respectively. Detailed diagrams of these measurement sites are provided in Figure 36 and Figure 43, respectively, in Chapter 6.

For each measurement, an unmodulated, 5.79 GHz carrier was transmitted from the reader and scattered by the RF tag. The RF tag modulated the backscatter using an m-sequence that was 31 bits long at a chip rate of 1 MHz. The modulated-backscatter signal was received by the two direct-conversion receivers and the in-phase (I) and quadrature (Q) baseband signals were digitized using analog-to-digital converter (ADC) boards contained in a personal computer and stored for later processing. To measure the fading as a function of position, the RF tag was placed on a linear positioner that was controlled by the personal computer. A measurement of the backscattered signal received from the RF tag was taken at points on a square grid that was 30 cm $\times$ 30 cm (approximately $6\lambda_o \times 6\lambda_o$) at a spatial sampling rate of 1 cm (approximately $\lambda_o/5$). From (29), it can be seen that this spatial sampling rate was slightly higher than the Nyquist sampling rate.

5.3 Overview of the Backscatter Testbed

Simplified block diagrams of the monostatic and bistatic backscatter testbeds are shown in Figure 22. The major components of each testbed were:

- **Microwave Signal Source:** An Agilent E8247C signal generator was used to provide both the unmodulated 5.79 GHz carrier transmitted to the RF tag as well as the local

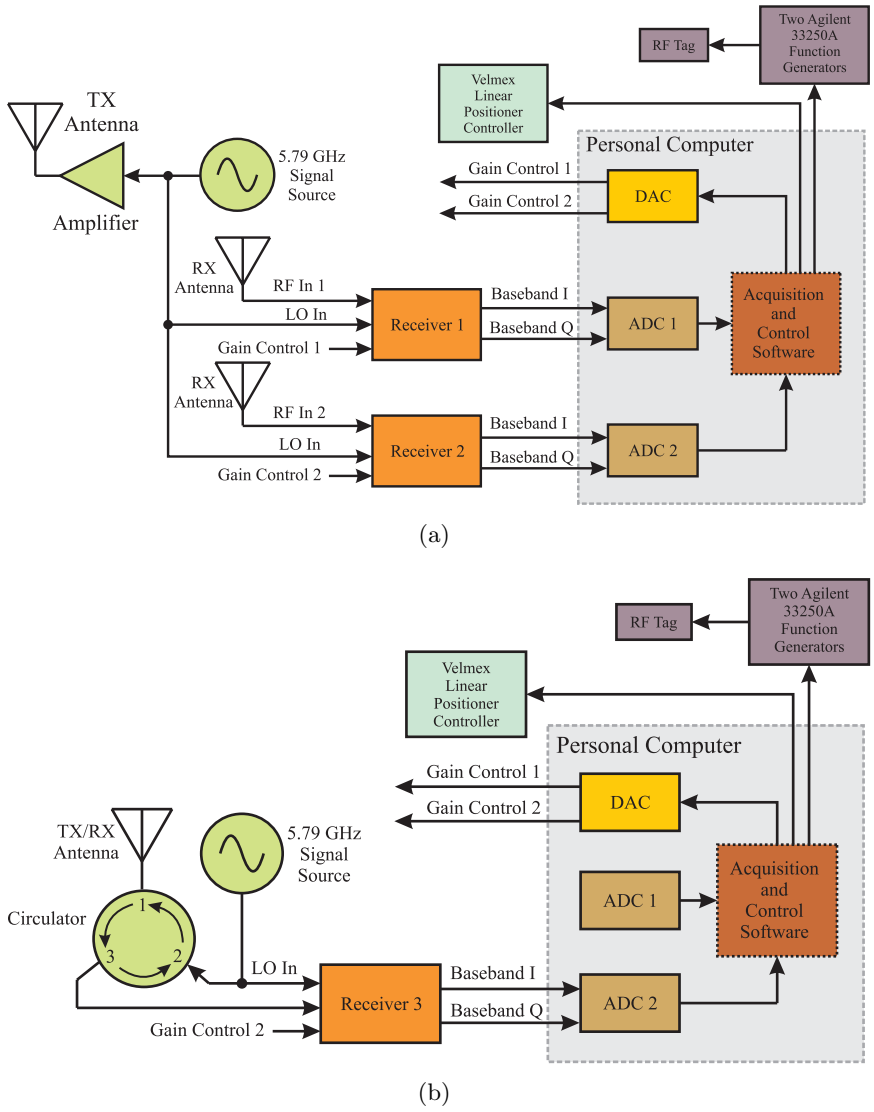

Figure 22: Simplified block diagrams of the (a) bistatic and (b) monostatic backscatter testbeds.

oscillator (LO) source for the direct-conversion receivers. Using a single signal source ensured that the measurements were phase-stable. The digital-to-analog converter (DAC) boards used to sample the receiver outputs and the function generators used to control the RF-tag modulation were locked to the 10 MHz reference signal provided by the Agilent E8247C signal generator.

- **Direct-Conversion Receivers:** Three custom, direct-conversion receivers were designed and prototyped for use in the backscatter testbed. These receivers allowed coherent channel measurements to be taken in the presence of a strong self-interference

signal.

- **RF Tags:** Two custom RF tags were designed and prototyped for this measurement campaign. Their motivation and design are presented in Section 5.3.2.

- **Reader Antennas:** Three 5.79 GHz patch antennas were designed and prototyped for use as the reader transmitter and receiver antennas.

- **Personal Computer:** A personal computer was used to control two ADC boards and one digital-to-analog converter (DAC) board. The ADCs were used to sample the baseband I and Q signals output from the direct-conversion receivers and a DAC was used to control the gain of the receivers. The ADC and DAC boards were controlled using a C++ program. All data processing and linear positioner control were accomplished using functions written in Matlab. Details of the software are provided in Appendix D.

- **Linear Positioner:** A linear positioner was used to move the RF tag through the channel. The screw-drive type positioner was made by Velmex, see Figure 23, and was controlled by a personal computer through a set of Matlab functions.

The direct-conversion receivers, RF tags, and reader antennas were all custom-designed and prototyped for this measurement campaign. The following sections discuss these components in more detail.

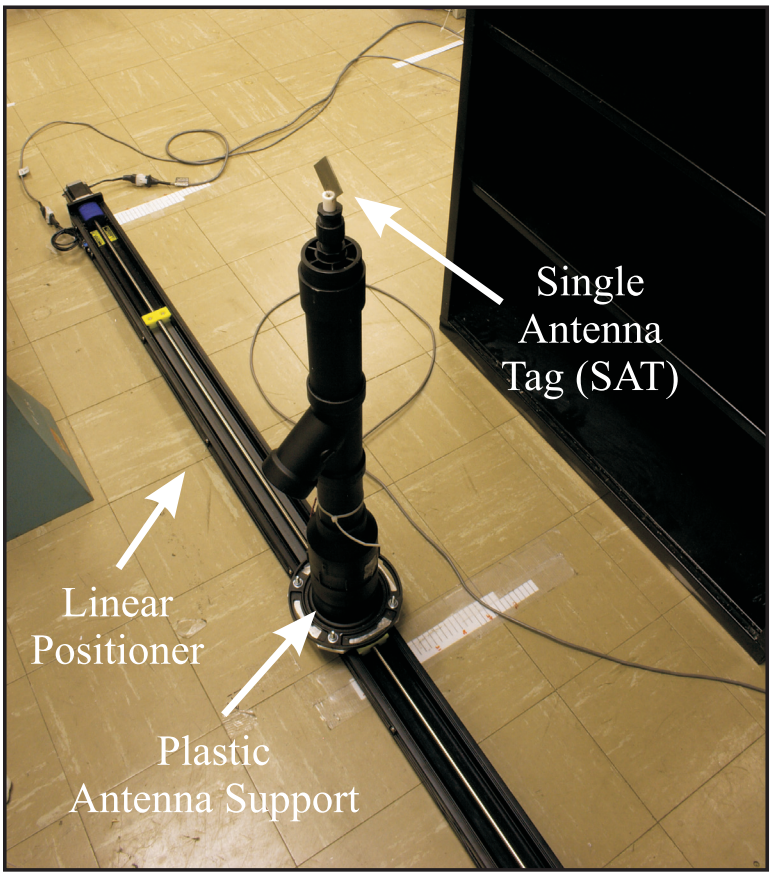

Figure 23: The linear positioner used to move the RF tag through the channel. The positioner is shown with the SAT attached.

5.3.1 Reader Antennas

Linearly-polarized patch antennas, shown in Figure 24, were used at the reader transmitter and receiver. These antennas were designed for 5.79 GHz on an FR4 substrate and each had a broadside gain of approximately 3.8 dBi. The antenna pattern of one of the patch antennas is shown in Figure 25.

5.3.2 RF Tags

Two RF tags were designed and prototyped for this measurement campaign. The first was a single-antenna tag (SAT) and the second a dual-antenna tag (DAT) whose block diagrams are shown in Figure 26.

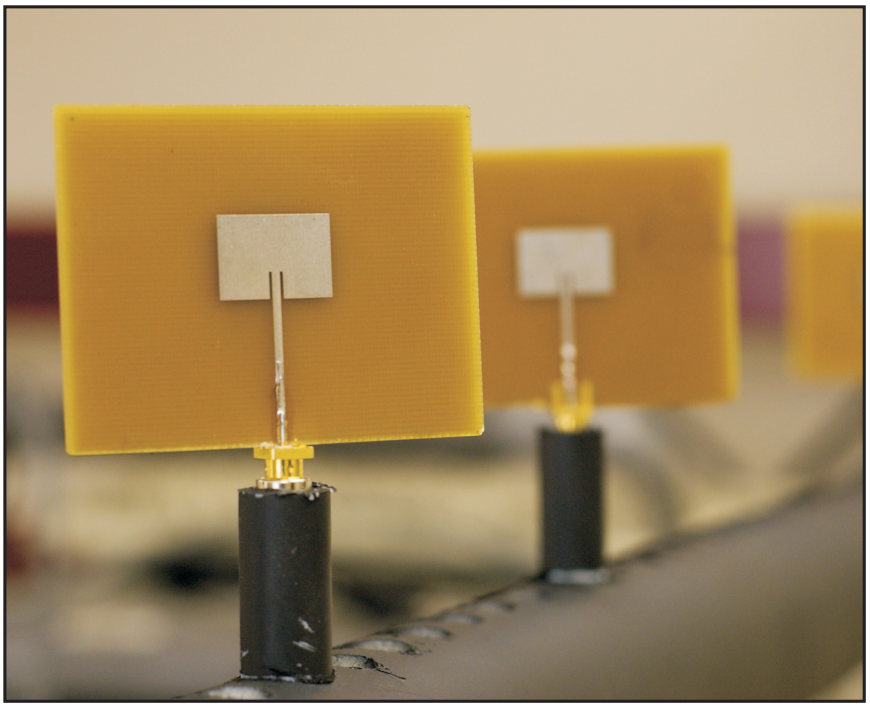

Figure 24: The 5.79 GHz, linearly-polarized patch antennas used at the testbed reader transmitter and receiver.

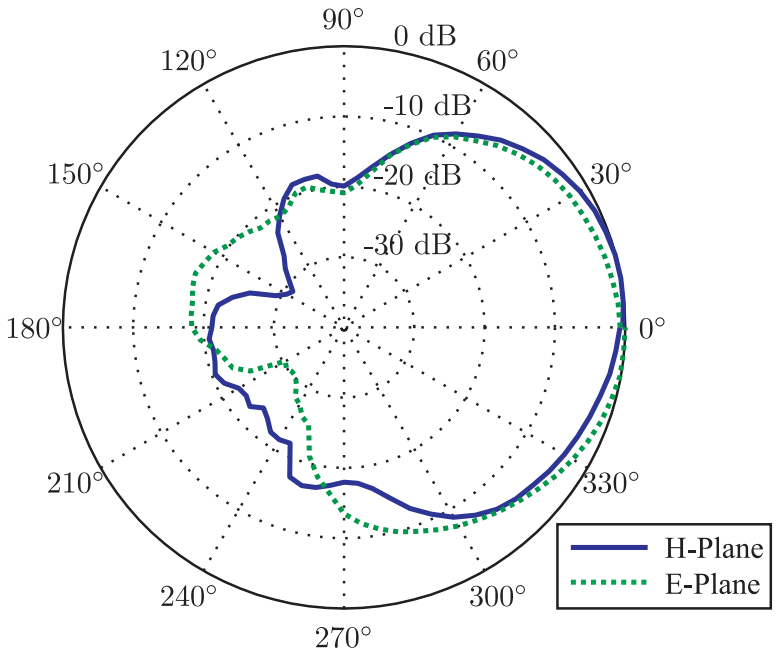

Figure 25: E- and H-plane antenna patterns of one of the reader patch antennas at 5.79 GHz.

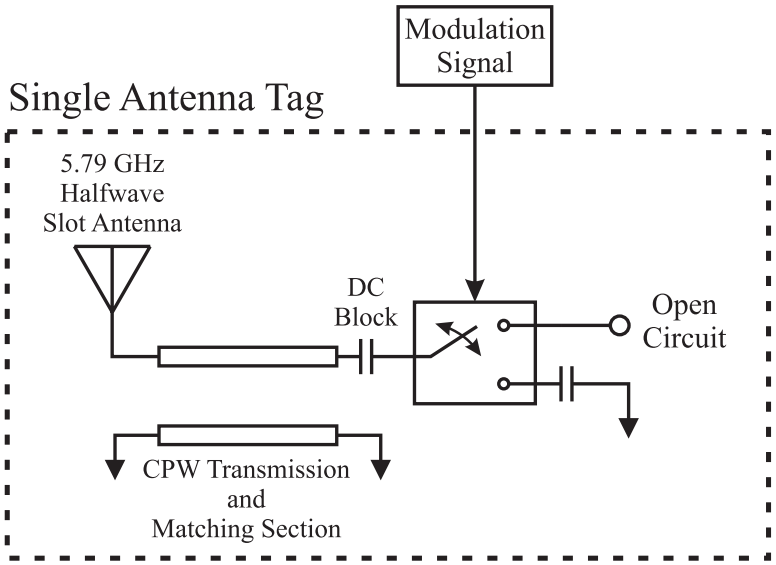

(a)

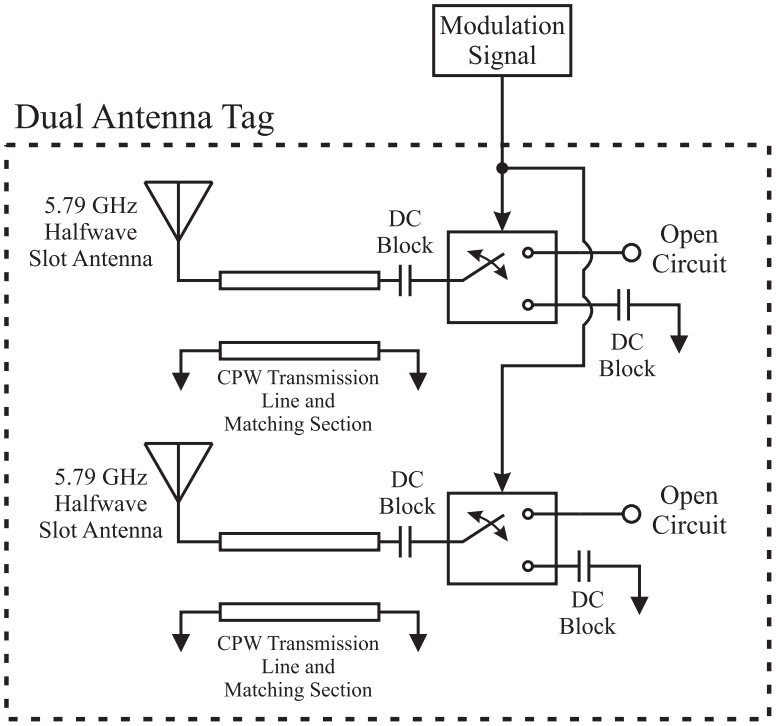

(b)

Figure 26: Block diagrams of the (a) SAT and (b) DAT.

The following factors motivated their design:

- **Equal Comparison:** For a fair comparison of fading with the SAT and DAT, the two RF tags must use the same type of antenna and the antennas of the DAT should be made on the same substrate.

- **Flexibility:** The SAT and DAT designs allow the backscattered signal to be modulated with an arbitrary bit-sequence – i.e., any amplitude shift keying (ASK) waveform. In this realization of the testbed, a differential bit-sequence was output from two Agilent 33250A function generators to control the RF-tag modulation; however, any source of differential binary signals could be used.

- **Decoupling:** Careful design was required to decouple the closely spaced antennas of the DAT. This was accomplished using orthogonal DAT antennas which were each impedance matched to the $50\,\Omega$ switch using Ansoft HFSS, a 3D electromagnetic and microwave software package.

Each tag consists of a 5.79 GHz slot antenna whose load was switched between an open and short circuit by a microwave gallium arsenide (GaAs), pseudomorphic, high electron mobility transistor (PHEMT) switch (M/A-Com MASW-007107 V2). Since it was not necessary to power an RFIC on the SAT or DAT, these extreme load values were chosen to maximize the backscattered power. See Section 2.2.3 for a discussion of RF-tag loads. The slot antenna is connected to the switch through an ungrounded, coplanar-waveguide (CPW) transmission line and matching section. A DC blocking capacitor (Mouser part number 766-C06BL851X5ZNX0T) was used at the switch input port and at the shorted output port per the datasheet recommendations. The switch was toggled using two digital control lines referenced to a third ground line. Photos of the SAT and DAT are provided in Figure 27. The RF-tag board layout was done in Cadence PCB Editor and the Cadence design files and Gerber files are stored on the Propagation Group's SVN server at `https://durgin-srv1.ece.gatech.edu/repos/RFID/trunk/Backscatter Radio/Hardware Design/RF Tag Board/`.

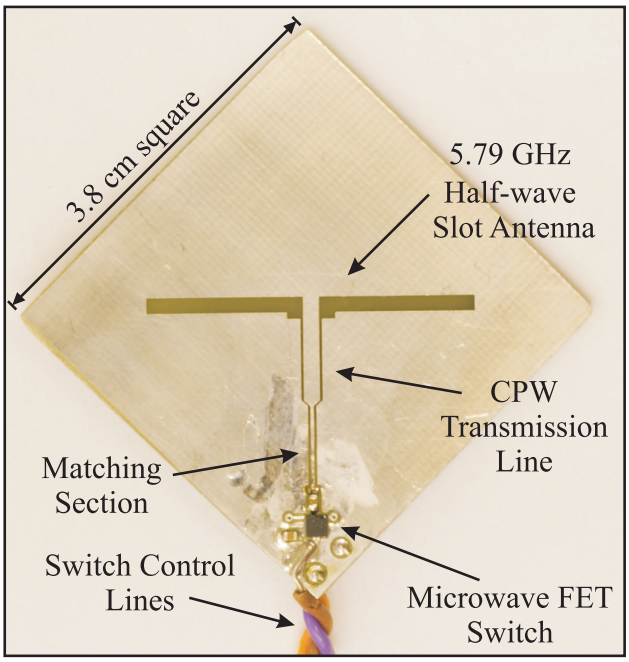

(a)

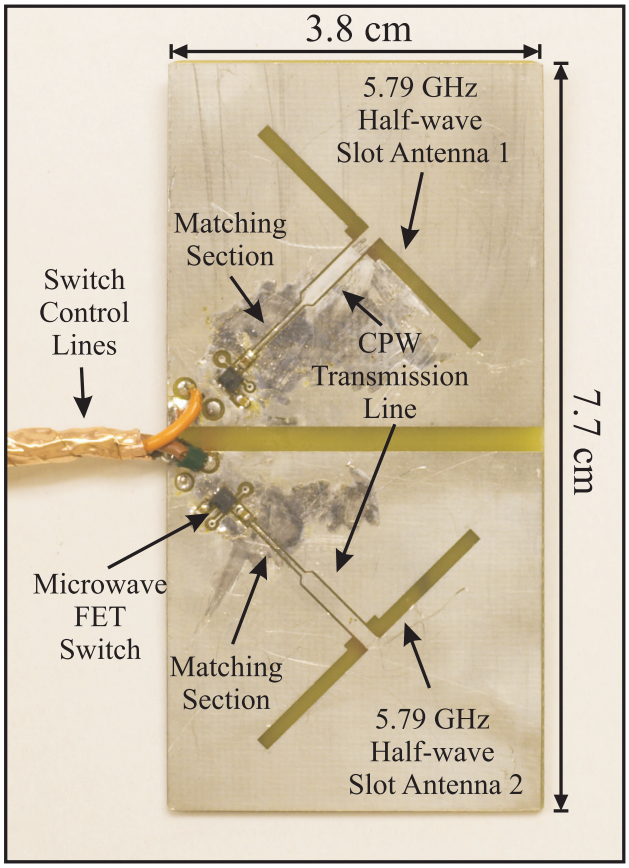

(b)

Figure 27: Photos of the (a) SAT and (b) DAT showing the 5.79 GHz slot antenna, coplanar-waveguide transmission line, matching section, and microwave FET switch.

One potential problem with the SAT and DAT designs was that the control lines from the signal source could act as an antenna and contribute to the modulated-backscatter signal. To measure the contribution from the control lines, the SAT and DAT antenna patterns were measured with and without their antennas shorted, as shown in Figures 28 - 30. When the antennas were shorted with copper tape, the measured pattern was only composed of signals backscattered from the control lines or other unwanted modulation sources. All of the pattern measurements showed that the backscatter modulated by the control lines was much smaller than that from the slot antennas. In general, the un-shorted antenna signal was at least 20 dB greater than that from the control lines and the two only became comparable near the nulls of the un-shorted antenna patterns.

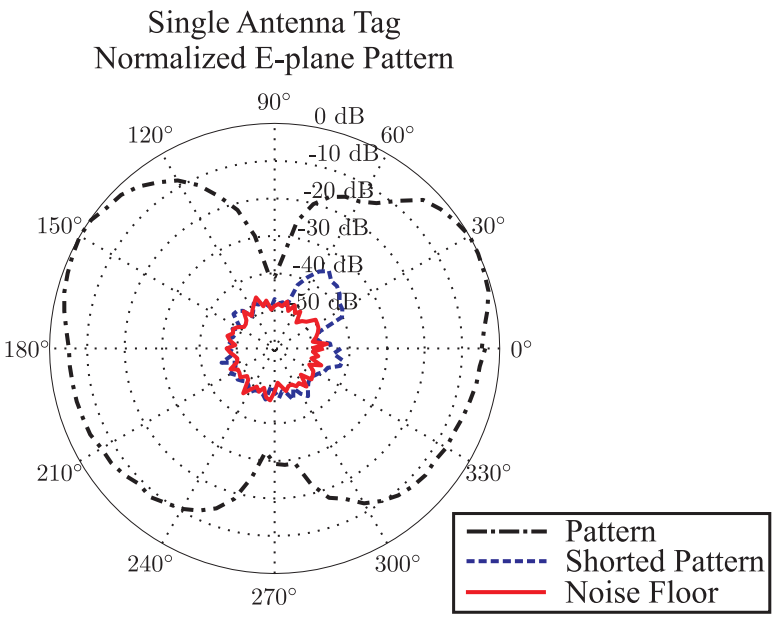

(a)

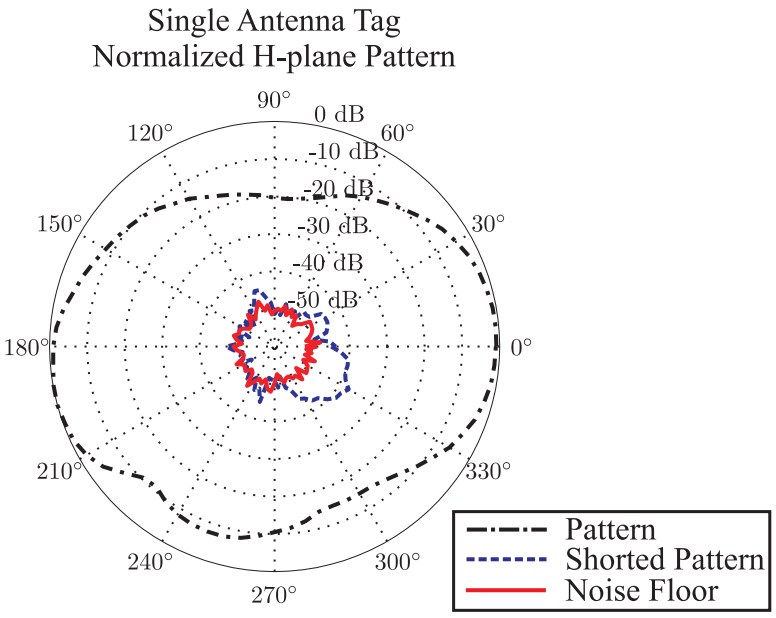

(b)

Figure 28: E- and H-plane patterns of the SAT in both its normal operating mode and with the antenna shorted. The noise floor of the pattern measurement is shown for reference and all of the patterns are normalized to the maximum power received from the three measurements.

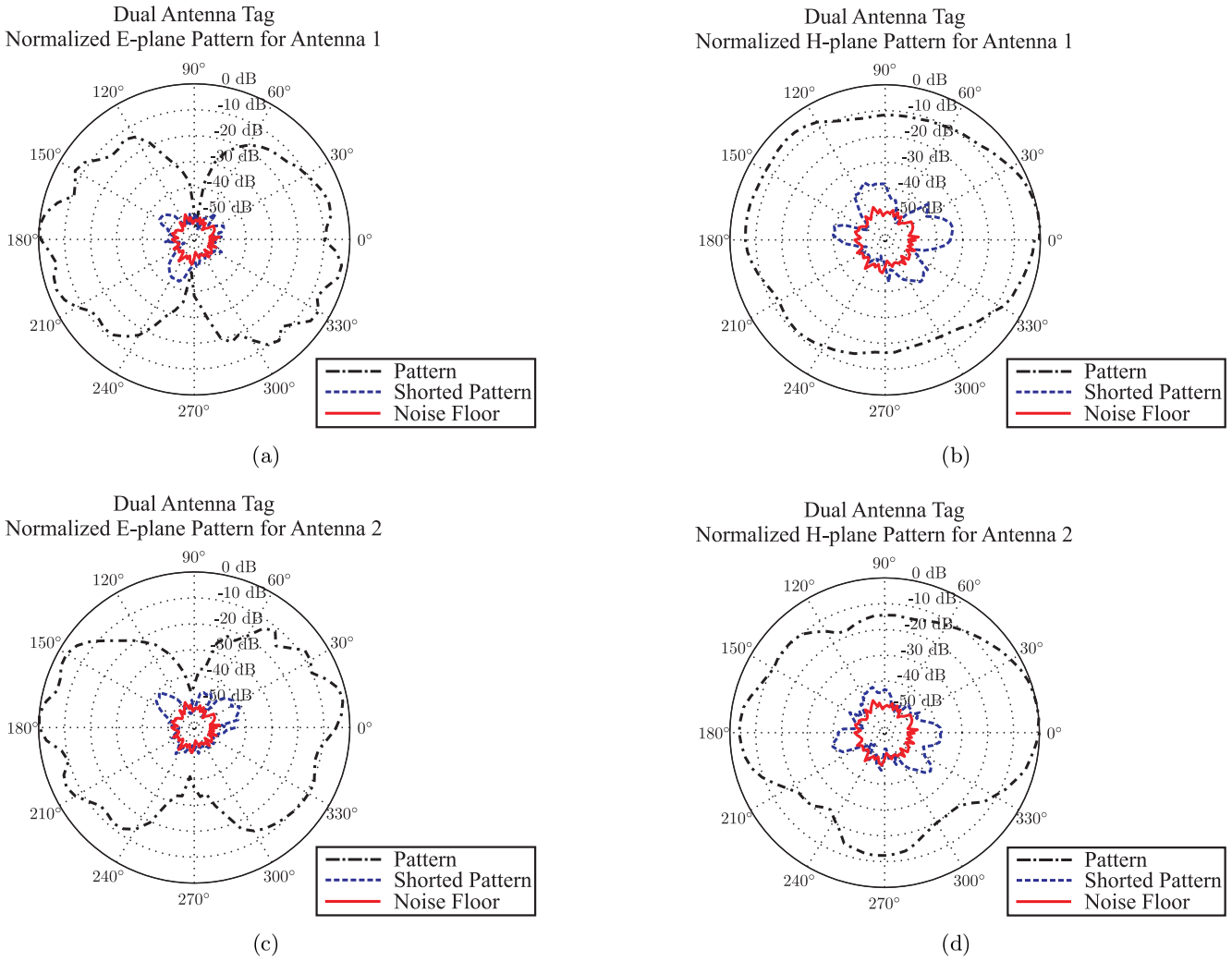

Figure 29: E- and H-plane patterns of DAT antenna 1 and 2 in both its normal operating mode and with each antenna shorted. The noise floor of the pattern measurement is shown for reference and the patterns are normalized to the maximum power received from the three measurements.

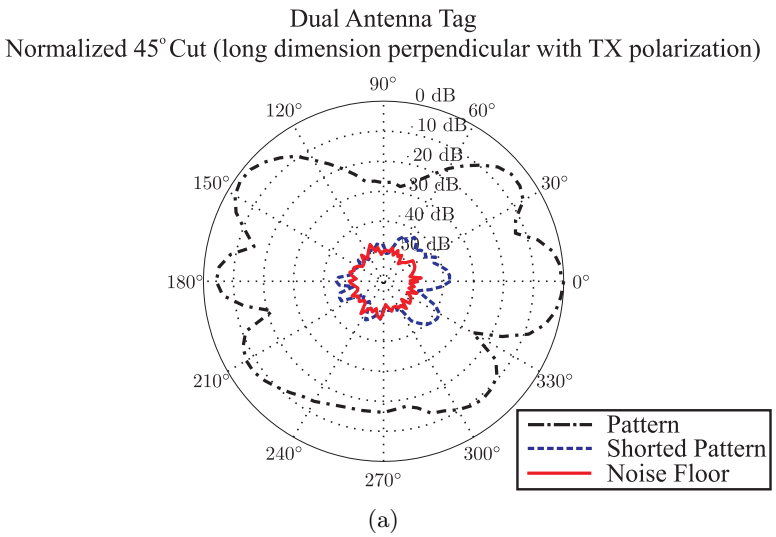

(a)

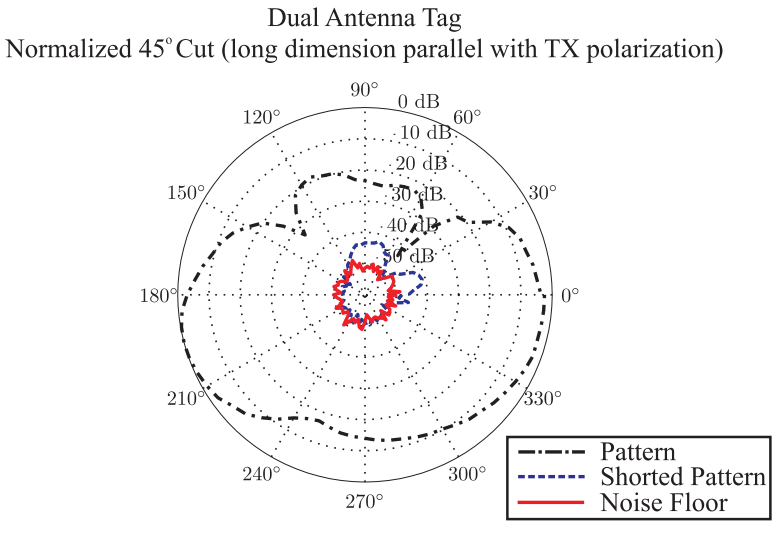

(b)

Figure 30: Antenna patterns of the DAT at an angle of 45° with respect to the polarization of the transmitter antenna. The figures show the pattern measured with the long dimension of the tag (a) perpendicular and (b) parallel to the transmitter polarization. The patterns with the antennas shorted and noise floor of the pattern measurement are shown for reference and the patterns are normalized to the maximum power received from the three measurements.

5.3.3 Direct-Conversion Receiver

A direct-conversion receiver, shown in Figure 31, was designed and prototyped for this measurement campaign. Each receiver was designed to meet the following goals:

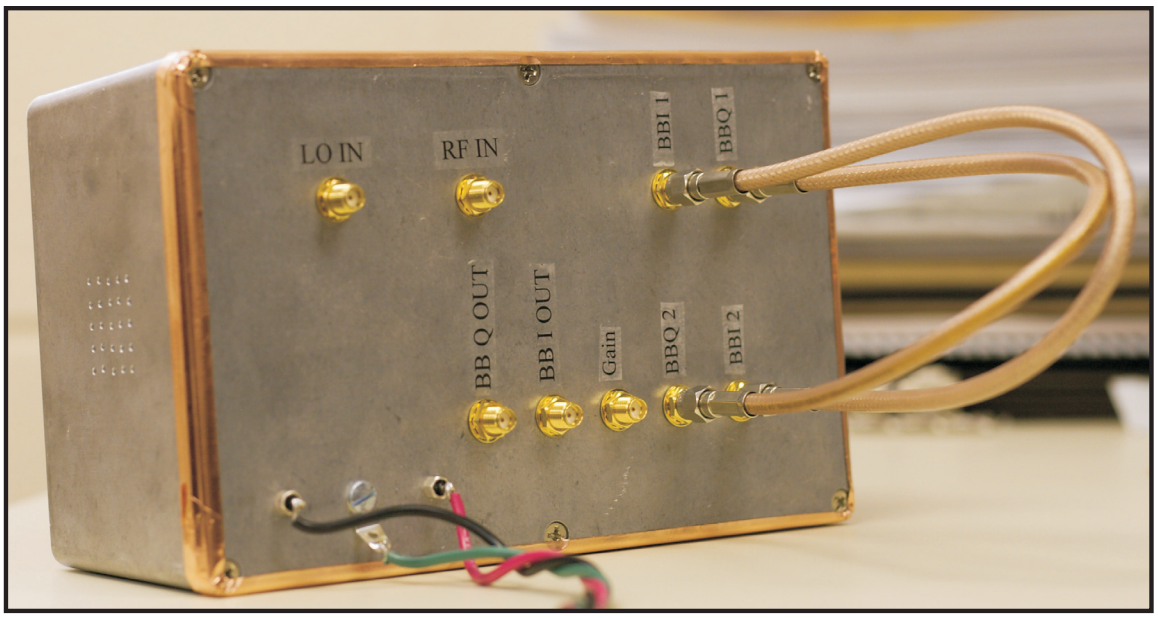

Figure 31: The direct-conversion receiver designed for the backscatter testbed. The receiver consists of two boards – the RF front-end board and the baseband amplification board. The two boards are connected through the external coaxial cables shown above.

Self-interference Mitigation: All backscatter-radio receivers must be able to receive the strong, unmodulated carrier – i.e., *self interference* – transmitted from the reader while still detecting the much weaker modulated backscatter from the RF tag. The custom receivers designed for this testbed blocked the self-interference signal after down-converting it to DC. While other methods for canceling self interference signals exist [69, 70], this method was straightforward to implement and prevented saturation of the baseband amplification board. The sensitivity and dynamic range of the receivers in the testbed are discussed in Section 5.6.

Coherent Reception: Coherent reception was required because it is possible for the envelope of the total received signal – i.e., the unmodulated carrier plus the modulated-backscatter signal – to remain constant as the tag switches between two modulation states.

For example, consider the backscattered signal shown in Figure 6 in Section 2.2.3.1. The backscattered signal received by the reader is proportional to the difference between $\tilde{S}_{\mathrm{A}}$ and $\tilde{S}_{\mathrm{B}}$, described by (14). In a backscatter channel, although the phase ϕ between $\tilde{\Gamma}_{\mathrm{A}}$ and $\tilde{\Gamma}_{\mathrm{B}}$ is fixed, their phase θ relative to $\tilde{C}$ is not. This phase can change with the reader transmitter and RF-tag position as well as with alterations in the RF-tag antenna impedance. Therefore, it is always possible that θ could change such that $\tilde{S}_{\mathrm{A}}$ and $\tilde{S}_{\mathrm{B}}$ have the same magnitude. In such a situation, an envelope receiver – which can only detect the magnitude of the signals – would not detect the difference between the modulation states.

$$\tilde{V}_{\mathrm{data}} = \frac{|\tilde{S}_{\mathrm{A}}| - |\tilde{S}_{\mathrm{B}}|}{2} = 0 \quad \text{since} \quad |\tilde{S}_{\mathrm{A}}| = |\tilde{S}_{\mathrm{B}}| \tag{30}$$

A coherent receiver, however, can differentiate between the two states because it measures both the magnitude and phase of $\tilde{S}_{\mathrm{A}}$ and $\tilde{S}_{\mathrm{B}}$.

It should be noted that backscatter measurements can be accomplished using a vector network analyzer which is available many RF laboratories. Though various methods exist, one way to separate the tag signal from waves scattered off objects in the channel is to make a measurement with no tag present. This background measurement can then be subtracted from measurements with tags present [47]. In this method, the input impedance of the RF-tag RFIC would have to be changed at a rate slower than the analyzer's sweep time so that each tag state can be detected. The direct-conversion receivers designed and prototyped for the backscatter testbed have the advantage that multiple RF tags can be measured simultaneously, they can receive backscatter signals modulated at a high rate, and, though not proven, likely have greater sensitivity in the presence of a self-interference signal.

5.4 Backscatter Testbed Signal Processing

As described in Section 3.1, the general equation that describes the baseband, modulated-backscatter signal received through the $M \times L \times N$ backscatter channel is

$$\tilde{\vec{\mathrm{y}}}(t, \vec{r}) = \frac{1}{2} \int_{-\infty}^{+\infty} \int_{-\infty}^{+\infty} \tilde{\mathbf{H}}^{b}(\tau_b; t, \vec{r}) \tilde{\mathbf{S}}(t - \tau_b) \tilde{\mathbf{H}}^{f}(\tau_f; t - \tau_b, \vec{r}) \tilde{\vec{\mathrm{x}}}(t - \tau_b - \tau_f) d\tau_b d\tau_f + \tilde{\vec{\mathrm{n}}}(t). \tag{31}$$

Several simplifications to (31) are possible for this measurement campaign.

1. **Narrowband Channel:** Since the signaling matrix, $\tilde{\mathbf{S}}(t)$, was chosen to generate a 31-bit m-sequence clocked at a chip-rate f_c of 1 MHz, the resulting passband bandwidth was narrowband at the chosen carrier frequency of 5.79 GHz.

2. **Static Channel:** Small-scale fading measurements are most easily accomplished in a static channel – i.e., a channel in which no scatterers vary as a function of time. To make sure that the channel was approximately static, the following efforts were made: measurement sites were chosen that did not contain moving objects and that were away from hallways with heavy traffic; no persons were allowed in the measurement site or in portions of adjacent rooms that might affect the measurements[1]; and fluorescent lights were were turned off during measurements.

   It may seem odd that the fluorescent lights were powered off, but it was found that their operation raised the noise floor of the testbed by several dB. This is because the plasma in the lights acted as a very good electrical conductor and, hence, a good scatterer. As the alternating current (AC) signal from the florescent ballast turned the lights on and off, the plasma acted as an RF-tag antenna and modulated backscatter. The spectrum of the backscattered noise from the lights resembled phase noise and extended up to 1 MHz away from the carrier frequency. Modulated backscatter from fluorescent lights has also been report by Ibrahim *et al.* at 915 MHz [71].

3. **Narrowband Transmitted Signal:** Since an unmodulated carrier was transmitted from the TX antennas, $\tilde{\vec{x}}(t)$ reduces to a constant $\tilde{\vec{x}}$ in the baseband representation. The transmitted signal can be reduced further to a scalar $\tilde{x}$ since only a single transmitter was used in this implementation of the backscatter testbed.

4. **Identity Signaling Matrix:** Since the same m-sequence was used to modulate the backscattered signal from each RF-tag antenna, the signaling matrix reduces to the identity signaling matrix discussed in Section 3.1.1, which can be written $\tilde{\mathbf{S}}(t) = \tilde{\mathrm{s}}(t)\mathbf{I}_{\mathrm{L}}$ where $\mathbf{I}_{\mathrm{L}}$ is the $L \times L$ identity matrix.

[1]This precaution was followed for the NLOS measurements; however, the LOS were not significantly affected by body movement. Therefore, people were allowed behind the testbed during LOS measurements.

Under these conditions, the baseband signal received at the n^{th} reader-receiver antenna can be written as

$$\tilde{\mathrm{y}}(t,\vec{r}) = \frac{1}{2}\tilde{\vec{\mathrm{h}}}^{b}(\vec{r})\mathbf{I}_{\mathrm{L}}\tilde{\vec{\mathrm{h}}}^{f}(\vec{r})\tilde{\mathrm{s}}(t)\tilde{x} + \tilde{\mathrm{n}}(t). \tag{32}$$

The sampled version of $\tilde{\mathrm{y}}(t,\vec{r})$, which is actually the sum of the I and Q components output from the receiver, is $\tilde{\mathrm{v}}[nT,\vec{r}]$ and can be written

$$\tilde{\mathrm{v}}[nT,\vec{r}] = \tilde{\mathrm{y}}_I[nT,\vec{r}] + j\tilde{\mathrm{y}}_Q[nT,\vec{r}] = \frac{1}{2}\tilde{\vec{h}}^{b}[\vec{r}\,]\mathbf{I}_{\mathrm{L}}\tilde{\vec{h}}^{f}[\vec{r}]\tilde{s}[nT]\tilde{x} + \tilde{\mathrm{n}}[nT], \tag{33}$$

where n denotes the sample number, $T = 1/f_s$, f_s is the sampling frequency, and $\tilde{\mathrm{y}}_I$ and $\tilde{\mathrm{y}}_Q$ are $N \times 1$ in-phase and quadrature signal vectors. Here, parentheses $(\cdot)$ denote continuous time functions and brackets $[\,\cdot\,]$ are used for discrete, or time-sampled, functions. It should be noted that $\tilde{\vec{h}}^{b}[\vec{r}\,]$, $\mathbf{I}_{\mathrm{L}}$, and $\tilde{\vec{h}}^{f}[\vec{r}]$ are non-scalar because L RF-tag antennas were used in the channel. Therefore, $\tilde{\mathrm{v}}[nT,\vec{r}]$ is the signal received at the n^{th} time sample.

Forty periods of the m-sequence were recorded at a rate of $f_s = 20$ MHz at each RF-tag position and filtered using a fast fourier transform. Recall that the spectrum of an m-sequence is composed of discrete frequencies spaced every f_c/L that have a sinc envelope [72]. The majority of the signal power is contained in the main lobe of the spectrum which is bounded by nulls at $\pm f_c$. Filtering was accomplished by transforming the sampled signal to the frequency domain; removing all but the frequency components of the sinc's main lobe, shown in Figure 32; and then transforming the filtered signal back to the time domain, $\tilde{\mathrm{z}}\,[nT,\vec{r}]$.

$$\tilde{\mathrm{z}}\,[nT,\vec{r}] = \tilde{h}_{\mathrm{filter}}[nT] \otimes \tilde{\mathrm{v}}[nT,\vec{r}] = \frac{1}{2}\tilde{\vec{h}}^{b}[\vec{r}\,]\mathbf{I}_{\mathrm{L}}\tilde{\vec{h}}^{f}[\vec{r}]\tilde{s}[nT]\tilde{x} + \tilde{\mathrm{n}}[nT] \tag{34}$$

where $\tilde{h}_{\mathrm{filter}}[nT]$ is the impulse response of the digital filter and $\otimes$ denotes the convolution. In (34), the same notation is used to express the filtered and unfiltered sampled signals, $\frac{1}{2}\tilde{\vec{h}}^{b}[\vec{r}\,]\mathbf{I}_{\mathrm{L}}\tilde{\vec{h}}^{f}[\vec{r}]\tilde{s}[nT]\tilde{x} + \tilde{\mathrm{n}}[nT]$, for simplicity. The filtered time domain signal $\tilde{\mathrm{z}}\,[nT,\vec{r}]$ was then correlated with a filtered copy of the ideal m-sequence, $\tilde{M}[nT] = \tilde{h}_{\mathrm{filter}}[nT] \otimes \tilde{s}[nT]$. The correlation between $\tilde{\mathrm{z}}\,[nT,\vec{r}]$ and $\tilde{M}[nT]$ can be written as,

$$\mathcal{R}_{\tilde{M},\tilde{z}}[\delta] = \sum_{n=0}^{N-\delta-1} \tilde{M}[nT+\delta]\,\tilde{\mathrm{z}}^{\,*}\,[\delta,\vec{r}]. \tag{35}$$

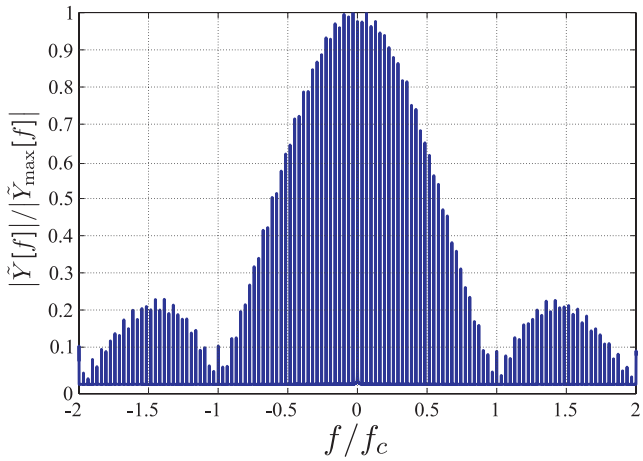

(a)

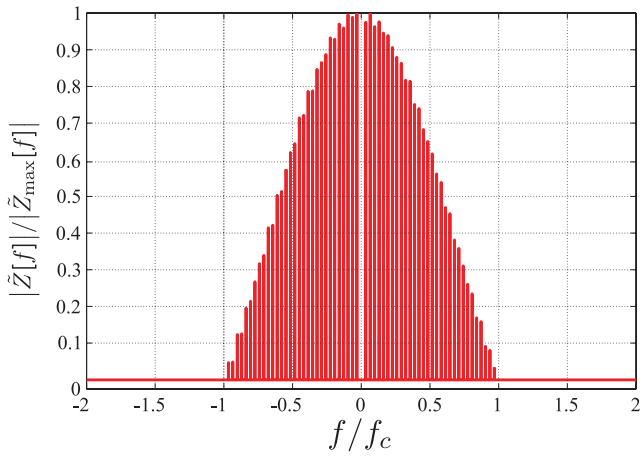

(b)

Figure 32: The (a) unfiltered spectrum of the m-sequence backscattered from an RF tag at a chip rate of 1 MHz. Note, full spectrum is not shown. After filtering, shown in (b), only the main lobe of the m-sequence spectrum remains. In this figure, the spectra's amplitudes are normalized by their maximum values.

where $\mathcal{R}_{X,Y}[\delta]$ is the correlation between $X[nT]$ and $Y[nT]$ with a time delay of δ. $X[nT]$ and $Y[nT]$ are vectors of time samples with length N and $(\cdot)^*$ denotes the complex conjugate. Substituting (34) into (35) gives

$$\mathcal{R}_{\tilde{M},\tilde{z}}[\delta] = \frac{1}{2}\tilde{\vec{h}}^b[\vec{r}]\mathbf{I}_{\mathrm{L}}\tilde{\vec{h}}^f[\vec{r}]\mathcal{R}_{\tilde{M},\tilde{s}}[\delta]\tilde{x} + \mathcal{R}_{\tilde{M},\tilde{n}}[\delta]. \tag{36}$$

where $\mathcal{R}_{\tilde{M},\tilde{s}}[\delta]$ is the correlation between measured and the filtered, ideal m-sequences and $\mathcal{R}_{\tilde{M},\tilde{n}}[\delta]$ is the correlation between the received noise and the filtered, ideal m-sequence. The result is a series of peaks that occur when the filtered, measured m-sequence and the filtered, ideal m-sequence completely overlap, shown in Figure 33. The final output $\tilde{\mathrm{w}}[nT, \vec{r}]$

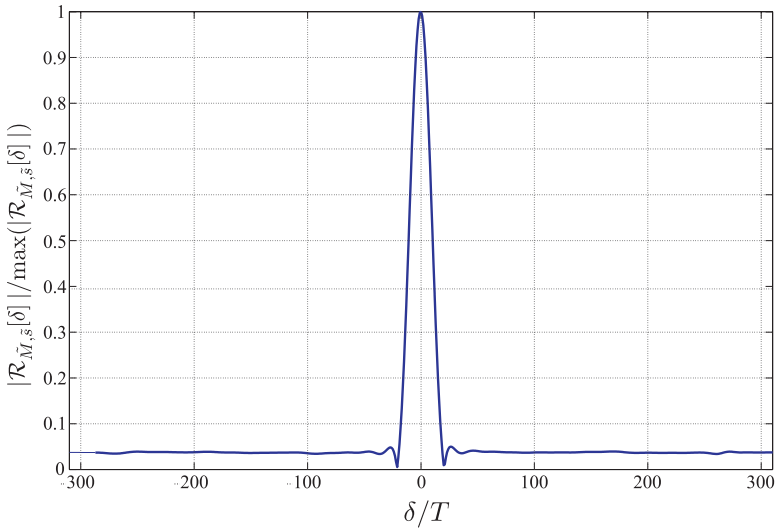

Figure 33: The peak of the correlation $\mathcal{R}_{\tilde{M},\tilde{s}}[\delta]$ of the filtered ideal and measured m-sequences normalized to its maximum value. The peak of the correlation occurs when the measured and ideal m-sequences are aligned.

is found by finding the maximum value of $\mathcal{R}_{\tilde{M},\tilde{z}}[\delta]$ and normalizing it by the maximum value of the autocorrelation of the filtered, ideal m-sequence:

$$\tilde{\mathrm{w}}[\vec{r}] = \frac{\max\{\mathcal{R}_{\tilde{M},\tilde{z}}[\delta]\}}{\max\{\mathcal{R}_{\tilde{M},\tilde{M}}[\delta]\}} = \frac{1}{2}\Big[\tilde{\vec{h}}^{b}[\vec{r}]\mathbf{I}_{\mathrm{L}}\tilde{\vec{h}}^{f}[\vec{r}]\tilde{x}\Big]^{*} + \tilde{\mathrm{n}}^{*}_{\mathrm{spread}}[\vec{r}] \tag{37}$$

where $\tilde{\mathrm{n}}^{*}_{\mathrm{spread}}[\vec{r}]$ is the complex conjugate of the noise that has been spread by correlation with $\tilde{M}$. The final channel coefficients $\tilde{\vec{h}}_{\mathrm{norm}}[\vec{r}]$ relative to the calibration measurements (see Section 5.5), are found from the complex conjugate of the correlated received signal $\tilde{\mathrm{w}}[\vec{r}]$ divided by the complex conjugate of the correlated calibration measurement $\tilde{\mathrm{w}}_{\mathrm{cal}}[\vec{r}]$,

$$\tilde{h}_{\mathrm{norm}}[\vec{r}] = \frac{\tilde{\mathrm{w}}^{*}[\vec{r}]}{\tilde{\mathrm{w}}^{*}_{\mathrm{cal}}[\vec{r}]} = \frac{\frac{1}{2}\tilde{\vec{h}}^{b}[\vec{r}]\mathbf{I}_{\mathrm{L}}\tilde{\vec{h}}^{f}[\vec{r}]\tilde{x} + \tilde{\mathrm{n}}_{\mathrm{spread}}}{\frac{1}{2}\tilde{\vec{h}}^{b}_{\mathrm{cal}}[\vec{r}]\mathbf{I}_{\mathrm{L}}\tilde{\vec{h}}^{f}_{\mathrm{cal}}[\vec{r}]\tilde{x}} = \tilde{\vec{h}}^{b}_{\mathrm{norm}}[\vec{r}]\mathbf{I}_{\mathrm{L}}\tilde{\vec{h}}^{f}_{\mathrm{norm}}[\vec{r}] + \tilde{\mathrm{n}} \tag{38}$$

where $\tilde{\vec{h}}^{b}_{\mathrm{norm}}[\vec{r}]$ and $\tilde{\vec{h}}^{f}_{\mathrm{norm}}[\vec{r}]$ are the forward and backscatter-link coefficients relative to the calibration measurement, $\tilde{\mathrm{n}}$ is a normalized spread noise term, and $(\cdot)^{*}$ is the complex conjugate. The calibration measurement $\tilde{\mathrm{w}}_{\mathrm{cal}}[\vec{r}]$ was processed in the exact same manner as $\tilde{\mathrm{w}}[\vec{r}]$. If the noise component in $\tilde{\vec{\mathrm{w}}}_{\mathrm{cal}}[\vec{r}]^{*}$ is negligible, the channel envelope α is found by taking the absolute value of $\tilde{h}_{\mathrm{norm}}[\vec{r}]$

$$\alpha = |\tilde{h}_{\mathrm{norm}}[\vec{r}]| \tag{39}$$

5.5 Testbed Calibration

In any high-frequency channel measurement, careful calibration of the system is important. In conventional transmitter-to-receiver systems, back-to-back calibration techniques are often used in which the transmitter is directly connected to the receiver (with any necessary attenuation). In a backscatter system, however, such a calibration is often not practical since the signal to be received must be scattered rather than transmitted. Therefore, for this measurement campaign, a free-space calibration was used. The SAT or DAT under test was placed 40.5 cm from the reader antennas and the signal received from the RF tag was recorded. The calibration measurements were conducted indoors, the polarizations were matched, and the tags were close enough to the reader antennas so that multipath signals were not significant. A diagram of the calibration setup for the monostatic and bistatic testbed is shown in Figure 34 and a photo of the SAT bistatic calibration is given in Figure 35. All of the measurement values reported in Chapter 6 are normalized by the complex calibration values, as described in Section 5.4.

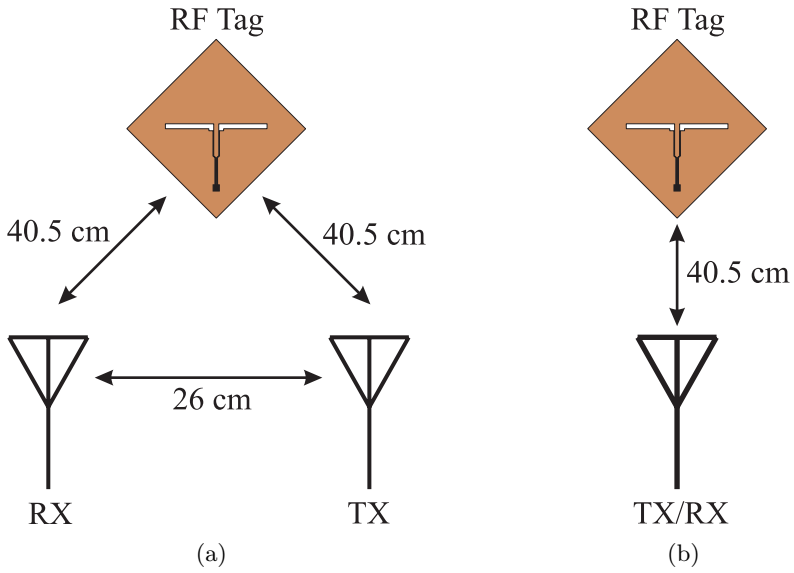

Figure 34: The calibration setup for the (a) bistatic and (b) monostatic measurements.

5.6 Testbed Sensitivity and Measurement Noise

In these measurements, it was important to ensure that noise did not significantly affect the measured signal, particularly for the small signals measured in a deep fade. If the measured

Figure 35: The SAT calibration measurement. The testbed transmitter and receiver antennas are spaced 26 cm apart and the SAT is positioned with a string 40.5 cm from both the transmitter and receiver antennas.

signal was dominated by noise, which is assumed to be a Gaussian random process, then the envelope distribution of the measured signal would appear to be Rayleigh. Such a distribution would be hard to distinguish from from the expected product-Rayleigh distribution for small envelope values. Therefore, the measured data was compared to the linear-scale mean of the noise power. Noise power measurements were made by sampling the received signal with no RF-tag modulation. If the measured data was less than 20 dB above the linear-scale mean noise power, it was not included in the calculated distribution estimate. If the measured envelope is written as $\alpha_{\text{meas}} = \alpha_{\text{true}} \pm \alpha_{\text{noise}}$, then the percent error caused by noise can be defined as

$$\begin{aligned} \text{Percent Error} &= 100 \times \frac{\alpha_{\text{meas}} - \alpha_{\text{true}}}{\alpha_{\text{true}}} \\ &= \pm 100 \times \frac{\alpha_{\text{noise}}}{\alpha_{\text{true}}} \\ &= \pm 100 \times 10^{(P_{\text{noise dBm}} - P_{\text{true dBm}})/20}. \end{aligned} \tag{40}$$

In (40), it is assumed that $P_{\text{true}} \geq P_{\text{noise}}$. A 20 dB difference between the noise power and the true signal power results in $\pm 10\%$ envelope error. Time averaging was used to lower the noise floor of the testbed and, hence, increase its sensitivity. A maximum of thirty-two

time averages were used resulting in a minimum noise floor, calculated from the linearly-averaged noise output of the two receivers, of -142 dBm. Since the maximum input power of the bistatic receivers is -12 dBm, the useful dynamic range of the testbed is 110 dB. The measured noise floor for the monostatic testbed was -142 dBm (with 32 time averages) and, since its maximum input power was -5 dBm, had a dynamic range of 117 dB. Though its dynamic range was larger, the monostatic testbed was not as sensitive as the bistatic testbed. This was because the transmit power had to be reduced to prevent power reflected from the transmitter/receiver antenna from driving the receiver into its nonlinear region.

CHAPTER VI

MEASUREMENT RESULTS

Chapter Overview: This chapter provides the following:

- Received power and phase plots of the backscattered signal measured at the reader as a function of RF-tag position.
- Measured estimates of the channel fading CDF demonstrating link correlation effects and pinhole diversity gains.
- Measured fade margins for NLOS and LOS backscatter channels.
- Measured diversity gains using maximal ratio combining at the reader receiver.

Fading measurements of the 5.79 GHz ($\lambda_o = 5.2$ cm), dyadic backscatter channel were taken under both NLOS and LOS conditions using the following testbed configurations: the monostatic reader with the SAT, the monostatic reader with the DAT, the bistatic reader with the SAT, and the bistatic reader with the DAT. The NLOS and LOS measurements are presented in two sections. In each section, estimates of the envelope CDFs – tabulated from the measured channel samples – are compared with the envelope CDFs derived in Chapter 3 and used to investigate link correlation effects (for the LOS measurements only), to see pinhole diversity gains, and to calculate link budget fade margins. The chapter concludes with a discussion of the conventional diversity gains that can be realized using MRC in the backscatter testbed.

6.1 Fading in the NLOS Backscatter Channel

NLOS measurements were made in room E558 of the Van Leer Building on the Georgia Institute of Technology main campus. These measurements were "through-wall" – i.e., the backscatter testbed reader was located in room 560, and the RF tag was located in room 558, as shown in Figure 36. The LOS was blocked by both the sheet-rock wall and a large,

metallic sheet (actually, the metallic stripline cavity shown in Figure 37) which was added for the purpose of creating a rich scattering environment. Such an environment was created at the RF tag by waves diffracting around the metallic sheet as well as those reflected off the many nearby scatterers. These scatterers included wooden workbenches, a drill press, metal book shelves, many miscellaneous objects on the floor and book shelves, and the floor (the RF tag and reader antennas were 86 cm above the floor). Additional multipath occurred at the reader because of a nearby desk. Details of the measurement procedure can be found in Chapter 5.

In this setup, only bistatic measurements were made because the sensitivity of the monostatic setup was not adequate for accurate measurements. A discussion of receiver sensitivity and noise can be found in Section 5.6.

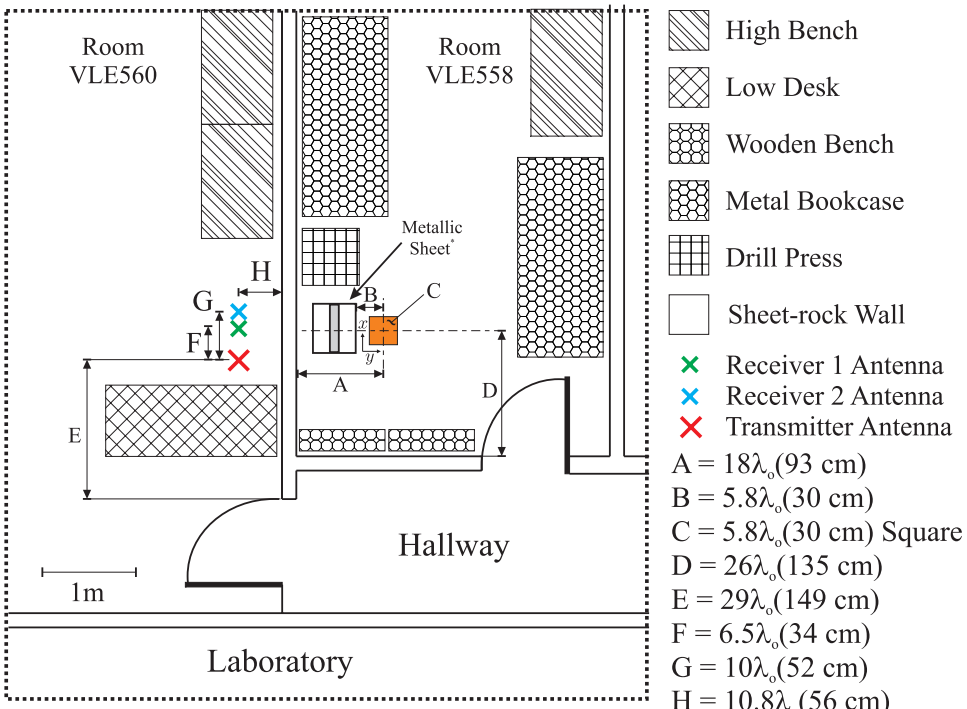

*Note: The base of the metallic sheet (actually a stripline cavity) is 53cm x 46cm. The actual metallic stripline (shown in gray) is 51cm x 10cm x 161cm.

Figure 36: The bistatic measurement setup between rooms E560 and E558 of the Van Leer Building on the Georgia Institute of Technology main campus. Coherent channel samples were taken at 5.79 GHz as the RF tag was moved uniformly across a 30 cm × 30 cm (approximately $6\lambda_o \times 6\lambda_o$) square in 1 cm (approximately $\lambda_o/5$) increments. In this figure, the area over which the tag was moved is denoted by the orange square and the RF tags and reader antennas were approximately 86 cm above the floor.

Figure 37: The metallic stripline cavity used as a metallic sheet to block the LOS for the NLOS measurements between rooms E560 and E558 of the Van Leer Building.

6.1.1 NLOS Spatial-Fading Plots

Before delving into the NLOS envelope distributions, it is useful to examine the channel samples plotted as a function of RF-tag position. Figure 38 and Figure 39 show the measured channel power in dB and phase in degrees of each RF-tag measurement position for the SAT and DAT, respectively. In both cases, two separate receiver antennas, separated by $3.5\lambda_o$, were used to collect data. The power is normalized to the maximum power recorded in each measurement area so that the magnitude of the fades can be easily seen. Each measurement set in Figure 38 and Figure 39 is plotted on the same scale and is oriented to match the measurement diagram provided in each figure.

Both the SAT and DAT plots show deep, rapid fades of up to 40 dB. Furthermore, the measured phase plots show no defined phase fronts; instead, the phase appears jumbled indicating the lack of a dominate specular wave.

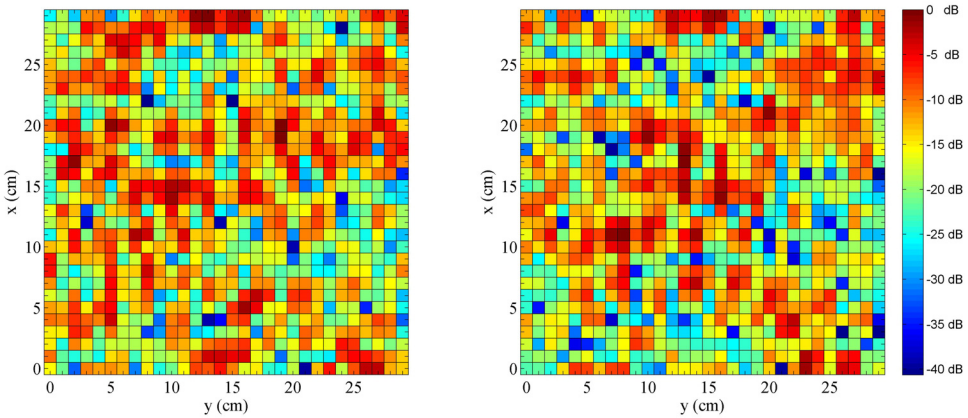

(a) Normalized channel power (in dB) received at RX 1 (left) and RX 2 (right).

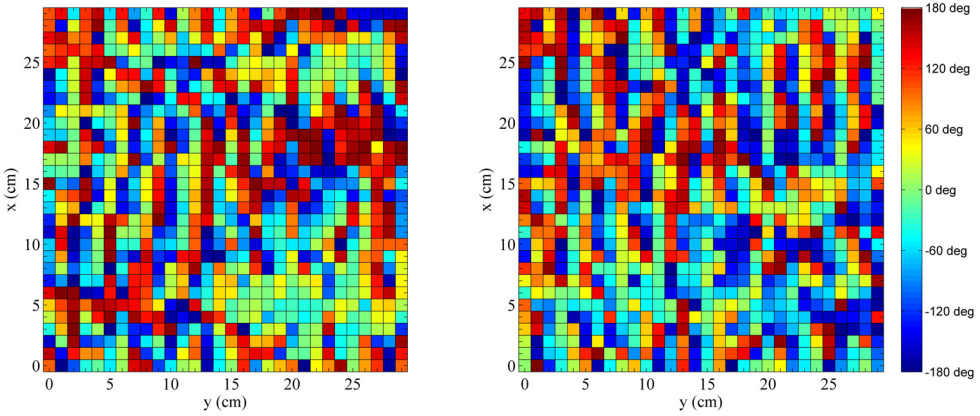

(b) The phase of the signal received (in degrees) at RX 1 (left) and RX 2 (right).

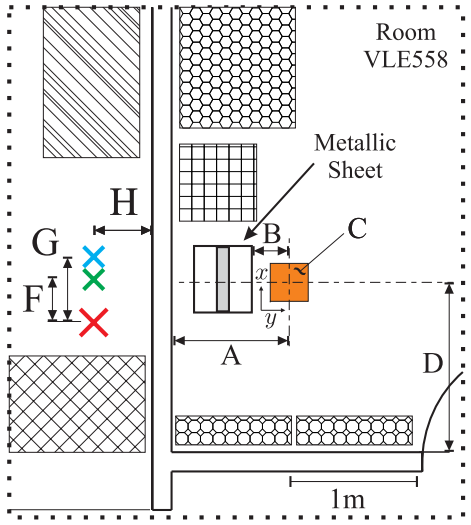

(c) The NLOS measurement diagram. The measured area is denoted by the orange square.

Figure 38: The (a) SAT measured power (in dB) relative to the maximum and (b) measured phase (in degrees) at each measurement position in the NLOS channel. The orientation of the measurements is shown in (c) and a full diagram of the measurement area is given in Figure 36. The coloring of each square represents the measured value of the channel power or phase at that particular RF-tag position.

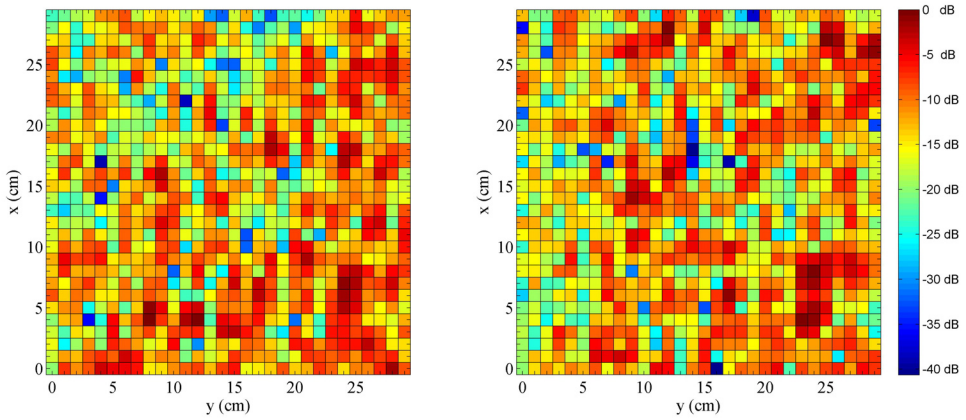

(a) Normalized channel power (in dB) received at RX 1 (left) and RX 2 (right).

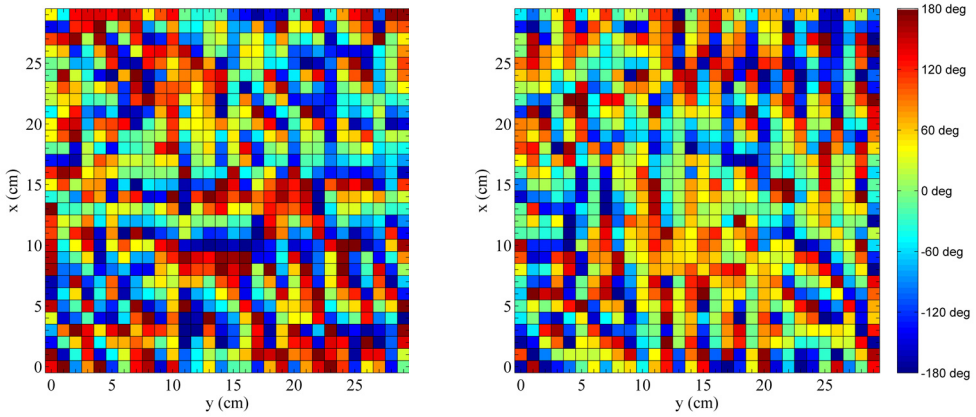

(b) The phase of the signal received (in degrees) at RX 1 (left) and RX 2 (right).

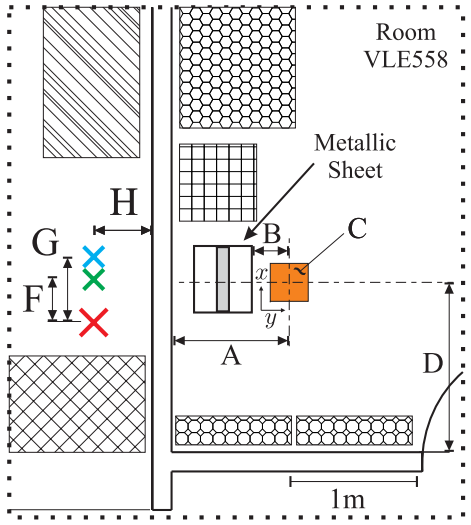

(c) The NLOS measurement diagram. The measured area is denoted by the orange square.

Figure 39: The (a) DAT measured power (in dB) relative to the maximum and (b) measured phase (in degrees) at each measurement position in the NLOS channel. The orientation of the measurements is shown in (c) and a full diagram of the measurement area is given in Figure 36. The coloring of each square represents the measured value of the channel power or phase at that particular RF-tag position.

As mentioned in Section 5.6, measurements that were within 20 dB of the measured noise floor were removed from all distribution calculations. For the NLOS SAT channel, shown in Figure 38, measurements at the following (X,Y) RF-tag positions were removed from the signal received at RX 1: (22,8), (22,15), (28,24). At RX 2, the following measurements were removed: (3,26), (3,29). For the NLOS DAT channel, shown in Figure 39, measurements at the following (X,Y) RF-tag positions were removed from the signal received at RX 2: (18,14). In Figures 38 - 39, the removed power and phase data points are assigned to -40 dB and -180 degrees, respectively.

6.1.2 Measured Estimates of the NLOS Backscatter-Channel CDF

Measured estimates of the NLOS envelope distributions for the SAT and DAT are shown in Figures 40 - 41 along with the corresponding analytic distributions of the Rayleigh-fading backscatter channel given by (26a) in Section 3.2. Visual inspection reveals that the measured estimates of the NLOS CDFs match those given by (26a) very well.

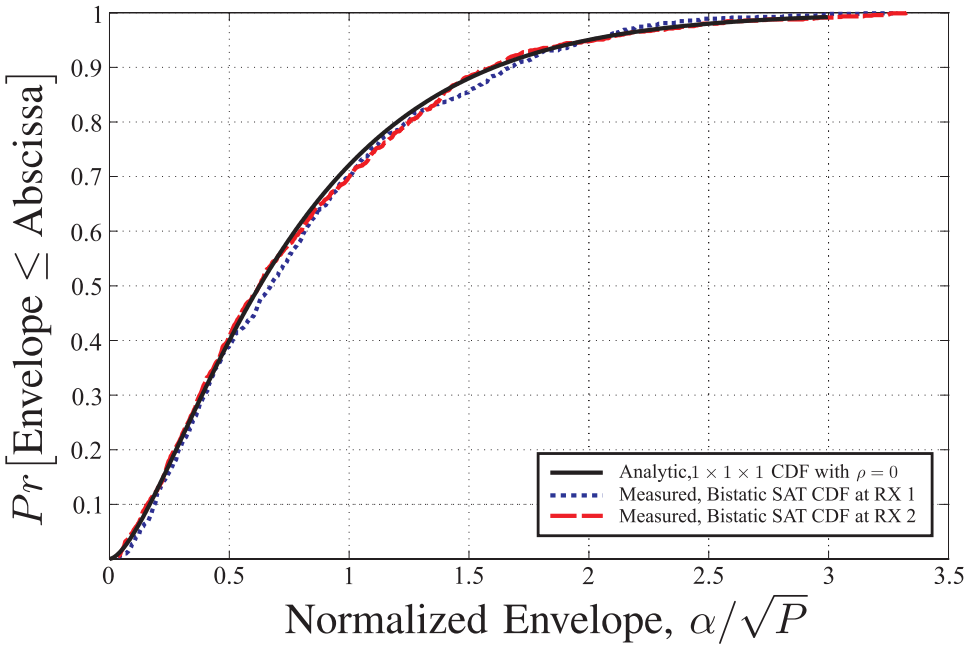

Figure 40: Measured estimates of the bistatic SAT CDF in the NLOS fading channel and the CDF of the derived, analytical, $1 \times 1 \times 1$ distribution; the measured CDF estimates at RX 1 and RX 2 are shown. The curves are plotted on axes normalized by the root of the power of each distribution $\sqrt{P}$ for unbiased comparisons.

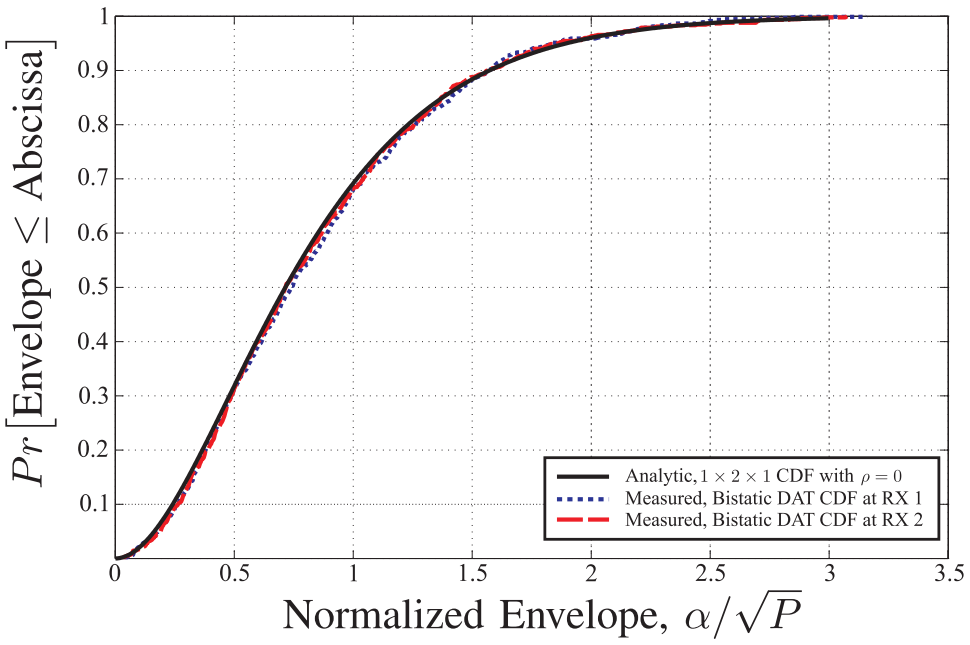

Figure 41: Measured estimates of the bistatic DAT CDF in the NLOS fading channel along with the CDF of the derived, analytical, $1 \times 2 \times 1$ distribution; the measured CDF estimates at RX 1 and RX 2 are shown. The curves are plotted on axes normalized by the root of the power of each distribution $\sqrt{P}$ for unbiased comparisons.

This observation was confirmed using two error measurements [21]. The first error measurement is the linear mean-square-error (MSE), simply calculated as the average squared difference between the estimated (i.e., the measured) and derived CDFs. The second is the logarithmic MSE, defined as

$$\text{Log MSE} = \frac{1}{N}\sum_{i}^{N}\Big[10\log_{10}[F_m(\alpha_i/\sqrt{P})] - 10\log_{10}[F(\alpha_i/\sqrt{P})]\Big]^2, \tag{41}$$

where $F_m(\cdot)$ is the measured estimate of the CDF, $F(\cdot)$ is the CDF of the derived, analytic distribution, and $\alpha_i/\sqrt{P}$ is the i^{th} envelope measurement normalized by the power of the distribution P. The logarithmic MSE is useful because it emphasizes the difference between the estimated and analytic CDFs for small envelope values – the region of most concern for backscatter-radio designers. The minimum mean square errors (MMSE) are presented in Table 9 and the measured estimates of the SAT CDF and the DAT CDF are compared to the CDFs derived from Equation (26a) and (27a) for the $1 \times 1 \times 1$, $1 \times 2 \times 1$, $1 \times 3 \times 1$, and $1 \times 4 \times 1$ channels (8 analytic CDFs in all). For the SAT measurements at RX 1 and RX 2, the analytic, $1 \times 1 \times 1$ CDF, calculated from (26a), minimizes the mean-square error. For

the DAT measurements, the analytic, $1 \times 2 \times 1$ CDF with $\rho_e = 0$ does the same, except that the linear MMSE indicates the best match at RX 1 is the $1 \times 3 \times 1$ CDF. In this case, however, since the CDFs for $1 \times L \times 1$ channels become very similar for large envelopes, the logarithmic MMSE is a more meaningful comparison.

Table 9: Best-fit results for the measured estimates of the bistatic SAT CDF and the bistatic DAT CDF compared to the derived, $1 \times 1 \times 1$, $1 \times 2 \times 1$, $1 \times 3 \times 1$, and $1 \times 4 \times 1$ CDFs for both $\rho = 0$ and $\rho = 1$.

	Linear MMSE		Logarithmic MMSE	
Measured CDF Estimate	MMSE	Best Match	MMSE	Best Match
SAT-CDF Estimate at RX 1	1.57E-4	$1 \times 1 \times 1$, $\rho = 0$	9.99E-2	$1 \times 1 \times 1$, $\rho = 0$
SAT-CDF Estimate at RX 2	9.85E-5	$1 \times 1 \times 1$, $\rho = 0$	1.13E-2	$1 \times 1 \times 1$, $\rho = 0$
DAT-CDF Estimate at RX 1	7.22E-5	$1 \times 3 \times 1$, $\rho = 0$	8.92E-2	$1 \times 2 \times 1$, $\rho = 0$
DAT-CDF Estimate at RX 2	4.12E-5	$1 \times 2 \times 1$, $\rho = 0$	9.62E-2	$1 \times 2 \times 1$, $\rho = 0$

6.1.3 Pinhole Diversity in the NLOS Backscatter Channel

Comparison of the bistatic SAT measurements and bistatic DAT measurements in the NLOS channel reveals that the pinhole diversity gains predicted in Chapter 3 do occur, as Figure 42 shows. The pinhole diversity gain is evidenced by the fact that the estimate of the SAT CDF is higher than that of the DAT CDF for normalized envelope values $\alpha/\sqrt{P}$ below approximately 0.8. While the gain can be seen in Figure 42(a), it is best seen in the logarithmic plots shown in Figure 42(b).

Pinhole diversity gains can also be seen by examining the fade margins calculated from the measured estimates of the NLOS distributions[1]. Table 10 shows that the fade margin required to maintain a given outage probability is reduced when using the DAT as opposed to the SAT. Furthermore, the fade margins calculated from the measured estimates of the distributions provide a good match with the fade margins derived from (26a) for the $1 \times 1 \times 1$ channel distribution and $1 \times 2 \times 1$ channel distribution.

[1]The fade margin is defined by Equation (15) in Section 2.2.4.

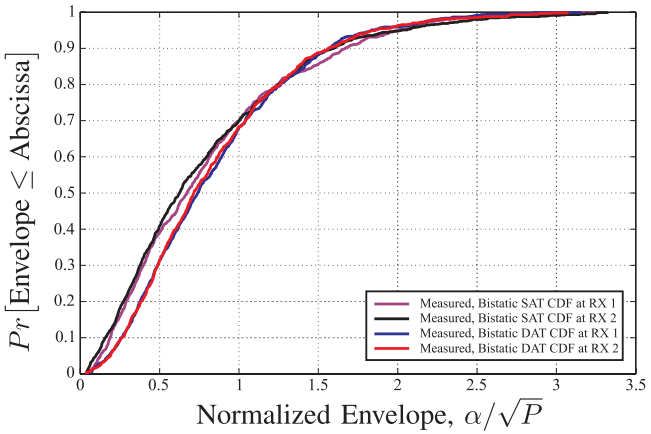

(a) The measured estimates of the CDF calculated from the bistatic SAT measurements and the bistatic DAT measurements at RX 1 and RX 2.

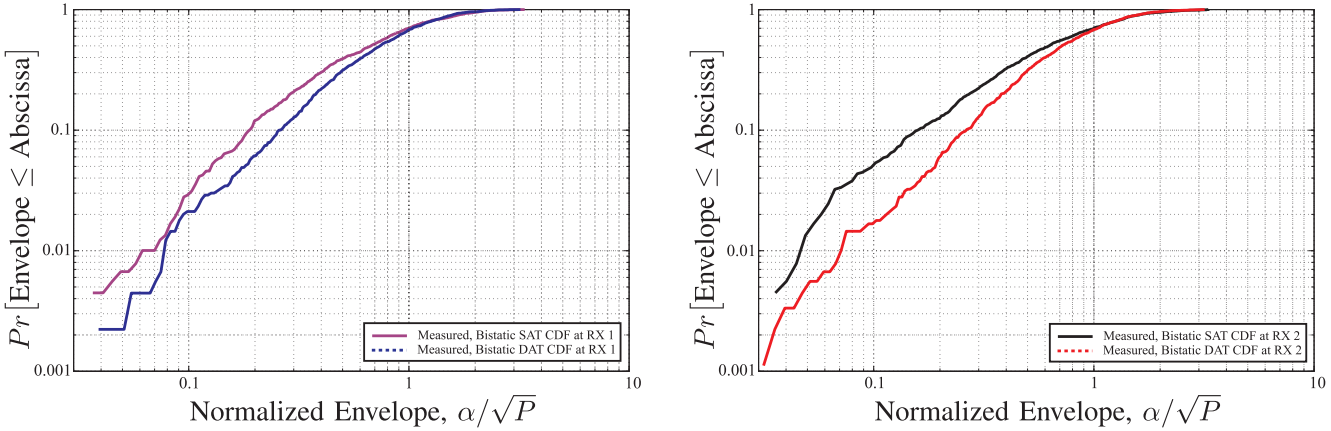

(b) The estimates of the bistatic CDF for the SAT and DAT measurements at RX 1 (left) and RX 2 (right) on log-log axes.

Figure 42: The (a) measured estimates of the SAT CDFs and DAT CDFs in the bistatic, NLOS backscatter channel on linear axes and (b) the same for measurements at RX 1 (left) and RX 2 (right) plotted on log-log axes. The CDF estimates are plotted on axes normalized by the root of the power of each distribution $\sqrt{P}$ for unbiased comparisons.

Note that the measured fade margins do not increase above approximately 29 - 30 dB for either RX 1 or RX 2 and result in significant differences with the derived fade margins. This error is likely caused by the limited number of small measured envelopes. As more data points with small envelope values are added, this error should decrease.

Table 10: NLOS fade margins in dB calculated from estimates of the SAT and DAT distributions measured at RX 1 and RX 2.

Outage Probability	Measured SAT		Derived $1 \times 1 \times 1^{\dagger}$	Measured DAT		Derived $1 \times 2 \times 1^{\dagger}$
	RX 1	RX 2		RX 1	RX 2	
0.5	3.4	4.1	4.1	2.6	2.9	2.9
0.1	14	16	15	12	12	12
0.05	18	20	20	15	14	16
0.01	24	27	28	22	23	24
0.005	29	29	32	25	26	26
0.001	29	29	42	28	30	36

† Fade margins calculated from the distribution given by (26a) in Section 3.2.1.

6.1.4 Discussion

The measured estimates of the NLOS CDFs agree well with the $M \times L \times N$ distributions presented in Section 3.2.1. These measurements show that pinhole diversity gains do occur and that (26a) is accurate for certain $1 \times 1 \times 1$ and $1 \times 2 \times 1$ channels that are NLOS and experience rich multipath. The agreement between the derived distributions and the measured distribution estimates also indicates that the modulated signals backscattered from each of the DAT antennas have small correlation – i.e., the assumption of fading independence between the signals from different RF-tag antennas made in Section 3.2 is valid for this case.

No attempt was made to separate large-scale and small-scale fading in the distribution estimates presented in this section. The agreement between the derived CDFs and the measured CDF estimates indicates that large-scale fading was not significant.

6.2 Fading in the LOS Backscatter Channel

LOS measurements were made in room E560 of the Van Leer Building on the Georgia Institute of Technology main campus, shown in Figure 43. Though a strong LOS existed between the testbed reader and the RF tag, multipath propagation was caused by the walls, floor, and ceiling of the room; laboratory desks and workbenches; and other miscellaneous objects located in the laboratory. Because the LOS was not obstructed for these measurements, adequate power was available for both monostatic and bistatic measurements.

6.2.1 LOS Spatial Fading Plots

Figures 44 - 46 show plots of the normalized received power in dB and signal phase in degrees as a function of RF-tag position. Like Figures 38 - 39, these figures display power normalized to the maximum recorded in each measurement and all of the LOS spatial plots are displayed on the same scale.

Examination of Figures 44 - 46 shows less severe fading than that evident in the NLOS measurements. Differences are also apparent between the monostatic, LOS measurement and the bistatic, LOS measurements – the deepest monostatic fades are approximately 20 dB while the maximum bistatic fades are approximately 12 dB. Unlike the jumbled phases measured in the NLOS measurements, well-defined phase fronts can be seen in each LOS measurement. The phase progression indicates the presence of a dominate specular wave reflecting off the concrete wall behind the RF tag.

As mentioned in Section 5.6, measurements that were within 20 dB of the measured noise floor were removed from all distribution calculations. For the LOS-measurement sets, however, all of the measurements were above this threshold and no measurements were removed. Like the NLOS measurements, no attempt was made to separate large-scale and small-scale fading in the LOS distribution estimates.

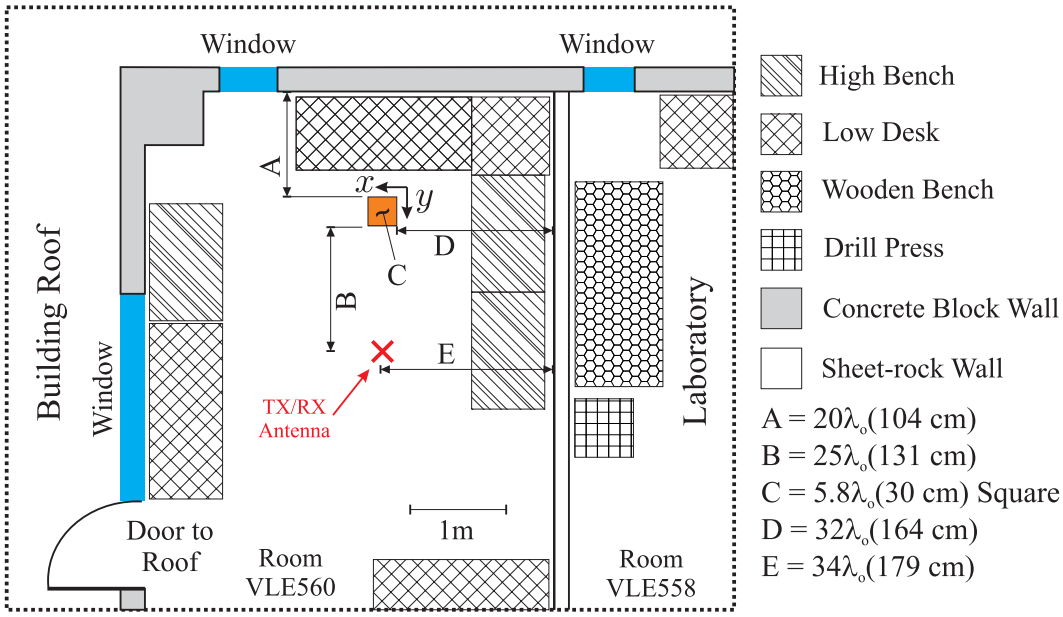

(a) The monostatic backscatter testbed.

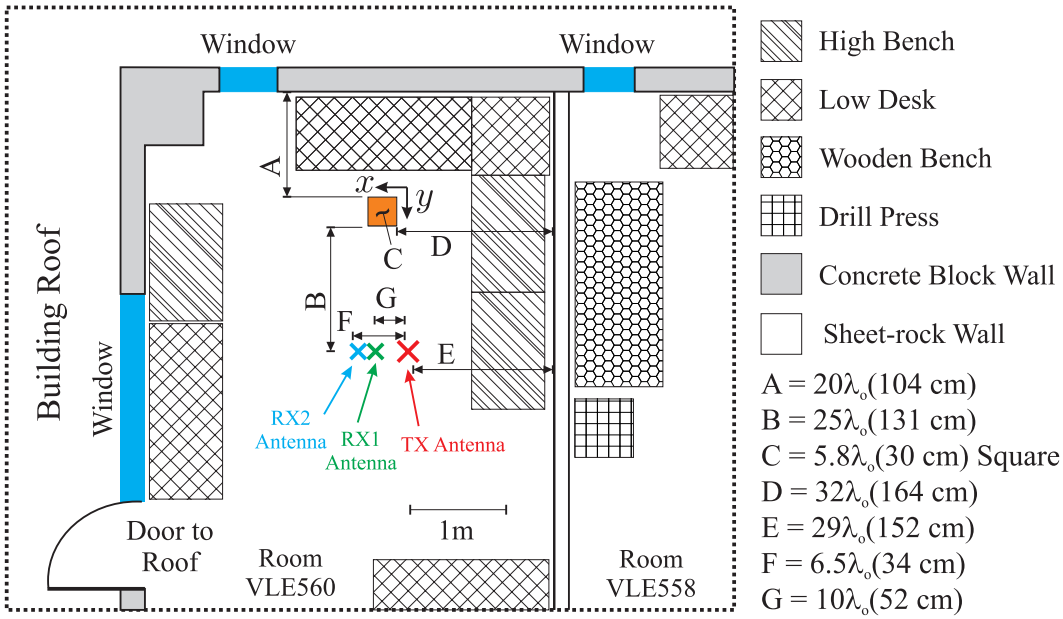

(b) The bistatic backscatter testbed.

Figure 43: The (a) monostatic and (b) bistatic measurement setup in room E560 of the Van Leer Building on the Georgia Institute of Technology main campus. Coherent channel samples were taken at 5.79 GHz as the RF tag was moved uniformly across a 30 cm × 30 cm (approximately $6\lambda_o \times 6\lambda_o$) square in 1 cm (approximately $\lambda_o/5$) increments. In these figures, the area over which the tag was moved is denoted by the orange square and the RF tags and reader antennas were approximately 178 cm above the floor.

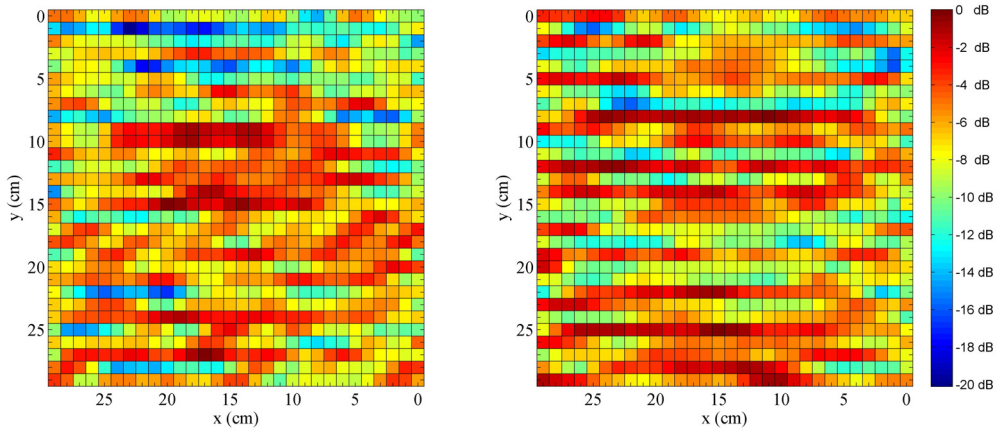

(a) Normalized channel power (in dB) received from the SAT (left) and DAT (right).

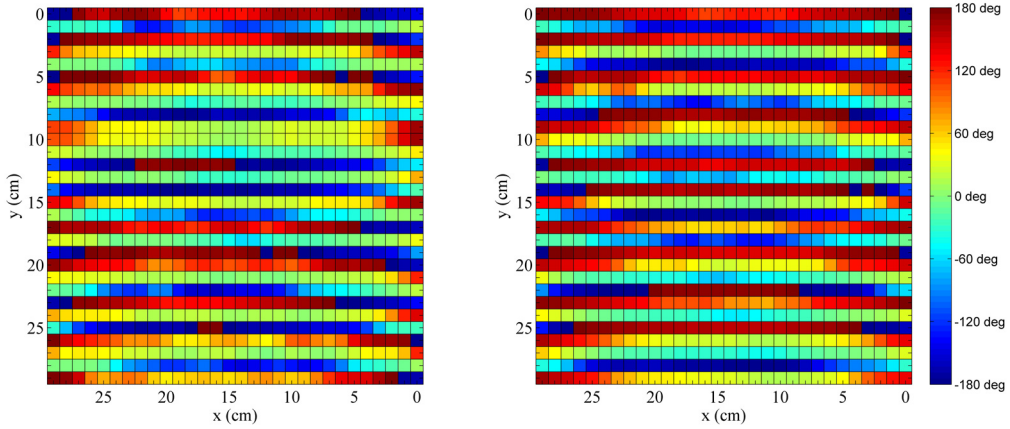

(b) The phase (in degrees) of the signal received from the SAT (left) and DAT (right).

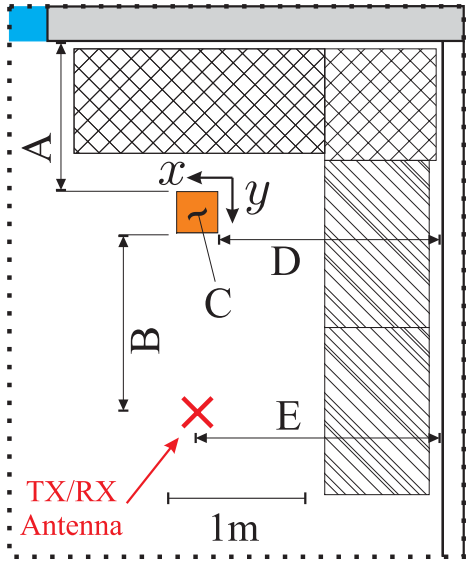

(c) The LOS, monostatic-testbed measurement diagram. The measured area is denoted by the orange square.

Figure 44: (a) Measured power (in dB) relative to the maximum along with (b) the measured phase (in degrees) from the SAT (left) and DAT (right) at each position in the LOS, monostatic channel. The orientation of the measurements is shown in (c). A full diagram of the measurement area is given in Figure 43.

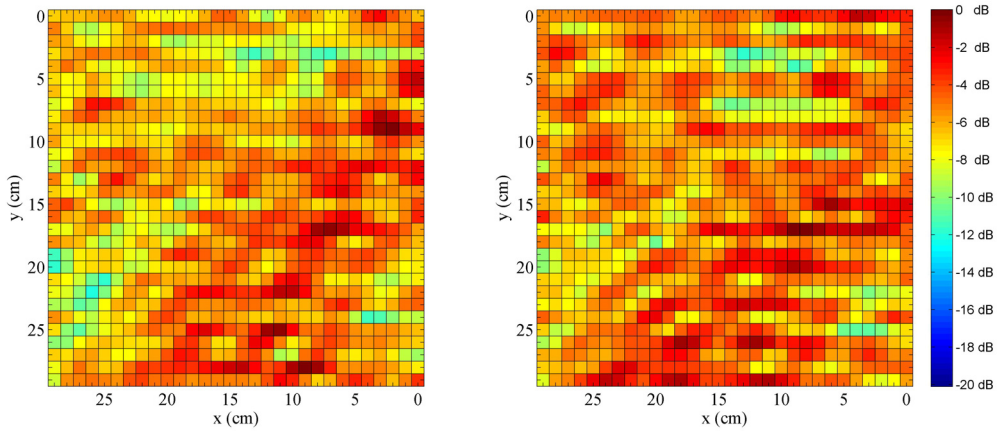

(a) Normalized channel power (in dB) received from the SAT at RX 1 (left) and RX 2 (right).

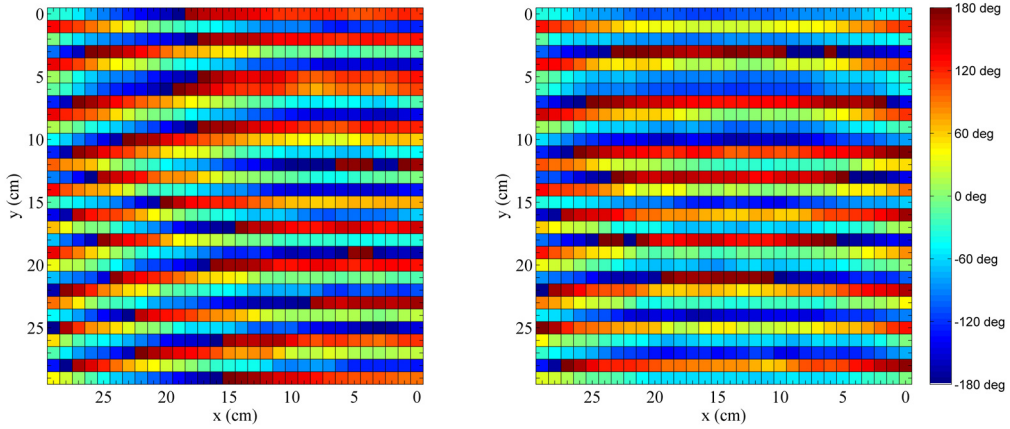

(b) The phase (in degrees) of the signal received from the SAT at RX 1 (left) and RX 2 (right).

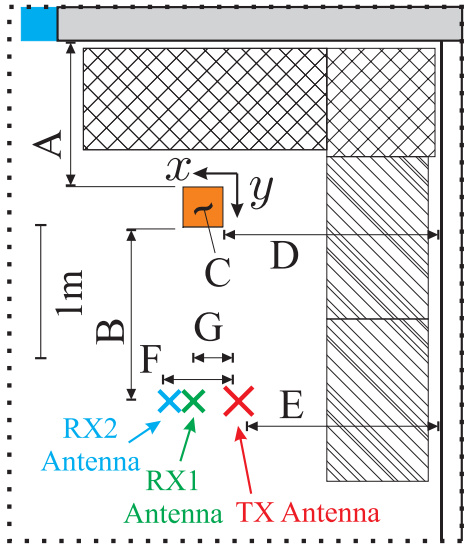

(c) LOS, bistatic-testbed measurement diagram. The measured area is denoted by the orange square.

Figure 45: (a) Measured power (in dB) relative to the maximum along with (b) the measured phase (in degrees) from the SAT at RX 1 (left) and RX 2 (right) for each position in the LOS, bistatic channel. The orientation of the measurements is shown in (c). A full diagram of the measurement area is given in Figure 43.

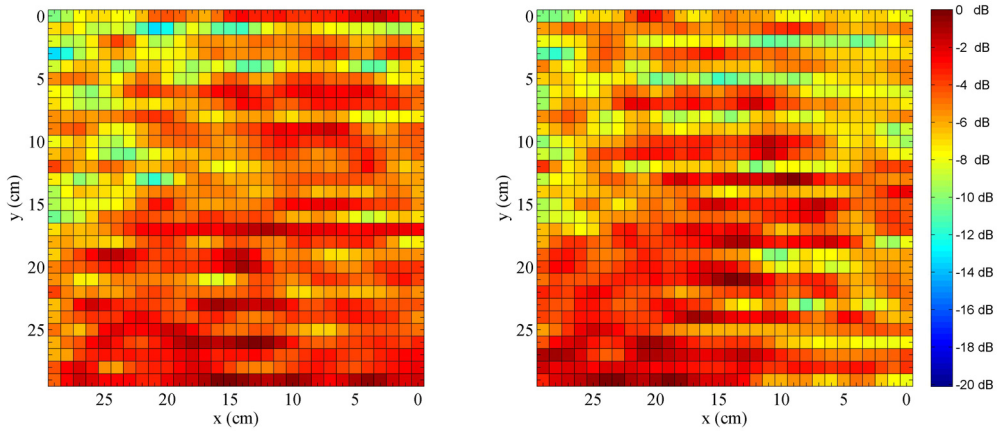

(a) Normalized channel power (in dB) received from the DAT at RX 1 (left) and RX 2 (right).

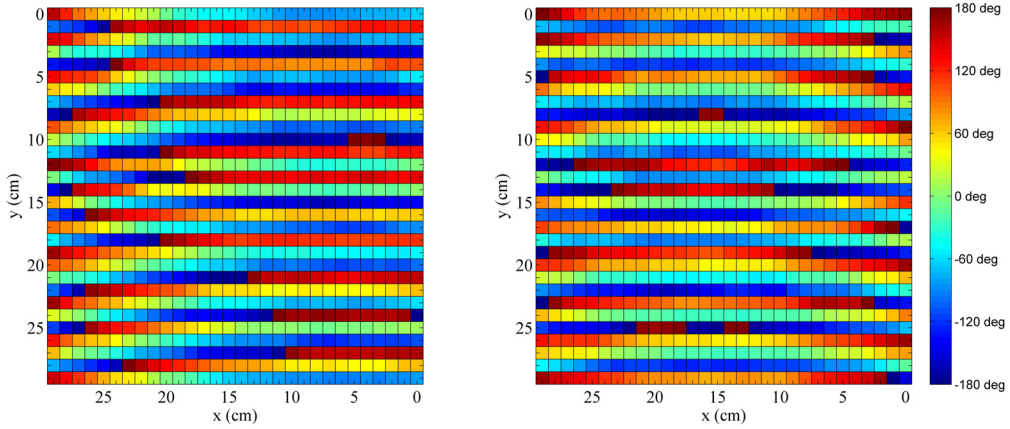

(b) The phase (in degrees) of the signal received from the DAT at RX 1 (left) and RX 2 (right).

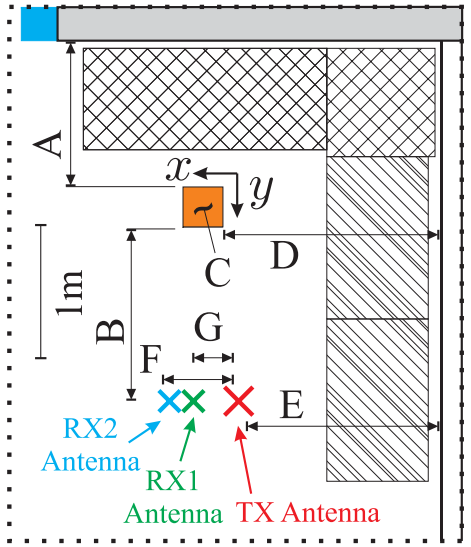

(c) LOS, bistatic-testbed measurement diagram. The measured area is denoted by the orange square.

Figure 46: (a) Measured power (in dB) relative to the maximum along with (b) the measured phase (in degrees) from the DAT at RX 1 (left) and RX 2 (right) for each position in the LOS, bistatic channel. The orientation of the measurements is shown in (c). A full diagram of the measurement area is given in Figure 43.

6.2.2 LOS Link-Correlation Effects

As with the NLOS measurements, estimates of the LOS fading CDFs were calculated from the measurements for fading analysis. Figure 47 compares estimates of the monostatic CDFs to estimates of the bistatic CDFs for both the SAT and DAT measurements in the LOS channel. One of the first observations that can be made is that, for both the SAT and DAT measurements, fading in the monostatic case is more severe than that in the bistatic case. The reason for this fading improvement is that link envelope correlation ρ_e is reduced by using spatially-separated transmitter and receiver antennas, as discussed in Section 3.3.3. Note that while the estimate of the monostatic CDF shows worse fading than that of the bistatic CDF for small envelope values, it also exhibits a higher probability of having a large envelope. The link correlation between the fading on the forward and backscatter links that causes a higher probability of destructive interference (fades) for the monostatic link also causes the probability of constructive interference (peaks) to be larger.

6.2.3 Pinhole Diversity Gains

Figure 48 plots the measured estimate of the SAT CDF and the measured estimate of the DAT CDF for the bistatic testbed and Figure 49 shows the same for the monostatic testbed. For the measured estimates of both the monostatic and bistatic CDFs, a pinhole diversity gain is observed; however, it is smaller than that observed in the NLOS measurements.

A small pinhole diversity gain indicates that, at least for small envelopes, the measured estimates of the SAT CDFs and the DAT CDFs are similar for this channel. This is confirmed by examining the linear and logarithmic MSEs. To calculate the MMSE for the LOS channels, the measured estimates of the CDFs were compared to the CDF of the signal received at the n^{th} reader antenna through the $M \times L \times N$ channel with Rician-fading links[2]. Comparisons of the measured CDF estimates were made to this derived distribution for K factors ranging from -9 dB to 16.5 dB in 0.25 dB increments. These MMSEs are given in Table 11.

[2]The derivation of this distribution is described in Section 3.2.2.

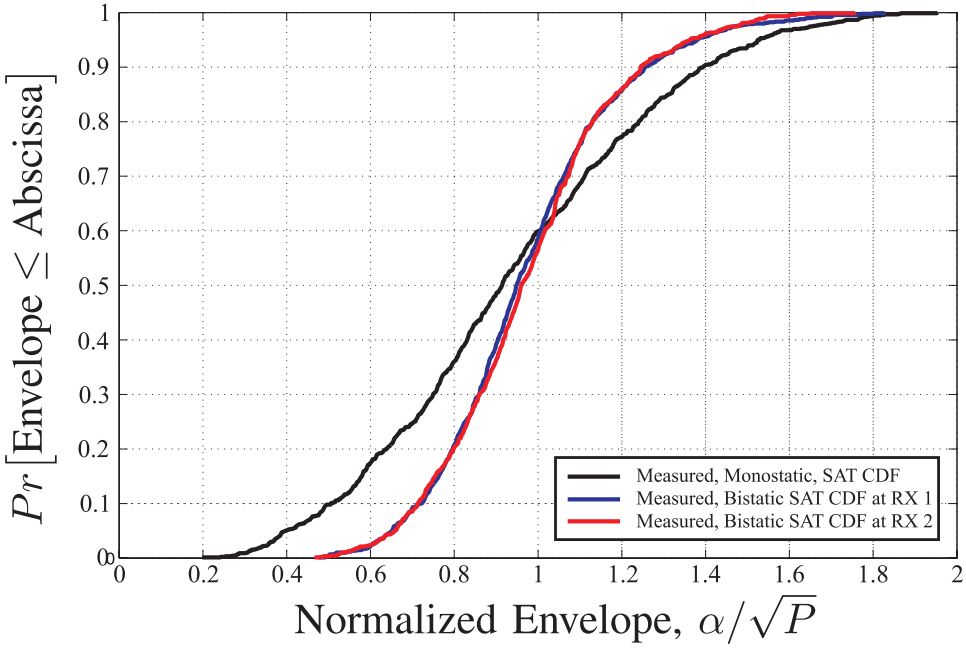

(a) Measured estimates of the monostatic SAT CDF and the bistatic SAT CDFs.

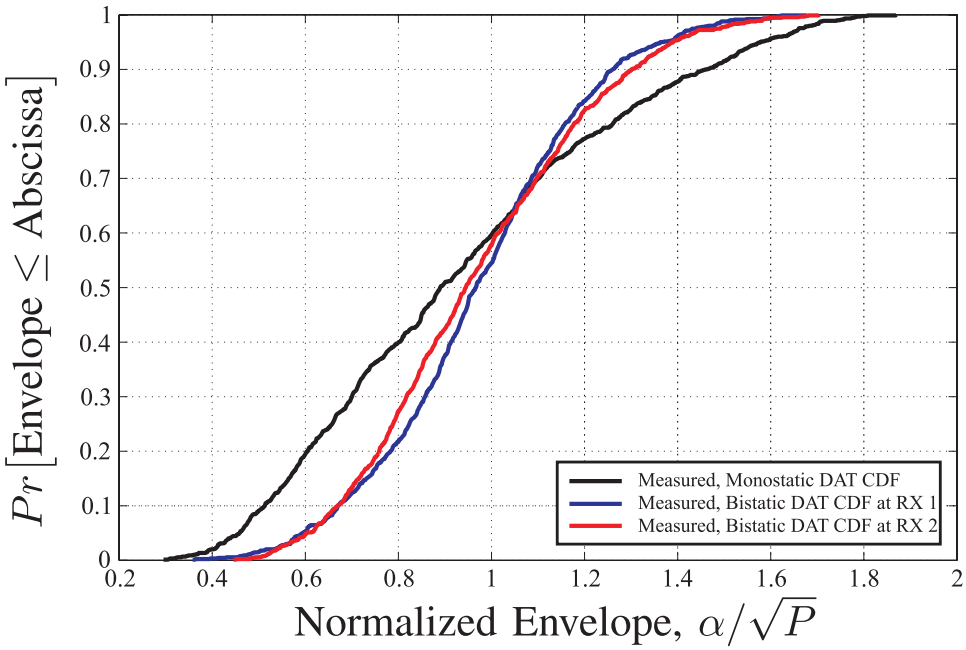

(b) Measured estimates of the monostatic DAT CDF and the bistatic DAT CDFs.

Figure 47: Comparison of the estimates of the monostatic and bistatic CDFs for the (a) SAT and (b) DAT measurements in the LOS channel. The CDF estimates are plotted on axes normalized by the root of the power of each distribution $\sqrt{P}$ for unbiased comparisons.

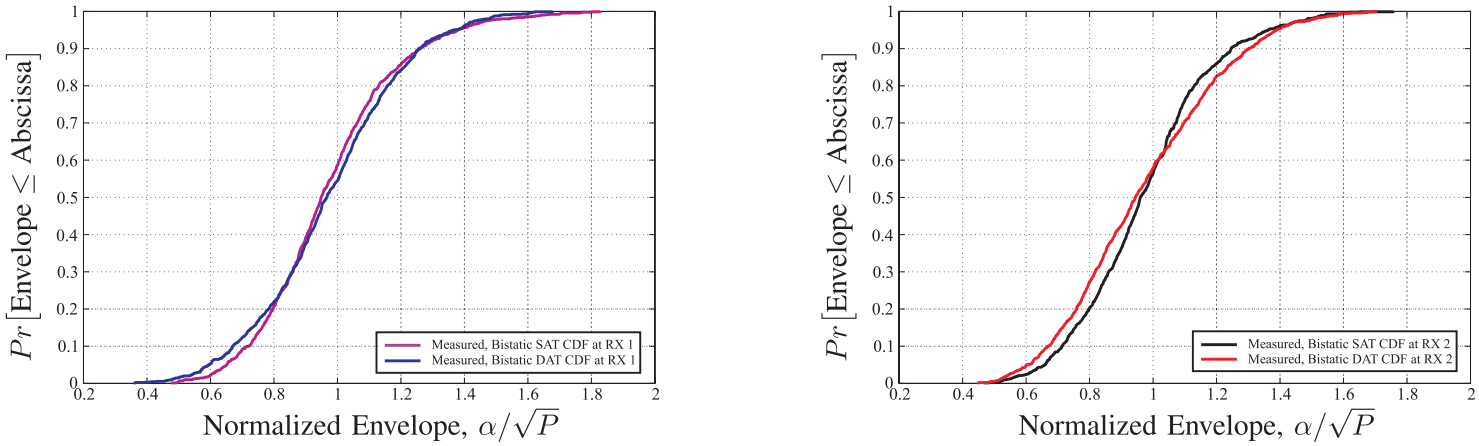

(a) Estimates of the bistatic SAT CDFs and the bistatic DAT CDFs measured at RX 1 (left) and RX 2 (right) and plotted on linear axes.

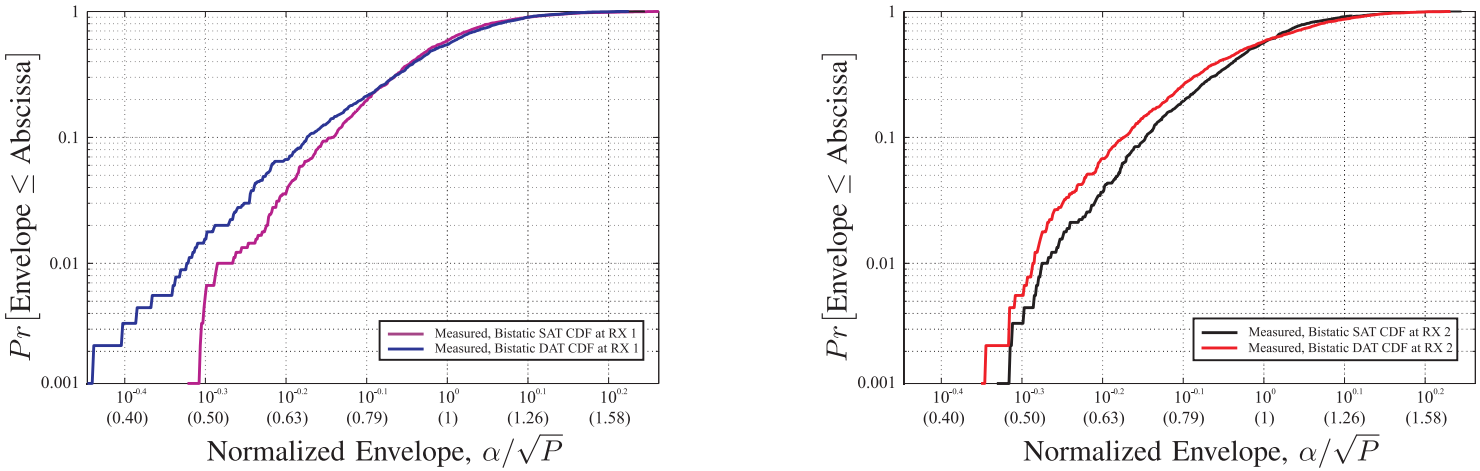

(b) Estimates of the bistatic SAT CDFs and the bistatic DAT CDFs measured at RX 1 (left) and RX 2 (right) and plotted on log-log axes.

Figure 48: The estimates of the SAT CDFs and the DAT CDFs for the LOS, bistatic backscatter channel measured at (a) RX 1 (left) and RX 2 (right) on linear axes and (b) RX 1 (left) and RX 2 (right) on log-log axes. The CDFs are plotted on axes normalized by the root of the power of each distribution $\sqrt{P}$ for unbiased comparisons.

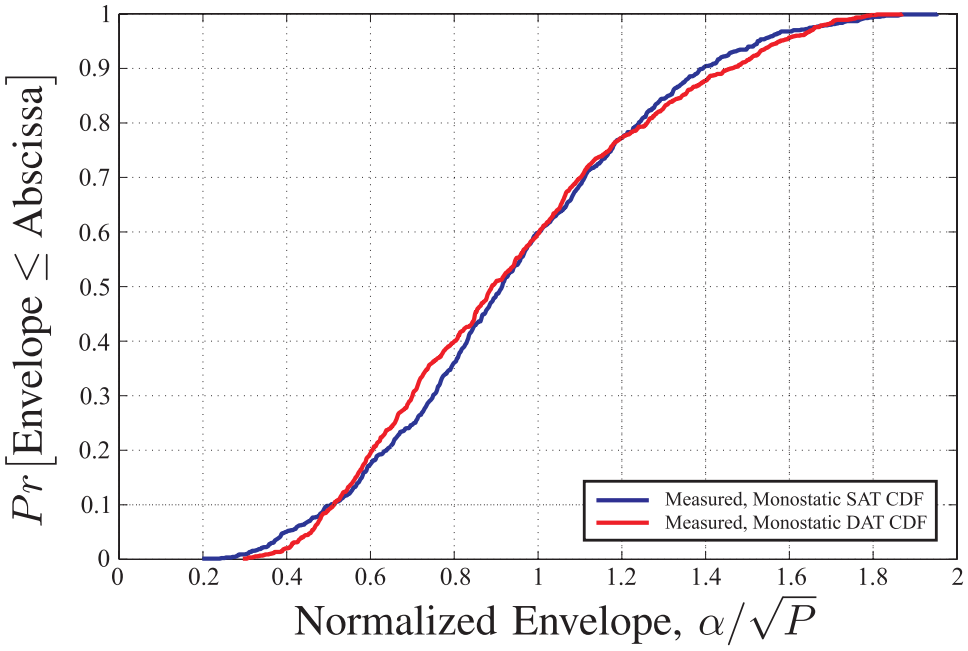

(a) The measured estimates of the SAT CDF and the DAT CDF for the LOS, monostatic backscatter channel plotted on linear axes.

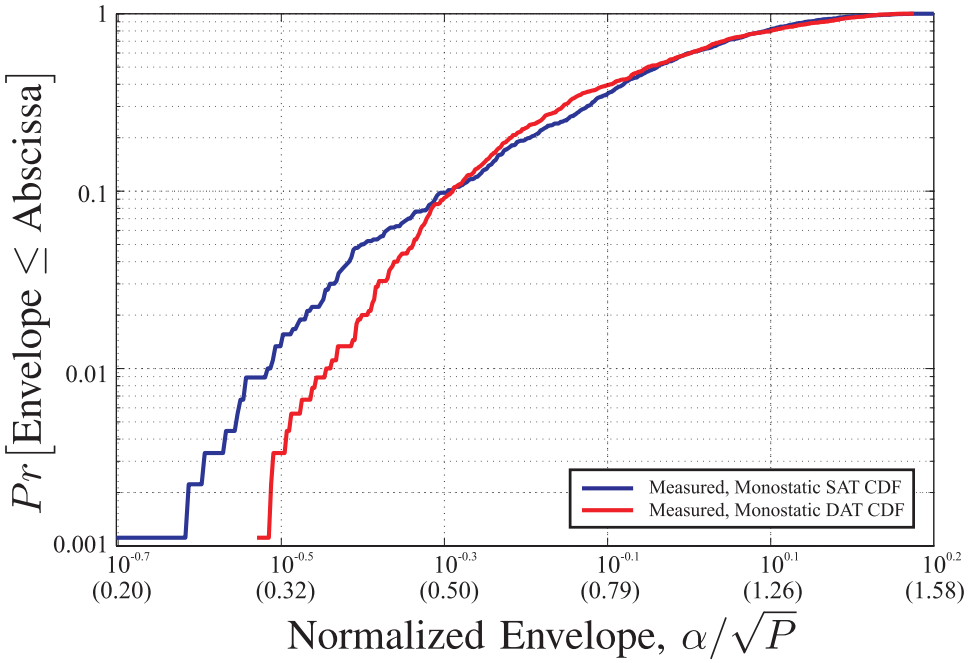

(b) The measured estimates of the SAT CDF and the DAT CDF for the LOS, monostatic backscatter channel plotted on log-log axes.

Figure 49: The measured estimates of the SAT CDF and the DAT CDF for the LOS, monostatic backscatter channel plotted on (a) linear and (b) log-log axes. The CDF estimates are plotted on axes normalized by the root of the power of each distribution $\sqrt{P}$ for unbiased comparisons.

Both the linear and logarithmic MMSEs indicate that the measured estimates of the bistatic SAT CDFs best fit the $1 \times 1 \times 1$ distribution with K between 13 - 13.5 dB. The measured estimates of the DAT CDFs best match the $1 \times 1 \times 1$ distribution with K between 11.75 - 12.75 dB. Similar matches are found for the measured estimates of the monostatic CDFs, shown in Table 12.

Table 11: The best-fit, LOS envelope distributions for the estimates of the bistatic distributions measured in the LOS channel. The measured distribution estimates were compared to numerical approximations of the distributions for the $1 \times 1 \times 1$, LOS channel and the $1 \times 2 \times 1$, LOS channel for $\rho_e = 0$ and K ranging from -9 dB to 16.5 dB in 0.25 dB increments.

Measured CDF Estimate	Best Fit $1 \times 1 \times 1$ LOS Distribution				Best Fit $1 \times 2 \times 1$ LOS Distribution			
	Linear MSE		Logarithmic MSE		Linear MSE		Logarithmic MSE	
	MMSE	K dB	MMSE	K dB	MMSE	K dB	MMSE	K dB
SAT at RX 1	1.56E-4	13	3.43E-1	13.5	1.87E-2	11.25	2.61E+1	16.5
SAT at RX 2	7.16E-5	13.25	2.43E-1	13.5	2.09E-2	11.75	3.11E+1	16.5
DAT at RX 1	1.10E-4	12.75	1.29E-1	12	1.89E-2	11.5	3.67E+1	8.5
DAT at RX 2	8.41E-5	11.75	7.28E-1	12.75	1.52E-2	11.25	2.78E+1	16.5

Table 12: The best-fit, LOS envelope distributions for the estimates of the monostatic distributions measured in the LOS channel. The measured distribution estimates were compared to numerical approximations of the distributions for the $1 \times 1 \times 1$, LOS channel and the $1 \times 2 \times 1$, LOS channel for $\rho_e = 0$ and K ranging from -9 dB to 16.5 dB in 0.25 dB increments.

Measured CDF Estimate	Best Fit $1 \times 1 \times 1$ LOS Distribution				Best Fit $1 \times 2 \times 1$ LOS Distribution			
	Linear		Logarithmic		Linear		Logarithmic	
	MMSE	K dB	MMSE	K dB	MMSE	K dB	MMSE	K dB
SAT	1.03E-4	8.5	8.21E-1	9	3.27E-3	9.75	1.55E+1	7.25
DAT	2.50E-4	7.75	1.19E+0	9.5	2.90E-3	8.75	1.31E+1	7.5

The best-fit for the measured estimate of the monostatic SAT CDF is the $1 \times 1 \times 1$ distribution with K between 8.5 - 9 dB while the measured estimate of the monostatic DAT CDF best fits the $1 \times 1 \times 1$ distribution with K between 7.75 - 9.5 dB.

As with the NLOS measurements, fade margins can be calculated from the measured

estimates of the LOS CDFs for the SAT and DAT. These are shown in Table 13 and reflect the previous observation that only a small pinhole diversity gain is available in this LOS channel. In other words, for both the monostatic and bistatic measurements, the difference between the SAT and DAT fade margins is very small.

Table 13: LOS fade margins (in dB) calculated from the measured distribution estimates.

Outage Probability	Monostatic		Bistatic			
	SAT	DAT	SAT		DAT	
			RX 1	RX 2	RX 1	RX 2
0.5	0.78	1.0	0.47	0.36	0.31	0.50
0.1	5.9	5.8	2.9	2.9	3.5	3.5
0.05	8.0	6.8	3.7	3.6	4.6	4.4
0.01	10	8.9	5.7	5.5	6.5	5.7
0.005	11	9.9	6.0	5.9	7.7	6.3
0.001	14	11	6.4	6.6	8.9	7.0

6.2.4 Discussion

Many of the LOS measurements discussed previously provide direct support for the backscatter channel theory presented in Chapter 3. First, Figure 47 shows that using separate, adequately-spaced reader transmitter and receiver antennas decreases link correlation in the LOS backscatter channel and provides a corresponding reduction in multipath fading. Second, Table 11 shows a very good match between the estimate of the SAT CDF measured in the bistatic channel and the numerically-approximated, $1 \times 1 \times 1$, LOS distribution for $K \approx 13$ dB. Third, very small pinhole diversity gains are realized for the LOS-monostatic and LOS-bistatic channels. This is expected because of the very high K factor of the LOS backscatter channel, as described in Section 3.3.4.

What is not expected is that the measured estimate of the LOS DAT CDF matches the numerically-approximated, $1 \times 1 \times 1$, LOS CDF more closely than the $1 \times 2 \times 1$, LOS CDF, shown in Table 11. Also, the severe fading predicted in Section 3.3.4 for the $1 \times 2 \times 1$

channel with a high K factor is not exhibited by the measured estimates of the DAT CDFs. Furthermore, the measured estimates of the monostatic SAT CDF and the monostatic DAT CDF match the numerically-approximated, $1 \times 1 \times 1$, LOS CDF with $\rho_e = 0$ quite well. These apparent discrepancies between the $M \times L \times N$, dyadic backscatter channel theory and measurements can be explained by additional correlation in the LOS channel.

The analytic envelope distributions for the NLOS channel presented in Section 3.2.1 and the numerical approximations of the $M \times L \times N$ envelope distributions for the LOS channel shown in Figure 16 and Figure 17 both assume that the total signal received at the n^{th} reader antenna is the sum of L, i.i.d., product-Rayleigh or L, i.i.d., product-Rician random variables, respectively. For the NLOS case, measurements confirmed that this was at least approximately true even though the RF-tag antennas were closely spaced. The high level of multipath propagation experienced by the RF tag resulted in a channel with a very small spatial coherence distance – i.e., the correlation of the channel as a function of space decreased rapidly [17]. This is not true, however, for the LOS measurements. The spatial coherence of the channel is much greater than that of the NLOS channel and results in correlation between the signals received from the two RF-tag antennas.

Consider the following: if the signal transmitted from the reader is approximated as a planewave, then the phase of the modulated-backscatter signal received from each RF-tag antenna is determined by the path length that the waves have traveled. The phase difference between these signals is

$$\text{Phase Difference} = \exp\Big\{ j \frac{2\pi}{\lambda} [\, \overline{R}_1 - \overline{R}_2] \Big\}, \tag{42}$$

where $\overline{R}_1 = |\vec{r}_1^{\,f}| + |\vec{r}_1^{\,b}|$ is the total path length from the reader to DAT antenna 1, $\overline{R}_2 = |\vec{r}_2^{\,f}| + |\vec{r}_2^{\,b}|$ is the total path length from the reader to DAT antenna 2, and λ is the wavelength, as shown in Figure 50. $\overline{R}_1$ and $\overline{R}_2$ can be written as the sum of their x and y components:

$$\overline{R}_1 = \sqrt{\left(r_{1\,\mathrm{x}}^{f}\right)^2 + \left(r_{1\,\mathrm{y}}^{f}\right)^2} + \sqrt{\left(r_{1\,\mathrm{x}}^{b}\right)^2 + \left(r_{1\,\mathrm{y}}^{b}\right)^2}, \tag{43}$$

$$\overline{R}_2 = \sqrt{\left(r_{1\,\mathrm{x}}^{f}\right)^2 + \left(r_{1\,\mathrm{y}}^{f} + \Delta_{\mathrm{tag}}\right)^2} + \sqrt{\left(r_{1\,\mathrm{x}}^{b}\right)^2 + \left(r_{1\,\mathrm{y}}^{b} - \Delta_{\mathrm{tag}}\right)^2}, \tag{44}$$

where $r_{1\,\mathrm{x}}^{f,b} = r_{2\,\mathrm{x}}^{f,b}$, $r_{2\,\mathrm{y}}^{f} = r_{1\,\mathrm{y}}^{f} + \Delta_{\mathrm{tag}}$ and $r_{2\,\mathrm{y}}^{b} = r_{1\,\mathrm{y}}^{b} - \Delta_{\mathrm{tag}}$. From (43) and (44), it can be seen that if $\Delta_{\mathrm{tag}} << r_{1\,\mathrm{x}}^{f,b}$ or $\Delta_{\mathrm{tag}} << r_{1\,\mathrm{y}}^{f,b}$, then $\overline{R}_1 \approx \overline{R}_2$ and the phase difference in (42) will

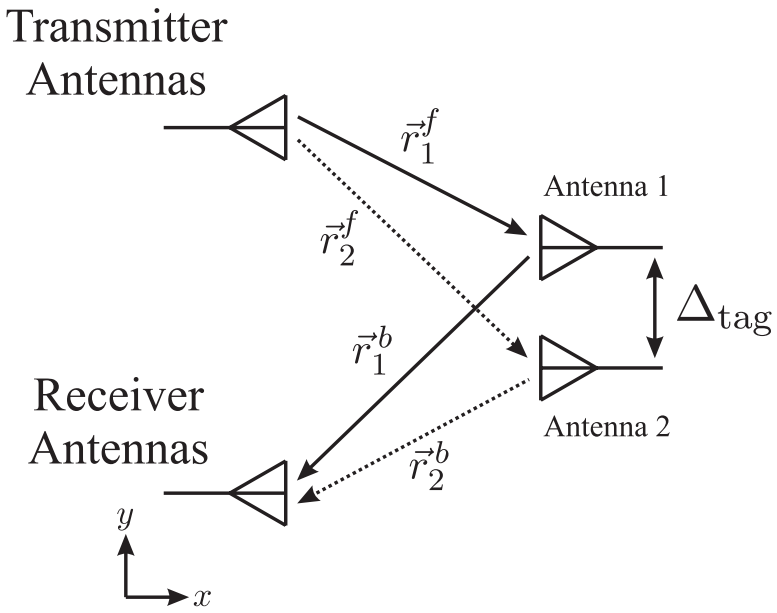

Figure 50: The separation distances between the reader and each antenna of the DAT. The total path length to DAT antenna 1 is $\overline{R}_1 = |\vec{r}_1^{\,f}| + |\vec{r}_1^{\,b}|$ and the total path length to DAT antenna 2 is $\overline{R}_2 = |\vec{r}_2^{\,f}| + |\vec{r}_2^{\,b}|$.

be very small. As a result, the received signal is not composed of two independent specular waves, as assumed in the numerically-approximated, $M \times L \times N$ distributions of the LOS backscatter channel, but of two specular waves with correlated phases. In essence, a single phase front propagates from the tag to the reader which makes the estimate of the DAT distribution resemble that of the SAT. In a strong LOS channel – such as the one measured in this section – RF-tag footprint restrictions will likely not allow Δ_{tag} to be large enough to reduce the correlation between the modulated-backscatter signals received from each DAT antenna to near zero. Instead, additional multipath propagation is required, as evidenced by the NLOS measurements.

Therefore, this correlation explains why the measured estimate of the DAT CDF closely matched that predicted for the SAT and explains why the severe fading predicted for the $1 \times 2 \times 1$ channel with a high K factor was not measured. Correlation between backscattered signals also explains why a larger range of K factors was shown to be the best fit by the linear and logarithmic MSE analysis. The linear MMSE is most sensitive to the CDF-fit for large envelope values while the logarithmic is more sensitive for small envelope values.

The large range of K factors indicates that the measured estimates of the LOS DAT CDFs do not exactly match either the derived, $1 \times 1 \times 1$-channel CDF or the derived, $1 \times 2 \times 1$-channel CDF; instead, they match something in between. This is caused by the additional correlation found in the LOS channel.

Another factor that may have influenced the measured estimates of the LOS DAT CDFs was unequal scattering from each RF-tag antenna. The backscatter from each DAT antenna was verified to be approximately equal (approximately 2-7 dB difference in received power) before each measurement. However, as the RF tag was moved through the channel, nulls and peaks in the DAT's antenna pattern may have caused unequal power to be received from each antenna.

6.3 Conventional Diversity Gains

The modulated-backscatter signals received at RX 1 and RX 2 in the NLOS, bistatic measurements and the LOS, bistatic measurements can be combined to demonstrate the fading gains realized using conventional diversity combining. It was impossible to gather enough channel samples to present conventional diversity gains in terms of BER, as was done in the Monte Carlo simulation results presented in Section 3.3.5; therefore, the estimated CDF and fade margins of the combined diversity branches are presented in Figures 51 - 52 and Table 14, respectively. The diversity branches from RX 1 and RX 2 were combined using MRC with the receiver having perfect knowledge of the channel. A noticeable reduction in fading is evident for the NLOS SAT measurements and the NLOS DAT measurements shown in Figure 51. An improvement is also seen for small envelope values in the LOS measurements, though not as large as those for the NLOS channel. In both the NLOS and LOS measurements, larger conventional diversity gains are realized for the DAT than for the SAT. This is because the multipath richness of the backscatter channel is increased by the DAT's two pinholes compared to the single pinhole of the SAT[3].

[3]Recall that RF-tag antennas act as pinholes in the dyadic backscatter channel. See Section 3.1.

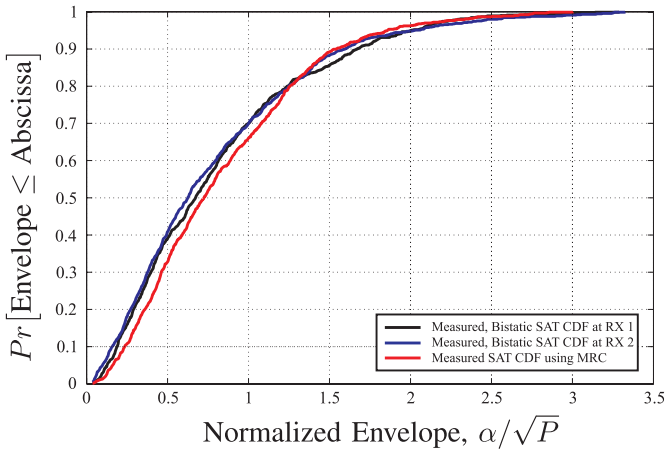

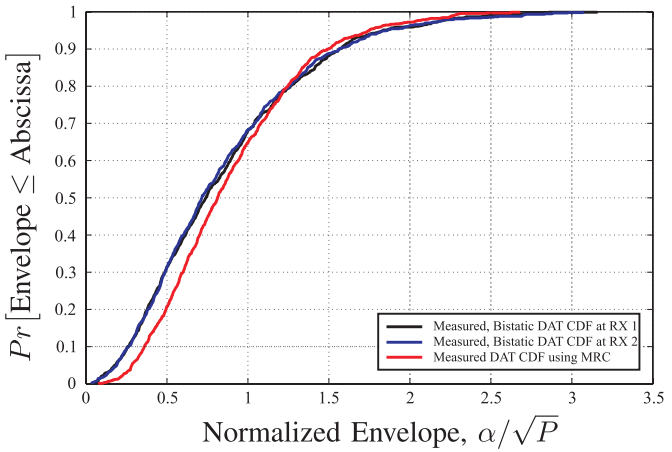

(a) Estimates of the bistatic, NLOS CDF with and without MRC for the (a) SAT and (b) DAT measurements plotted on linear axes.

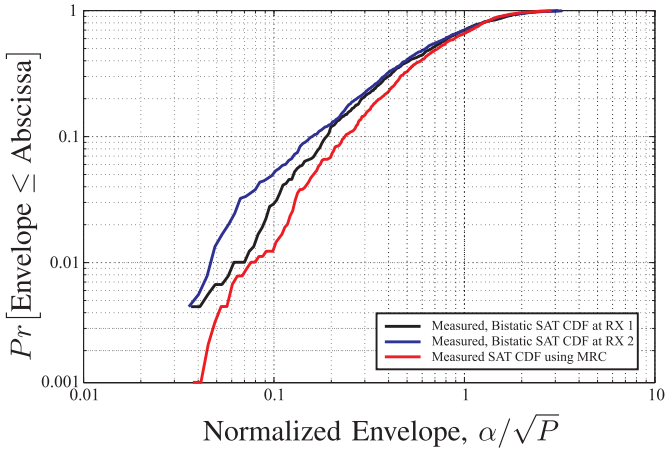

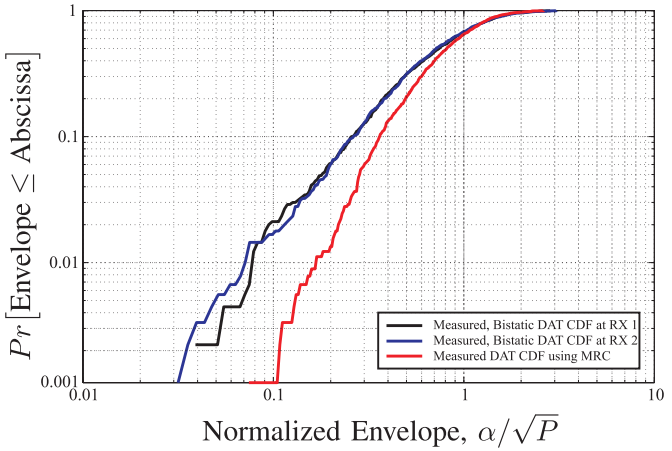

(b) Estimates of the bistatic, NLOS CDF with and without MRC for the (a) SAT and (b) DAT measurements plotted on log-log axes.

Figure 51: Estimates of the bistatic, NLOS CDFs with and without MRC for the (a) SAT and (b) DAT measurements. The CDFs are plotted on axes normalized by the root of the power of each distribution $\sqrt{P}$ for unbiased comparisons.

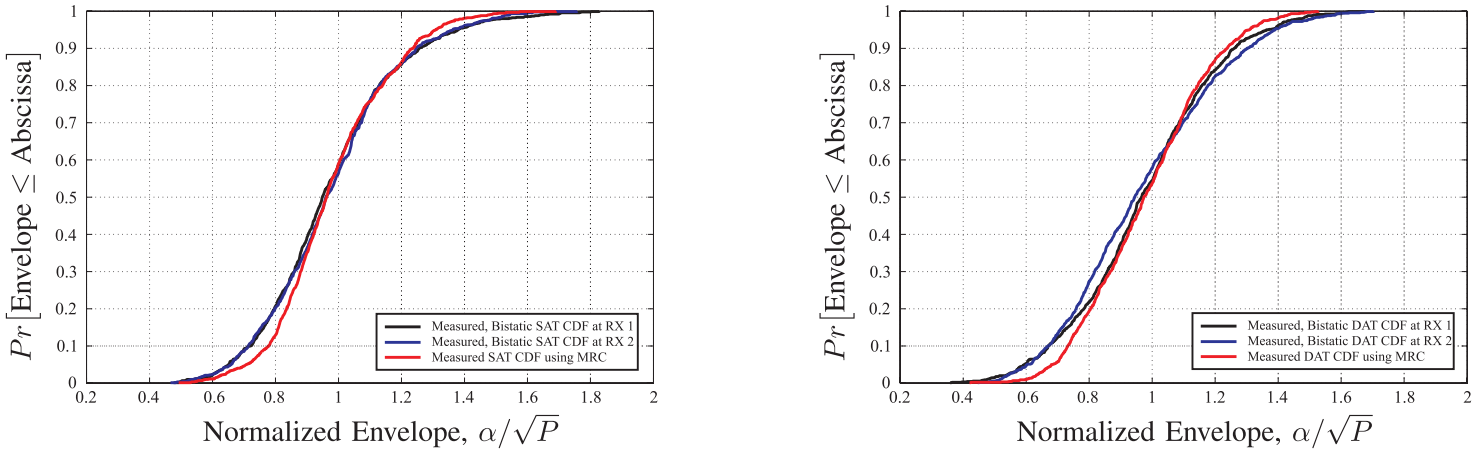

(a) Estimates of the bistatic, LOS CDF with and without MRC for the (a) SAT and (b) DAT measurements plotted on linear axes.

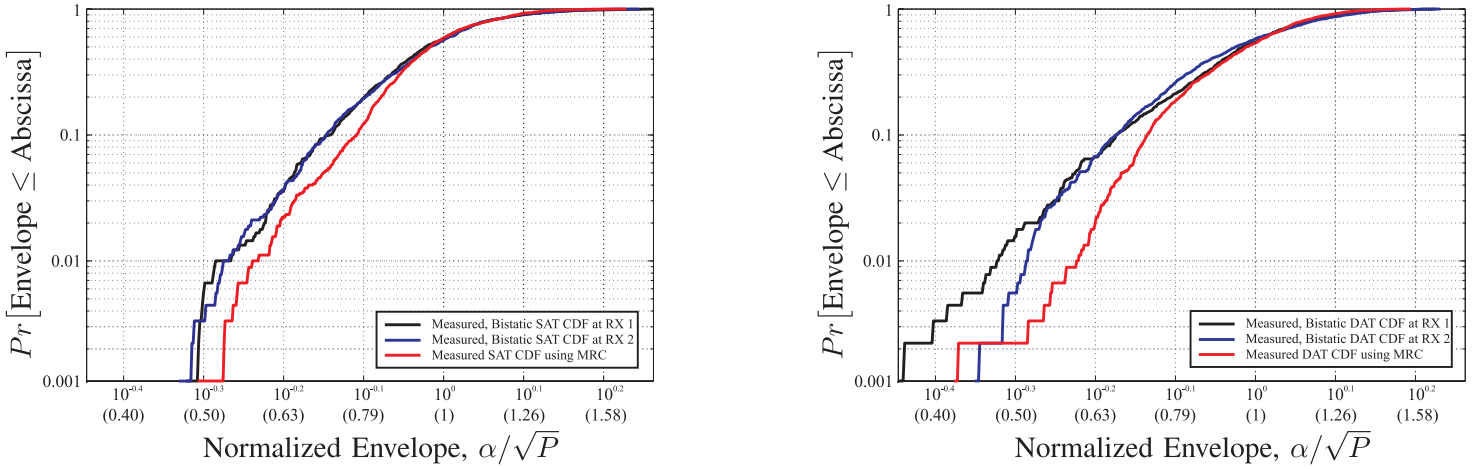

(b) Estimates of the bistatic, LOS CDF with and without MRC for the (a) SAT and (b) DAT measurements plotted on log-log axes.

Figure 52: Estimates of the bistatic, LOS CDFs with and without MRC for the (a) SAT and (b) DAT measurements. The CDFs are plotted on axes normalized by the root of the power of each distribution $\sqrt{P}$ for unbiased comparisons.

Table 14: Fade margins (in dB) calculated with and without MRC from the measured distribution estimates of both the bistatic, NLOS channel and the bistatic, LOS channel.

Outage Probability	NLOS				LOS			
	MRC		SAT†	DAT†	MRC		SAT†	DAT†
	SAT	DAT	RX 1/2	RX 1/2	SAT	DAT	RX 1/2	RX 1/2
0.5	2.8	1.8	3.4/4.1	2.6/2.9	0.3	0.23	0.47/0.36	0.31/0.50
0.1	13	8.8	14/16	12/12	2.2	2.7	2.9/2.9	3.5/3.5
0.05	16	11	18/20	15/14	3.0	3.4	3.7/3.6	4.6/4.4
0.01	22	16	24/27	22/23	4.8	4.5	5.7/5.5	6.5/5.7
0.005	26	18	29/29	25/26	5.3	5.3	6.0/5.9	7.7/6.3
0.001	29	23	29/29	28/30	6.2	7.5	6.4/6.6	8.9/7.0

† No MRC performed.

CHAPTER VII

CONCLUSIONS

In short, this research has sought an answer to the following question:

> *Can multipath fading be reduced for backscatter-radio systems using multiple antennas at the reader transmitter, receiver, and RF tag?*

The answer was found to be a resounding yes. It was found that small-scale multipath fading can be reduced in backscatter-radio systems by the following:

Using Multiple-Antenna RF Tags: New fading distributions derived for the $M \times L \times N$, dyadic backscatter channel have shown that using multiple RF-tag antennas to modulate backscatter can reduce fading on the signal received at one of the reader receiver antennas. This gain, known as a pinhole diversity gain, is available in backscatter channels in which the K factor of the forward and backscatter links is less than approximately 3 dB. As multipath fading is decreased (i.e., a higher K factor), measurements show that the signal received from a multiple-antenna RF tag will have a distribution very similar to that of a single-antenna RF tag. In other words, pinhole diversity gains are best realized in channels that experience heavy small-scale multipath fading. As multipath propagation decreases, there is no penalty for using multiple RF-tag antennas.

The theory has shown that pinhole diversity gains can, in some cases, result in up to a 78% increase in RF-tag read range. Pinhole diversity gains have been confirmed through the first fading measurements of the $M \times L \times N$, dyadic backscatter channel at 5.8 GHz. Cumulative distribution functions tabulated from the NLOS measurements matched those from the derived fading distributions well and exhibited the predicted pinhole diversity gains.

Reducing Link Correlation: Using spatially-separated, reader transmitter and receiver antennas will decrease fading on the modulated-backscatter signal received by the reader.

Fading is reduced because the spatial separation reduces link correlation between fading on the forward and backscatter links. This was demonstrated by fading measurements in both LOS (Rician-fading forward and backscatter links) and NLOS (Rayleigh-fading forward and backscatter links) channels. In backscatter channels with Rayleigh-fading links, reducing link correlation can reduce fading to the same extent as using multiple RF-tag antennas. For instance, it was shown that, in backscatter channels with Rayleigh-fading forward and backscatter links, a channel with fully-correlated links and two RF-tag antennas has equivalent fading to channel with zero link correlation and a single RF-tag antenna. Therefore, careful attention must be paid to the design of reader transmitter and receiver antennas.

Using Antenna Arrays: Using antenna arrays at the reader transmitter or receiver will allow conventional diversity gains to be realized. Fading measurements confirmed this and showed that using RF tags with multiple antennas will increase conventional diversity gains.

These fade reducing techniques may best be realized using frequencies higher than the commonly used 902-928 MHz and 2400-2483.5 MHz ISM bands. It was shown, through example, that several potential advantages are offered by the 5725-5850 MHz ISM frequency band – higher antenna gain, smaller antenna size, additional bandwidth, and, in some cases, increased object immunity.

In summary, this research has provided both theory and measurements that show the effectiveness of using multiple antennas to reduce multipath fading in backscatter-radio systems. The small-scale multipath fade reduction offered by multiple antennas will make backscatter-radio systems with increased range and communication reliability possible.

7.1 Summary of Original Work Completed

This research has made the following original contributions to the field of backscatter radio and to the wireless community in general:

- Synthesized a detailed description of the general, $M \times L \times N$backscatter channel.

- Provided two link budgets for backscatter-radio systems and a discussion of the propagation and high-frequency effects that influence backscatter-radio operation.
- Derived new, analytic envelope distributions for the $M \times L \times N$, dyadic backscatter channel with Rayleigh-fading forward and backscatter links.
- Demonstrated small-scale multipath fade reductions through pinhole diversity gains, by reducing link correlation, and using conventional diversity combining at the reader.
- Designed and prototyped the first 5.8 GHz backscatter testbed for backscatter-channel, multipath-fading measurements.
- Made the first multipath-fading measurements of the signal received from RF tags using multiple antennas and made the first backscatter fading measurements at 5.8 GHz.

7.2 Future Work

As with any research project, more questions have been raised and opportunities uncovered than could possibly be pursued in this dissertation. Therefore, the following topics will be left for future research:

- Fully functional RF-tag development – develop an RFIC that integrates the multi-antenna signaling techniques discussed in this dissertation and allows backscatter to be modulated with an arbitrary waveform.
- Frequency-selective fading – Explore frequency selective fading in the $M \times L \times N$, dyadic backscatter channel and see if any of the envelope distributions derived in this dissertation could be applied.
- Backscatter Space-time Block Codes – Develop new or adapt existing space-time block codes for use in modulated-backscatter communication.
- TWDP Fading – Formalize the relationship between the $1 \times 2 \times 1$, LOS channel discussed in Section 3.3.4 and the two-wave with diffuse power (TWDP) fading distributions previously reported [65].

- Multi-tag Experiments – Use the 5.8 GHz backscatter testbed to measure how the presence of multiple RF tags affects multipath fading on the signal backscattered from one of the RF tags.

- Ultra-wideband Modulated Backscatter – Investigate the use of ultra-wideband for short-distance, high data rate, modulated-backscatter communication.

- Sensor Development – Use the multi-antenna techniques outlined in this work to develop passive, long-range, reliable backscatter sensors.

7.3 Publications and Presentations

Much of the research presented in this dissertation has been published in, presented at, or submitted to refereed journals and conferences. The papers listed below are all related to the research in this dissertation and include work from the author's MS degree:

7.3.1 Refereed Publications in Major Technical Journals

1) J. D. Griffin, G. D. Durgin, A. Haldi, B. Kippelen, "RF tag Antenna Performance on Various Materials Using Radio Link Budget," *IEEE Antennas and Propagation Letters*, vol. 5, pp. 247-250, 2006.

2) J. D. Griffin, G. D. Durgin, "Link Envelope Correlation in the Backscatter Channel," *IEEE Communications Letters*, vol. 11, no. 9, pp. 735-737, September 2007.

3) J. D. Griffin, G. D. Durgin, "Gains For RF Tags Using Multiple Antennas," *IEEE Transactions on Antennas and Propagation*, vol. 56, no. 2, pp. 563-570, 2008.

4) J. D. Griffin and G. D. Durgin, "Complete Link Budgets for Backscatter Radio and RFID Systems," *IEEE Antennas and Propagation Magazine*, accepted for April, 2009.

7.3.2 Conference Papers and Presentations

1) J. D. Griffin, G. D. Durgin, A. Haldi, B. Kippelen, "Radio Link Budgets For 915 MHz RFID Antennas Placed on Various Objects," *Texas Wireless Symposium*, Austin, Texas, October 2005.

2) G. D. Durgin, J. D. Griffin, "Measurements and Link Budgets for 915 MHz RFID Antennas Placed on Various Objects," Book of Extended Abstracts, *International Workshop on Radio Frequency Identification (RFID) and Wireless Sensors*, November 2005.

3) J. T. Prothro, G. D. Durgin, J. D. Griffin, "The Effects of a Metal Ground Plane on RFID Tag Antennas," *IEEE Antennas and Propagation Symposium 2006*, Albuquerque, New Mexico, July, 2006.

4) J. D. Griffin, G. D. Durgin, A. Haldi, B. Kippelen, "How to Construct a Test Bed for RFID Antenna Measurements," *IEEE Antennas and Propagation Symposium 2006*, Albuquerque, New Mexico, July, 2006.

5) J. D. Griffin, G. D. Durgin, A. Haldi, B. Kippelen, "Gain Reduction for RF Tag Antennas Attached to Various Materials," a poster presentation at the *Materials and Devices for Information Technology Research (MDITR) Annual Retreat*, University of Washington, February, 2007.

6) J. D. Griffin, G. D. Durgin, "Reduced Fading for RFID Tags with Multiple Antennas," *IEEE Antennas and Propagation Symposium 2007*, Honolulu, Hawaii, June, 2007.

7) J. D. Griffin, G. D. Durgin, "Reduced Link Correlation Using Multiple Antennas," in *Proceedings of the First International EURASIP Workshop on RFID Technology*, Vienna, Austria, September 2007.

8) J. D. Griffin and G. D. Durgin, "Understanding Backscatter Radio Propagation through New Radio Link Budgets," a presentation at the *2009 USNC/URSI National Radio Science Meeting*, Boulder, CO, January 2009.

9) J. D. Griffin and G. D. Durgin, "Multipath Fading Measurements for Multi-Antenna Backscatter RFID at 5.8 GHz," in *Proceedings of the 2009 International IEEE Conference on RFID*, Orlando, FL, accepted.

10) M. S. Trotter, J. D. Griffin, and G. D. Durgin, "Power Optimized Waveforms for Improving the Range and Reliability of RFID Systems," in *Proceedings of the 2009 International IEEE Conference on RFID*, Orlando, FL, accepted.

APPENDIX A

IMPORTANT SMALL-SCALE FADING DISTRIBUTIONS

To benefit from the material presented in this dissertation, a firm understanding of several probability density functions (PDF) is necessary. This appendix provides definitions and parameters for the Rician, Rayleigh, and product-Rayleigh PDFs based on work by Simon [73].

A.1 The Rician Distribution

The Rician distribution [74] is one of the most important fading distributions used in channel analysis. It is often used to analyze the fading that occurs on the envelope of the signal received through a transmitter-to-receiver channel whose propagation can be described by the sum of a strong, specular wave and many diffuse, multipath waves. Such a scenario often occurs when a LOS exists between the transmitter and receiver. The diffuse, multipath waves can be modeled as a zero-mean, complex-Gaussian random variable and the presence of the unfading specular wave simply adds a nonzero mean. Therefore, the Rician random variable $\mathbf{A}$ is equal to the envelope of a complex-Gaussian random variable with nonzero mean.

$$\mathbf{A} = ||\mathbf{Z}|| = ||\mathbf{X} + j\mathbf{Y}|| \tag{45}$$

where $\mathbf{X} \sim \mathcal{N}(\mu_x, \sigma^2/2)$, $\mathbf{Y} \sim \mathcal{N}(\mu_y, \sigma^2/2)$, σ^2 is the variance of $\mathbf{A}$, $\mu_{x,y}$ are the means of and $\mathbf{X}$ and $\mathbf{Y}$, $\mu_x = \mu_y \neq 0$. In this appendix, $\mathcal{N}(\mu, \sigma^2)$ denotes a normal distribution with mean μ and variance σ^2. A derivation of the distribution is given by [17] on page 126, and the result is presented below. From [73], the PDF of a Rician random variable is

$$f_{\mathbf{A}}(\alpha) = \frac{2\alpha}{\sigma^2} \exp\left(-\frac{\alpha^2 + a^2}{\sigma^2}\right) \mathrm{I}_0\left(\frac{2\alpha a}{\sigma^2}\right), \quad \alpha \geq 0 \tag{46}$$

where $a = \sqrt{\mu_x^2 + \mu_y^2}$ and $\mathrm{I}_0(\cdot)$ is a modified Bessel function of the first kind. The average power of the distribution is

$$\mathrm{P}_{\mathrm{av}} = \sigma^2\left(1 + \frac{a^2}{\sigma^2}\right) \tag{47}$$

It is common to define K, the Rician K factor, as ratio of the non-fading specular power and the diffuse, multipath power. Using this definition, average power can be written

$$\mathrm{P}_{\mathrm{av}} = \sigma^2(1 + K) \tag{48}$$

The cumulative density function (CDF) of a Rician random variable is

$$F_{\mathbf{A}}(\alpha) = 1 - Q\left(\frac{\sqrt{2}a}{\sigma}, \frac{\sqrt{2}\alpha}{\sigma}\right), \quad \alpha \geq 0 \tag{49}$$

where $Q(\cdot, \cdot)$ is the first order Marcum Q-function [73] defined as

$$Q(\delta, \beta) = \int_{\beta}^{\infty} x \exp\left(-\frac{x^2 + \delta^2}{2}\right)\mathrm{I}_0\Big(\delta x\Big) \tag{50}$$

In words, the Marcum Q-function is the integral of the Rician PDF from β to ∞ and gives the probability that the Rician random variable is greater than β.

A.2 The Rayleigh Distribution

The Rayleigh distribution [75] is simply a special case of the Rician distribution in which no specular wave is present. In mathematical terms, a Rayleigh random variable is equal to the envelope of a zero-mean, complex-Gaussian random variable.

$$\mathbf{A} = ||\mathbf{Z}|| = ||\mathbf{X} + j\mathbf{Y}|| \tag{51}$$

where $\mathbf{X} \sim \mathcal{N}(0, \sigma^2/2)$ and $\mathbf{Y} \sim \mathcal{N}(0, \sigma^2/2)$. Hence, the Rician specular term $a^2 = 0$ and (46) reduces to the the PDF of a Rayleigh random variable

$$f_{\mathbf{A}}(\alpha) = \frac{2\alpha}{\sigma^2}\exp\left(-\frac{\alpha^2}{\sigma^2}\right), \quad \alpha \geq 0 \tag{52}$$

A derivation of the Rayleigh distribution is given by [17] on pages 116 - 118. The average power of this distribution is

$$\mathrm{P}_{\mathrm{av}} = \sigma^2 \tag{53}$$

The CDF of a Rayleigh random variable is [73]

$$f_{\mathbf{A}}(\alpha) = 1 - \exp\left(-\frac{\alpha^2}{\sigma^2}\right), \quad \alpha \geq 0 \tag{54}$$

A.3 The Product-Rayleigh Distribution

The product-Rayleigh distribution is the distribution resulting from the multiplication of two random variables with Rayleigh distributions. Therefore, for this distribution, $\mathbf{A}$ is the envelope of the product of two complex-Gaussian random variables.

$$\mathbf{A} = ||\mathbf{BC}|| = ||(\mathbf{X} + j\mathbf{Y})(\mathbf{W} + j\mathbf{V})|| \tag{55}$$

where $\mathbf{X}, \mathbf{Y} \sim \mathcal{N}(0, \sigma_A^2/2)$ and $\mathbf{W}, \mathbf{V} \sim \mathcal{N}(0, \sigma_B^2/2)$. The PDF of $\mathbf{A}$ is given by Simon[1] [73] as

$$f_{\mathbf{A}}(\alpha, \rho) = \frac{4\alpha\left(1 - |\rho|^2\right)}{\sigma_A^2\sigma_B^2\left(1-\rho^2\right)^2} \mathrm{I}_0\left(\frac{2\alpha|\rho|}{\sigma_A\sigma_B\left(1-\rho^2\right)}\right) \mathrm{K}_0\left(\frac{2\alpha}{\sigma_A\sigma_B\left(1-\rho^2\right)}\right) \tag{56}$$

for $\alpha \geq 0$. In (56), I_0 is a zero-order, modified bessel function of the first kind and K_0 is a zero-order, modified bessel function of the second kind. The correlation between $\mathbf{B}$ and $\mathbf{C}$ is indicated by ρ, the normalized correlation coefficient, and is defined as

$$\begin{aligned} \rho &= \frac{\mathrm{Cov}(\mathbf{X}, \mathbf{W})}{\sqrt{\mathrm{Cov}(\mathbf{X}, \mathbf{X})\mathrm{Cov}(\mathbf{W}, \mathbf{W})}} = \frac{2\,\mathrm{Cov}(\mathbf{X}, \mathbf{W})}{\sigma_A\sigma_B} \\ &= \frac{\mathrm{Cov}(\mathbf{Y}, \mathbf{V})}{\sqrt{\mathrm{Cov}(\mathbf{Y}, \mathbf{Y})\mathrm{Cov}(\mathbf{V}, \mathbf{V})}} = \frac{2\,\mathrm{Cov}(\mathbf{Y}, \mathbf{V})}{\sigma_A\sigma_B} \end{aligned} \tag{57}$$

where $-1 \leq \rho \leq 1$ and $\mathrm{Cov}(\cdot\,, \cdot)$ is the covariance operator. It is assumed that

$$\frac{\mathrm{Cov}(\mathbf{X}, \mathbf{Y})}{\sqrt{\mathrm{Cov}(\mathbf{X}, \mathbf{X})\mathrm{Cov}(\mathbf{Y}, \mathbf{Y})}} = \frac{\mathrm{Cov}(\mathbf{W}, \mathbf{V})}{\sqrt{\mathrm{Cov}(\mathbf{W}, \mathbf{W})\mathrm{Cov}(\mathbf{V}, \mathbf{V})}} = 0 \tag{58}$$

In other words, the real parts of $\mathbf{B}$ and $\mathbf{C}$ have correlation ρ; likewise, the imaginary parts of $\mathbf{B}$ and $\mathbf{C}$ have correlation ρ. The correlation between the real and imaginary parts of $\mathbf{B}$ and $\mathbf{C}$ is zero. Since $\mathbf{B}$ and $\mathbf{C}$ are complex-Gaussian random variables, it is implied that the real and imaginary parts of $\mathbf{B}$ and $\mathbf{C}$ are independent.

[1] Equation (56) differs from that given by Simon [73] in that it has been normalized to satisfy $\int_0^\infty f_{\mathbf{A}}(\alpha, \rho) d\alpha = 1$

A.4 The Product-Rician PDF

The PDF of the product of two independent Rician random variables is [73]

$$f_{\mathbf{A}}(\alpha) = \frac{4}{\sigma_f^2\sigma_b^2}\exp[-K_b - K_f] \times \sum_{i=0}^{\infty}\sum_{l=0}^{\infty}\frac{1}{(i!)^2(l!)^2}\left(\frac{K_b}{\sigma_b^2}\right)^i\left(\frac{K_f}{\sigma_f^2}\right)^l\left(\frac{\sigma_b}{\sigma_f}\right)^{i-l} \times \alpha^{i+l+1}\mathrm{K}_{(i-l)}\left(\frac{2\alpha}{\sigma_b\sigma_f}\right) \quad (59)$$

where $\mathbf{A}$ is the random channel envelope; α is the index of the distribution; K_f and K_b are the Rician K factors of the forward and backscatter links, respectively; σ_f^2 and σ_b^2 are the variances of the forward and backscatter links, respectively; and $\mathrm{K}_\nu(\cdot)$ is a modified bessel function of the second kind with order ν. The power of the product of two independent Rician random variables is

$$\mathbf{E}\{\mathbf{A}^2\} = \sigma_b^2\sigma_f^2\exp[-(K_b+K_f)]{}_1\mathrm{F}_1(2;1;K_b){}_1\mathrm{F}_1(2;1;K_b) \quad (60)$$

$$= \sigma_b^2\sigma_f^2(1+K_b)(1+K_f) \quad (61)$$

where ${}_1\mathrm{F}_1(a;b;z)$ is a confluent, hypergeometric function of the first kind [76]. The average power received at the n^{th} reader-receiver antenna through the $M \times L \times N$ backscatter channel is

$$\mathbf{E}\{\mathbf{A}^2\} = ML\sigma_b^2\sigma_f^2(1+K_b)(1+K_f) \quad (62)$$

APPENDIX B

THE $M \times L \times N$ BACKSCATTER-CHANNEL PDF DERIVATION

This appendix presents the derivation of the distribution of the signal received at the n^{th} reader-receiver antenna through the Rayleigh-fading, $M \times L \times N$, dyadic backscatter channel. As discussed previously, the signal received at the n^{th} reader-receiver antenna is proportional to the sum of L, i.i.d., complex-Gaussian products. Therefore, the envelope of the signal is

$$\mathbf{A} = |\tilde{\mathrm{h}}^{b}| \times |\tilde{\mathrm{h}}^{f}| \tag{63}$$

where $\tilde{\mathrm{h}}^{b}$ and $\tilde{\mathrm{h}}^{f}$ are correlated, zero-mean, complex-Gaussian random variables with variances σ_b^2 and $M\sigma_f^2$, respectively. The PDF of the sum of L, i.i.d. random variables can be found from the product of their characteristic functions (CF). Therefore, this derivation proceeds by finding the CF of (56), raising it to the L^{th} power, and transforming the resulting CF back into a PDF.

The CF of (56) is found using the Hankel transform [17]:

$$\Phi(\nu) = \int_0^\infty f_{\mathbf{A}}(\alpha)\mathrm{J}_0(\nu\alpha)d\alpha \tag{64}$$

Substituting (56) into (64), solving, and then raising the result to the L^{th} power yields:

$$\Phi(\nu;\rho) = \left[\frac{\sigma_b^4\sigma_f^4M^2}{16}\frac{\left(1-\rho^2\right)^4}{\left(1-|\rho|^2\right)^2} \times \left(\nu^2 + \frac{4\left(|\rho|-1\right)^2}{\sigma_b^2\sigma_f^2M\left(1-\rho^2\right)^2}\right) \times \left(\nu^2 + \frac{4\left(|\rho|+1\right)^2}{\sigma_b^2\sigma_f^2M\left(1-\rho^2\right)^2}\right)\right]^{-L/2} \tag{65}$$

Equation (65) is the CF of the general, $M \times L \times N$, dyadic backscatter channel with link correlation ρ. The PDF of (65) is found using the inverse Hankel transform [17]:

$$f_{\mathbf{A}}(\alpha) = \alpha\int_0^\infty \Phi(\nu)\mathrm{J}_0(\nu\alpha)\nu d\nu \tag{66}$$

However, this integral is difficult to solve analytically. Therefore, two special cases will be considered: the case where $\tilde{\mathrm{h}}^b$ and $\tilde{\mathrm{h}}^f$ are independent ($\rho = 0$) and the case where $\tilde{\mathrm{h}}^b$ and $\tilde{\mathrm{h}}^f$ are completely correlated ($\rho = 1$).

B.1 Independent Channels ($\rho = 0$)

In (65), if ρ approaches zero in the limit, the following CF results:

$$\Phi(\nu) = \left(\frac{4}{\nu^2\sigma_b^2\sigma_f^2 M + 4}\right)^L \tag{67}$$

Applying the inverse Hankel transform to (67) yields the PDF of the $M \times L \times N$, dyadic backscatter channel with independent forward and backscatter links.

$$f_{\mathbf{A}}(\alpha, 0) = \alpha^L \left(\frac{2}{\sqrt{M}\sigma_b\sigma_f}\right)^{1+L} \frac{2^{1-L}}{\Gamma(L)} \mathrm{K}_{(1-L)}\left(\frac{2\alpha}{\sqrt{M}\sigma_b\sigma_f}\right) \tag{68}$$

The mean and variance of (68) were found by direct application of their definitions.

$$\mathbf{E}\{\mathbf{A}\} = \frac{\sqrt{M}\sigma_b\sigma_f}{\Gamma(L)} \Gamma\Big(\frac{3}{2}\Big)\Gamma\Big(L + \frac{1}{2}\Big) \tag{69}$$

The variance of $\mathbf{A}$ is given by $\mathrm{Cov}(\mathbf{A}, \mathbf{A}) = \mathbf{E}\{\mathbf{A}^2\} - \mathbf{E}\{\mathbf{A}\}^2$ where $\mathrm{Cov}(\cdot, \cdot)$ is the covariance operator. Solving for the variance requires the power (or second moment) of the distribution to be known. The second moment is

$$\mathbf{E}\{\mathbf{A}^2\} = ML\sigma_b^2\sigma_f^2 \tag{70}$$

Hence, the variance of $\mathbf{A}$ is:

$$\mathrm{Cov}(\mathbf{A}, \mathbf{A}) = ML\sigma_b^2\sigma_f^2 \left(1 - \frac{\Gamma^2\Big(\frac{3}{2}\Big)\Gamma^2\Big(L + \frac{1}{2}\Big)}{L\Gamma^2(L)}\right) \tag{71}$$

The mean and variance reduce to:

$$\mu_{\mathbf{A}} = \frac{\sqrt{M}\sigma_b\sigma_f}{2} \frac{\pi(2L)!}{4^L L!(L-1)!} \tag{72}$$

and

$$\sigma_{\mathbf{A}}^2 = ML\sigma_b^2\sigma_f^2 \left(1 - \frac{L}{4}\left[\frac{\pi(2L)!}{4^L(L!)^2}\right]^2\right). \tag{73}$$

It can be shown that (68) integrates to 1.

B.2 Dependent Channels ($\rho = 1$)

In (65), as ρ approaches one in the limit, the following CF results:

$$\Phi(\nu) = \left(\frac{1}{\nu^2 \sigma_b^2 \sigma_f^2 M + 1} \right)^{L/2} \tag{74}$$

The PDF is found using the inverse Hankel transform. Solving using the same method as for (68), the PDF for the $1 \times L \times 1$, dyadic backscatter channel with fully-correlated forward and backscatter links is:

$$f_{\mathbf{A}}(\alpha, \rho = 1) = \alpha^{L/2} \left(\frac{1}{\sigma_b \sigma_f \sqrt{M}} \right)^{1+L/2} \frac{2^{1-L/2}}{\Gamma\left(\frac{L}{2}\right)} \mathrm{K}_{(1-L/2)} \left(\frac{\alpha}{\sigma_b \sigma_f \sqrt{M}} \right) \tag{75}$$

Again, the mean and variance of (75) can be solved by direct application of their definitions. For reference, the power of the PDF is

$$\mathbf{E}\{\mathbf{A}^2\} = 2ML\sigma_b^2\sigma_f^2. \tag{76}$$

The mean and variance are, respectively:

$$\mathbf{E}\{\mathbf{A}\} = \frac{2\sqrt{M}\sigma_b\sigma_f}{\Gamma\left(\frac{L}{2}\right)} \Gamma\left(\frac{3}{2}\right) \Gamma\left(\frac{L}{2} + \frac{1}{2}\right) \tag{77}$$

$$\mathrm{Cov}(\mathbf{A}, \mathbf{A}) = 2ML\sigma_b^2\sigma_f^2 \left(1 - \frac{2\Gamma^2\left(\frac{3}{2}\right)\Gamma^2\left(\frac{L}{2} + \frac{1}{2}\right)}{L\Gamma^2\left(\frac{L}{2}\right)} \right) \tag{78}$$

The mean and variance reduce to:

$$\mu_{\mathbf{A}} = \sqrt{M}\sigma_b\sigma_f\Psi \tag{79}$$

where

$$\Psi = \begin{cases} \dfrac{\pi L!}{2^L (L/2-1)!(L/2)!} & \text{for even } L, \\ \dfrac{2^L \left[(L/2-1/2)!\right]^2}{2(L-1)!} & \text{for odd } L, \end{cases}$$

and

$$\sigma_{\mathbf{A}}^2 = 2ML\sigma_b^2\sigma_f^2 \left(1 - \frac{\Lambda}{2L}\right) \tag{80}$$

where

$$\Lambda = \begin{cases} \left[\dfrac{\pi L!}{2^L (L/2)!(L/2-1)!}\right]^2 & \text{for even } L, \\ \left[\dfrac{2^{L-1}\left[(L/2-1/2)!\right]^2}{(L-1)!}\right]^2 & \text{for odd } L. \end{cases}$$

It can be shown that (75) integrates to 1.

B.3 The Limit for Large L

According to the central limit theorem, as L approaches infinity in the limit, (68) and (75) will become Rayleigh distributions. The simplest way to show this is by taking the limit of the CF given by (65). To prevent the power of the distribution from becoming infinite as $L \to \infty$, the variance of (65) is normalized by L, as shown in (81).

$$\frac{\sigma_b^2 \sigma_f^2 M}{L} = \frac{\sigma^2}{L} \tag{81}$$

The limit then yields:

$$\begin{aligned} \lim_{L\to\infty} \Phi(\nu;\rho) &= \lim_{L\to\infty} \left[\frac{\sigma^4}{16L^2} \frac{\left(1-\rho^2\right)^4}{\left(1-|\rho|^2\right)^2} \left(\nu^2 + \frac{4L\left(|\rho|-1\right)^2}{\sigma^2\left(1-\rho^2\right)^2}\right)\left(\nu^2 + \frac{4L\left(|\rho|+1\right)^2}{\sigma^2\left(1-\rho^2\right)^2}\right)\right]^{-L/2} \\ &= \lim_{L\to\infty} \left[\left(\frac{\nu^2\sigma^2\left(1-\rho^2\right)^2}{4L\left(|\rho|-1\right)^2} + 1\right)\left(\frac{\nu^2\sigma^2\left(1-\rho^2\right)^2}{4L\left(|\rho|+1\right)^2} + 1\right)\right]^{-L/2} \\ &= \exp\left(-\frac{\nu^2\sigma^2\left(1-\rho^2\right)^2}{8\left(|\rho|-1\right)^2}\right) \exp\left(-\frac{\nu^2\sigma^2\left(1-\rho^2\right)^2}{8\left(|\rho|+1\right)^2}\right) \\ &= \exp\left(-\frac{\nu^2\sigma^2}{4}\left(|\rho|^2+1\right)\right) \end{aligned} \tag{82}$$

Applying the inverse Hankel transform to (82) and substituting $\sigma_b^2\sigma_f^2 M$ for σ^2 gives the corresponding PDF:

$$f_{\mathbf{A}}(\alpha) = \frac{2\alpha}{\sigma_b^2\sigma_f^2 M\left(|\rho|^2+1\right)} \exp\left(\frac{-\alpha^2}{\sigma_b^2\sigma_f^2 M\left(|\rho|^2+1\right)}\right) \tag{83}$$

Equation (83) is a Rayleigh PDF with the following mean and variance:

$$\mathbf{E}\{\mathbf{A}\} = \frac{1}{2}\sqrt{\pi\sigma_b^2\sigma_f^2 M\left(|\rho|^2+1\right)} \tag{84}$$

$$\mathrm{Cov}(\mathbf{A},\mathbf{A}) = \left(1-\frac{\pi}{4}\right)\sigma_b^2\sigma_f^2 M\left(|\rho|^2+1\right) \tag{85}$$

If L is allowed to approach ∞ in the limit of the mean and variance of (68) (described by (69) and (71), respectively), it can be shown that they are equal to (84) and (85) evaluated for $\rho = 0$, respectively. The same can be shown of the mean and variance of (75), described by (77) and (78), respectively.

B.4 A Note on Link Envelope Correlation

It should be noted that, while (65) holds for any value of M, L, or ρ, care must be taken in the choice of ρ so that the correlation matrix is positive semi-definite [52]. The ij^{th} entry of the correlation matrix $\mathbf{V}$ – the correlation matrix of $\tilde{\mathbf{H}}^f$ and $\tilde{\mathbf{H}}^b$ – is

$$V_{ij} = \frac{\text{Cov}(A_i, A_j)}{\sigma_i \sigma_j} \tag{86}$$

where A_k is the k^{th} element of

$$\vec{A} = [\tilde{\text{h}}^f_{11}, \tilde{\text{h}}^f_{21}, \cdots, \tilde{\text{h}}^f_{lm}, \tilde{\text{h}}^b_{11}, \tilde{\text{h}}^b_{21}, \cdots, \tilde{\text{h}}^b_{nl}]^{\text{T}}$$

(a column vector formed from the entries of the forward and backscatter-link matrices), σ_i is the standard deviation of the i^{th} element of $\vec{A}$, and $\text{Cov}(x, y)$ is the covariance between the scalars x and y. The positive semi-definite constraint places a limit on ρ that is a function of M; however, for the $1 \times L \times 1$ discussed in this dissertation, ρ may vary between zero and one ($0 \leq \rho \leq 1$) while satisfying this constraint.

APPENDIX C

TESTBED SETUP AND MEASUREMENT GUIDE

As described in Chapter 5, many pieces of test and measurement equipment and custom electronics were interfaced to create the backscatter testbed. This appendix gives details of the connections, calibration, and software commands required to operate the testbed.

C.1 Testbed Connections

The connections for the backscatter testbed presented in this dissertation are shown in Figure 53 and Figure 54 and the necessary DC power supply connections are shown in Figure 55. Photographs of the testbed and connections are shown in Figures 56 - 61.

It can be seen from both Figure 53 and Figure 54 that many components were used to condition the 80 MHz clock signal for the Exacq ADC boards. The low-pass filters removed harmonics output from the signal generator and added loss to keep the amplifier operating in its linear region. The bias tee was used to add a DC offset to the 80 MHz sinusoid. The DC offset was required for the Exacq ADC boards to correctly sense the clock signal; without it, the ADC would not consistently return signal samples.

In the bistatic testbed, receivers 1 and 2 were used because of their high sensitivity. In the monostatic testbed, however, reflections from the transmitter/receiver antenna that were received through the circulator (see Figure 54) tended to saturate these receivers. Instead, receiver 3 was used because of its ability to operate linearly with a larger input signal.

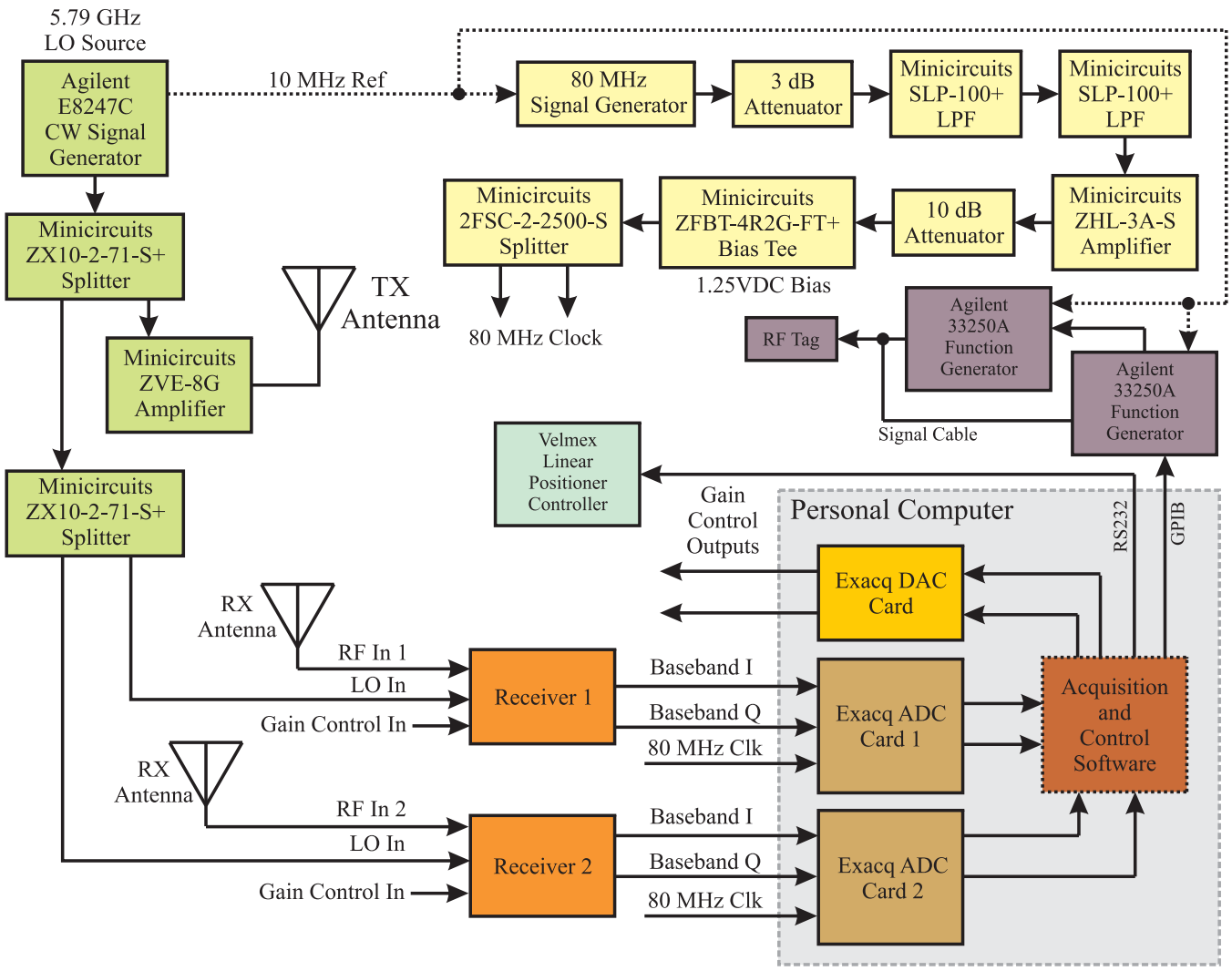

Figure 53: A detailed block diagram of the bistatic backscatter testbed used for the fading measurements reported in Chapter 6.

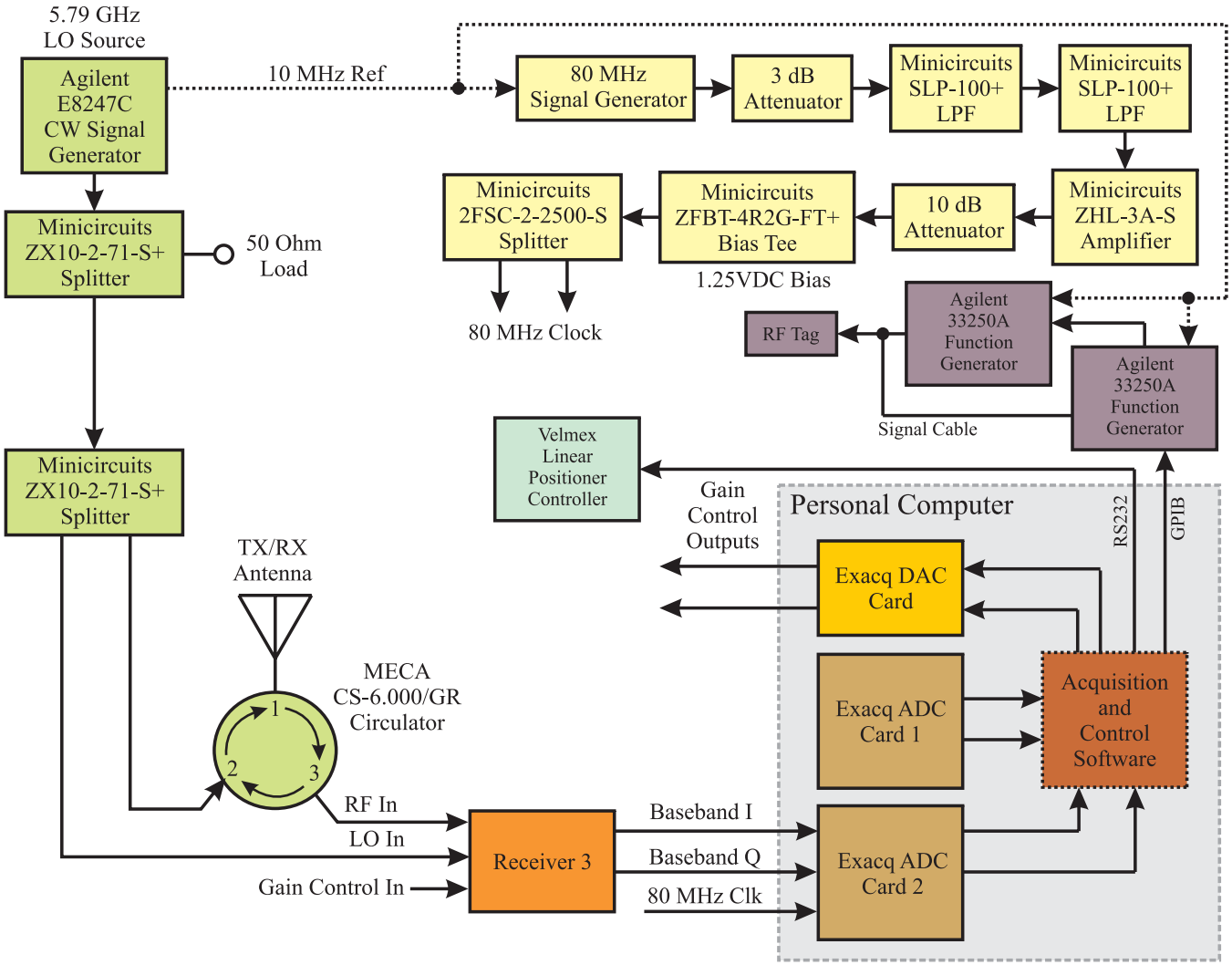

Figure 54: A detailed block diagram of the monostatic backscatter testbed used for the fading measurements reported in Chapter 6.

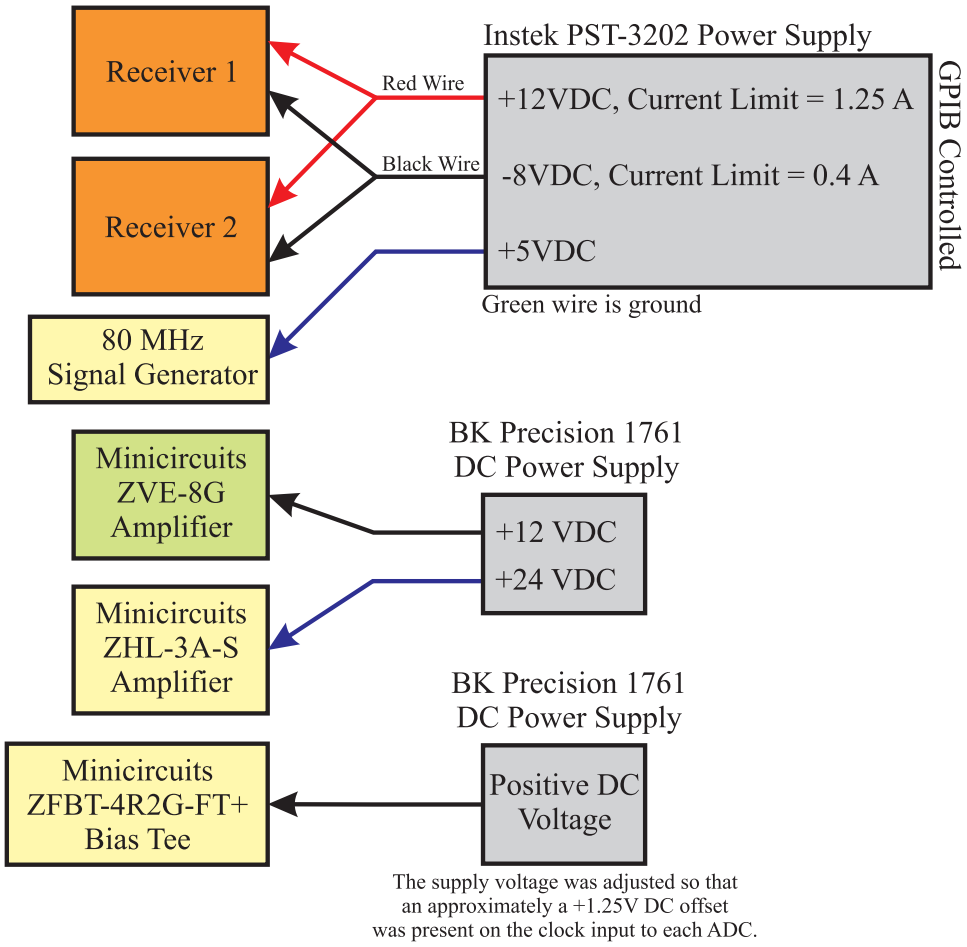

Figure 55: Block diagram of the power supply connections necessary for the backscatter testbed.

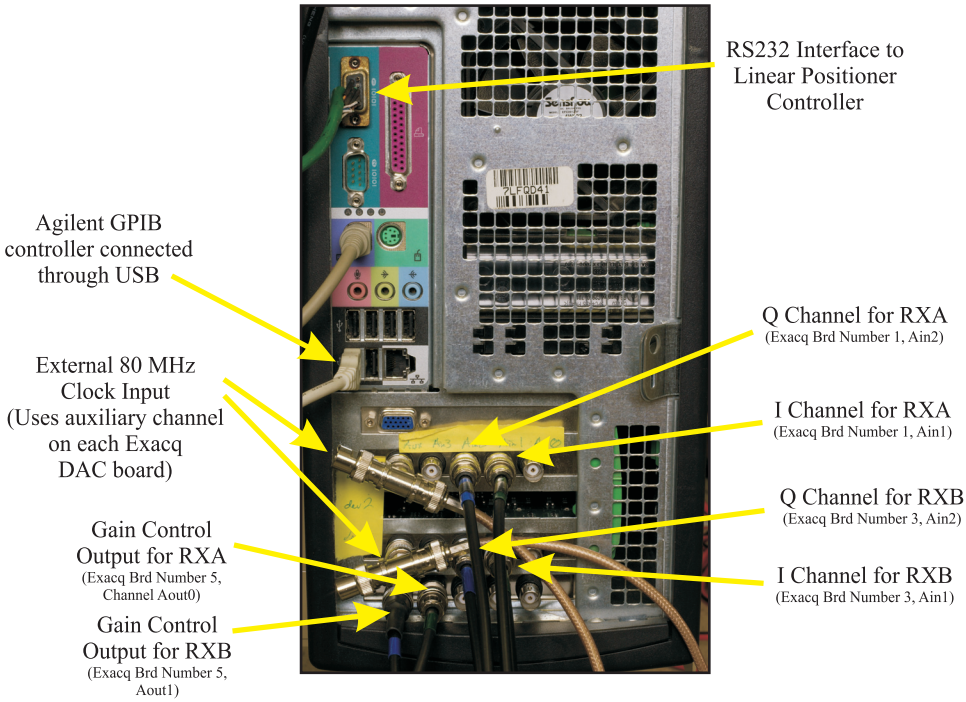

Figure 56: The back of the personal computer used to control the backscatter testbed. The RS232 cable used to control the linear positioner, the USB to GPIB controller, and the connections associated with the Exacq ADC and DAC boards are shown. In this figure, the ADCs associated with each receiver are label as they are represented in the software – RXA and RXB. See Appendix D for more information.

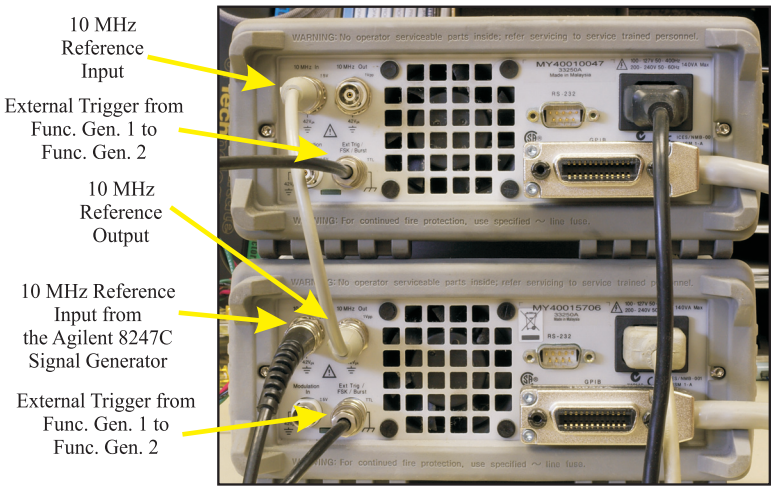

Figure 57: A photo showing the connections between the two Agilent 33250A function generators used to output the differential, pseudo-random bit sequence for the RF tags. The pseudo-random code was loaded into the memory of each function generator by the Matlab control software through the GPIB.

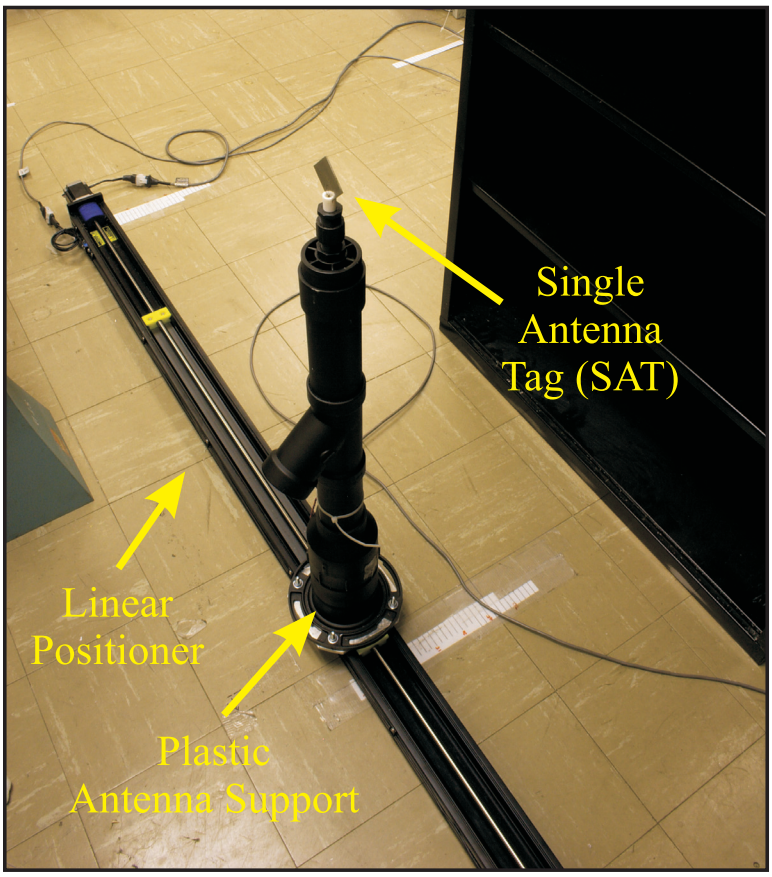

Figure 58: The Velmex linear positioner with the single-antenna RF tag attached to the RF-tag stand. The RF-tag stand is made from polyvinyl chloride (PVC) pipe sections.

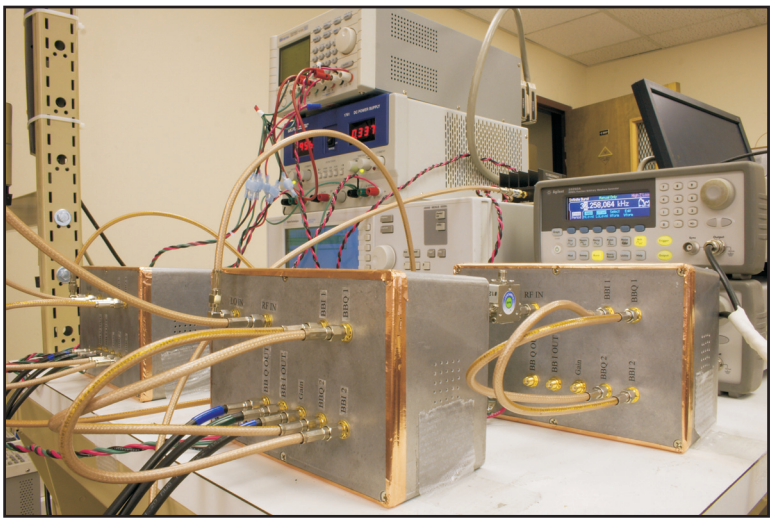

Figure 59: The receivers used in the backscatter testbed for multipath-fading measurements.

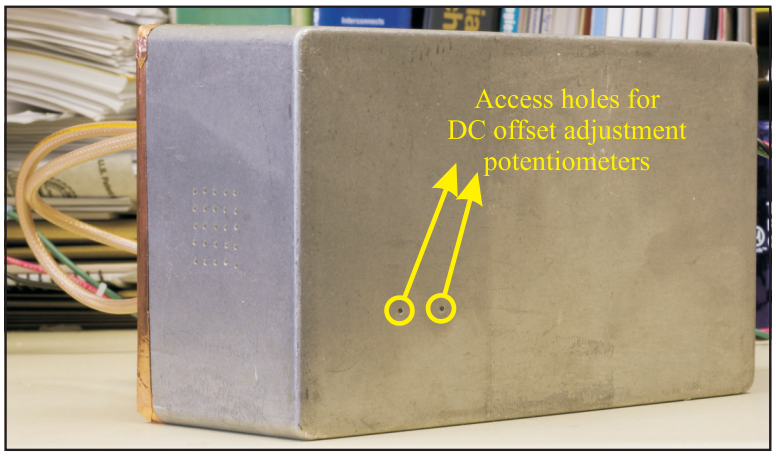

Figure 60: The back of a direct-conversion receiver showing the holes that provide access to the potentiometers used to null the DC offset of the I and Q channels.

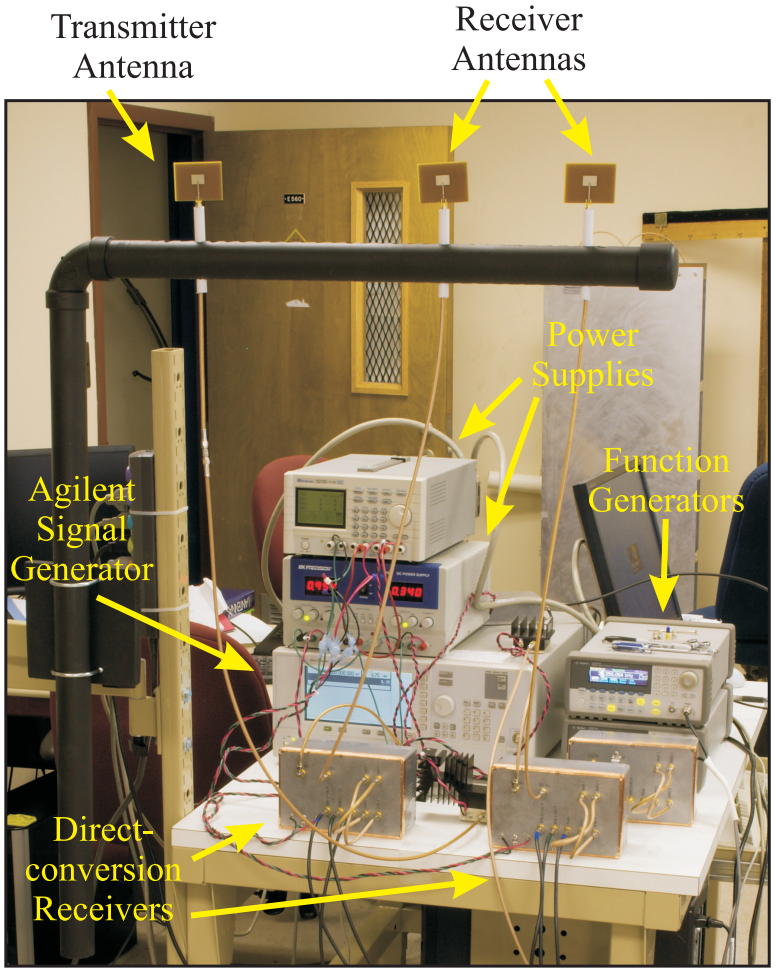

Figure 61: The bistatic backscatter testbed showing the transmitter antenna, two receiver antennas, the two direct-conversion receivers, the 5.79 GHz signal generator, and the power supplies. The transmitter and receiver antennas were held in place by a polyvinyl chloride (PVC) stand.

C.2 Testbed Calibration

Before each measurement set was made, the following calibration procedure was followed:

1. The system – including all signal sources and DC power supplies – was powered on and allowed to warm up for at least 10-20 minutes before any calibration adjustments or measurements.

2. The RF input of each receiver was terminated with a 50 Ω load and the gain of the receiver was set to its maximum value (0.28 VDC)[1]. The DC offset of the I and Q channels was then zeroed by adjusting two potentiometers with a small screwdriver through two holes (see Figure 60) in the back of each receiver. The DC was offset was adjusted so that it was within ±10mV of the ground reference.

3. The conducted power output to the transmitter antenna was measured with a spectrum analyzer. For the bistatic measurements, approximately 29 dBm was incident on the transmitter patch antenna while only approximately 3 dBm was transmitted in the monostatic setup. The monostatic transmitted power was limited by reflections from the transmitter/reciever antenna that could saturate the RF input of the receiver.

4. As an optional step, the power input into the LO ports of each receiver was measured. This power was approximately 2 dBm for each measurement.

5. After completing steps 1 - 4, the RF tag was placed on its stand and positioned, as described in Section 5.5, for the calibration measurement. With the RF tag in place, the power of the self-interference signal was measured at the receiver RF input port using a spectrum analyzer. If the self-interference power did not exceed the upper limit of the receiver given in Table 20 in Section E.5.2, then the calibration proceeded; otherwise the transmit power or the position of the antennas was adjusted. Note that the self-interference power depends heavily on the proximity of the

[1]This is the voltage that is specified in `ExacqPutData.exe` as described in Appendix D.4, not the actual voltage present at the receiver's gain input.

transmitter/receiver antennas to scatterers (including the user's body); therefore, it is important to measure the self-interference with the antennas in the positions used for fading measurements. If the DAT was being calibrated, a measurement was first taken to verify that each RF-tag antenna was backscattering a signal. To do this, one of the RF-tag slot antennas was covered with conductive copper tape and the backscattered signal from the other antenna was measured. Then, the tape was moved to the other antenna and the measurement repeated. The calibration measurement for the RF tag was taken using no time averaging.

C.3 Software Commands

The high level Matlab function used to control the testbed is `RunTestbed(teststructs,1)`. `Teststructs` is an m-file that contains all of the test parameters in an array of structs. The second argument of `RunTestbed()` is the array index specifying which struct is to be run. Usually, the size of the struct array is one and therefore, `k` = 1. Details of `testructs` and the other software used for this testbed is given in Appendix D.

APPENDIX D

SOFTWARE DESCRIPTION

This appendix briefly describes the software used for the measurement campaign presented in this dissertation. The goal of this section is to enable to the reader to take a measurement; hence, only the most important functions necessary for operating the testbed will be discussed.

D.1 Overview

Both C++ and Matlab programs were interfaced to collect data from the testbed. The Matlab function `RunTestbed()` is the top-level program called to operate the testbed. Via subfunctions, `RunTestbed` calls `ExacqGetDataAGCAVG.exe` which controls the Exacq ADC and DAC boards as well as the receiver gains for data collection. `ExacqGetDataAGCAVG.exe` outputs each collected data point into an ASCII file whose name is specified by the calling Matlab function. Each ASCII file contains time sampled data corresponding to a particular RF-tag position. All C++ development was done with Dev-C++ 4.9, a free development environment that uses Mingw – a compiler based on the GNU compiler collection (GCC). It is available for no cost at `http://www.bloodshed.net/devcpp.html`.

All of the software developed for the testbed is permanently archived on the Propagation Group's Subversion (SVN) server at `https://durgin-srv1.ece.gatech.edu/repos/RFID/trunk/Backscatter Radio/Code/BackscatterTestbed/Code`. It may be accessed through an SVN client such as Tortoise SVN which is available for download at `http://tortoisesvn.net/`. The header files and libraries for communicating with the Exacq DAC boards were provided by Exacq Technologies and are located in the same directory on the SVN server.

D.2 Matlab Function Description

This section provides a brief description of some of the Matlab functions required to operate the testbed. It is important to note that all of the software was designed to always operate two direct-conversion receivers (receiver box 1, 2, or 3). In the software, the two receivers are called RXA and RXB. Which physical receiver is assigned to RXA or RXB is determined in `teststrucs.m`.

D.2.1 Functions for Testbed Operation

teststrucs.m: This file contains an array of structs that specifies all of the information required to make a measurement. Each struct in the array corresponds to a different set of measurement parameters. Usually, only one struct is included in the array. The struct fields and typical values are as follows:

- `k = 1;` – Specifies the index of the struct in the array `s` of teststructs. The first index should always be set to 1. If additional structs are desired, then k can be set to k = k + 1.
- `s(k).ReceiverBoxes = [1 2];` – Specifies the number of the physical receiver to be used as RXA and RXB. Two and only two receivers must always be specified. They are always entered in the order [RXA RXB].
- `s(k).N = 5;` – This specifies the number of shift register bits used to generate the *m*-sequence that is output from the two function generators that modulate the backscattered signal.
- `s(k).ChipRate_Hz = 1e6;` – The chip rate (in Hz) or the rate at which new bits are output from the function generators to drive the RF tags.
- `s(k).PNPeriods = 40;` – The number of periods of the *m*-sequence to be collected during each ADC acquisition.
- `s(k).SampleRate_Hz = 20000000;` – The rate in Hz at which the Exacq ADC boards sample the I and Q outputs of the receivers.
- `s(k).SampleNum = (2^(s(k).N)-1)*1/(s(k).ChipRate_Hz)*s(k).PNPeriods* s(k).SampleRate_Hz;` – Calculates the number of samples to be collected. Because of memory limitations on the Exacq ADC boards, SampleNum cannot exceed 29952.
- `s(k).LOFreq_MHz = 5790;` – Specifies the frequency in MHz to be transmitted to the RF tag and used as the receiver LO.
- `s(k).LOPower_dBm = 9.75;` – The power in dBm to be output from the CW signal generator. This power was reduced to 2 dBm by splitters and attenuators before being input into the receivers.

- `s(k).PosSupply_V = 12;` – Specifies the positive DC voltage in volts output by the Instek PST-3202 power supply. This is the positive DC supply for the receivers.
- `s(k).PosCurrentLim_A = 1.25;` – Specifies the current limit in amps for the positive DC supply of the Instek PST-3202 power supply. This limits the current for the positive DC supply of the receivers.
- `s(k).NegSupply_V = 8;` – Specifies the negative DC voltage in volts output by the Instek PST-3202 power supply. This is the negative DC supply for the receivers.
- `s(k).NegCurrentLim_A = .4;` – Specifies the current limit in amps for the negative DC supply of the Instek PST-3202 power supply. This limits the current for the negative DC supply of the receivers.
- `s(k).TestFileName = 'ChannelData.dat';` – This is an obsolete entry in teststructs.m.
- `s(k).TestFileNameMat = 'ChannelData.mat';` – The name of the file to which processed, complex channel samples are stored.
- `s(k).AvgCnt = 16;` – The number of sample sets that are time-averaged.
- `s(k).PositionX_cm = 50:80;` – Specifies the points in centimeters on the X axis that are to be sampled.
- `s(k).PositionY_cm = 2:30;` – Specifies the points in centimeters on the Y axis that are to be sampled.
- `s(k).MotorNumber = 1;` – The number of the linear positioner motor. This is always set to 1.
- `s(k).UsePositioner = true;` – If set to true, then the linear positioner is initialized and used to move the RF tag. If set to false, then the positioner is not used and may be disconnected.
- `s(k).FuncGenAttached = true;` – If set to true, the function generators will be initialized through the GPIB; else, if set to false, the program does not communicate with the function generators and they can be disconnected from the GPIB cables. This is useful if the m-sequence has already been loaded into the function generators and they need to be moved a long distance from the testbed personal computer.
- `s(k).ProcessDataFlag = false;` – If set to true, data will be processed as each sample set is recorded; else, the data will simply be stored for later processing. Processing data as each sample set is recorded increases the test time significantly.
- `s(k).UseGainControl = true;` – If set to true, the gain control algorithm will be used when taking samples; otherwise, data samples will be recorded with gains that are specified manually. See Appendix D.4 for more information.
- `s(k).TXRXASpacing_cm = 34;` – The distance in centimeters between the transmit antenna and the RXA receiver antenna.
- `s(k).TXRXBSpacing_cm = 52;` – The distance in centimeters between the transmit antenna and the RXB receiver antenna.

- `s(k).TXPwratAntenna_dBm = 29.5;` – The power in dBm measured at the input of the transmitter antenna.
- `s(k).TXAntennaGain_dBi = 4.8;` – The transmitter antenna gain. This is recorded for reference and is not used anywhere in the code.
- `s(k).RXAntennaGain_dBi = 4.8;` – The receiver antenna gain. This is recorded for reference and is not used anywhere in the code.
- `s(k).RXASelfInputPower_dBm = -20.7;` – The self-interference power at the RF input port of RXA.
- `s(k).RXBSelfInputPower_dBm = -20.1;` – The self-interference power at the RF input port of RXB.
- `s(k).Notes = '';` – A variable to enter any pertinent notes.

RunTestbed(ssa,k): This is the master control function for the testbed. To make a measurement, call `RunTestbed(teststructs,1)` at the Matlab command prompt. The test will be run according to the parameters specified in teststructs.m. Since teststructs.m can contain an array of test structures, you must specify which element of the array you wish to execute. For all of the measurements reported in this dissertation, k = 1. This function always operates as though two receiver boxes were attached; in practice, one may be physically disconnected. In the software, the two receivers are designated RXA and RXB. The function proceeds as follows:

1. Prompts the user to enter a folder in which to store data. It is important to store each measurement in its own folder. Otherwise, the testbed software will overwrite the raw data files (the *.dat files). The program will also place a copy of `teststructs.m` in the folder so that it is clear to which measurement the *.dat files belong.

2. Creates two receiver objects, one for RXA and one for RXB. The receiver objects are used to pass, store, and process the data within the Matlab program.

3. Creates GPIB objects for communicating with the CW signal generator (the LO source), the Instek PST-3202 power supply, and the two Agilent 33250A function generators.

4. Places the linear positioner at its initial position – X = 1 cm. The Y position is moved manually by the user.

5. Prompts the user to move the linear positioner to its initial Y position.

6. The function then begins the data collection loop. With the positioner at its initial Y position, the linear positioner moves across the specified X range. At each X position, `RunTestbed.m` calls `GetDataAGCAVG()` to collect the raw data samples from the Exacq ADC boards.

7. After samples have been recorded at all of the X positions corresponding to a particular Y value, the user is prompted to move the linear positioner to the next Y position and the data collection loop repeats.

GetDataAGCAVG(tt,PosX,PosY,PathName,varargin): This function is called by the `RunTestbed()` function and, in turn, calls the `ExacqGetDataAGCAVG.exe` program to collect data samples from the Exacq ADC boards. Here, tt is the current measurement struct specified in teststructs.m, PosX and PosY are the current X and Y position of the RF tag in centimeters, PathName is the path to the folder where raw data measurements are stored, and varagin contains the receiver objects. `ExacqGetDataAGCAVG.exe` gathers data from the specified Exacq ADC boards and writes the raw ASCII data to the *.dat files in the folder specified by the user. If s(k).ProcessDataFlag = true, then `RunTestbed()` will read the ASCII data from the *.dat file and store the raw measurement data in the CurrentIdata or CurrentQdata fields of the RXA and RXB objects for later processing by the `ProcessData()` function. Otherwise, once `ExacqGetDataAGCAVG.exe` records the data in the *.dat file, control will return to `RunTestbed()`. If the UseGainControl flag is set in `teststructs.m`, then `ExacqGetDataAGCAVG.exe` automatically adjusts the gain of the each receiver; otherwise, samples are taken at the manually specified gain settings. See Section D.4 for information on how to manually set the receiver gain.

ProcessData(tt(k),RXA,RXB): If the ProcessDataFlag is set in `teststructs.m`, then this function is called from the `RunTestbed()` function. `ProcessData()` processes the raw

data samples stored in the CurrentIdata or CurrentQdata fields of the RXA and RXB objects, respectively, according to the method outlined in Section 5.4. The resulting complex channel samples are stored in the RXGainNormChannelCoef_V field of the RXA or RXB receiver objects. Here, tt is the current measurement struct specified in teststructs.m and RXA and RXB are the receiver objects.

D.2.2 Functions for Data Processing

Many Matlab functions were written to process and visualize the measured data. For the sake of brevity, only a few will be highlighted here.

The `ProcessFileData(k)` function is called to process raw data samples recorded by the backscatter testbed. `ProcessFileData(k)` prompts the user to select the folder containing the data files. The folder must contain a copy of teststructs.m to specify the measurement parameters associated with the data. The index of the struct array to be read from teststructs.m is a required argument and is usually set to k = 1. `ProcessFileData()` reads the raw data samples from the *.dat file contained in the specified folder and then calls `ProcessData()` to process the raw data (just as `RunTestbed(teststructs,1)` does if the ProcessDataFlag is set in `teststructs.m`). The processed channel samples are stored in the same folder with the file name specified by the TestFileNameMat field in `teststruct.m`.

Once the raw data samples have been processed, several functions can be called to estimate the measured fading distribution and to plot the measurements:

- `MakePDF(monoorbi,VarInterp,numbins)` – This function returns the PDF and CDF of the measured values normalized by the calibration measurements.
- `MakeMRCPDF(monoorbi,VarInterp,numbins)` – This function returns the PDF and CDF of the measured values normalized by the calibration measurements after MRC combining has been performed.
- `PlotSpatialPowerData(VarInterp)` – This function plots the power (in dBm) of each measured data point relative to the calibration measurement. The data points are plotted on an (x,y) grid and normalized to the maximum measured value.

- `PlotSpatialPhaseData(VarInterp)` – This function plots the phase (in degrees) of each measured data point relative to the calibration measurement. The data points are plotted on an (x,y) grid.

In each of the above functions, monoorbi is used to specify that the measurements were taken either with the monostatic testbed or with the bistatic testbed. VarInterp is used to specify the desired number of interpolated data points. If VarInterp is nonzero, an FFT based interpolation method is used; otherwise, no interpolation is performed. For all of the results presented in this dissertation, VarInterp was set to zero. The last argument, numbins, specifies the number of bins into which normalized data points are grouped during calculation of the data histogram.

In each of these functions, the processed data is first normalized by the calibration measurements by calling `CalData(MonoOrBi,VarInterp,PrompText)`. Therefore, by calling `MakePDF()`, `MakeMRCPDF()`, `PlotSpatialPowerData()`, or `PlotSpatialPhaseData()` the user will be prompted to locate both the processed data samples and calibration measurements. After the data is normalized to the calibration measurements, the user is prompted to specify the location of the noise floor and corresponding calibration measurements. The noise floor measurements are normalized to calibration data and any measured data points that are within 20 dB of the noise floor are discarded. More information is given in Section 5.6.

D.3 C++ Function Description

Two C++ programs were written for the backscatter testbed. The first, `ExacqPutData.exe`, allows the gains of the direct-conversion receivers to be set manually. Its use is described in Section D.4. The second and more important program is `ExacqGetDataAGCAVG.exe` which is called by the Matlab function `GetDataAGCAVG()` to sample and return measured data from the Exacq ADC boards. When called, `ExacqGetDataAGCAVG.exe` initializes the Exacq ADC boards, records samples of the I and Q baseband signals, and then outputs the samples to either the console screen or the specified ASCII file. `ExacqGetDataAGCAVG.exe` can return sampled data with or without automatic gain control (AGC). If the AGC flag

is set by the `-a` switch, `ExacqGetDataAGCAVG.exe` takes small sample sets and adjusts the gain of each receiver until they are operating in their linear gain region. The full number of samples, specified by the `-n` switch, are then recorded. The assumption is that the channel is static while the AGC loop adjusts the receiver gains and records the final samples. If time averaging is used, multiple sample sets are recorded; therefore, calling `ExacqGetDataAGCAVG.exe` with the following switches would result in a total of 8192 raw signal samples: `ExacqGetDataAGCAVG.exe -n 1024 -g 8`. The multiple sampled sets are recorded in sequential order in the *.dat file. A complete list of the command line switches for `ExacqGetDataAGCAVG.exe` are as follows:

-v – Specifies verbose mode. `ExacqGetDataAGCAVG.exe` will return its current status to the console.

-b – Specifies the ExacqDeviceNumber from which data is to be read. The device numbers can be changed from the Exacq Control Center. More than one board can be entered. For example, to read from Exacq boards 1 and 2, use '-b 1 2'

-c – Specifies the channels to be read. For the Exacq CH3160 ADC boards, valid channels are 0,1,2,3. Two channels must be specified for each receiver in the order [RXAI RXAQ RXBI RXBQ] where, for example, RXAI is the I channel of RXA. For example: -c 0 1 0 1 is a valid switch.

-n – The number of requested samples. The program will round this to the next largest multiple of 2048.

-r – The rate at which samples are to be taken in Hz. This is the same for all ADC boards specified.

-i – The input voltage range (in Volts) of the Exacq A/Ds. Valid ranges are: 0.050 V, 0.100 V, 0.200 V, 0.500 V, 1 V, 2 V, 5 V. Four values, one for each channel of each receiver must be specified. The order is: RXA0 RXA1 RXB0 RXB1 where RXA1 specifies channel 1 of RXA an so on. If using AGC, these values are ignored.

-e – External clock flag: If set, an external clock is used; otherwise the internal clock is used for data collection.

-f – File Output Flag: If set, data is written to the file specified by the following argument. Else, data is written to the console screen.

-t – Wait for 2.75 volt trigger on Ain0 before taking data. Note, when triggering, this channel is high impedance, DC coupled and cannot be used for analog input. This switch was not used in the testbed reported in this dissertation.

-x – Specifies which physical receiver is used. The first receiver listed is associated with the first specified Exacq Board and the second box with the second board.

-a – Use automatic gain control.

-d – Specifies the number of the Exacq DAC board (defaults to 5).

-z – Specifies the DAC channels used for gain control on the specified receiver boxes. The first channel is listed is used for the first specified receiver and the second channel for the second specified receiver.

-g – Specifies the number of time averages to be performed. If AGC is used, `ExacqGetDataAGCAVG.exe` takes several small sample sets to adjust the receiver gains and then repeatedly records the number of sample sets specified by the `-g` switch. The size of each sample set is determined by the `-n` switch.

-? – Lists a description of each input argument.

Default switches: -b 1 2 -c 1 2 1 2 -n 2048 -r 20000000 -i 5 5 5 5 -d 5 -z 0 1 -x 1 2 -g 1

D.4 Manual Gain Control

The gain of the receiver was controlled by the Exacq DAC board connected through a PCI interface in the personal computer. A C++ program was written to allow manual control of the gain by calling `ExacqPutData.exe` at the MSDOS command prompt. For example, the following command can be issued from the command line to set the gain to its maximum value: `C:\<current directory>\exacqputdata.exe -d5 -o0 0.28`. This command is useful for adjusting the receiver's DC offset. For this command, `<current directory>` is the directory in which the executable file is located; `-d5` specifies the internal address of the Exacq DAC board (this was always set to 5 for the measurements reported in this dissertation, but can be changed using the Exacq Control Center software provided with the Exacq boards); `-o` specifies the channel, 0 or 1, on which the voltage will be output; and the last number, `0.28` is the voltage (in volts) to be output. The Exacq DAC board expects a 50 Ω load, but the receivers provide a high impedance load. Therefore, the voltage set by the Exacq DAC board must be set to half the desired value. Since the maximum linear gain voltage for the receivers is 0.55 V (see Appendix E.5.2), 0.28 V was output to set the receiver to its maximum linear gain.

APPENDIX E

DIRECT-CONVERSION RECEIVER DESIGN AND OPERATION

This appendix gives the design rationale and details of the direct-conversion receivers used in the backscatter testbed described in Chapter 5.

E.1 Receiver Requirements

As outlined in Section 5.3.3, the major motivations for designing and prototyping custom receivers were the desire to mitigate large self-interference signals and provide coherent reception. Furthermore, to maximize the utility of the backscatter testbed, it was desired that the receivers operate over the entire 5725-5850 MHz ISM frequency band with high sensitivity for long-range tag measurements.

With these goals in mind, a direct-conversion receiver was designed and prototyped. The receiver was implemented on two, four-layer FR4 printed circuit boards (PCB) – a high-frequency RF front-end board shown in Figure 63 and a low frequency baseband amplification board shown in Figure 64. The boards were mounted in a metal box and sealed with copper tape, shown in Figure 31. The cost of a single direct-conversion receiver was approximately \$400 – \$340 for parts and \$66 for the custom printed circuit board (PCB). The custom PCBs were manufactured by Advanced Circuits, `http://www.4pcb.com`.

E.2 Receiver Design Rationale

Before the architecture of the receiver was chosen, a method for mitigating self-interference was selected. Two options were considered. The first approach, known as active carrier cancelation, reduces the self-interference signal while amplifying the desired modulated-backscatter signal before the signal is down-converted [69, 70]. In this approach, a copy of the received signal is subtracted from the original signal to reduce the amplitude of the self-interference signal. This method is effective when the desired modulated-backscatter

signal is so small that directly attenuating the received signal would bury the modulated-backscatter signal in the receiver's noise floor. A second approach is to directly convert the self-interference signal to a zero intermediate frequency (IF) and block or adaptively cancel it from the baseband signal. Filtering the DC signal with a blocking capacitor is by far the simplest method to remove the self-interference; however, a very large capacitor is required so that the cut-off frequency of the high-pass filter (formed by the series capacitor) is below the first spectral component of the desired signal. One drawback to this approach is that large capacitors are slow to respond to time-varying DC offsets [77]. Even so, this method – directly converting the self-interference signal to zero IF and filtering with a DC blocking capacitor – was chosen in order to minimize receiver complexity.

The chosen self-interference blocking technique can be used with either a heterodyne or homodyne receiver architecture. In a heterodyne receiver, the RF signal is mixed to a non-zero IF, amplified, filtered, and then mixed to baseband. In a homodyne – or *direct-conversion* – receiver, the RF signal is mixed directly to baseband where it is then filtered and amplified. In either receiver architecture, the self-interference cannot be removed until the RF signal has been converted to a zero IF; therefore, any amplification before the baseband stage will amplify both the desired modulated-backscatter signal and the undesired self-interference. A direct-conversion receiver has the advantage that most of the amplification occurs at the baseband stage after the self-interference signal has been removed. This prevents self-interference from saturating the baseband amplifiers and requires fewer components than a heterodyne receiver. Therefore, the direct-conversion architecture was chosen.

The direct-conversion architecture, however, is not without its difficulties. B. Razavi [77] has outlined the following challenges of the direct-conversion architecture:

E.2.1 DC Offsets

In a direct-conversion receiver, a portion of the LO signal will leak back to the input of the mixer where it mixes with itself causing a DC offset at the baseband stage. While this is a significant problem for many direct-conversion receiver applications, in this design, the

self-interference DC blocking capacitor will remove any DC offsets caused by self-mixing.

E.2.2 I/Q Mismatch

In any I/Q receiver, whether direct-conversion or heterodyne, the amplitude and phase of the I and Q channels will not match exactly. This problem is largely due to imperfectly matched hardware. Therefore, the I/Q mismatch of each receiver was carefully characterized and, as shown in Section E.5.1, the resulting errors were found to be tolerable.

E.2.3 Even Order Distortion

Unlike superheterodyne receivers, direct-conversion receivers are susceptible to second-order intermodulation products. However, since the testbed was to be used in a fairly controlled environment, it was not expected that second-order intermodulation products would cause problems. If they did, the testbed could be moved to a location with fewer interferers.

E.2.4 Flicker Noise

Flicker noise is inversely proportional to frequency and dominates other sources of noise at low frequencies. Avoiding this type of noise is one of the benefits of directly sampling an IF (i.e., not converting the signals to a zero IF); however, if the self-interference is to be converted to a DC voltage and blocked, flicker noise will be present. The effect of flicker noise can be reduced by using a modulation whose spectrum is not close to DC. For example, the first non-zero spectral component of an m-sequence is given by the ratio of the chip-rate f_c over the length of the m-sequence L [72]. Therefore, through careful choice of f_c and L, the spectrum of the m-sequence can be moved away from DC.

E.2.5 LO Leakage

It was already noted that LO leakage will result in a baseband DC offset caused by self-mixing, but the LO leakage can also find its way to the LNA input and radiate from the receiving antenna. Though greatly attenuated, this signal can act as interference to other nearby receivers. In this high-frequency backscatter testbed, the radiated LO leakage signal will not interfere with other backscatter receivers, but will be received as additional self-interference and will not affect the channel measurements. Measurements of LO leakage

from the receiver's RF input are presented in Appendix E.5.3.

E.3 Direct-conversion Receiver Overview

Figure 62 shows a simplified block diagram of the direct-conversion receiver designed for the backscatter testbed. The RF input is bandpass filtered, passed through a low-noise amplifier (LNA), and then mixed with the externally provided LO signal to shift the spectrum to baseband. The signal is then low-pass filtered to remove the LO leakage and harmonics (not shown), passed through a DC blocking capacitor to remove the self-interference signal, amplified by a baseband variable gain amplification stage, and then passed through a low-pass, anti-aliasing filter. A more detailed block diagram of the receiver is provided in Figure 63 and Figure 64. The direct-conversion receiver was prototyped on two boards – the RF front-end board and the baseband amplification board. Photos of these boards are given in Figures 65 - 66.

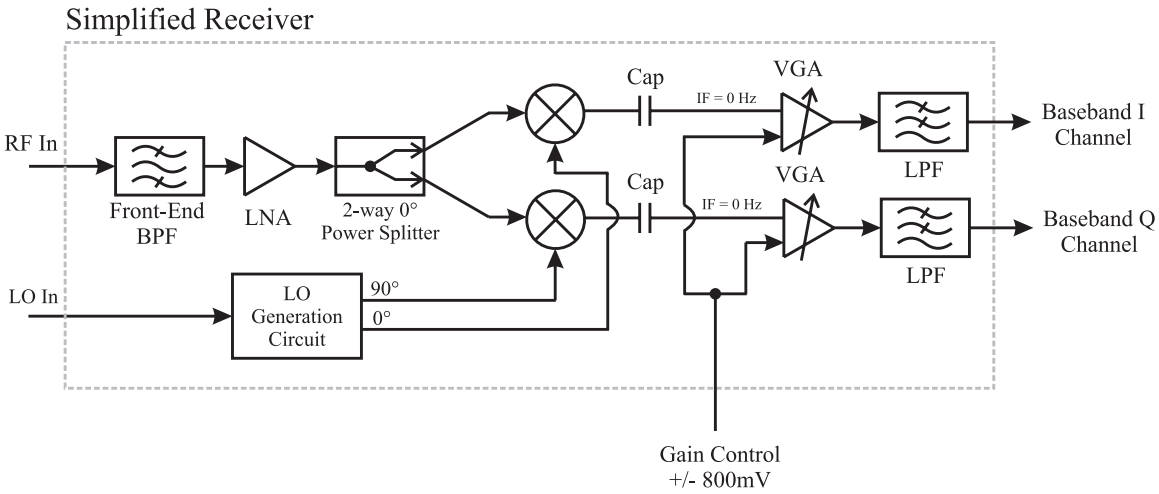

Figure 62: A simplified block diagram of the direct-conversion receiver. The maximum input range of the gain control voltage was ±800mV, though testing showed that the maximum linear gain voltage range was less, as shown in Table 20 of Appendix E.5.2.

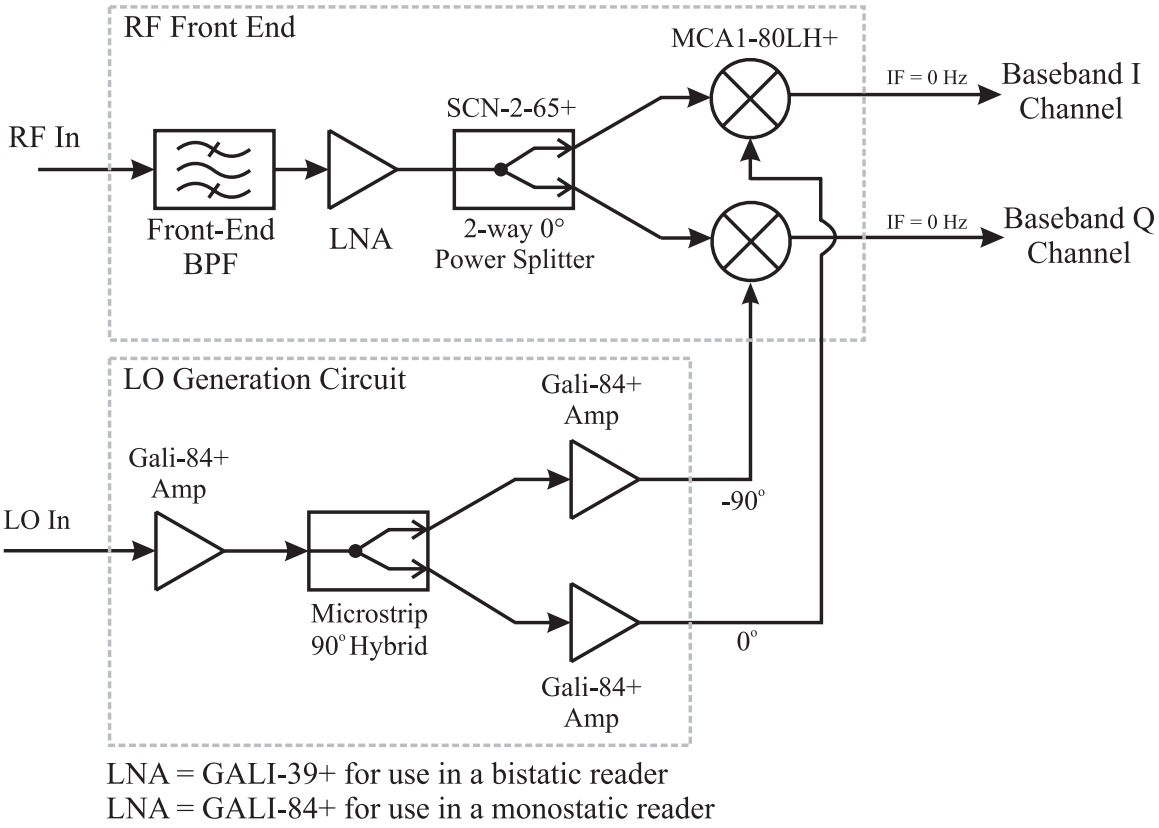

Figure 63: The RF front-end board of the direct-conversion receiver.

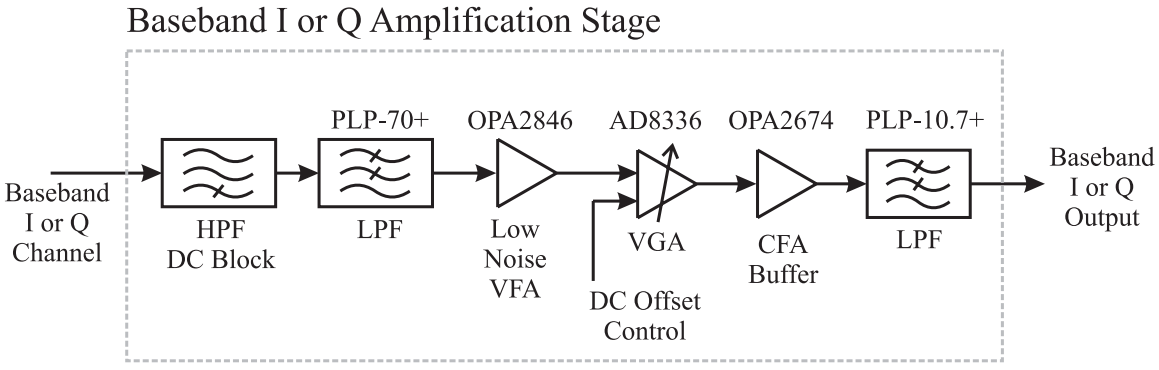

Figure 64: The baseband I or Q amplification stage of the direct-conversion receiver.

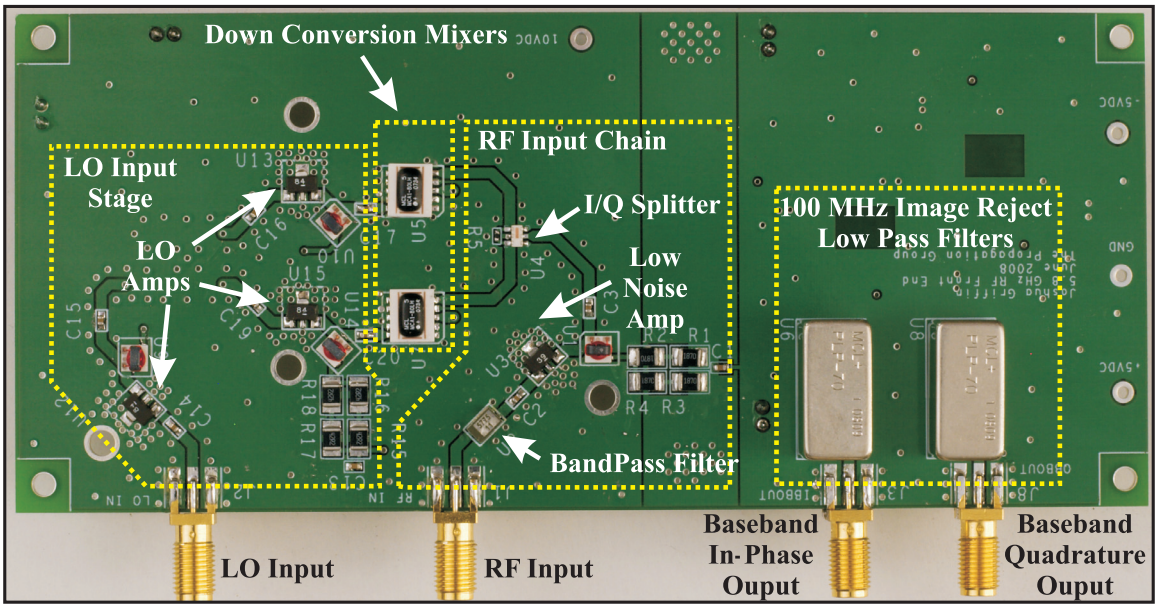

(a)

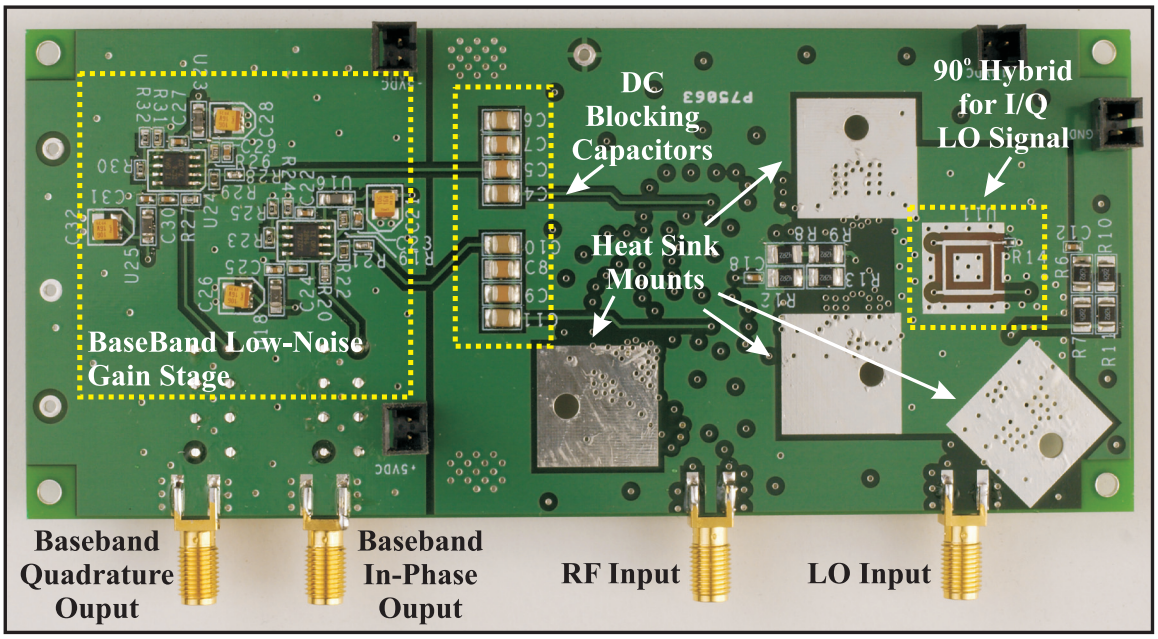

(b)

Figure 65: Photos of the (a) top and (b) bottom of the RF front-end receiver board.

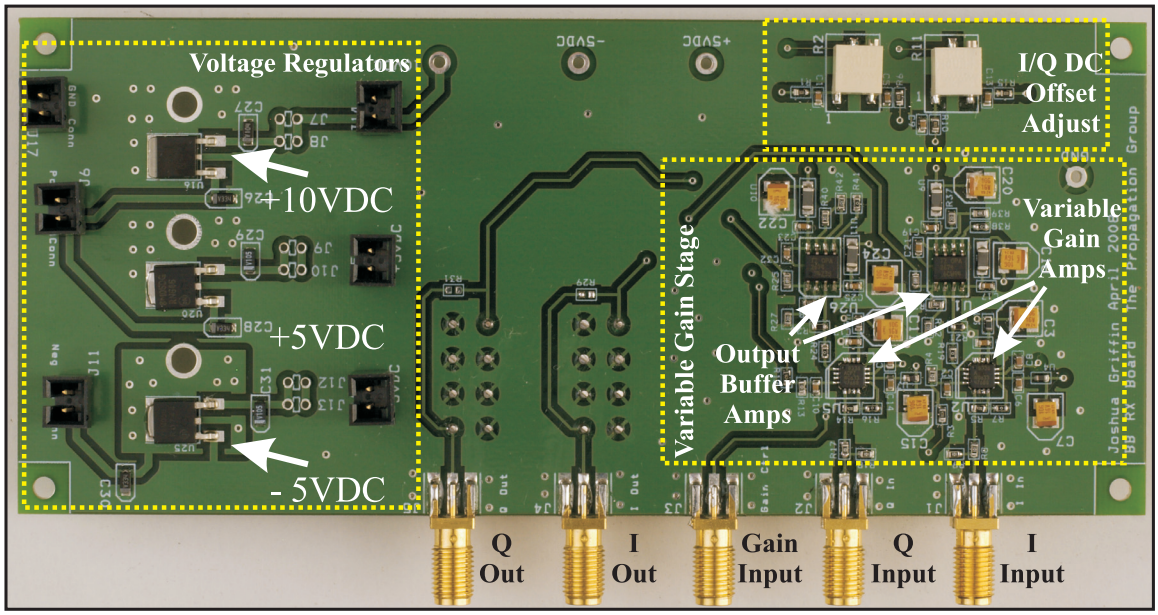

(a)

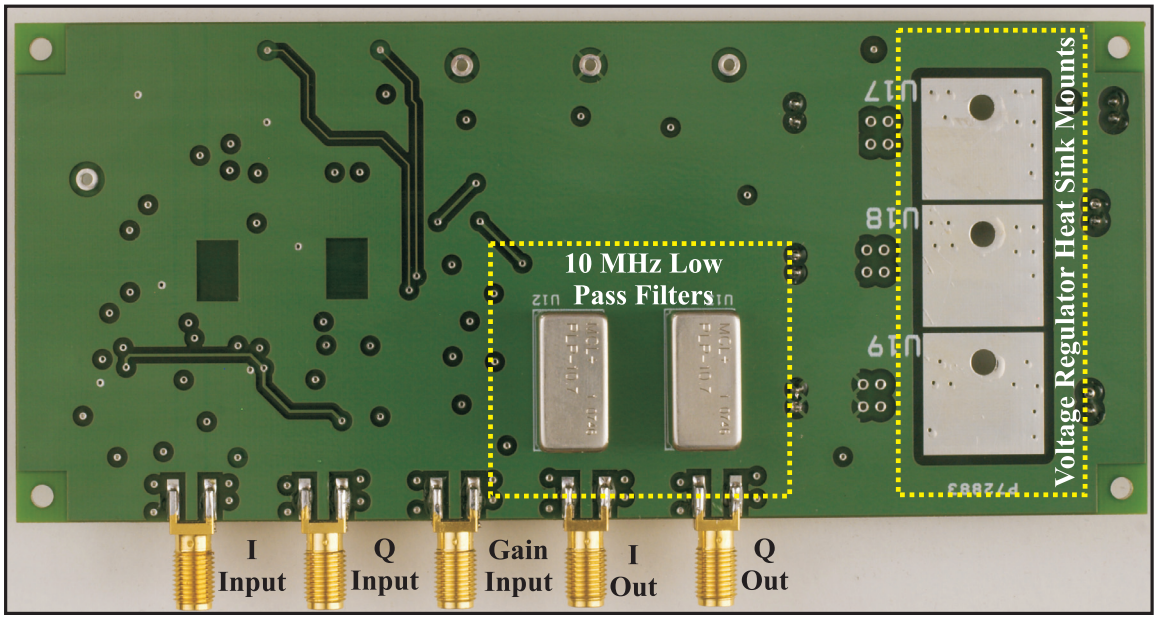

(b)

Figure 66: Photos of the (a) top and (b) bottom of the baseband amplification board.

E.3.1 Components

A brief description of each of the major receiver components is provided in the following paragraphs. A complete list of all of the components used on the RF front-end and baseband-amplification boards are provided in Tables 17 - 19.

Front-End Filter: The front-end, bandpass filter is the TOKO TDFM2A dielectric filter. It spans the 5.8 GHz ISM band with a bandwidth of 150 MHz centered at 5775 MHz.

Low Noise Amplifier: Two configurations of the direct-conversion receiver are possible. The first configuration is intended for use in the bistatic testbed and uses the Minicircuits GALI-39+ as the LNA. This amplifier provides a low noise figure, high gain, and good isolation in a surface mount package. For the monostatic testbed receiver, the GALI-84+ is used as the LNA. It is has a higher noise figure than the GALI-39+, but can handle more input power – its 1 dB compression point is approximately 5-6 dB higher than the GALI-39+.

High-Frequency Mixer: The Minicircuits MCA1-80LH+ is was chosen to down-convert the received RF signals because of its high 1 dB compression point, good LO-RF isolation, and good RF and IF port voltage standing-wave ratios (VSWR). The mixer requires a 10 dBm LO signal.

Baseband DC Block Filter: Four parallel capacitors provide 188 μF to block baseband DC signals. This high capacitance was chosen to provide a low cut-off frequency for the high pass filter formed by the series capacitor.

Baseband Filter: 125 MHz of passband bandwidth is available in the 5725-5850 MHz ISM frequency band. This translates to 62.5 MHz of baseband bandwidth. The Minicircuits PLP-70+ 70 MHz, low-pass filter is used to filter out the high-frequency LO signal that leaks through the mixer and to reject power received in the FM broadcast bands from 88 - 108 MHz.

Baseband-Amplification Stage: Three amplifiers are used in the baseband-amplification stage. The first, Texas Instrument's OPA2846, is a low-noise, voltage-feedback operational amplifier (VFA) set to provide an inverting voltage gain of 50 (in the linear scale). To minimize the noise figure of the receiver, it is important for the first stage of baseband amplification to have a small noise figure and high gain since there is quite a bit of loss in the RF down-conversion stage. This amplifier is located on the RF front-end board. The second amplifier, located on the baseband amplification board, is the AD8336 variable gain, VFA from Analog Devices. A DC current is injected into the non-inverting input of the amplifier to provide DC offset adjustment. The DC offset on both the I and Q channels can be adjusted with two 10-turn potentiometers. The final amplifier is the Texas Instruments OPA2674. It is a current-feedback operational amplifier (CFA) configured as a non-inverting, unity gain buffer to drive a 50Ω load. The overall linear gain of each receiver is presented in Appendix E.5.2.

Anti-Aliasing Filter: The final component of the baseband amplifier board is a Mini-circuits PLP-10.7+ 10 MHz low-pass filter. This filter was chosen to minimize aliasing at the 20 MHz sampling rate used by the Exacq ADC boards to sample the baseband I and Q outputs.

LO Generation Circuit: This circuit amplified, split, and phase-shifted the LO signal for mixing with the received RF signal. A detailed block diagram of the LO generation circuit is shown in Figure 63. To operate properly, a 5.79 GHz, 2 dBm signal is injected into the LO connector of the receiver. The signal is amplified by a Minicircuits GALI-84+ amplifier and then split and phase-shifted using a 90^o hybrid microstrip circuit. The 90^o hybrid was design using the theory provided by Pozar [62] and optimized using Ansoft HFSS, a 3D electromagnetic and microwave software package. The 90^o hybrid was optimized for 5.79 GHz operation and, since it is a narrowband device, its performance will degrade as the LO frequency is shifted.

Table 17: List of components for the RF front-end board.

Quantity	Part Reference	Value	Part Number	Cost
Parts Purchased from Digikey at http://www.digikey.com				
12	*C1,C12,C13,C18 C22,C23,C24,C25 C27,C29,C30,C31*	0.1μF	399-1281-1-ND	\$0.12
4	*C21,C26,C28,C32*	10μF	495-2238-1-ND	\$0.45
8	*C4,C5,C6,C7 C8,C9,C10,C11*	47μF	490-3888-1-ND	\$2.76
4	*J4,J5,J6,J7*	Power Pins	WM4800-ND	\$0.92
1	*R5*	100Ω	P100LCT-ND	\$0.10
2	*R19,R26*	91Ω	RR08Q91DCT-ND	\$0.14
4	*R20,R21,R27,R28*	50Ω	RR08Q49.9DCT-ND	\$0.14
2	*R22,R29*	1kΩ	RHM1.00KHCT-ND	\$0.08
1	*R14*	50Ω	P49.9LCT-ND	\$0.10
6	*R23,R24,R25 R30,R31,R32*	0Ω	P0.0GCT-ND	\$0.07
12	*R6,R7,R8,R9 R10,R11,R12,R13 R15,R16,R17,R18*	42.2Ω	541-42.2AACT-ND	\$0.29
4	*R1,R2,R3,R4*	91Ω	P91ACT-ND (or 541-42.2AACT-ND for GALI-84+)	\$0.08
4	*U16,U18,U23,U25*	Ferrite Choke	240-2401-1-ND	\$0.09
2	*U17,U24*	OPA2846 Op Amp	296-16853-5-ND	\$6.40
4	*U19,U20,U21,U22*	Testpoint	50XXK-ND	\$0.32

Continued on next page

Table 17 – continued from previous page

Quantity	Part Reference	Value	Part Number	Cost
4		HeatSink	345-1041-ND	$0.49
Parts Purchased from Mini-Circuits at http://www.minicircuits.com				
1	*U3*	LNA	GALI-39+ (or GALI-84+)	$2.40
1	*U4*	2-way, 0° Power Splitter	SCN-2-65+	$2.50
2	*U5,U7*	10 dB LO Mixer	MCA1-80LH+	$14.95
2	*U6,U8*	70 MHz LPF	PLP-70+	$13.70
3	*U12,U13,U15*	High Power Amp	GALI-84+	$4.00
4	*U1,U9,U10,U14*	RF Choke	TCCH-80+	$3.45
Parts Purchased from Richardson Electronics at http://www.rell.com				
1	*U2*	Front-End BPF	TDFM2A-5775V-11	$5.00
Parts Purchased from Lighthorse Technologies, Inc. at http://www.rfconnector.com				
4	*J1,J2,J3,J8*	SMA Connector	LTI-SASF55MGT	$4.89
Parts Purchased from Mouser at http://www.mouser.com				
7	*C2,C3,C14,C15 C16,C17,C19,C20*	DC Block	766-C06BL851X5ZNX0T	$2.59

Table 18: List of components for the baseband board

Quantity	Part Reference	Value	Part Number	Cost
Parts Purchased from Digikey at http://www.digikey.com				

Continued on next page

Table 18 – continued from previous page

Quantity	Part Reference	Value	Part Number	Cost
16	*C1,C2,C4,C5 C6,C9,C10,C12 C13,C14,C17 C19,C21,C23,C25 C32*	0.1μF	399-1281-1-ND	\$0.12
8	*C3,C7,C11,C15 C18,C20,C22,C24*	10μF	495-2238-1-ND	\$0.45
2	*C8,C16*	1nF	PCC1952CT-ND	\$0.18
3	*C26,C28,C30*	0.33μF	493-2339-1-ND	\$0.18
1	*C27*	0.1μF	493-2336-1-ND	\$0.21
2	*C29,C31*	1μF	493-2396-1-ND	\$0.19
6	*J6,J11,J14,J15 J16,J17*	Power Pins	WM4800-ND	\$0.92
6	*J7,J8,J9,J10 J12,J13*	JUMPER	WM4000-ND	\$0.17
4	*R1,R6,R10,R15*	2kΩ	311-2.0KDCT-ND	\$0.17
2	*R2,R11*	10kΩ	3269P-1-103LF-ND	\$4.43
4	*R3,R5,R12,R14*	301Ω	311-301DCT-ND	\$0.14
6	*R4,R8,R9,R13 R17,R18*	100Ω	RR08P100DCT-ND	\$0.14
8	*R7,R16,R19,R29 R24,R31,R38,R41*	0Ω	P0.0GCT-ND	\$0.07
2	*R21,R26*	453Ω	P453HCT-ND	\$0.07
2	*R20,R25,*	50Ω	RR08Q49.9DCT-ND	\$0.14
8	*R22,R23,R27,R28*	300Ω	RR08P300DCT-ND	\$0.14

Continued on next page

Table 18 – continued from previous page

Quantity	Part Reference	Value	Part Number	Cost
	R37,R39,R40,R42			
2	*U1,U26*	OPA2674 Op Amp	296-15212-5-ND	$2.75
2	*U2,U5*	AD8336 Variable Gain Amp	AD8336ACPZ-R7CT-ND	$9.30
4	*U3,U4,U6,U7*	Ferrite Choke	490-1018-1-ND	$0.06
4	*U8,U9,U10,U11*	Ferrite Choke	240-2401-1-ND	$0.09
1	*U16*	10VDC Regulator	296-11140-1-ND	$0.78
3	*U17,U18,U19*	HeatSink	345-1041-ND	$0.49
1	*U20*	+5VDC Regulator	MC78M05ACDTRKGOSCT-ND	$0.77
1	*U25*	-5VDC Regulator	MC79M05CDTRKGOSCT-ND	$0.58
4	*U77,U78,U79,U80*	Testpoint	50XXK-ND	$0.32
Parts Purchased from Lighthorse Technologies, Inc. at http://www.rfconnector.com				
5	*J1,J2,J3,J4,J5*	End Launch SMA	LTI-SASF55MGT	$4.89
Parts Purchased from Mini-Circuits at http://www.minicircuits.com				
2	*U12,U13*	10.7 MHz LPF	PLP-10.7+	$13.70

Table 19: Miscellaneous components for the direct-conversion receiver.

Quantity	Part Reference	Value	Part Number	Cost
Parts Purchased from Mouser at http://www.mouser.com				
2	N/A	Feed Thru Filter	657-54F-785-005	$7.56
1	N/A	GND Connector	534-7313	$0.15
1	N/A	Aluminum Enclosure	546-1590E	$21.54
7	N/A	1/4 in. 4-40 Machine Screws	534-9400	$0.14
4	N/A	2 inch 4-40 standoffs	534-2207	$1.39
7	N/A	4-40 Hex nuts	534-9600	$0.05
7	N/A	#4 Washer	524-11-142C	$3.33 for 100
Parts Purchased from Digikey at http://www.digikey.com				
9	N/A	Power Connector	WM2900-ND	$0.44

E.4 Receiver Schematics

This section presents detailed electrical schematics of the RF front-end board and the baseband amplification board used in the direct-conversion receiver. Figures 67 - 71 show the schematic of the RF front-end board while Figures 72 - 76 display the schematic of the RF baseband amplification board. In each schematic, the reference numbers (e.g. C1, C2, etc.) correspond to those given in Tables 17 - 19. All of the schematics were developed using the Cadence Design Entry program which was used to output a netlist for the board layout. The board layout was begun using OrCAD Layout Plus, but because

of licensing issues, this program was replaced with Cadence PCB Editor. Therefore, the baseband amplification board layout was completed in OrCAD Layout Plus and the RF front-end board layout was done in Cadence PCB Editor. Cadence design files and Gerber files for each of the boards are archived on the Propagation Group's SVN server at `https://durgin-srv1.ece.gatech.edu/repos/RFID/trunk/Backscatter Radio/Hardware Design/Receiver Board/`.

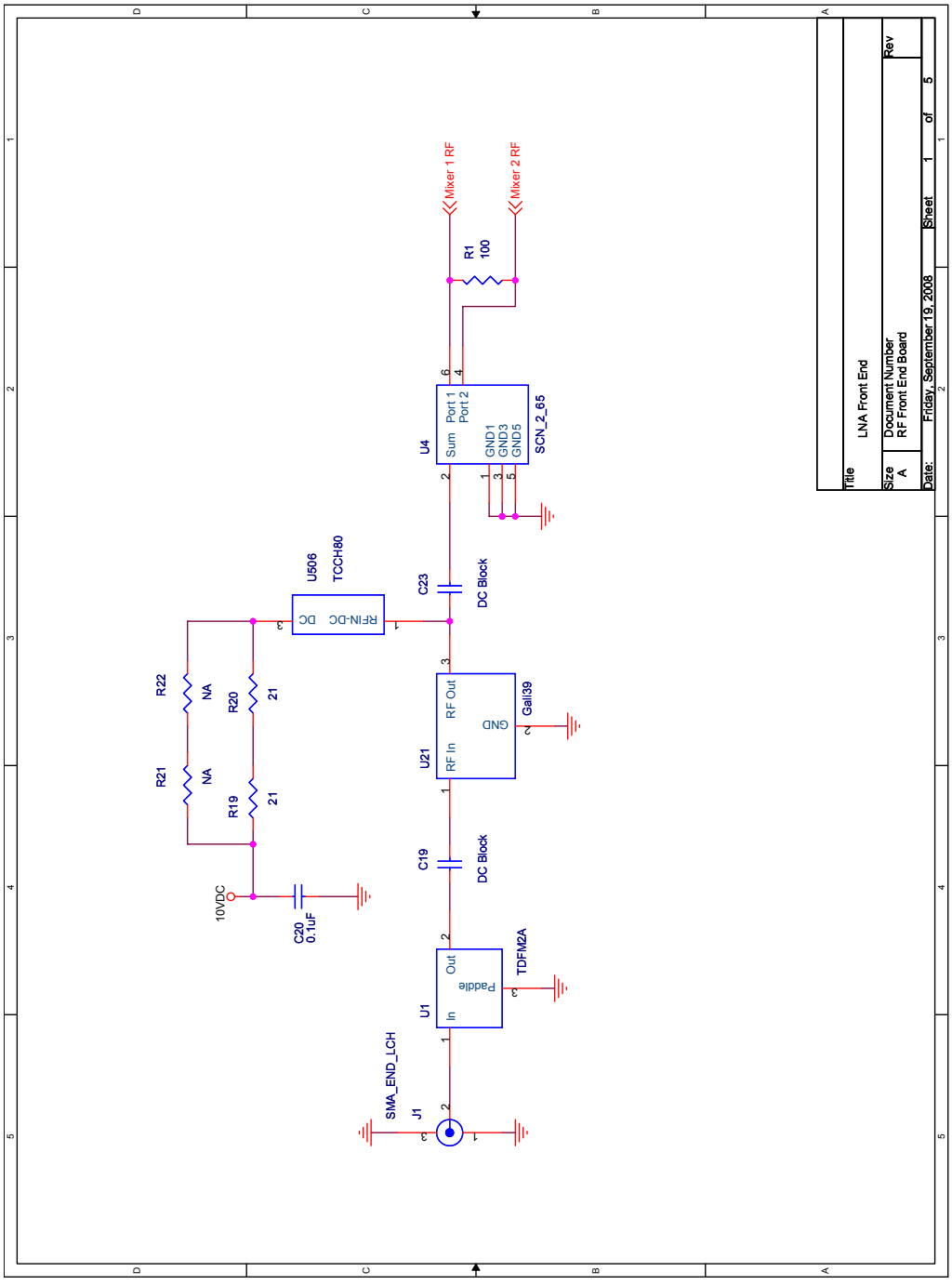

Figure 67: RF front-end board schematic: page 1.

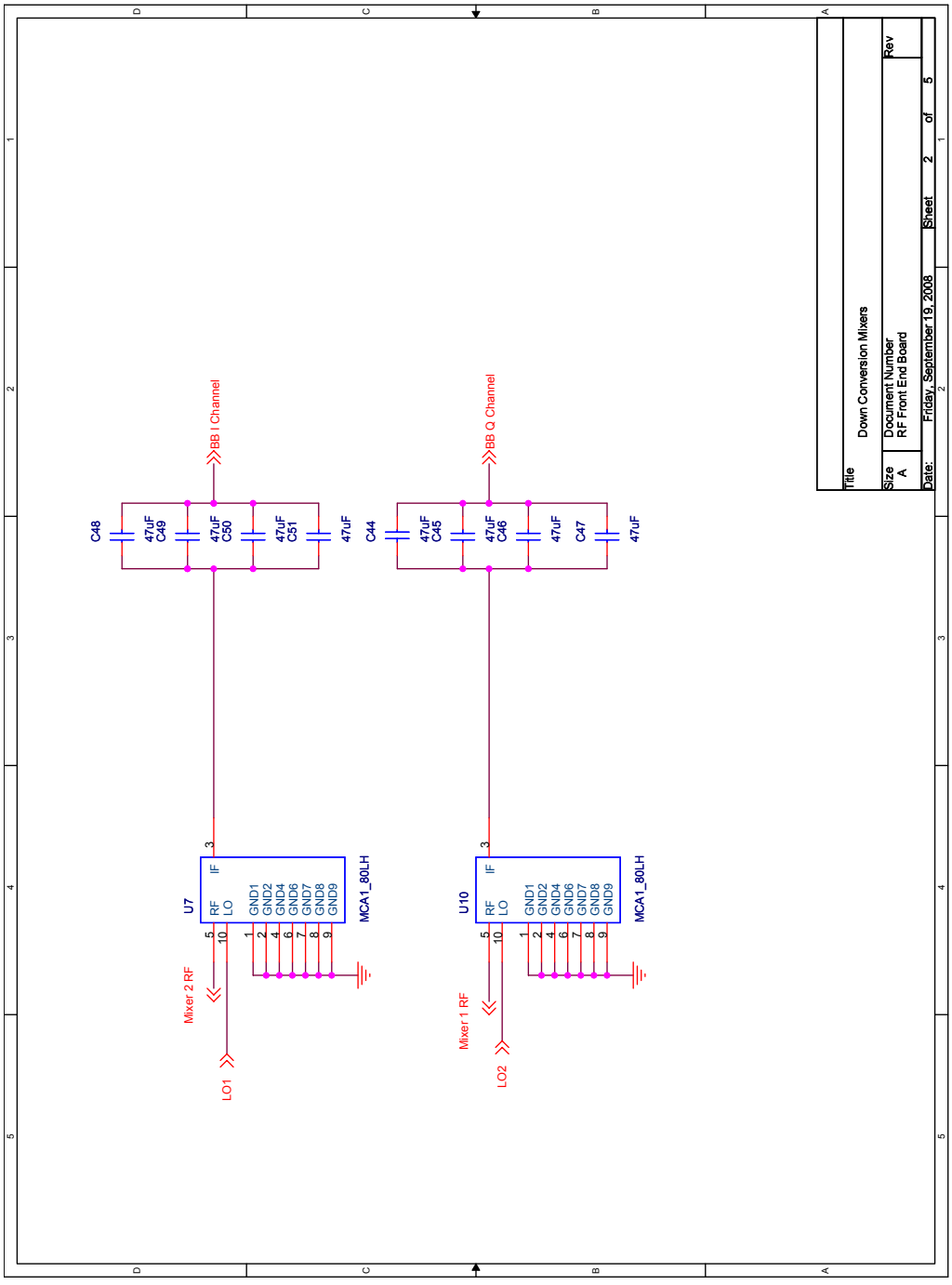

Figure 68: RF front-end board schematic: page 2.

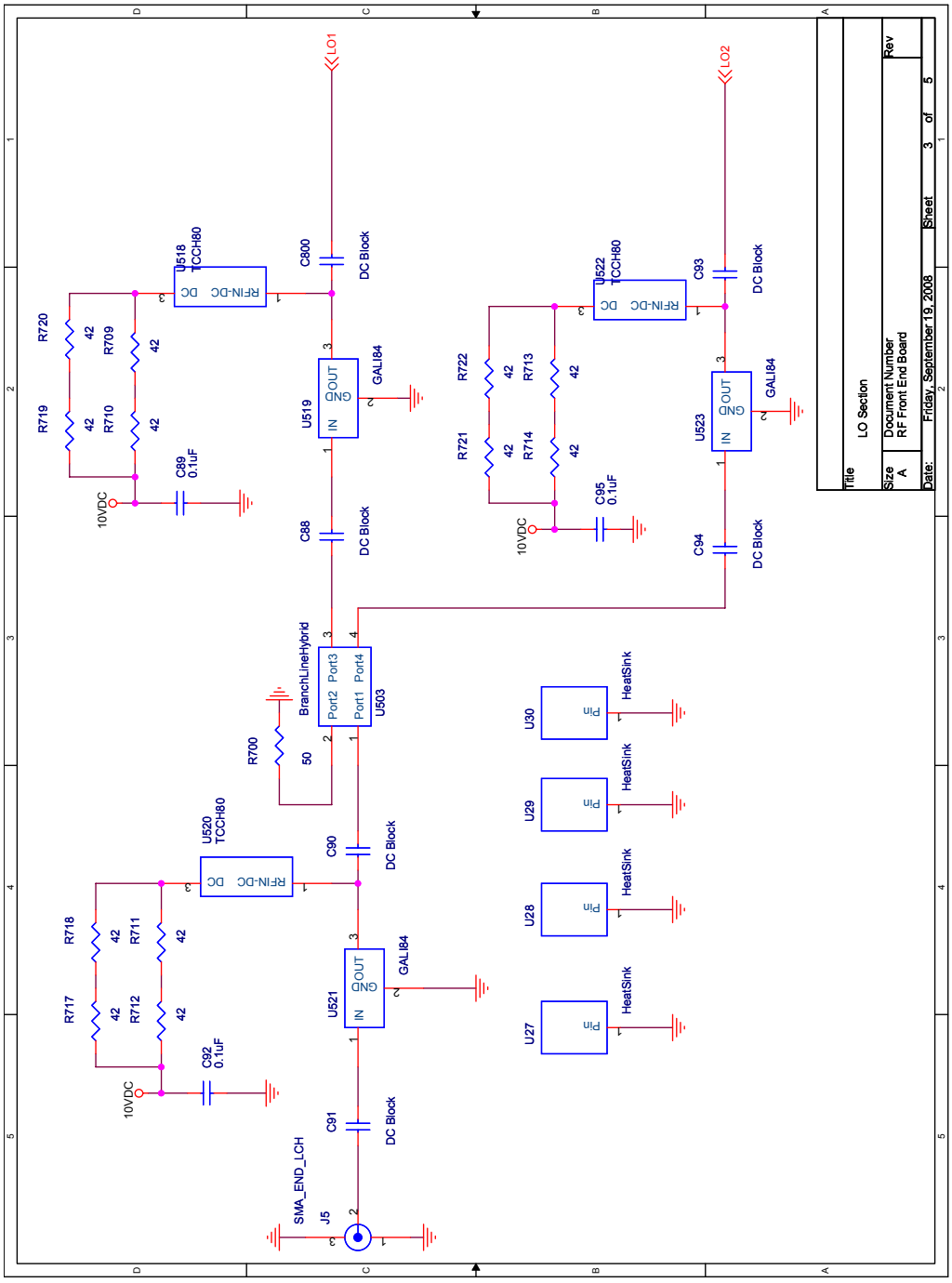

Figure 69: RF front-end board schematic: page 3.

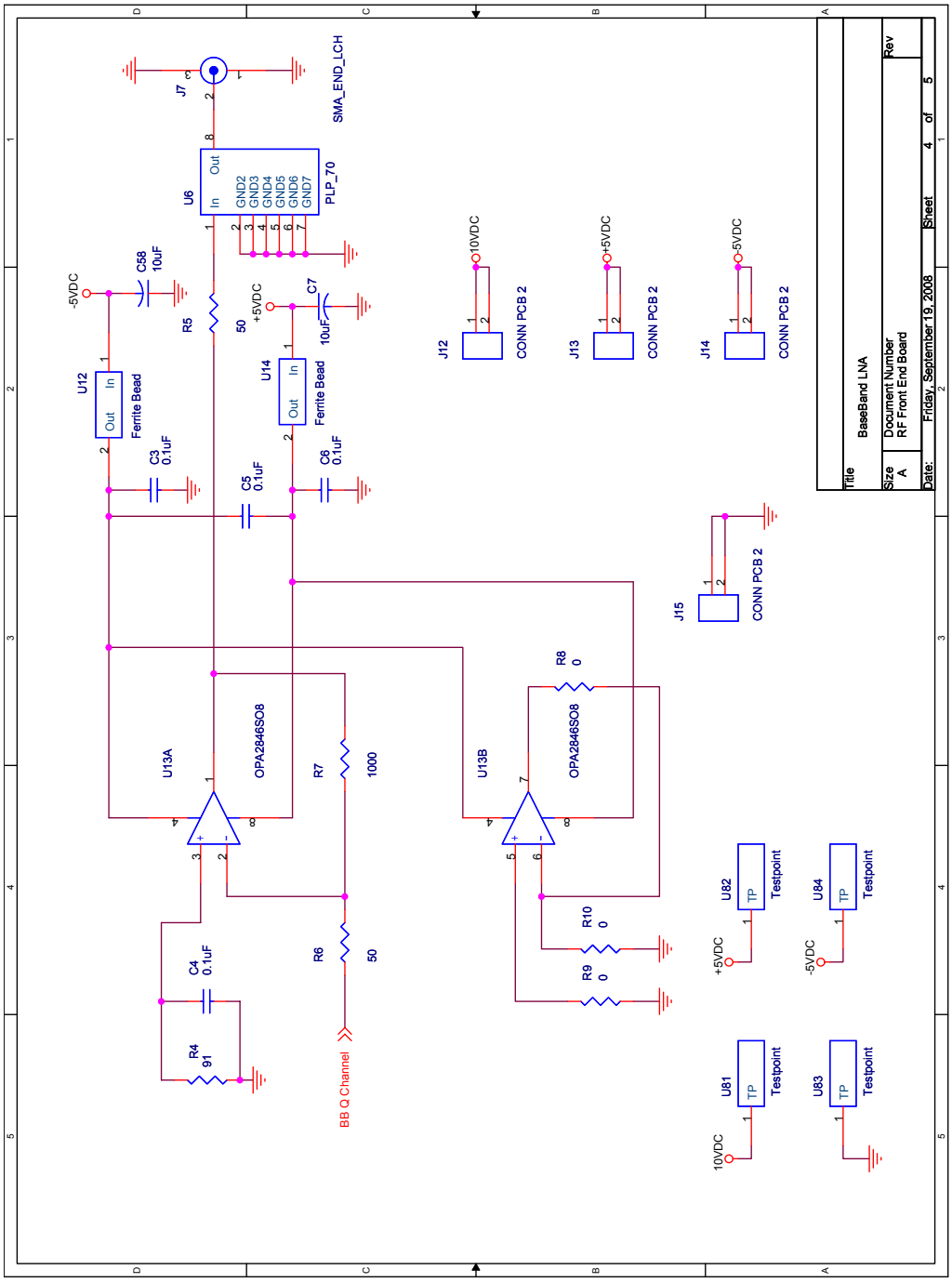

Figure 70: RF front-end board schematic: page 4.

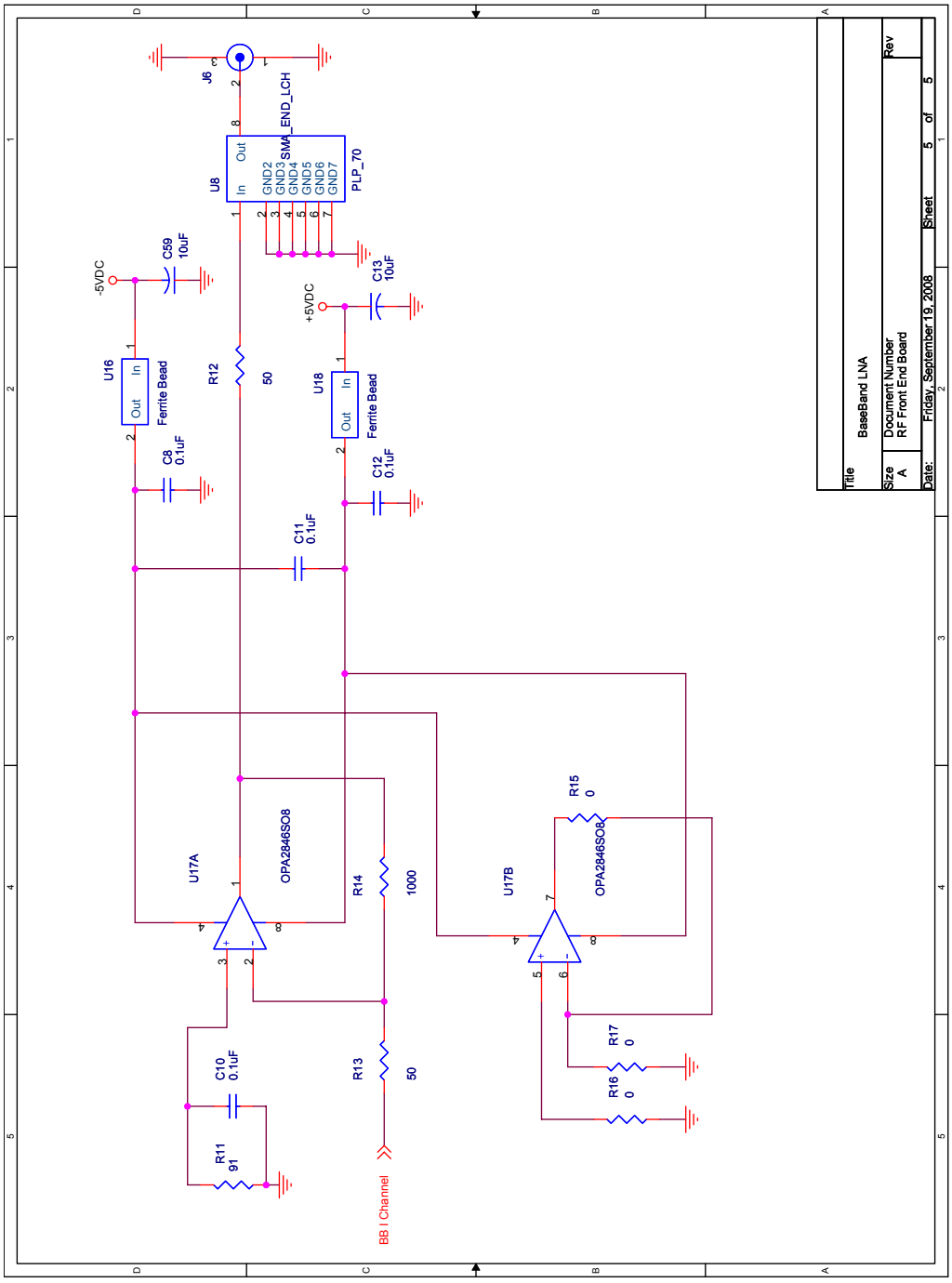

Figure 71: RF front-end board schematic: page 5.

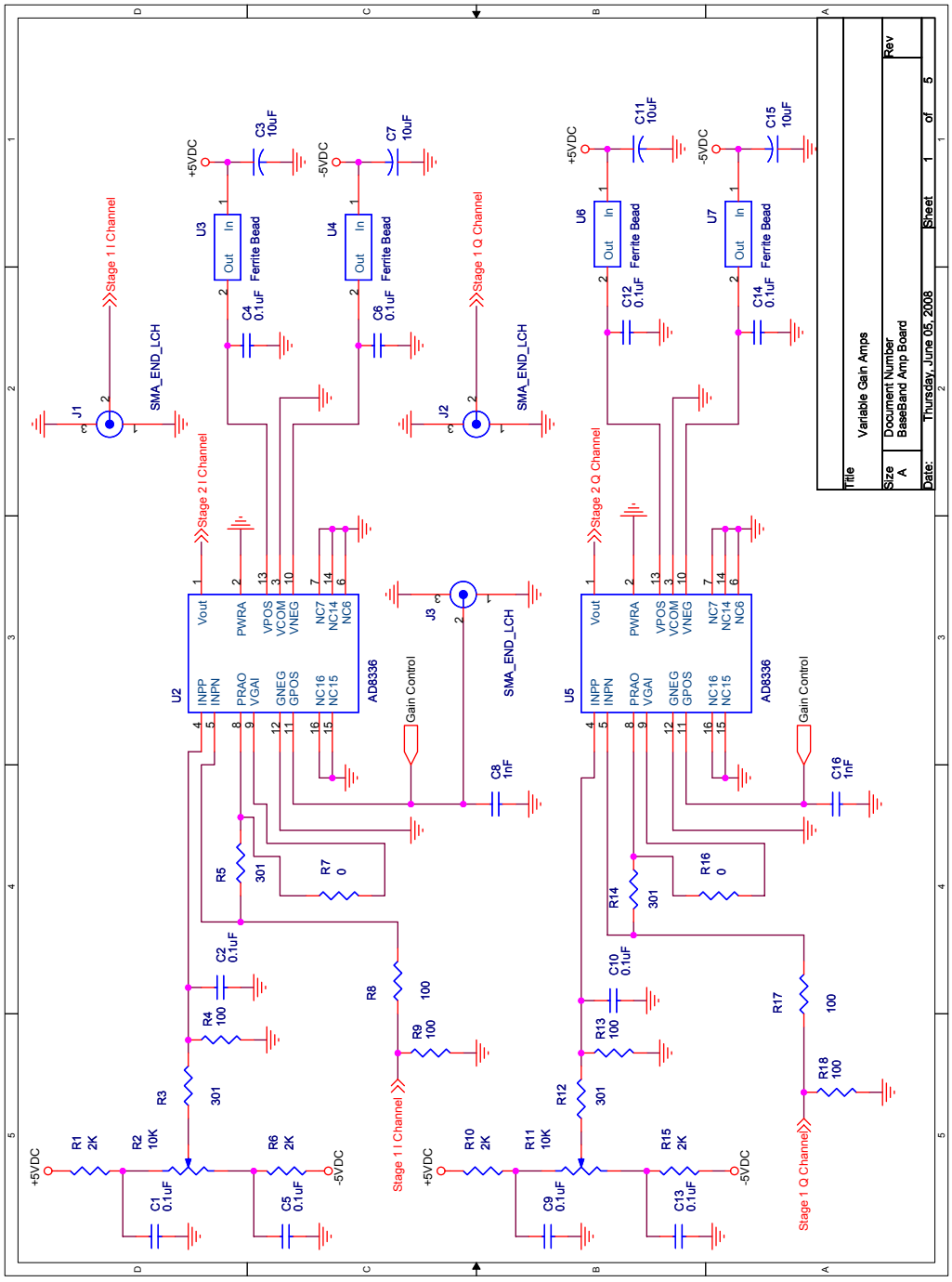

Figure 72: Baseband board schematic: page 1.

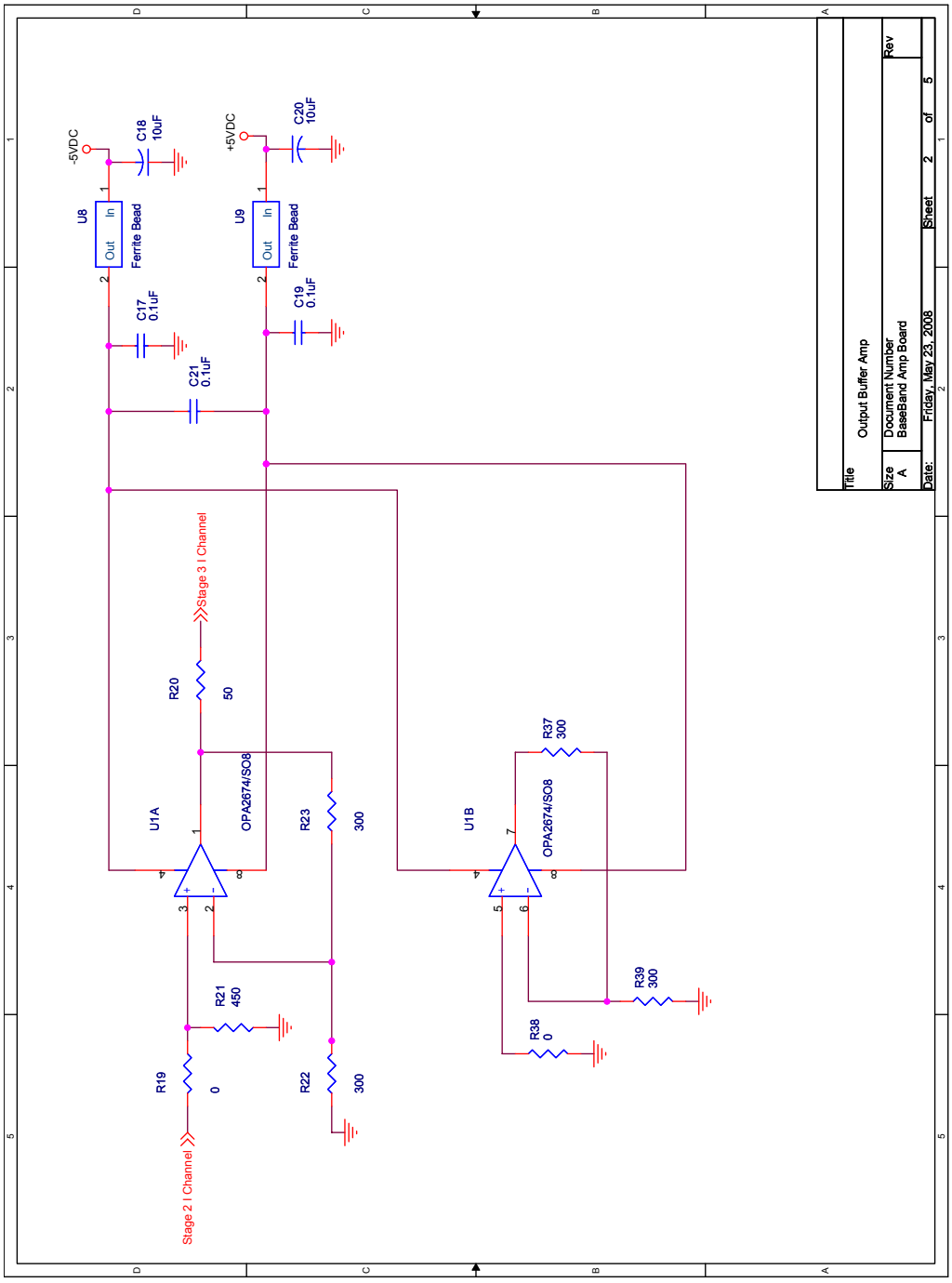

Figure 73: Baseband board schematic: page 2.

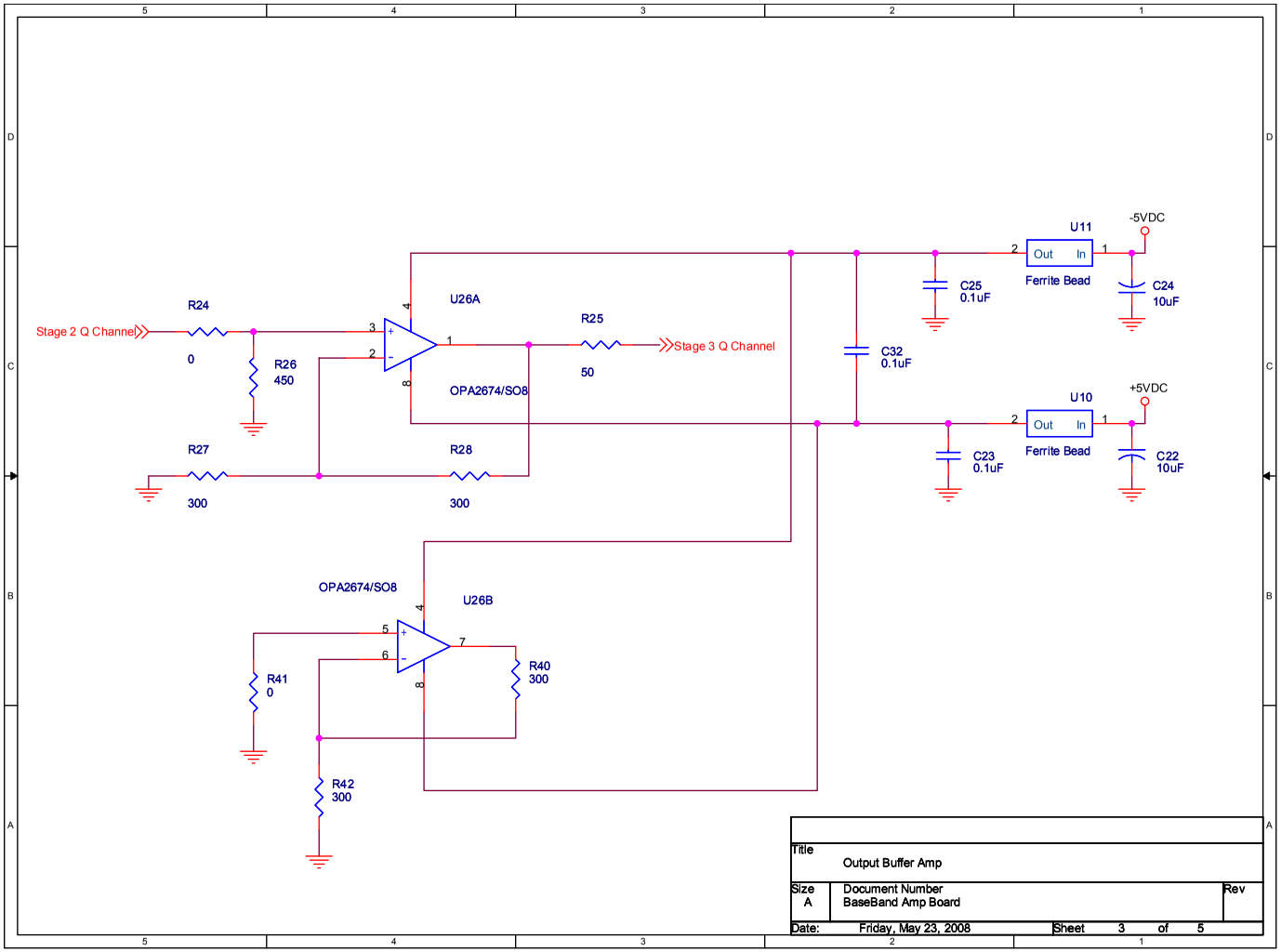

Figure 74: Baseband board schematic: page 3.

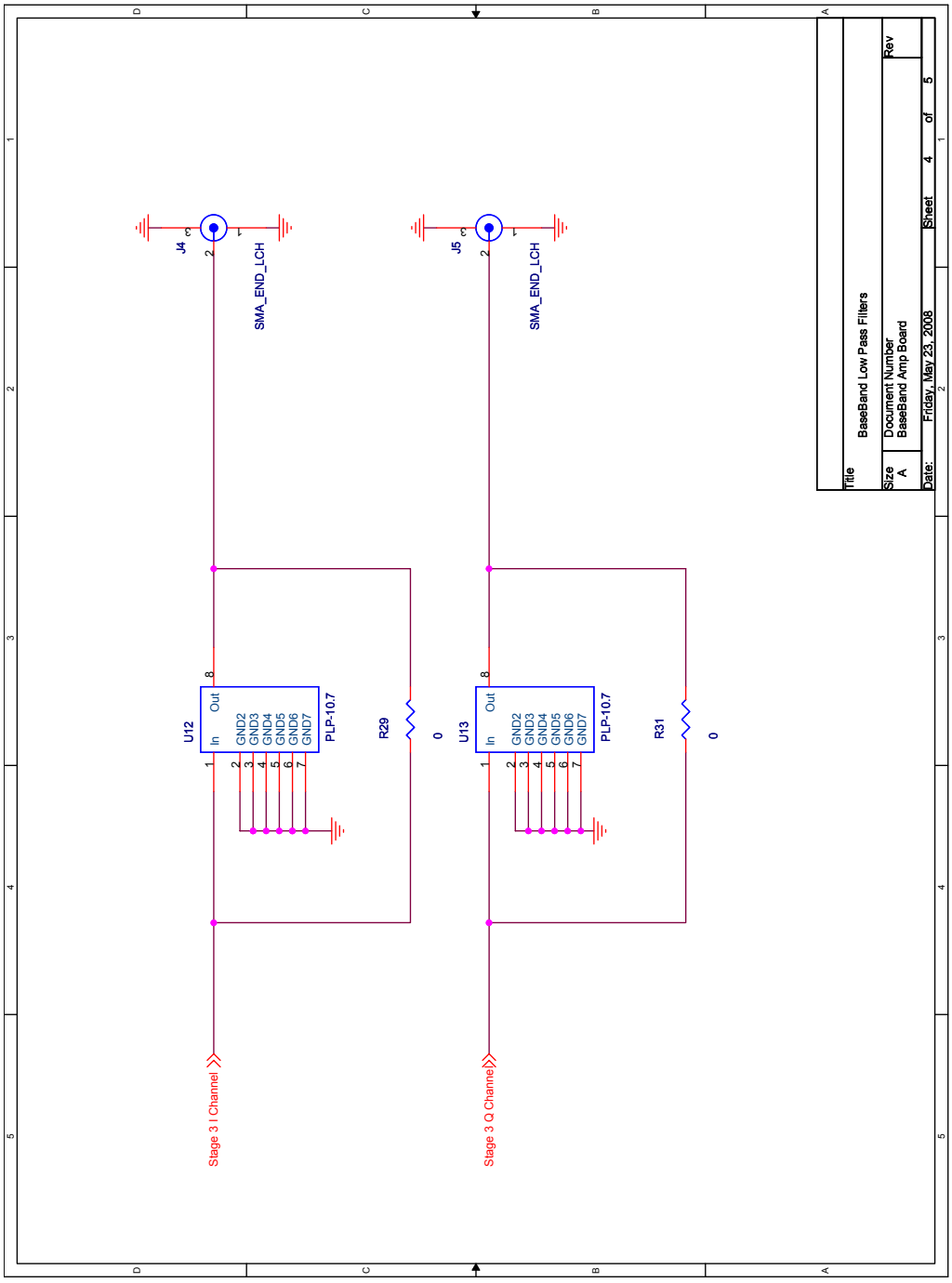

Figure 75: Baseband board schematic: page 4.

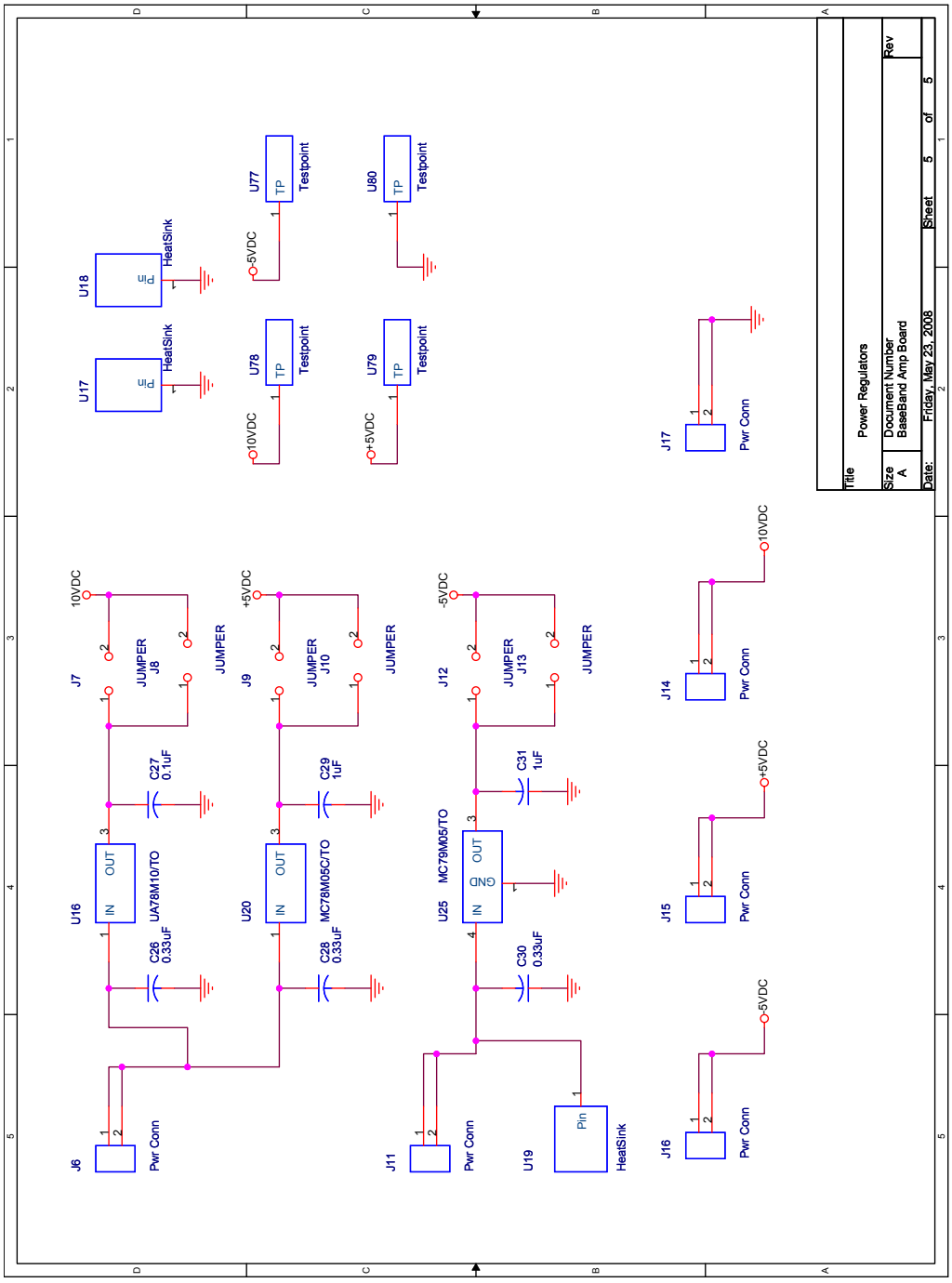

Figure 76: Baseband board schematic: page 5.

E.5 Receiver Characterization

This section outlines the procedure used to characterize the performance of the three direct-conversion receivers. The important performance metrics that were measured for each receiver are:

- Relative I and Q amplitude and phase errors.
- Linear gain range.
- The return loss of each receiver port.
- LO leakage from the receiver's RF input.

The I and Q amplitude and phase errors and the linear gain range were measured using the setup shown in Figure 77 and the return loss and LO leakage were measured using an Agilent E5071B network analyzer. The setup shown in Figure 77 was fully automated through Matlab programs using the GPIB and was able to sample the receiver's I and Q output as a function of receiver gain, RF input frequency, and RF input power.

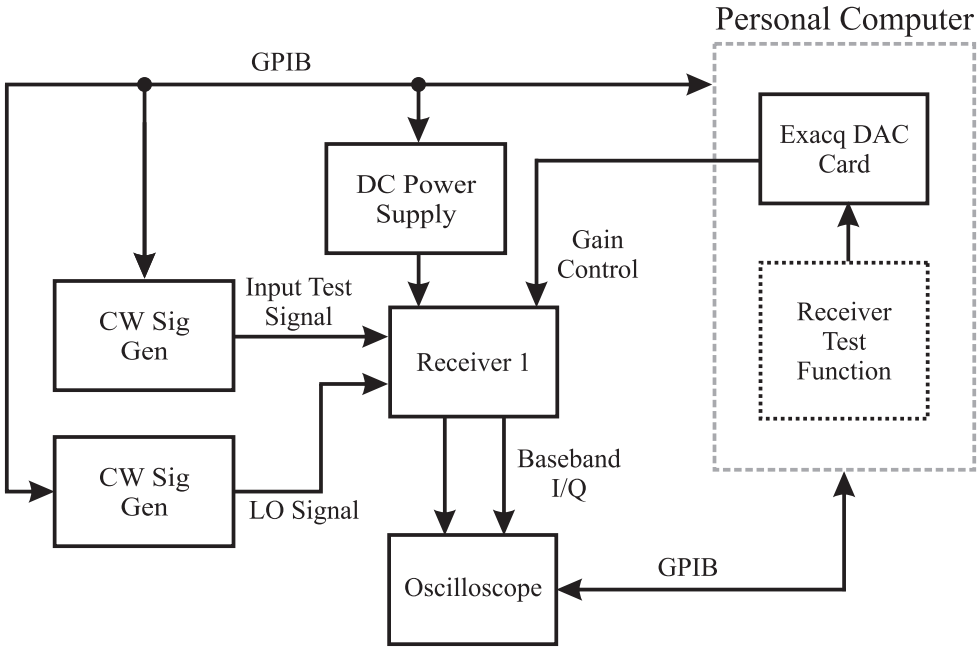

Figure 77: The test equipment setup for characterizing the direct-conversion receivers used in the backscatter testbed.

E.5.1 Relative I and Q Amplitude and Phase Errors

The relative I and Q amplitude and phase errors were measured to determine the total amplitude and phase error produced on the final combined signal. A procedure for measuring and correcting relative amplitude and phase errors was presented by Churchill *et al.* [78] which used digital filtering of the sampled I and Q signals to determine two correction factors. The relative amplitude and phase errors between the I and Q signals can be backsolved from the correction factors. In the formulation by Churchill *et al.*, the baseband I and Q signals – corresponding to a received RF tone – with relative amplitude and phase errors can be written as

$$I = A(1+\epsilon)\cos(2\pi ft) + a \tag{87}$$

$$Q = A\sin(2\pi ft + \phi) + b \tag{88}$$

where A is the amplitude, f is the frequency, ϕ is the relative phase error, ϵ is the relative amplitude error, and a and b are DC offsets. If no errors are present, the I and Q terms of (87) and (88) reduce to a cosine and sine wave, respectively – the expected baseband output corresponding to a sinusoid received at the RF input. Figures 78 - 80 plot the relative phase error ϕ (in degrees) and the relative amplitude imbalance (in the dB scale) for each receiver. In these plots, the relative amplitude imbalance is defined as

$$\text{Relative Amplitude Imbalance} = 10\log_{10}(1+\epsilon) \tag{89}$$

The blue lines represent the measured relative amplitude and phase errors for different RF input power levels[1]. The figures show that some of the measurements were affected by noise and examination of the data indicated that this was the case for measurements corresponding to low RF input power levels. Some of the extremely noisy measurements were removed from the figures to aid in visualization, but the global maximum error and median error at each frequency – calculated using all of the measurements in each figure – are shown.

[1] These measurements were too numerous to label individually.

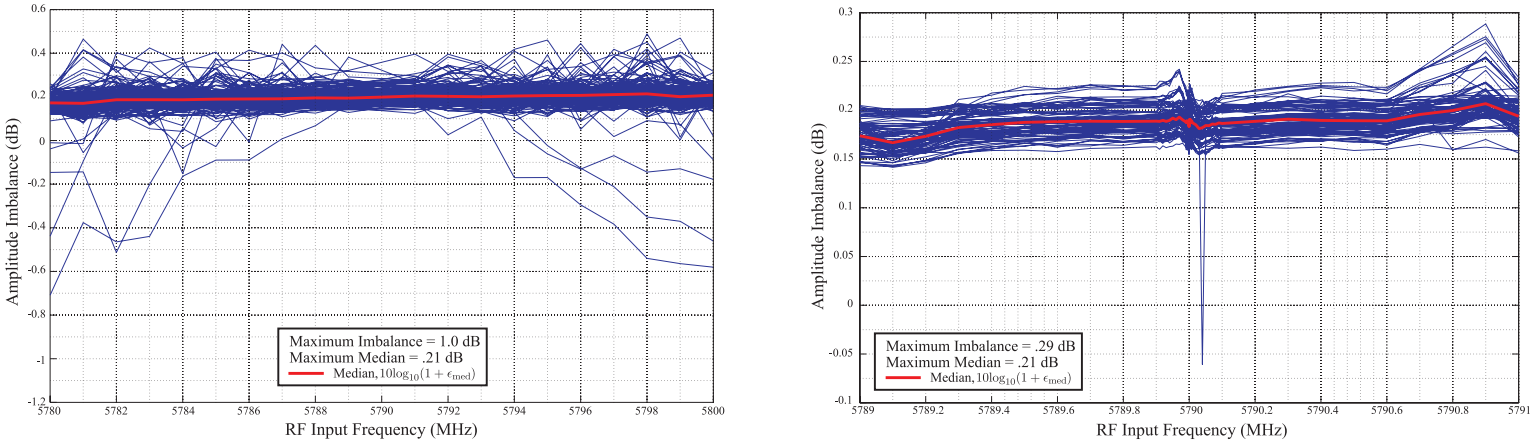

(a) Receiver 1 amplitude error measurements.

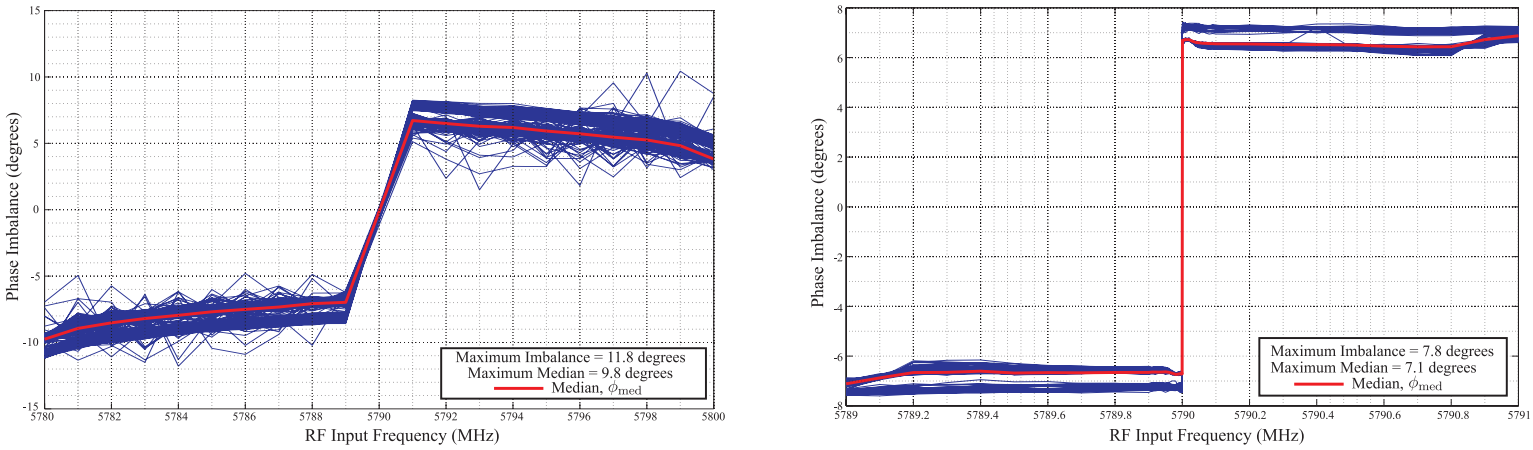

(b) Receiver 1 phase error measurements.

Figure 78: The measured relative amplitude and phase errors for receiver 1. The relative amplitude errors are shown in the dB scale and the global maximum error and median error at each frequency are shown.

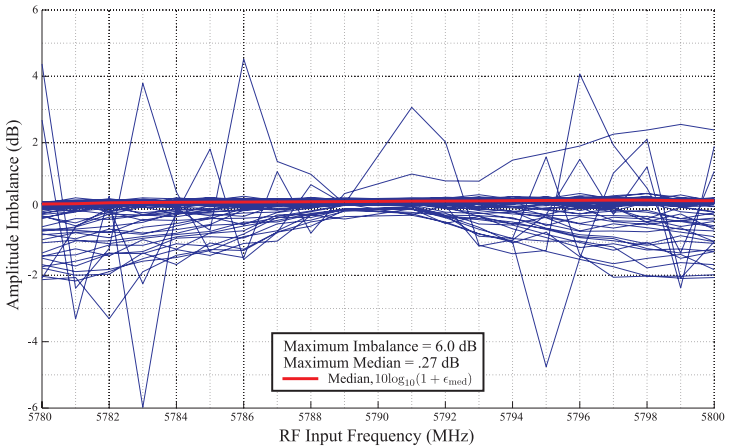

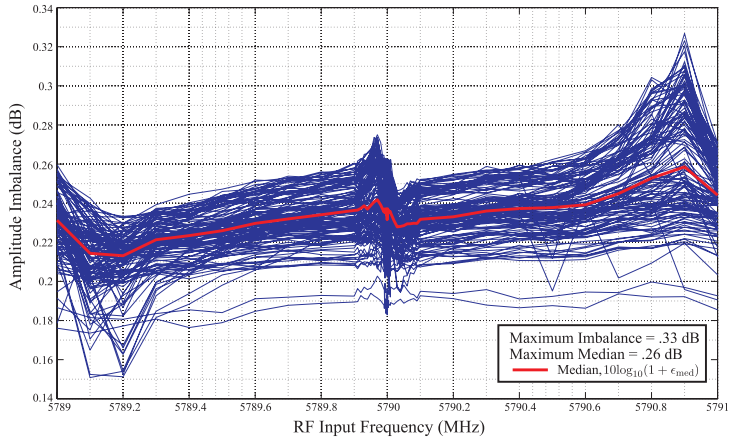

(a) RX2 amplitude error measurements.

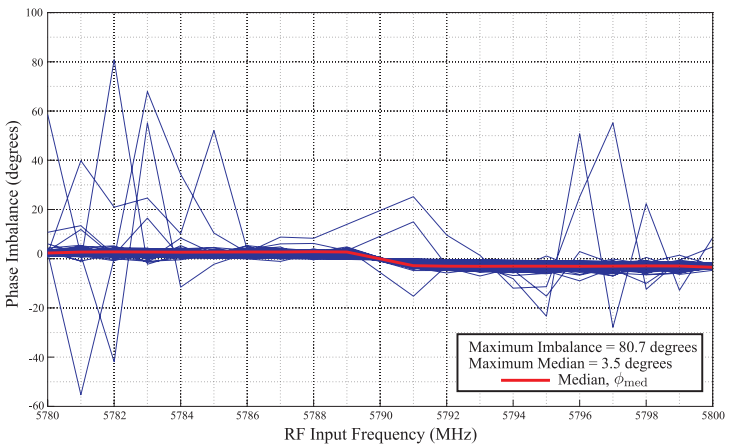

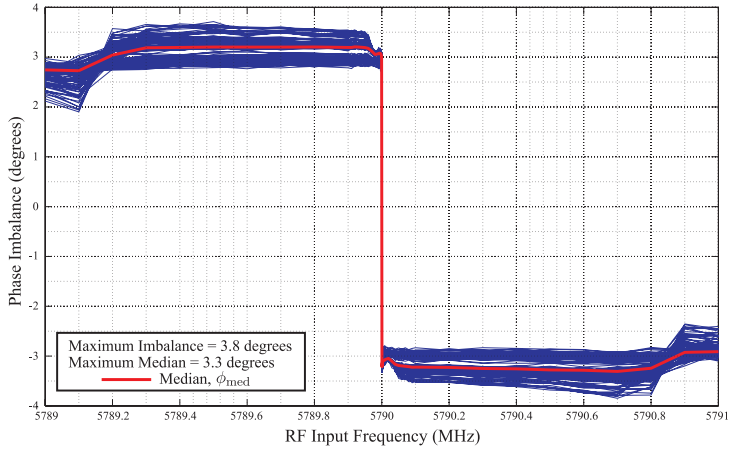

(b) RX2 phase error measurements.

Figure 79: The measured relative amplitude and phase errors for receiver 2. The relative amplitude errors are shown in the dB scale and the global maximum error and median error at each frequency are shown.

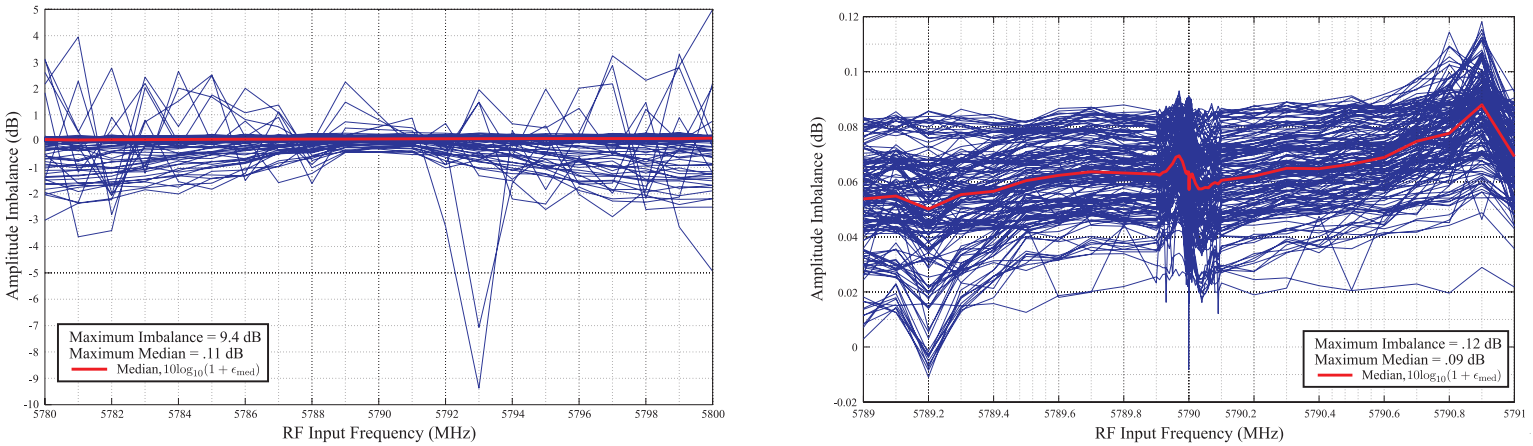

(a) RX3 amplitude error measurements.

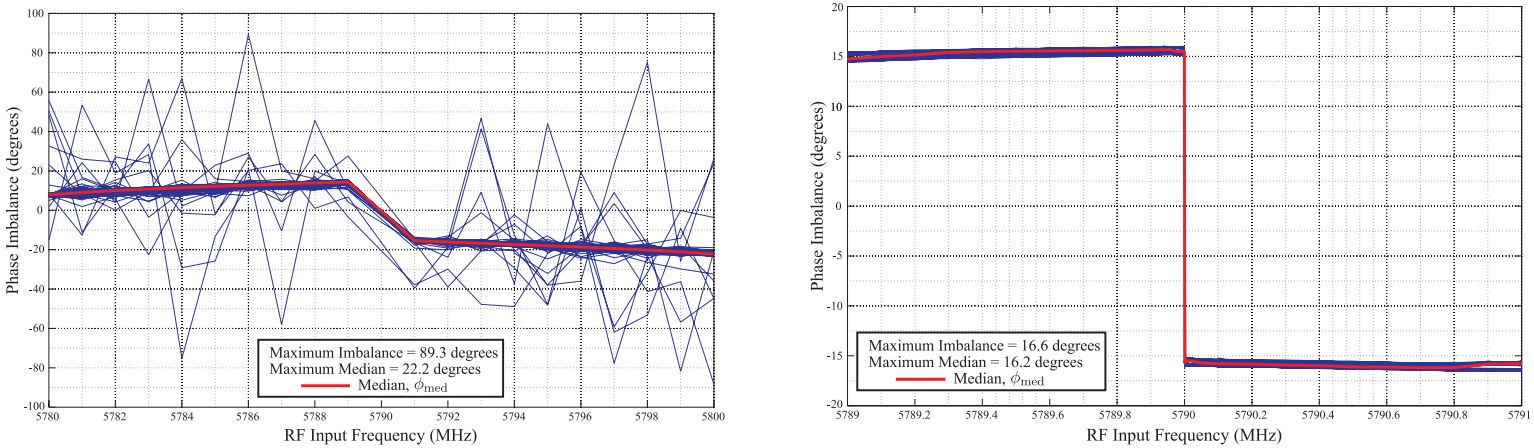

(b) RX3 phase error measurements.

Figure 80: The measured relative amplitude and phase errors for receiver 3. The relative amplitude errors are shown in the dB scale and the global maximum error and median error at each frequency are shown.

The total amplitude error and the total phase error of the combined I and Q signals were calculated from the median relative amplitude errors $(1 + \epsilon_{\text{med}})$ and median phase errors ϕ_{med} shown in Figures 78 - 80. To calculate the total peak amplitude and phase errors for each frequency, two vectors were formed from several sampled periods of the signals with and without imbalance errors, described by (90) and (91), respectively.

$$T_{\text{error}}[k] = (1 + \epsilon_{\text{med}}) \cos[2\pi f k] + j \sin[2\pi f k + \phi_{\text{med}}] \tag{90}$$

$$T_{\text{ideal}}[k] = \cos[2\pi f k] + j \sin[2\pi f k] \tag{91}$$

For each frequency, the total percent amplitude error A_k and total phase error P_k of the k^{th} time sample were calculated as shown in (92) and (93), respectively.

$$A_k = 100 \times \frac{|T_{\text{error}}[k]| - |T_{\text{ideal}}[k]|}{|T_{\text{ideal}}[k]|} \tag{92}$$

$$P_k = \angle T_{\text{error}}[k] - \angle T_{\text{ideal}}[k] \tag{93}$$

In (93), the subtraction accounts for the 2π periodicity of the phase. The total peak amplitude error and the total peak phase error were found by taking the maximum of (92) and (93) over the full range of k for each measured frequency. These total peak errors are plotted in Figures 81 - 83. For receiver 1 and 2, the total peak amplitude error is less than 10% and the total peak phase error is less than 10^{o} for all measured frequencies. For receiver 3, the total peak amplitude error is less than 20% and the total peak phase error is less than 25^{o}. The poorer performance of receiver 3 is likely caused by an impedance mismatch between the LNA (Minicircuits GALI-84+) and the down-conversion mixers. However, for the envelope distribution measurements presented in this dissertation, total peak amplitude errors were of most concern and considered acceptable.

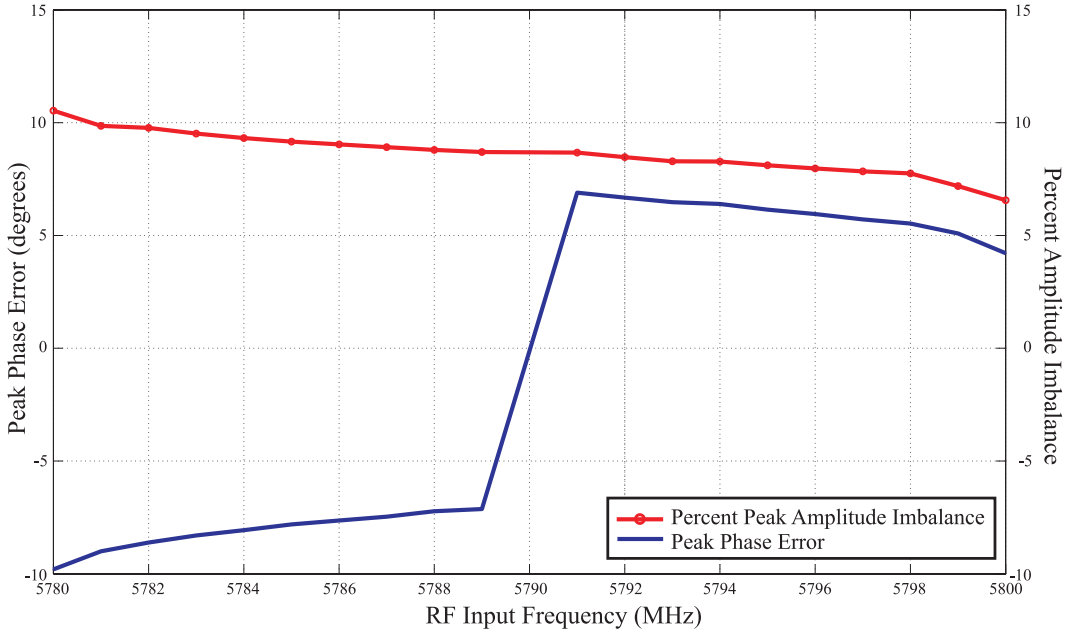

(a)

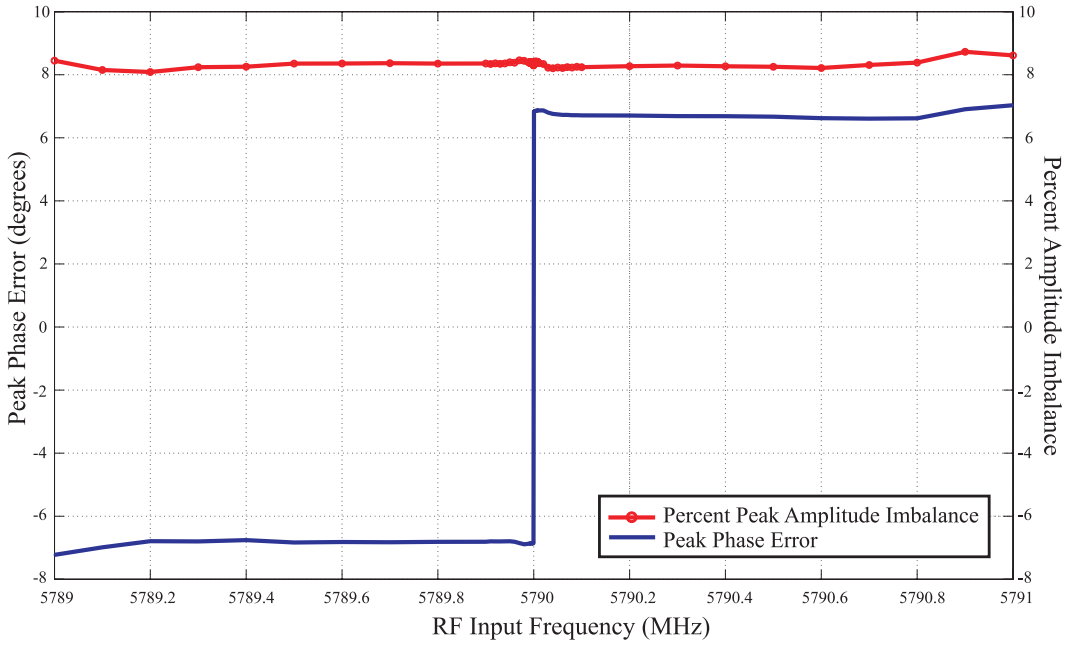

(b)

Figure 81: The total peak amplitude and total peak phase error of the combined I and Q signals for receiver 1. These errors are calculated from equations (92) and (93) using the median relative amplitude and phase errors given in Figure 78.

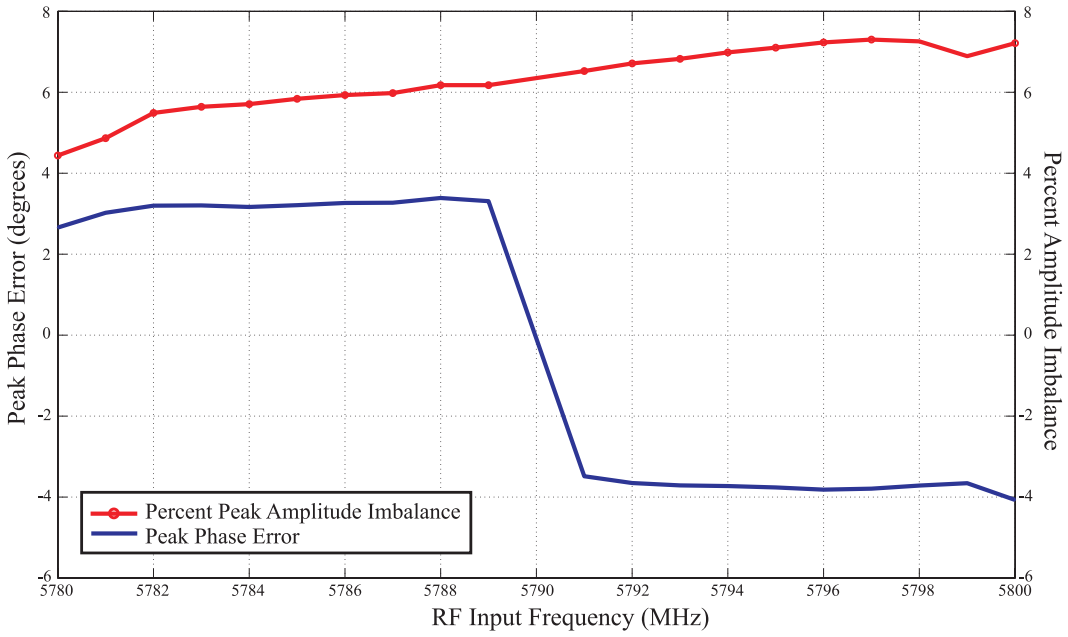

(a)

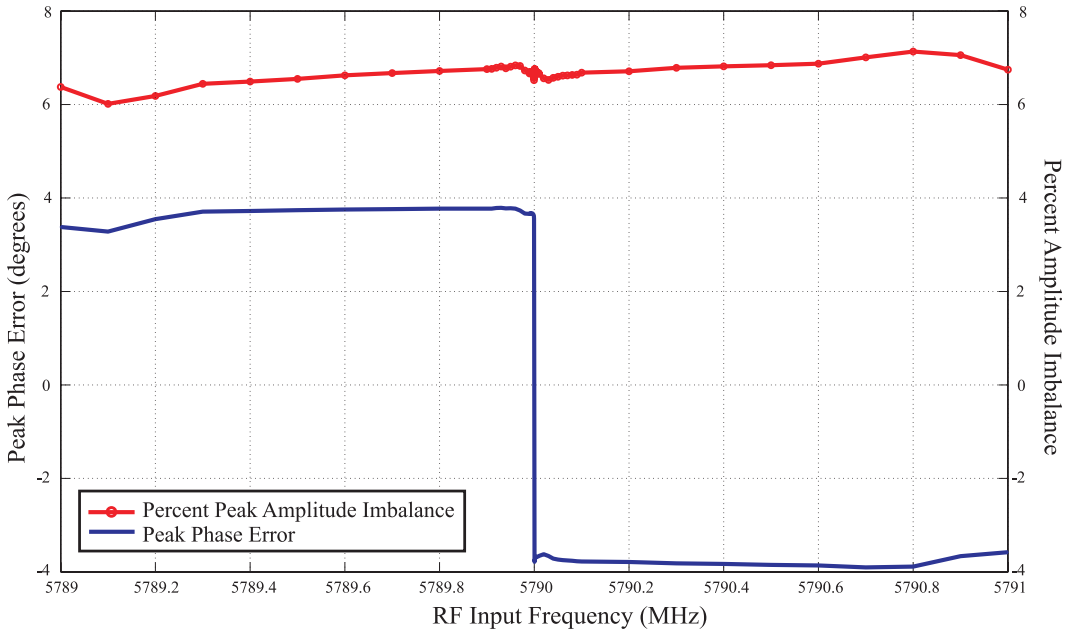

(b)

Figure 82: The total peak amplitude and total peak phase error of the combined I and Q signals for receiver 2. These errors are calculated from equations (92) and (93) using the median relative amplitude and phase errors given in Figure 79.

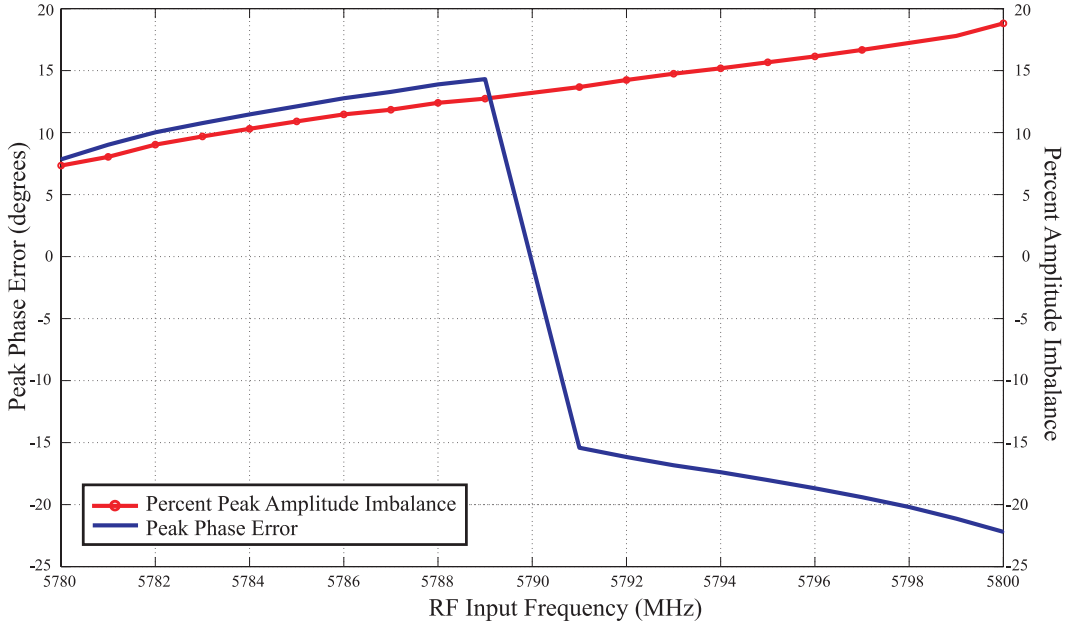

(a)

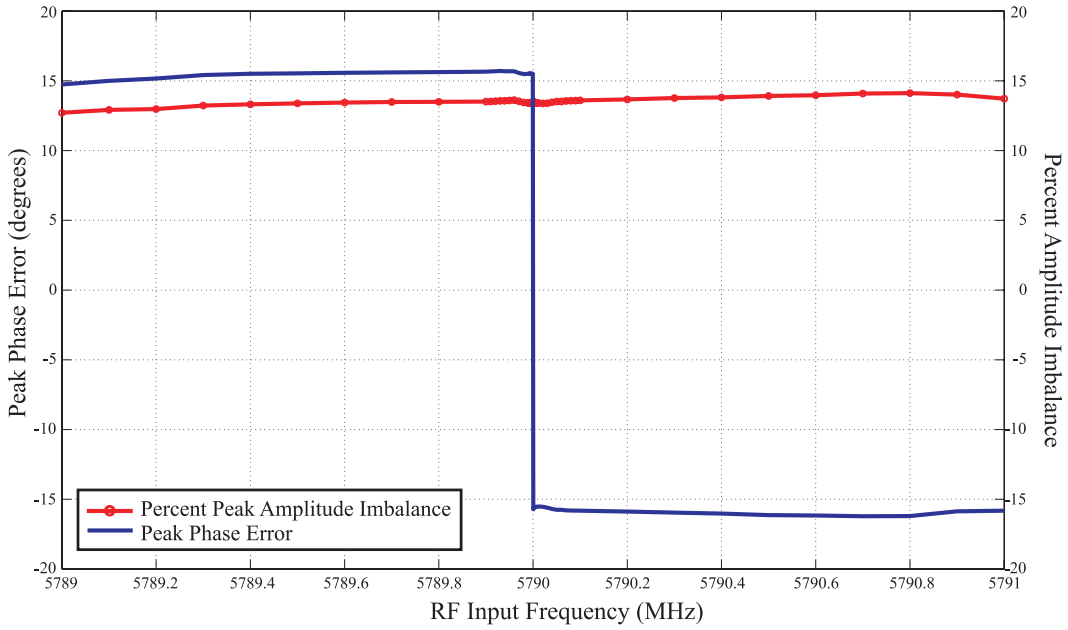

(b)

Figure 83: The total peak amplitude and total peak phase error of the combined I and Q signals for receiver 3. These errors are calculated from equations (92) and (93) using the median relative amplitude and phase errors given in Figure 80.

E.5.2 Receiver Linear Gain Region

The test setup shown in Figure 77 was also used to determine the linear operating region of each receiver. Figures 84 - 86 show plots of the RF input power versus the baseband output power for the I and Q channels of each receiver. The linear region for each receiver is the region to the left and below the vertical and horizontal black lines. The region to the right of the vertical line is where the baseband amplification board saturates while the region above the horizontal is where the high-frequency LNA saturates. Figures 87 - 89 show the total receiver gain measured at the I and Q outputs as a function of the gain control voltage V_{gain} for a given RF input power level. The RF input power level was chosen to avoid saturating the LNA in order to determine the maximum linear range of the baseband amplifiers. These figures were used to approximate the gain of each receiver with a linear equation which is shown graphically by the black line in Figures 87 - 89. These equations and the linear limits of each receiver are summarized in Table 20.

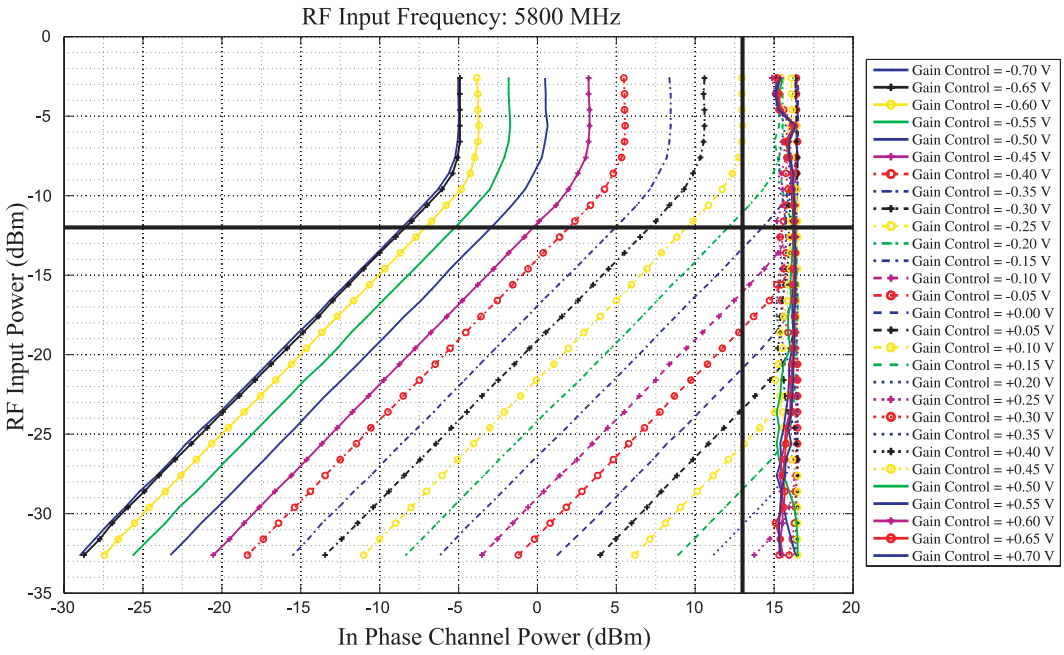

(a)

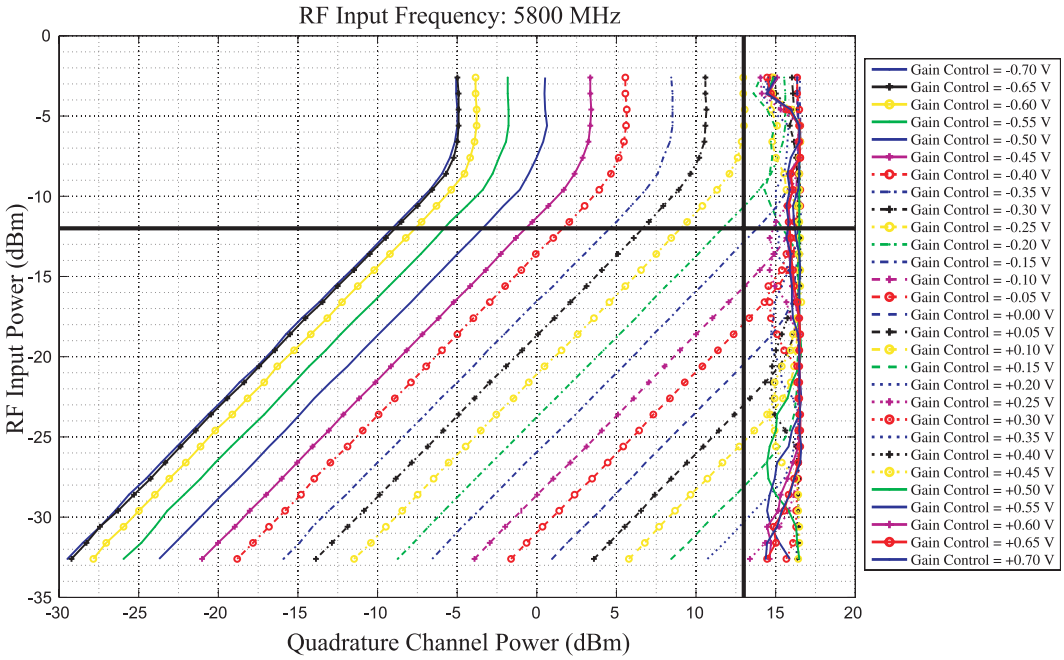

(b)

Figure 84: The RF input power versus the baseband output power for the (a) I and (b) Q channels of receiver 1. The region to the left and below the black lines is the linear operating region of the receiver.

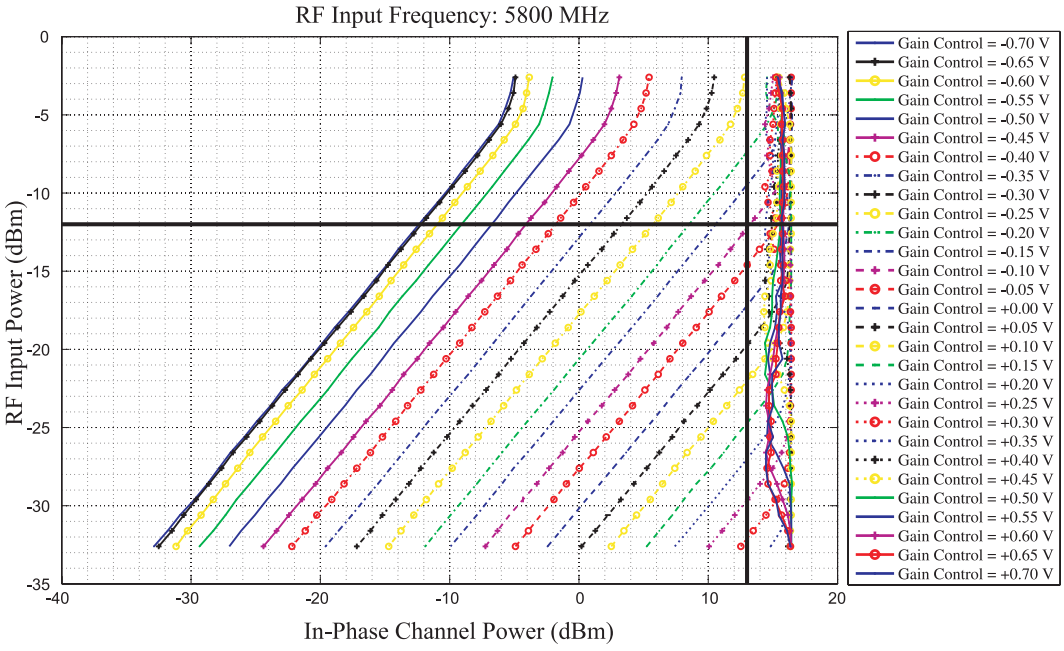

(a)

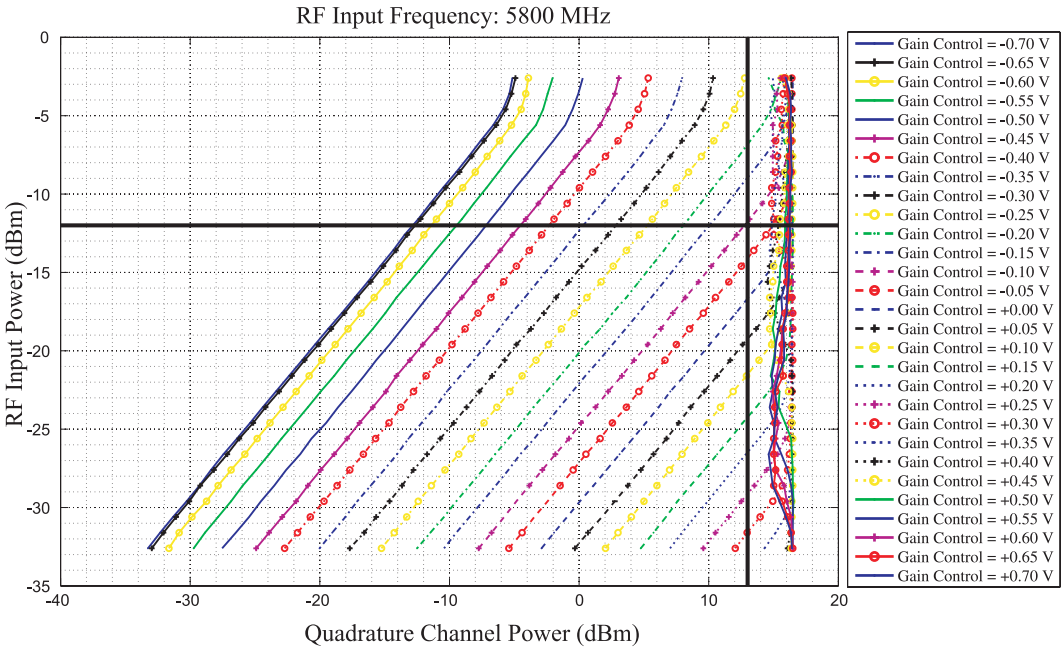

(b)

Figure 85: The RF input power versus the baseband output power for the (a) I and (b) Q channels of receiver 2. The region to the left and below the black lines is the linear operating region of the receiver.

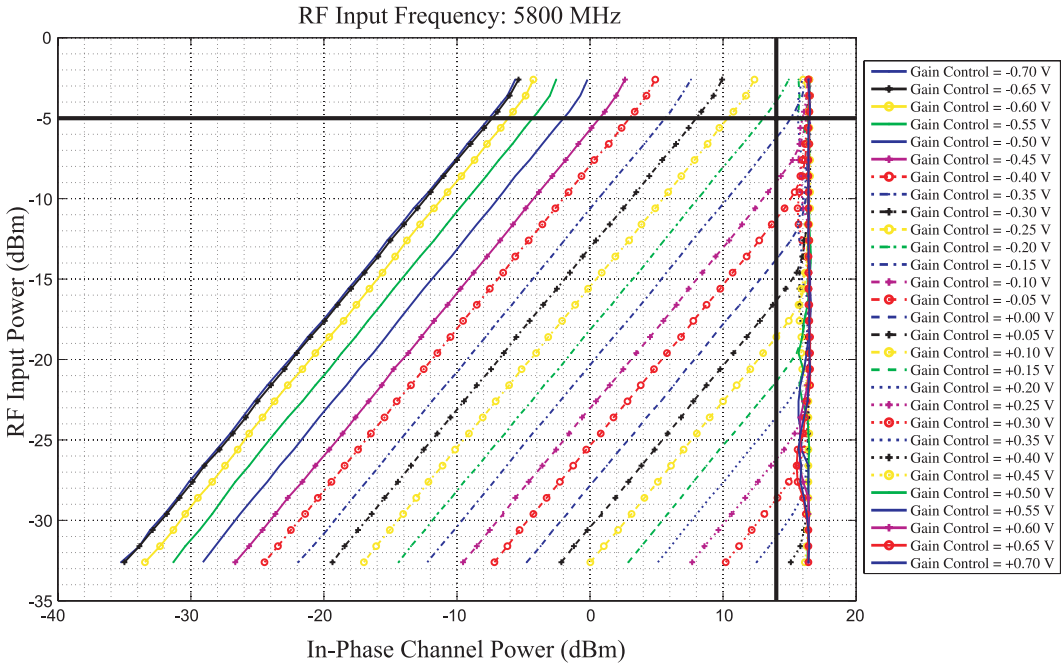

(a)

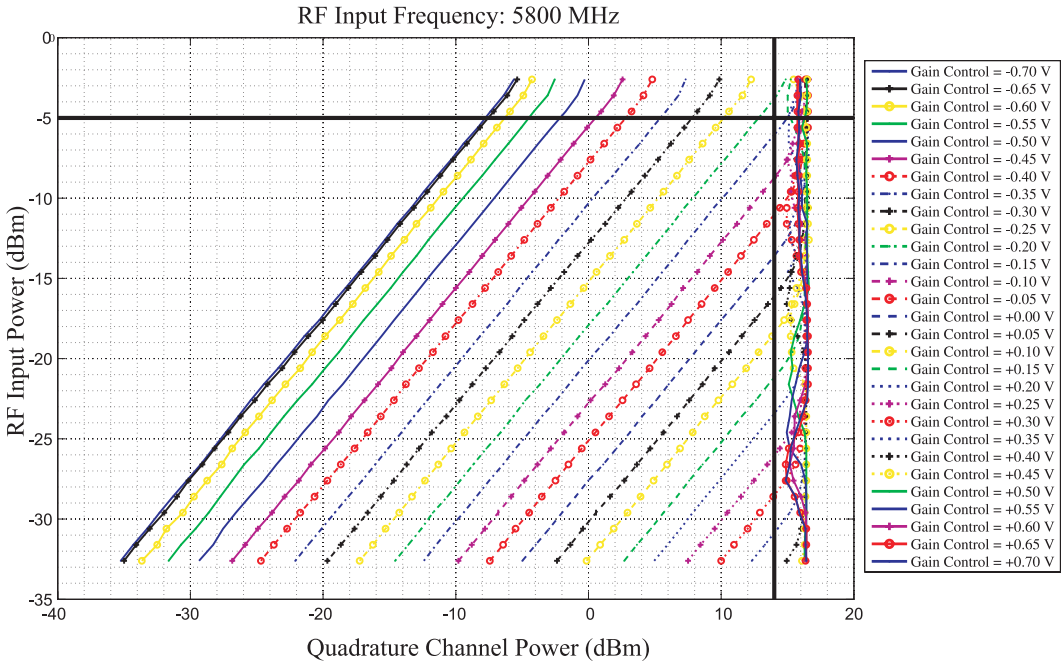

(b)

Figure 86: The RF input power versus the baseband output power for the (a) I and (b) Q channels of receiver 3. The region to the left and below the black lines is the linear operating region of the receiver.

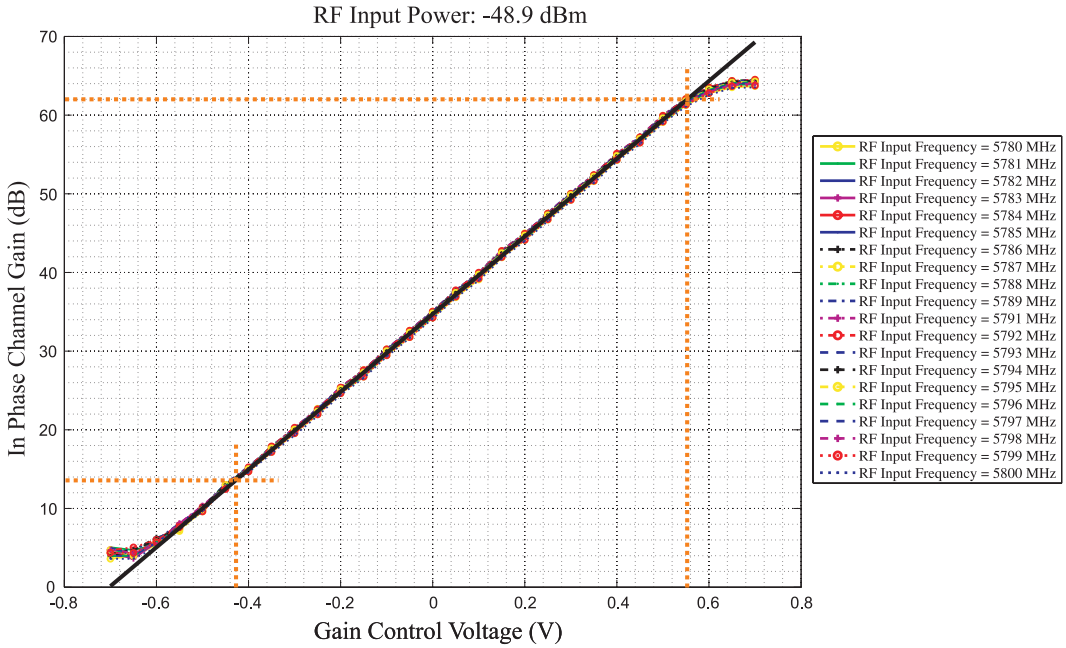

(a)

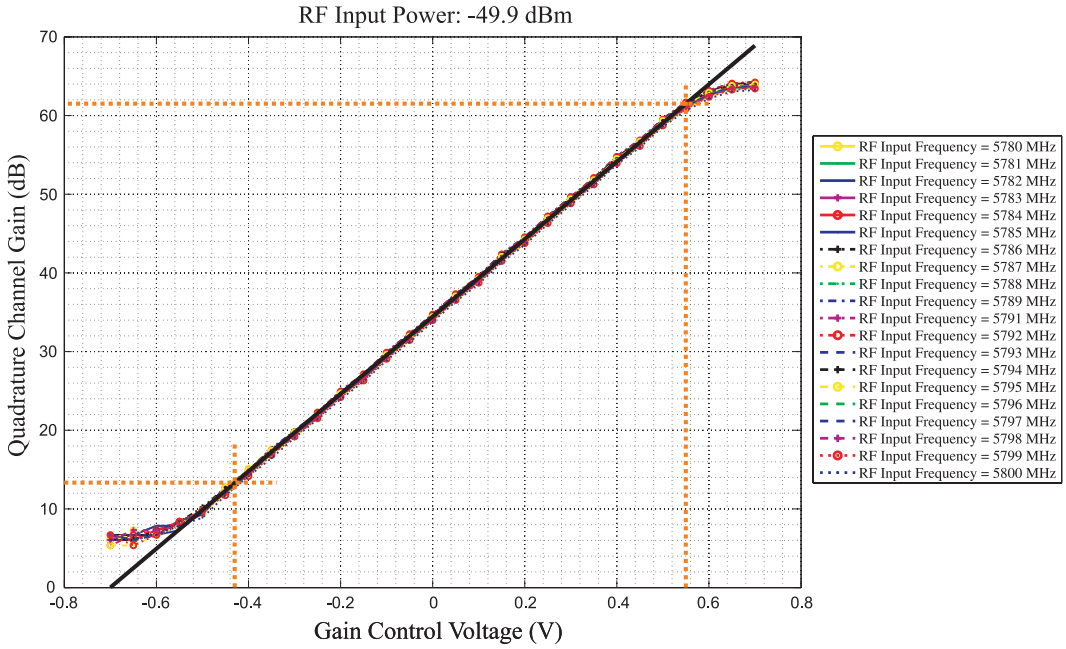

(b)

Figure 87: The total gain of receiver 1 measured at the (a) I and (b) Q channels as a function of the gain control voltage V_{gain} for a given RF input power level. The orange lines mark the upper and lower limits of the linear gain region.

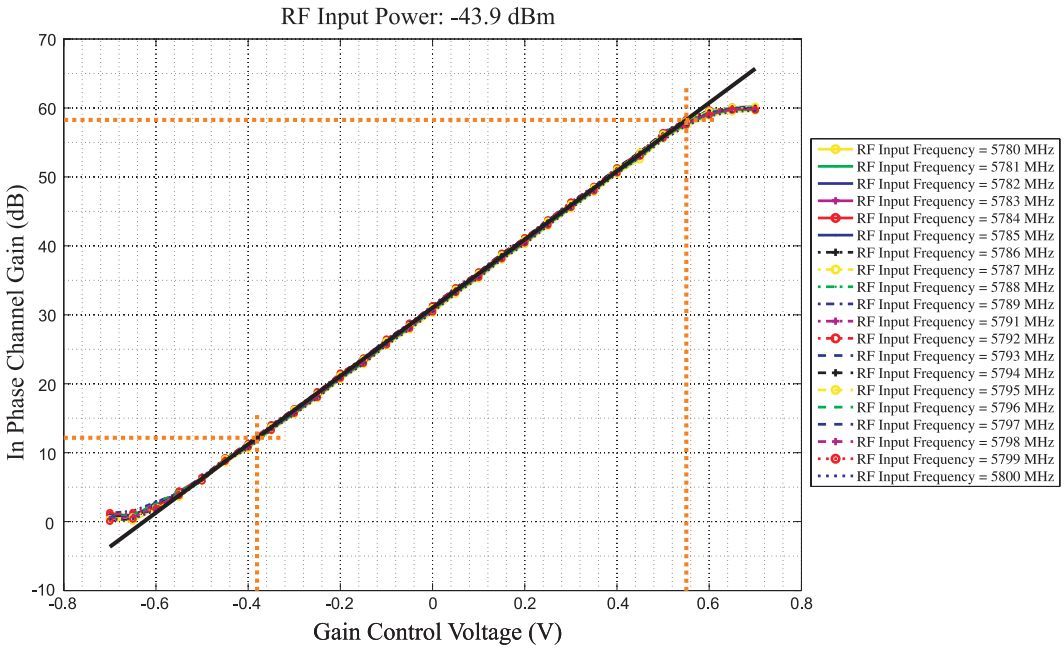

(a)

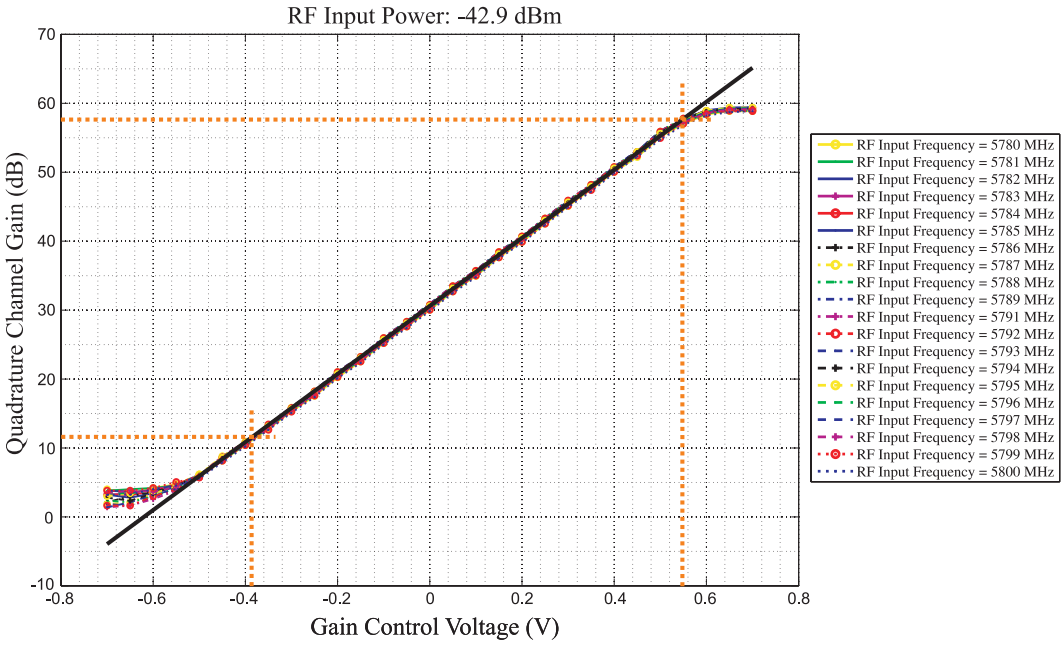

(b)

Figure 88: The total gain of receiver 2 measured at the (a) I and (b) Q channels as a function of the gain control voltage V_{gain} for a given RF input power level. The orange lines mark the upper and lower limits of the linear gain region.

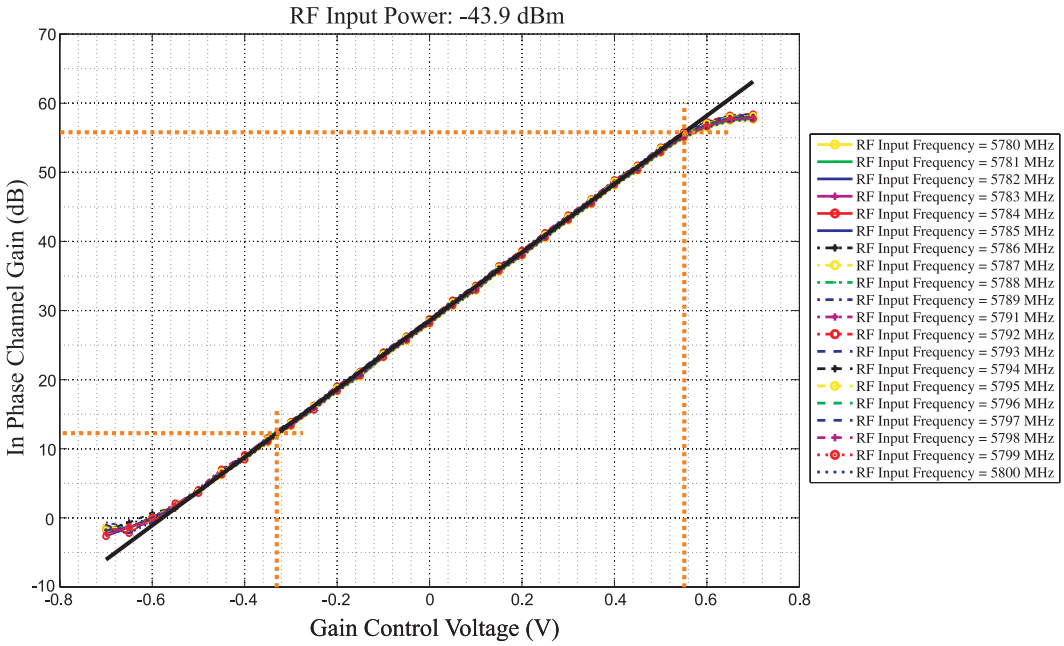

(a)

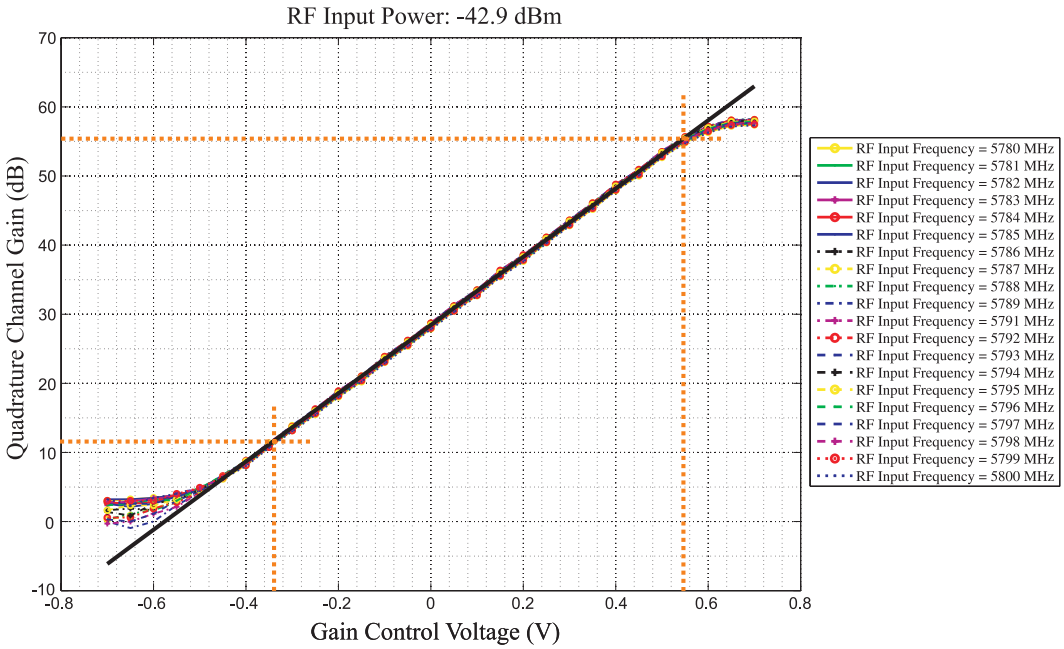

(b)

Figure 89: The total gain of receiver 3 measured at the (a) I and (b) Q channels as a function of the gain control voltage V_{gain} for a given RF input power level. The orange lines mark the upper and lower limits of the linear gain region.

Table 20: The limits of the linear region for each receiver and the equation approximating the receiver linear gain at both the I and Q output.

Receiver 1	
RF Input Power Limit (dBm):	-12
I and Q Baseband Output Power Limit (dBm):	13
Linear Gain Voltage Range (V):	$-0.43 \leq V_{\text{gain}} \leq 0.55$
I Channel Gain Equation (dB)†:	$\text{Gain}_{\text{I}} = 49.39\, V_{\text{gain}} + 34.7$
Q Channel Gain Equation (dB)†:	$\text{Gain}_{\text{Q}} = 49.187\, V_{\text{gain}} + 34.46$
Receiver 2	
RF Input Power Limit (dBm):	-12
I and Q Baseband Output Power Limit (dBm):	13
Linear Gain Voltage Range (V):	$-0.38 \leq V_{\text{gain}} \leq 0.55$
I Channel Gain Equation (dB)†:	$\text{Gain}_{\text{I}} = 49.39\, V_{\text{gain}} + 34.7$
Q Channel Gain Equation (dB)†:	$\text{Gain}_{\text{Q}} = 49.351\, V_{\text{gain}} + 34.609$
Receiver 3	
RF Input Power Limit (dBm):	-5
I and Q Baseband Output Power Limit (dBm):	13
Linear Gain Voltage Range (V):	$-0.34 \leq V_{\text{gain}} \leq 0.55$
I Channel Gain Equation (dB)†:	$\text{Gain}_{\text{I}} = 49.39\, V_{\text{gain}} + 34.7$
Q Channel Gain Equation (dB)†:	$\text{Gain}_{\text{Q}} = 49.366\, V_{\text{gain}} + 28.43$

$^{\dagger}\text{Gain}_{\text{I}}$ and Gain_{Q} are in the dB scale and V_{gain} has units of Volts.

E.5.3 Return Loss and LO Leakage Measurements

The return loss and LO leakage through the RF input port were measured using an Agilent E5071B network analyzer. The measurements for each receiver are presented in Figures 90 - 92.

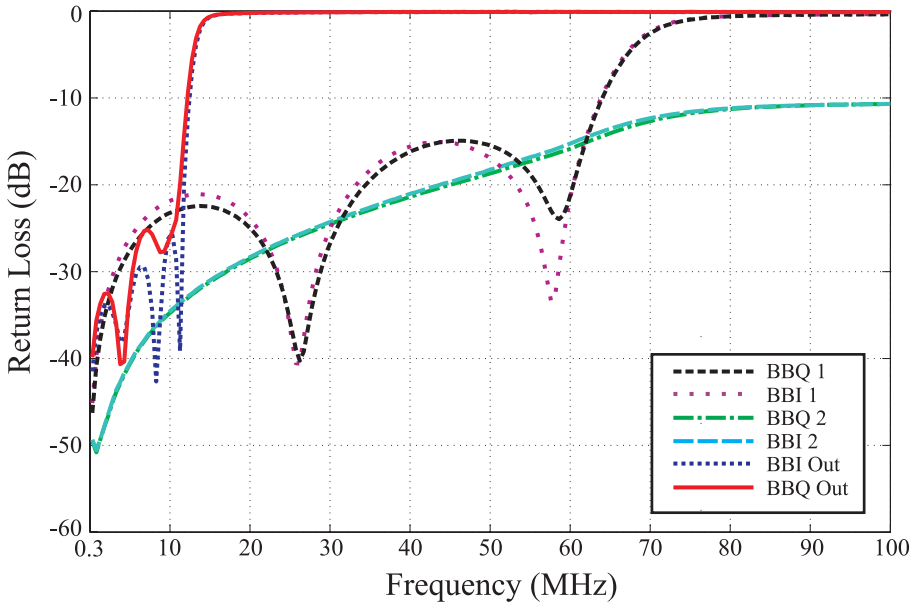

(a)

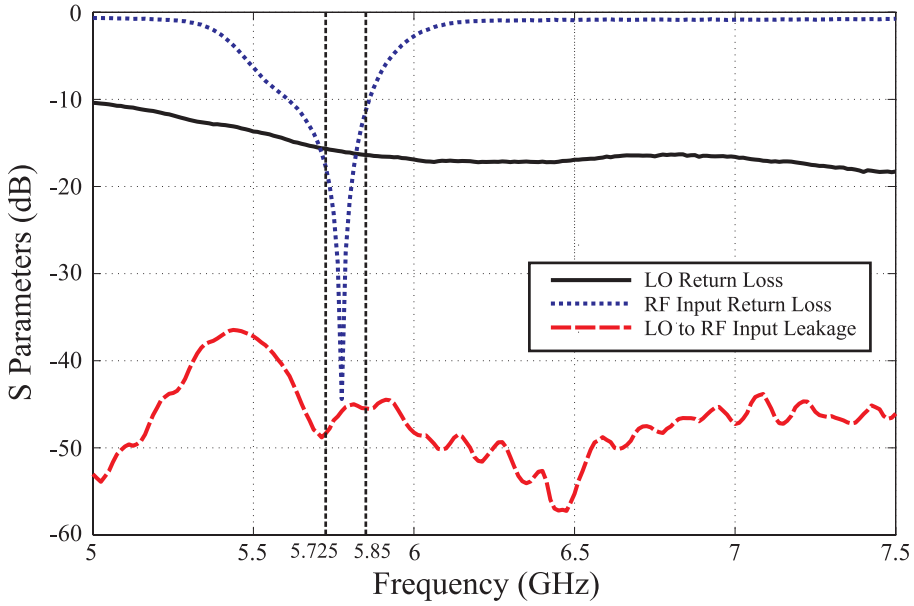

(b)

Figure 90: The (a) return loss for the baseband ports and (b) return loss and LO leakage at the ports on the RF front-end board for receiver 1.

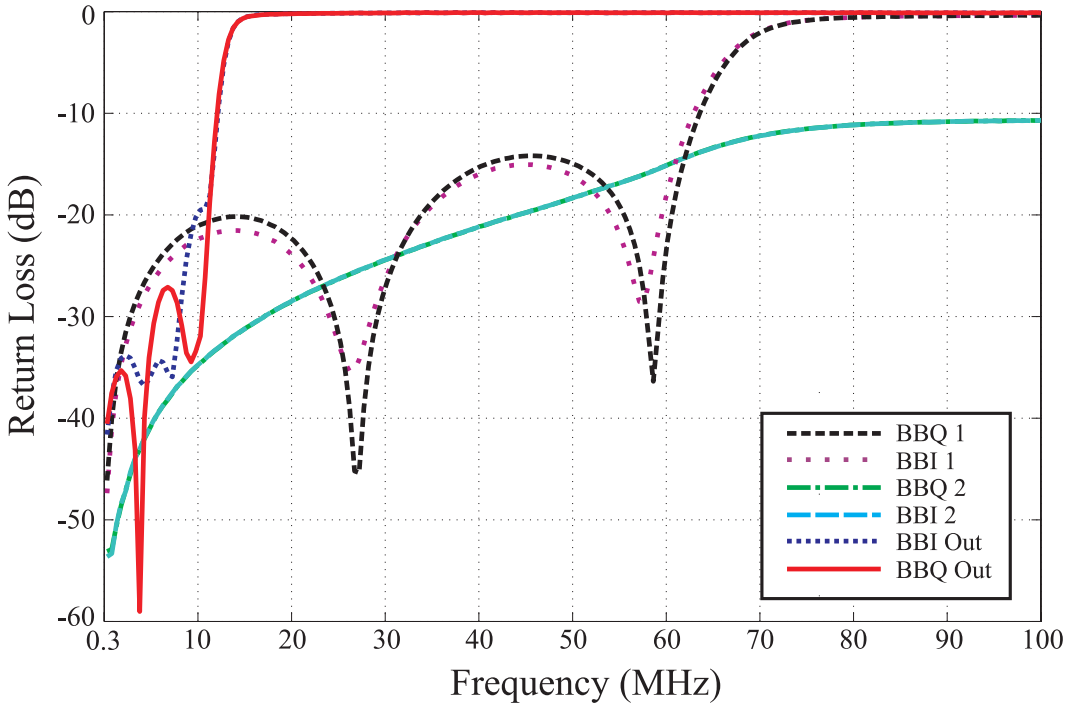

(a)

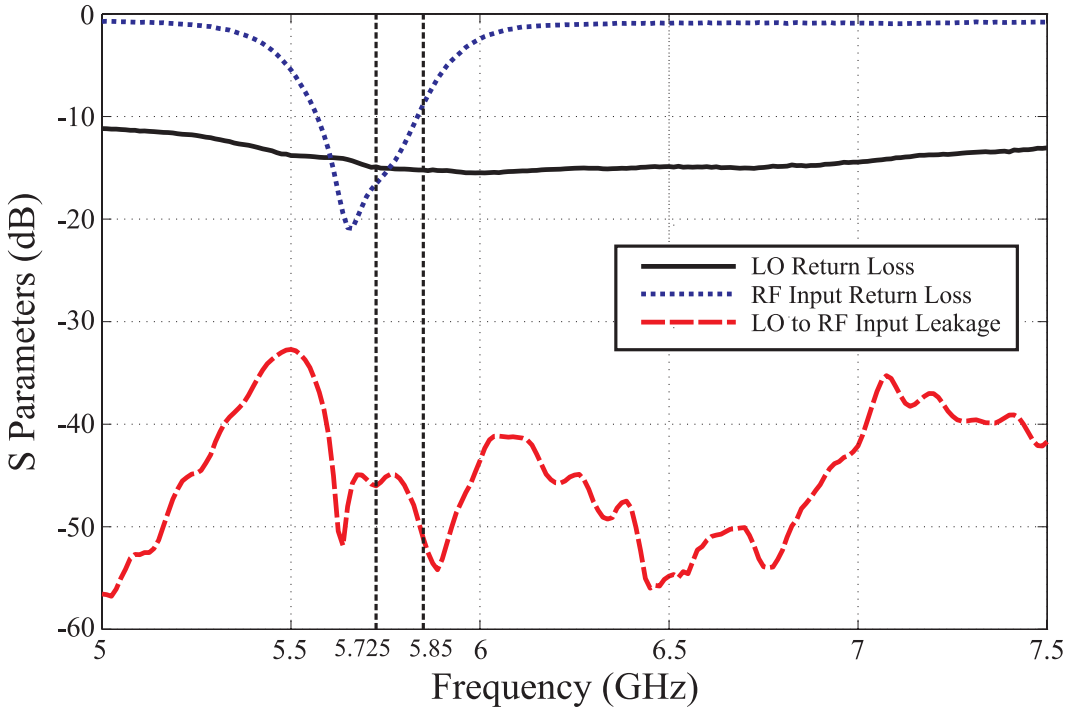

(b)

Figure 91: The (a) return loss for the baseband ports and (b) return loss and LO leakage at the ports on the RF front-end board for receiver 2.

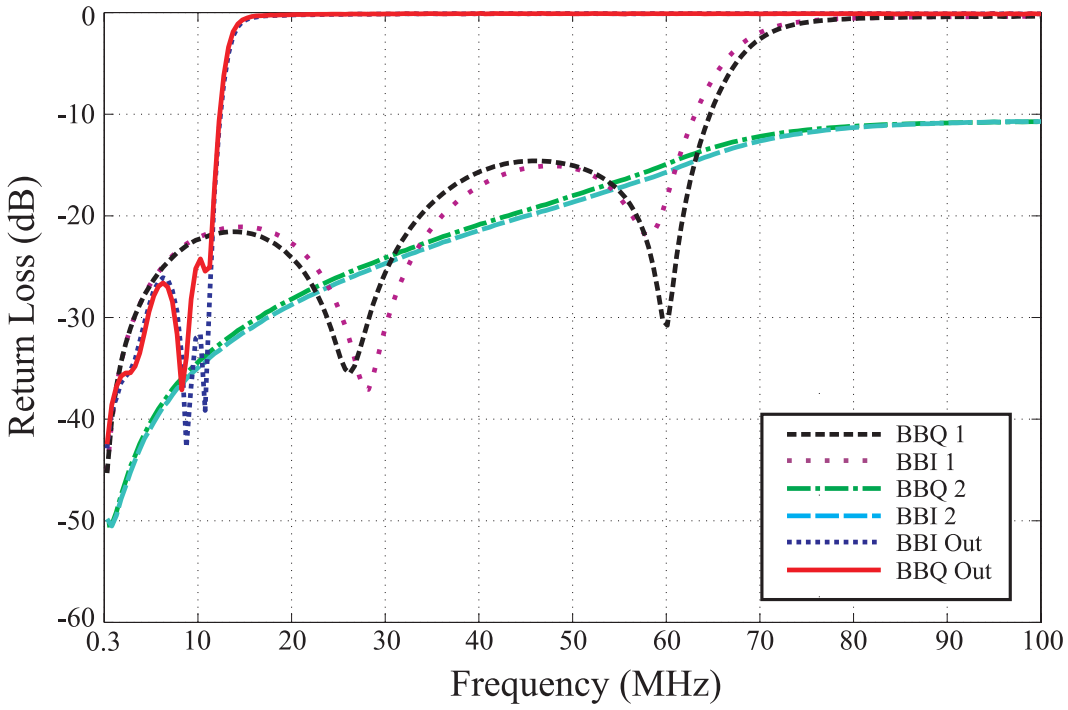

(a)

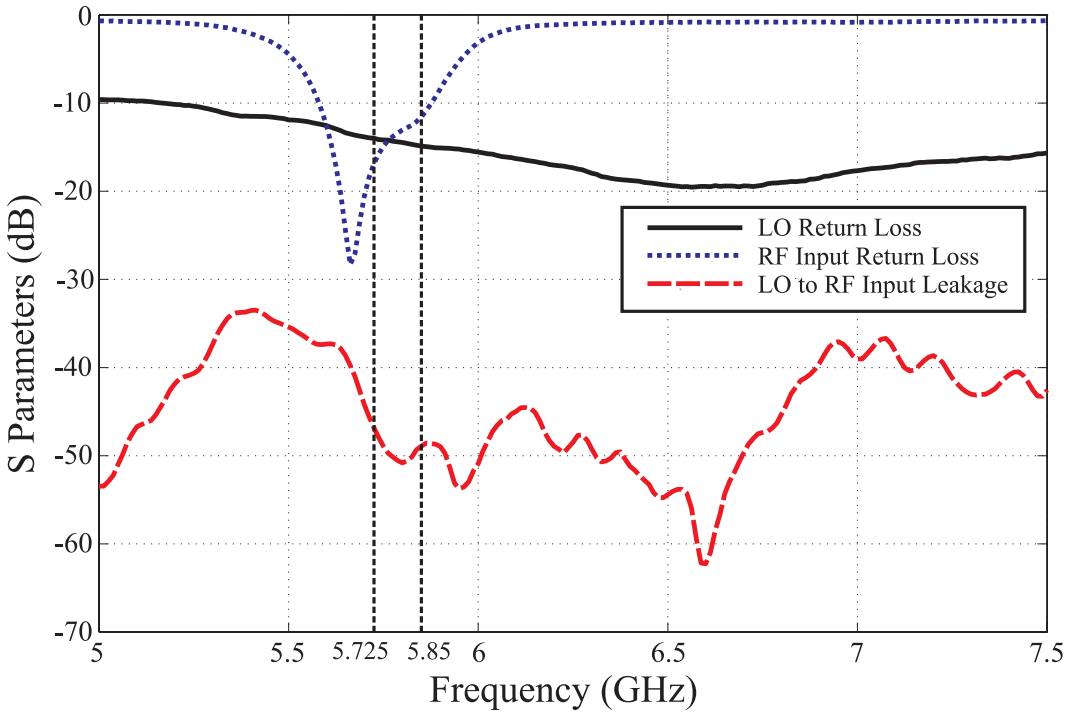

(b)

Figure 92: The (a) return loss for the baseband ports and (b) return loss and LO leakage at the ports on the RF front-end board for receiver 3.

REFERENCES

[1] H. Stockman, "Communication by Means of Reflected Power," *Proceedings of the I.R.E*, vol. 36, no. 10, pp. 1196–1204, 1948.

[2] J. Landt, "The History of RFID," *IEEE Potentials*, vol. 24, no. 4, pp. 8–11, 2005.

[3] K. Finkenzeller, *RFID Handbook: Fundamentals and Applications in Contactless Smart Cards and Identification*, 2nd ed. New York: John Wiley and Son LTD, 2003.

[4] P. Nikitin, K. V. S. Rao, and S. Lazar, "An Overview of Near Field UHF RFID," in *IEEE International Conference on RFID*, Grapevine, TX, 2007, pp. 167–174.

[5] J. D. Griffin and G. D. Durgin, "Gains for RF Tags Using Multiple Antennas," *IEEE Transactions on Antennas and Propagation*, vol. 56, no. 2, pp. 563–570, 2008.

[6] D. M. Dobkin, *The RF in RFID: Passive UHF RFID in Practice*. Burlington, MA: Newnes, 2008.

[7] K. V. S. Rao, P. V. Nikitin, and S. F. Lam, "Antenna Design for UHF RFID Tags: A Review and a Practical Application," *IEEE Transactions on Antennas and Propagation*, vol. 53, no. 12, pp. 3870–3876, 2005.

[8] K. Penttilä, L. Sydänheimo, and M. Kivikoski, "Implementation of Tx/Rx Isolation in an RFID Reader," *Int. J. Radio Frequency Identification Technology and Applications*, vol. 1, no. 1, pp. 74–89, 2006.

[9] V. Pillai, H. Heinrich, D. Dieska, P. V. Nikitin, R. Martinez, and K. V. S. Rao, "An Ultra-Low-Power Long Range Battery/Passive RFID Tag for UHF and Microwave Bands With a Current Consumption of 700 nA at 1.5 V," *IEEE Transactions on Circuits and Systems I: Regular Papers*, vol. 54, no. 7, pp. 1500–1512, 2007.

[10] J. P. Curty, N. Joehl, C. Dehollain, and M. J. Declercq, "Remotely Powered Addressable UHF RFID Integrated System," *IEEE Journal of Solid-State Circuits*, vol. 40, no. 11, pp. 2193–2202, 2005.

[11] U. Karthaus and M. Fischer, "Fully Integrated Passive UHF RFID Transponder IC with 16.7-μW Minimum RF Input Power," *IEEE Journal of Solid-State Circuits*, vol. 38, no. 10, pp. 1602–1608, 2003.

[12] A. Rohatgi and G. D. Durgin, "Implementation of an Anti-Collision Differential-Offset Spread Spectrum RFID System," in *Proceedings of the IEEE Antennas and Propagation Society International Symposium*, 2006, pp. 3501–3504.

[13] S.-R. Lee, S.-D. Joo, and C.-W. Lee, "An Enhanced Dynamic Framed Slotted ALOHA Algorithm for RFID Tag Identification," in *Proceedings of the Second Annual International Conference on Mobile and Ubiquitous Systems: Networking and Services (MobiQuitous05)*, 2005, pp. 166–172.

[14] Y. Zhang, M. G. Amin, and S. Kaushik, "Localization and Tracking of Passive RFID Tags Based on Direction Estimation," *International Journal of Antennas and Propagation*, vol. 2007, Article ID 17426, 9 pages, 2007. doi:10.1155/2007/17426.

[15] E. Cantatore, T. C. T. Geuns, G. H. Gelinck, E. van Veenendaal, A. F. A. Gruijthuijsen, L. Schrijnemakers, S. Drews, and D. M. de Leeuw, "A 13.56-MHz RFID System Based on Organic Transponders," *Solid-State Circuits, IEEE Journal of*, vol. 42, no. 1, pp. 84–92, Jan. 2007.

[16] P. Nikitin and K. V. S. Rao, "Antennas and Propagation in UHF RFID Systems," in *IEEE International Conference on RFID*, Las Vegas, TX, 2008, pp. 277–288.

[17] G. D. Durgin, *Space-Time Wireless Channels*. Upper Saddle River, NJ, USA: Prentice Hall, 2003.

[18] J. Mitsugi, "UHF Band RFID Readability and Fading Measurements in Practical Propagation Environment," in *Auto-ID Labs White Paper Series*, 2005, pp. 37–44.

[19] J. Mitsugi and Y. Shibao, "Multipath Identification Using Steepest Gradient Method for Dynamic Inventory in UHF RFID," in *International Symposium on Applications and the Internet*, Hiroshima, Japan, 2007.

[20] M. Polivka, M. Svanda, and P. Hudec, "Analysis and Measurement of the RFID System Adapted for Identification of Moving Objects," in *36th European Microwave Conference*, 2006, pp. 729–732.

[21] D. Kim, M. A. Ingram, and W. W. Smith, Jr., "Measurements of Small-scale Fading and Path Loss for Long Range RF Tags," *IEEE Transactions on Antennas and Propagation*, vol. 51, no. 8, pp. 1740–1749, 2003.

[22] S. R. Banerjee, R. Jesme, and R. A. Sainati, "Performance Analysis of Short Range UHF Propagation as Applicable to Passive RFID," in *2007 IEEE International Conference on RFID*, Gaylord Texan Resort, Grapevine, TX, USA, March 2007, pp. 30–36.

[23] ——, "Investigation of Spatial and Frequency Diversity for Long Range UHF RFID," in *IEEE Antennas and Propagation Society International Symposium*, San Diego, CA, USA, July 2008, pp. 1–4.

[24] W. C. Jakes, Ed., *Microwave Mobile Communications*. New York: IEEE Press, 1974.

[25] H.-C. Liu, Y.-F. Chen, and Y.-T. Chen, "A Frequency Diverse Gen2 RFID System with Isolated Continuous Wave Emitters," *Journal of Networks (JNW)*, vol. 2, no. 5, pp. 54–60, 2007.

[26] M. Ingram, M. Demirkol, and D. Kim, "Transmit Diversity and Spatial Multiplexing for RF Links Using Modulated Backscatter," in *Proceedings of the International Symposium on Signals, Systems, and Electronics*, Tokyo, Japan, July 2001.

[27] H. Abderrazak, B. Slaheddine, and B. Ridha, "A Transponder Anti-Collision Algorithm Based on a Multi-Antenna RFID Reader," in *Proceedings of the IEEE Information and Communication Technologies Conference*, vol. 2, 2006, pp. 2684–2688.

[28] T. B. Hansen and M. L. Oristaglio, "Method for Controlling the Angular Extent of Interrogation Zones in RFID," *Antennas and Wireless Propagation Letters*, vol. 5, no. 1, pp. 134–137, 2006.

[29] D. Hähnel, W. Burgard, D. Fox, K. Fishkin, and M. Philipose, "Mapping and Localization with RFID Technology," in *Proceedings of the 2004 IEEE International Conference on Robotics and Automation*, vol. 1, New Orleans, LA, 2004, pp. 1015–1020.

[30] J. Wang, M. Amin, and Y. Zhang, "Signal and array processing techniques for RFID readers," R. M. Rao, S. A. Dianat, and M. D. Zoltowski, Eds., vol. 6248, no. 1. SPIE, 2006, p. 624807. [Online]. Available: http://link.aip.org/link/?PSI/6248/624807/1

[31] J. S. Kim, K. H. Shin, S. M. Park, W. K. Choi, and N. S. Seong, "Polarization and Space Diversity Antenna Using Inverted-F Antennas for RFID Reader Applications," *Antennas and Wireless Propagation Letters*, vol. 5, no. 1, pp. 265–268, 2006.

[32] A. Rahmati, Z. Lin, M. Hiltunen, and R. Jana, "Reliability Techniques for RFID-Based Object Tracking Applications," in *37th Annual IEEE/IFIP International Conference on Dependable Systems and Networks (DSN'07)*, Edinburgh, UK, 2007, pp. 113–118.

[33] M. Mi, M. H. Mickle, C. Capelli, and H. Swift, "RF Energy Harvesting with Multiple Antennas in the Same Space," *IEEE Antennas and Propagation Magazine*, vol. 47, no. 5, pp. 100–106, 2005.

[34] V. Pillai, H. Heinrich, K. V. S. Rao, and R. Martinez, "A Stacked Antenna Broad-band RFID Front-end for UHF and Microwave Bands," in *Proceedings of the ACM Great Lakes Symposium on VLSI*. Boston, MA, United States: Association for Computing Machinery, New York, United States, 2004, pp. 104–108.

[35] L. Chiu, T. Y. Yum, W. S. Chang, Q. Xue, and C. H. Chan, "Retrodirective Array for RFID and Microwave Tracking Beacon Applications," *Microwave and Optical Technology Letters*, vol. 48, no. 2, pp. 409–411, 2006.

[36] G. M. Coutts, R. R. Mansour, and S. K. Chaudhuri, "A Frequency Steerable Multi-Mode Parasitic Patch Array for Passive RFID Applications," in *IEEE MTT-S International Microwave Symposium Digest*, 2006, pp. 186–189.

[37] J. D. Griffin and G. D. Durgin, "Complete Link Budgets for Backscatter Radio and RFID Systems," *IEEE Antennas and Propagation Magazine*, accepted for April, 2009.

[38] W. L. Stutzman and G. A. Thiele, *Antenna Theory and Design*, 2nd ed. Hoboken, NJ: John Wiley and Sons, 1998.

[39] G. T. Ruck, Ed., *Radar Cross Section Handbook*. New York - London: Plenum Press, 1970, vol. 1-2.

[40] P. Nikitin and K. V. S. Rao, "Performance Limitations of Passive UHF RFID Systems," in *Proceedings of IEEE Antenna and Propagation Society International Symposium*, Albuquerque, New Mexico, 2006, pp. 1011–1014.

[41] K. V. S. Rao, P. V. Nikitin, and S. F. Lam, "Impedance Matching Concepts in RFID Transponder Design," in *IEEE Workshop on Automatic Identification Advanced Technologies*, 2005, pp. 39–42.

[42] D. M. Dobkin and S. M. Weigand, "Environmental Effects on RFID Tag Antennas," in *IEEE MTT-S International Microwave Symposium Digest*, 2005, pp. 135–138.

[43] Y. Tikhov and J. H. Won, "Impedance-matching Arrangement for Microwave Transponder Operating over Plurality of Bent Installations of Antenna," *Electronics Letters*, vol. 40, no. 10, pp. 574–575, 2004.

[44] J. Siden, P. Jonsson, T. Olsson, and G. Wang, "Performance Degradation of RFID System Due to the Distortion in RFID Tag Antenna," in *Conference Proceedings of Microwave and Telecommunication Technology*. Sevastopol, Crimea, Ukraine: Weber Co., 2001, pp. 371–373.

[45] G. De Vita and G. Iannaccone, "Design Criteria for the RF Section of UHF and Microwave Passive RFID Transponders," *IEEE Transactions on Microwave Theory and Techniques*, vol. 53, no. 9, pp. 2978–2990, 2005.

[46] J. T. Prothro and G. D. Durgin, "Improved Performance of a Radio Frequency Identification Tag Antenna on a Metal Ground Plane," Master's thesis, The Georgia Institute of Technology, 2007. [Online]. Available: http://www.propagation.gatech.edu/Archive/PG_TR_070515_JTP/PG_TR_070515_JTP.pdf

[47] P. V. Nikitin and K. V. S. Rao, "Theory and Measurement of Backscattering from RFID Tags," *IEEE Antennas and Propagation Magazine*, vol. 48, no. 6, pp. 212–218, 2006.

[48] K. Penttilä, M. Keskilammi, L. Sydänheimo, and M. Kivikoski, "Radar Cross-Section Analysis for Passive RFID Systems," *IEE Proceedings on Microwaves, Antennas and Propagation*, vol. 153, no. 1, pp. 103–109, 2006.

[49] F. Fuschini, C. Piersanti, F. Paolazzi, and G. Falciasecca, "Analytical Approach to the Backscattering from UHF RFID Transponder," *IEEE Antennas and Wireless Propagation Letters*, vol. 7, pp. 33–35, 2008.

[50] R. B. Green, "The General Theory of Antenna Scattering," Ph.D. dissertation, Ohio State University, 1963.

[51] P. V. Nikitin, K. V. S. Rao, and R. D. Martinez, "Differential RCS of RFID Tag," *Electronics Letters*, vol. 43, no. 8, pp. 431–432, 2007.

[52] J. D. Griffin and G. D. Durgin, "Link Envelope Correlation in the Backscatter Channel," *IEEE Communications Letters*, vol. 11, no. 9, pp. 735–737, 2007.

[53] J. D. Griffin, G. D. Durgin, A. Haldi, and B. Kippelen, "RF Tag Antenna Performance on Various Materials Using Radio Link Budgets," *IEEE Antennas and Wireless Propagation Letters*, vol. 5, pp. 247–250, 2006.

[54] J. D. Parsons, *The Mobile Radio Propagation Channel*, 2nd ed. West Sussex, England: John Wiley and Sons, 2000.

[55] S. Chiu, I. Kipnis, M. Loyer, J. Rapp, D. Westberg, J. Johansson, and P. Johansson, "A 900 MHz UHF RFID Reader Transceiver IC," *IEEE Journal of Solid-State Circuits*, vol. 42, no. 12, pp. 2822–2833, 2007.

[56] D. M. Dobkin and S. M. Weigand, "UHF RFID and tag antenna scattering, Part I: Experimental results," *Microwave Journal, Euro-Global Edition*, vol. 49, no. 5, pp. 170–190, 2006.

[57] D. Chizhik, G. J. Foschini, and R. A. Valenzuela, "Capacities of Multi-Element Transmit and Receive Antennas: Correlations and Keyholes," *Electronics Letters*, vol. 36, no. 13, pp. 1099–1100, 2000.

[58] D. Chizhik, G. J. Foschini, M. J. Gans, and R. A. Valenzuela, "Keyholes, Correlations, and Capacities of Multielement Transmit and Receive Antennas," *IEEE Transactions on Wireless Communications*, vol. 1, no. 2, pp. 361–368, 2002.

[59] V. Erceg, S. J. Fortune, J. Ling, J. Rustako, A. J., and R. A. Valenzuela, "Comparisons of a Computer-Based Propagation Prediction Tool with Experimental Data Collected in Urban Microcellular Environments," *IEEE Journal on Selected Areas Communications*, vol. 15, no. 4, pp. 677–684, 1997.

[60] D. Gesbert, H. Bölcskei, D. A. Gore, and A. J. Paulraj, "Outdoor MIMO Wireless Channels: Models and Performance Prediction," *IEEE Transactions on Communications*, vol. 50, no. 12, pp. 1926–1934, 2002.

[61] C. S. Patel, G. L. Stüber, and T. G. Pratt, "Statistical Properties of Amplify and Forward Relay Fading Channels," *IEEE Transactions on Vehicular Technology*, vol. 55, no. 1, pp. 1–9, 2006.

[62] D. M. Pozar, *Microwave Engineering*, 3rd ed. Hoboken, NJ: John Wiley and Sons, 2005.

[63] J. N. Pierce and S. Stein, "Multiple Diversity with Nonindependent Fading," *Proceedings of the IRE*, vol. 48, pp. 89–104, 1960.

[64] R. G. Vaughan and J. B. Andersen, "Antenna Diversity in Mobile Communications," *IEEE Transactions on Vehicular Technology*, vol. VT-36, no. 4, pp. 149–172, 1987.

[65] G. D. Durgin, T. S. Rappaport, and D. A. de Wolf, "New Analytical Models and Probability Density Functions for Fading in Wireless Communications," *IEEE Transactions on Communications*, vol. 50, no. 6, pp. 677–684, 2002.

[66] D. T. Auckland, W. Klimczak, and G. D. Durgin, "Maximizing Throughput with Ultra-Compact Diversity Antennas," in *Proceedings of the IEEE Vehicular Technology Conference 2003-Fall*, vol. 1, Orlando, FL, USA, 2003, pp. 178–182.

[67] Y. Yamada, K. Kagoshima, and K. Tsunekawa, "Diversity Antennas for Base and Mobile Stations in Land Mobile Communication Systems," *IEICE Transactions*, vol. E74, no. 10, pp. 3202–3209, 1991.

[68] R. W. Dixon, *Spread Spectrum Systems with Commercial Applications*, 3rd ed. New York: Wiley Interscience, 1994.

[69] A. Safarian, A. Shameli, A. Rofougaran, M. Rofougaran, and F. De Flaviis, "An Integrated RFID Reader," in *IEEE International Solid-State Circuits Conference*, San Francisco, CA, 2007, pp. 218–219, 598.

[70] J. Lee, J. Choi, K. H. Lee, B. Kim, M. Jeong, Y. Cho, H. Yoo, K. Yang, S. Kim, S.-M. Moon, J.-Y. Lee, S. Park, W. Kong, J. Kim, T.-J. Lee, B.-E. Kim, and B.-K. Ko, "A UHF Mobile RFID Reader IC with Self-Leakage Canceller," in *IEEE Radio Frequency Integrated Circuits (RFIC) Symposium*, 2007, pp. 273–276.

[71] G. Ibrahim, J. Sensening, and T. Al-Mahdawi, "Dynamic Reflection of RF Signals from Fluorescent Lights: Their Spectral Analysis and Effects on Backscattered RFID Tag Signals," in *2007 IEEE Sarnoff Symposium*, April 30 – May 2 2007 2007, pp. 1–5.

[72] R. J. Pirkl and G. D. Durgin, "Optimal Sliding Correlator Channel Sounder Design," *IEEE Transactions on Wireless Communications*, vol. 7, no. 9, pp. 3488–3497, 2008.

[73] M. K. Simon, *Probability Distributions Involving Gaussian Random Variables: A Handbook for Engineers and Scientists*. Norwell, MA: Kluwer Academic Publishers, 2002.

[74] S. O. Rice, "Statistical Properties of a Sine Wave Plus Random Noise," *Bell System Technical Journal*, vol. 27, no. 1, pp. 109–257, January 1948.

[75] ——, "Mathematical Analysis of Random Noise," *Bell System Technical Journal*, vol. 23, pp. 282–332, July 1944.

[76] E. W. Weisstein, "Confluent Hypergeometric Function of the First Kind," from MathWorld – A Wolfram Web Resource. http://mathworld.wolfram.com/ConfluentHypergeometricFunctionoftheFirstKind.html.

[77] B. Razavi, "Design Considerations for Direct-Conversion Receivers," *IEEE Transactions on Circuits and Systems-II: Analog and Digital Signal Processing*, vol. 44, no. 6, pp. 428–435, 1997.

[78] F. E. Churchill, G. W. Ogar, and B. J. Thompson, "The Correction of I and Q Errors in a Coherent Processor," *IEEE Transactions on Aerospace and Electronic Systems*, vol. AES-17, no. 2, pp. 131–137, 1981.

VITA

Joshua Griffin received his BS in Engineering from LeTourneau University in 2003, his MS in Electrical and Computer Engineering (ECE) from the Georgia Institute of Technology in 2005, and his PhD in ECE at the Georgia Institute of Technology in 2009. In 2004, he joined The Propagation Group at Georgia Tech where he began researching UHF and microwave radio propagation, wireless communication using scattered waves, and radio frequency identification (RFID) applications. His expertise is the study of multipath fading experienced by backscatter RFID systems and methods to reduce it using multiple antennas. He has successfully published his work in several journals and presented at numerous conferences and universities around the world. In 2006, he participated in a three-month research exchange program with the Sampei Laboratory at Osaka University in Osaka, Japan. In 2009, he accepted a post-doctoral position with Disney Research Pittsburgh and works on backscatter RFID systems in collaboration with researchers at Carnegie Mellon University.